Radiation tolerance and performance of planar pixel assemblies for the Phase-2 Upgrade of the CMS Inner Tracker

Dissertation
zur Erlangung des Doktorgrades
an der Fakultät für Mathematik, Informatik und Naturwissenschaften
Fachbereich Physik
der Universität Hamburg

vorgelegt von
Bianca Raciti

Hamburg
2025

Gutachter/innen der Dissertation:
Prof. Dr. Erika Garutti
Dr. Antonio Cassese

Zusammensetzung der Prüfungskommission:
Dr. Antonio Cassese
Prof. Dr. Elisabetta Gallo
Prof. Dr. Erika Garutti
Dr. Katja Krüger
Prof. Dr. Daniela Pfannkuche

Vorsitzende/r der Prüfungskommission:
Prof. Dr. Daniela Pfannkuche

Datum der Disputation:
10.12.2025

Vorsitzender des Fach-Promotionsausschusses PHYSIK:
Prof. Dr. Wolfgang J. Parak

Leiter des Fachbereichs PHYSIK:
Prof. Dr. Markus Drescher

Dekan der Fakultät MIN:
Prof. Dr.-Ing. Norbert Ritter

A Maria Chiara.

Abstract

The aim of this work is to evaluate the performance of planar hybrid pixel detectors designed for the High-Luminosity (HL-LHC) Upgrade of the Inner Tracker of the Compact Muon Solenoid (CMS) experiment at CERN. The HL-LHC will deliver a peak instantaneous luminosity of $7.5 \times 10^{34}\,\mathrm{cm^{-2}\,s^{-1}}$, resulting in a total expected fluence for planar sensors of around $\phi_{\mathrm{eq}} = 1 \times 10^{16}\,\mathrm{cm^{-2}}$ after an integrated luminosity of $3000\,\mathrm{fb^{-1}}$.

To operate under such extreme radiation levels and high track densities, the new n^+-in-p sensors will feature pixels with pitches of $25{\times}100\,\mu\mathrm{m}^2$, covering an area six times smaller than their Phase-1 counterparts. This work focuses on the characterization of 150 µm thick planar sensors manufactured by Hamamatsu Photonics K.K. These sensors are bump-bonded to the RD53B_CMS readout chip and tested using a 5.2 GeV electron beam at the DESY II test beam facility. Key observables such as cluster size, noise, threshold, hit efficiency, and spatial resolution are measured as a function of both the applied bias voltage and the beam incidence angle.

The modules are characterized before and after irradiation with 24 GeV/c protons to fluences up to $\phi_{\mathrm{eq}} = 1 \times 10^{16}\,\mathrm{cm^{-2}}$. For perpendicular incidence, hit efficiencies exceeding the corresponding fluence-dependent benchmarks are achieved for bias voltages as low as 5 V before irradiation, and in the range of 400 V–500 V after irradiation, for all thresholds under study, while keeping the amount of disabled pixels below the 1% limit, fulfilling the requirements for the second layer of the Phase-2 pixel detector. These measurements reveal that the optimal efficiency is achieved for a charge threshold of 1200 $\mathrm{e^-}$ and a bias voltage of 600 V for all investigated fluences.

A spatial resolution of circa 3 µm was measured before irradiation at the optimal track incidence angle, degrading to about 4 µm after irradiation to the highest fluence under exam.

The characterization of these assemblies included in-depth studies of the correlation between crosstalk and readout timing in the first half-size demonstrator (RD53A) and in the pre-series version of the chips (RD53B_CMS). By using the integrated charge injection circuit, crosstalk levels well-below the established 10% limit were measured for the optimal readout scheme, meeting the associated requirement.

Zusammenfassung

Ziel dieser Arbeit ist die Untersuchung der Leistungsfähigkeit von planaren hybriden Pixeldetektoren, die für das High-Luminosity Upgrade (HL-LHC) des Inner Trackers des Compact Muon Solenoid (CMS) Experiments am CERN entwickelt wurden. Der HL-LHC hat eine maximale instantane Luminosität von bis zu $7.5 \times 10^{34}\,\mathrm{cm}^{-2}\,\mathrm{s}^{-1}$. Nach zehn Jahren Laufzeit entspricht dies einer integrierten Luminosität von $3000\,\mathrm{fb}^{-1}$, was zu maximalen Fluenzen von $\phi_{\mathrm{eq}} = 1 \times 10^{16}\,\mathrm{cm}^{-2}$ für planare Sensoren führt.

Um unter solch extremen Strahlungsbedingungen und hohen Teilchendichten betrieben werden zu können, verfügen die neuen n^+-in-p Sensoren über Pixel mit Abmessungen von $25\times100\,\mu\mathrm{m}^2$, die sechsmal kleiner als ihre Vorgänger in Phase-1. Diese Arbeit konzentriert sich auf die Charakterisierung von 150 µm dicken planaren Sensoren, die von Hamamatsu Photonics K.K. hergestellt wurden. Die Sensoren wurden mit dem RD53B_CMS-Auslesechip per *fine pitch bump-bonding* verbunden und mit einem 5.2 GeV Elektronenstrahl an der DESY-II-Teststrahlanlage vermessen. Wichtige Observablen wie Clustergröße, Rauschen, Schwellwert, Treffereffizienz und Ortsauflösung wurden in Abhängigkeit von angelegter Bias-Spannung und Einfallswinkel des Strahls untersucht.

Die Module wurden vor und nach Bestrahlung mit 24 GeV/c Protonen bis zu Fluenzwerten von $\phi_{\mathrm{eq}} = 1 \times 10^{15}\,\mathrm{cm}^{-2}$ charakterisiert. Für senkrechten Einfall wurden bereits bei Bias-Spannungen von 10 V vor Bestrahlung sowie im Bereich von 400 V bis 500 V nach Bestrahlung, für alle untersuchten Schwellwerte Effizienzen oberhalb der fluenzabhängigen Benchmarkwerte erreicht. Dabei blieb der Anteil maskierter Pixel stets unter 1 %, womit die Anforderungen für die zweite Lage des Phase-2-Pixeldetektors erfüllt werden. Es zeigte sich, dass die optimale Effizienz für einen Schwellwert von 1200 e^- und eine Bias-Spannung von 600 V für alle betrachteten Fluenzwerte erreicht wird.

Vor der Bestrahlung wurde eine Ortsauflösung von etwa 3 µm bei optimalem Einfallswinkel gemessen, die sich nach Bestrahlung bis zur höchsten untersuchten Fluenz auf etwa 4 µm verschlechtert.

Die Charakterisierung dieser Module umfasste zudem detaillierte Untersuchungen der Korrelation zwischen Crosstalk und Auslesetiming sowohl im ersten halbgroßen Demonstratorchip (RD53A) als auch in der Vorserienversion (RD53B_CMS). Unter Verwendung des integrierten Ladungsinjektionsschaltkreises konnten Crosstalk-Werte deutlich unterhalb der festgelegten Grenze von 10 % nachgewiesen werden, womit die entsprechenden Anforderungen erfüllt sind.

Contents

1. Introduction

The Standard Model of particle physics (SM) represents our most comprehensive theoretical framework for describing fundamental particles and their interactions [1]. It has been extensively validated through decades of experimental results from both lepton and hadron colliders, and the last missing piece – the Higgs boson – was discovered at the Large Hadron Collider (LHC) in 2012 [2, 3]. Despite its success, the SM leaves several key questions unanswered. Extensions to the SM, such as Supersymmetry [4] and Grand Unified Theories [5], attempt to address these limitations and predict the existence of new particles, some of which could lie at the TeV scale: within reach of the LHC's energy range.

To enhance its discovery potential and improve the statistical precision of its measurements, the LHC will undergo a major upgrade in the coming years. The High-Luminosity LHC (HL-LHC) phase will significantly increase both the instantaneous and integrated luminosity of the machine. The Compact Muon Solenoid (CMS) experiment [6], one of the main detectors at the LHC, will undergo a substantial upgrade in preparation for this phase [7], and its current pixel detector will be completely replaced by the Inner Tracker (IT) to meet the more demanding operating conditions.

The increased instantaneous luminosity will result in significantly higher particle fluxes, requiring finer pixel granularity to control detector occupancy. At the same time, the cumulative radiation damage will increase due to the higher integrated luminosity. To mitigate these effects, the upgraded sensors will have a reduced thickness, enhanced radiation tolerance, and a surface six times smaller than their current counterparts.

The assemblies investigated in this work are hybrid planar pixel detectors featuring a "bitten" sensor design, developed to reduce capacitive crosstalk between neighboring pixels. These sensors, produced by Hamamatsu Photonics K.K., are bump-bonded to the RD53B_CMS readout chip (also known as CROCv1), the first full-scale prototype developed after the half-sized RD53A demonstrator chip. As of the time of writing, modules based on the RD53C_CMS readout chip – the final iteration intended for installation in the CMS Inner Tracker – are undergoing qualification at the production centers. The availability of RD53B_CMS enabled, for the first time, the characterization of full-size pixel modules at the DESY II test beam facility, and the study of key observables such as efficiency, spatial resolution, and crosstalk, both before and after irradiation. To support this development, a new data acquisition system, Ph2_ACF [8], was introduced. Specifically designed for the HL-LHC upgrade, it enabled performance studies at the test beam,

it is currently serving as a cornerstone for quality-control procedures at the production centers, and will be deployed in the final detector for both the Inner Tracker and Outer Tracker.

The primary aim of this thesis is to demonstrate that planar pixel sensors with the bitten design, when coupled to the RD53B_CMS readout chip, satisfy all the requirements for operation at the HL-LHC. In particular, this work investigates the dependence of critical observables on the readout threshold and the accumulated fluence, reflecting the expected operating conditions throughout the detector's lifetime.

Additionally, a strong correlation between the timing of the readout and the effective threshold is identified and explored in detail for both the RD53A and the RD53B_CMS flavours of the readout chip, revealing its key role in evaluating the correct crosstalk levels within the 25 ns bunch-crossing window.

Complementing the experimental results, a simulation of the sensor assemblies was performed using the Allpix Squared [9] framework. This simulation includes a realistic model of both the sensor geometry and the readout electronics, embedded within a representation of the test beam setup. The agreement between the simulated and measured results confirms the robustness of the simulation chain, and demonstrates the potential of the framework as a predictive tool for exploring the detector response under varying conditions.

This thesis is structured as follows: Chapter 2 introduces the fundamental operating principles of silicon detectors and their role in the CMS experiment, which is described in Chapter 3. Chapter 4 details the specific sensors and readout chips studied in this work, while Chapter 5 discusses the interplay between readout timing and the measured crosstalk levels. The test beam setup used for the characterization is described in Chapter 6, and the methodology for data analysis is presented in Chapter 7. Results from test beam measurements are reported in Chapter 8. Finally, Chapter 9 presents a validation of a simulation framework for non-irradiated sensors using the experimental data.

2. Physics of silicon pixel sensors

2.1. Silicon: properties and concepts

A detailed discussion of the physics of semiconductor devices and the key properties of silicon can be found in [10], which serves as the foundation for the following brief overview. Detector-grade silicon is monocrystalline and has a diamond-like lattice structure. In crystals, the discrete energy levels of individual atoms merge into energy bands due to atomic interactions. The highest energy band occupied at a temperature $T = 0\,\mathrm{K}$ is called the *valence band*, while the band above is known as the *conduction band*.

Silicon is classified as a semiconductor. Figure 2.1 illustrates the schematic energy band diagrams of a conductor, semiconductor, and insulator. In conductors, the valence band is either partially filled or it overlaps with the conduction band, allowing electrons to move freely and contribute to the electrical current. In semiconductors and insulators, the valence and conduction bands are separated by an energy gap known as the *bandgap* (E_g). The key difference between them lies in the size of the bandgap, which determines the likelihood of thermal excitation of electrons from the valence band to the conduction band. In this case, an electron in the conduction band and a vacant state in the valence band, referred to as a *hole*, can both contribute to an electric current. In semiconductors, the bandgap is typically circa 1 eV. For high-purity silicon, the bandgap is 1.12 eV at room temperature. The number of free charge carriers in semiconductors – electrons in the conduction band and holes in the valence band – can be controlled by introducing specific impurities into the crystal, with a process known as *doping*. These impurities are classified as either *donors* or *acceptors*. In silicon, atoms such as arsenic or phosphorus act as donors, introducing additional energy states just below the conduction band. The ionization energy of phosphorus in silicon, for example, is measured at 0.046 eV [11], making these atoms highly likely to be ionized at room temperature. This process adds extra negative charge carriers to the semiconductor, making the material n-type. Similarly, acceptor atoms like boron and aluminum introduce additional vacant states near the valence band. At room temperature, these states are typically filled, leaving holes in the valence band. The electrons from the valence band are accepted, and the material is called p-type. Figure 2.2 schematically shows the concentrations of charge carriers (n and p) in intrinsic, n-type, and p-type semiconductors. These concentrations are calculated from the product of the density of states and the Fermi-Dirac distribution, $N(E) \cdot \mathrm{F}(E)$, integrated over the conduction or valence band. The system is assumed to be in thermal equilibrium and

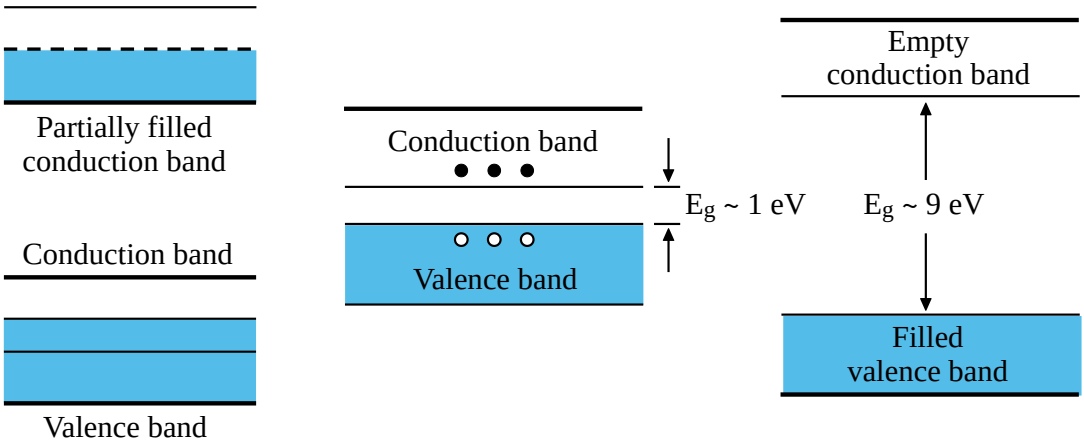

Figure 2.1.: Schematic band diagrams for a conductor (left), semiconductor (center), and insulator (right). Filled circles represent thermally excited electrons, open circles indicate empty states (holes) in the valence band. Adapted from [10].

non-degenerate, meaning the doping levels are lower than the effective densities of states in the conduction and valence bands. Detailed calculations can be found in [11].

Another key concept in silicon device physics is the p-n junction. Following [12], p-n junction is the name given to the boundary between n-type and p-type regions within a semiconductor. Due to differences in electron concentrations, electrons diffuse from the n-type to the p-type region, where they recombine with holes. Similarly, holes diffuse from the p-type to the n-type region and recombine with electrons. This process creates a space charge region, positive on the n-type side and negative on the p-type side, known as the *depletion region*, as it is largely devoid of free charge carriers. The resulting space charge generates an electric field that opposes further diffusion, and equilibrium is eventually established. Figure 2.3 illustrates the depletion region, electric field, and electric potential for an abrupt, one-dimensional p-n junction at equilibrium. The donor and acceptor densities are labeled N_D and N_A ($N_D \approx 10^{19}\,\mathrm{cm}^{-3}$ and $N_A \approx 4 \times 10^{14}\,\mathrm{cm}^{-3}$ in our sensor design), and the depletion region widths in the p-type and n-type regions are denoted as W_{Dp} and W_{Dn}, respectively. The potential difference between the p-type and n-type regions is referred to as the *built-in potential*, Ψ_{bi}.

The silicon sensors studied in this work feature a junction between a highly doped n-type region, known as the n^+ region, and a p-type material. For an abrupt junction where the donor concentration is much greater than the acceptor concentration, the total width $W = W_{Dp} + W_{Dn}$ of the depletion region is mainly determined by the p-type side:

$$W \approx \sqrt{\frac{2\varepsilon_{\mathrm{Si}}\varepsilon_0}{eN_A}(\Psi_{\mathrm{bi}} + V_{\mathrm{bias}})}\,, \tag{2.1}$$

where e represents the elementary charge, ε_0 is the vacuum permittivity, $\varepsilon_{\mathrm{Si}}$ denotes the relative permittivity of silicon, and V_{bias} is an additional positive voltage applied between the n^+ side of the junction and the p^+ implant on the backside. As the bias voltage applied

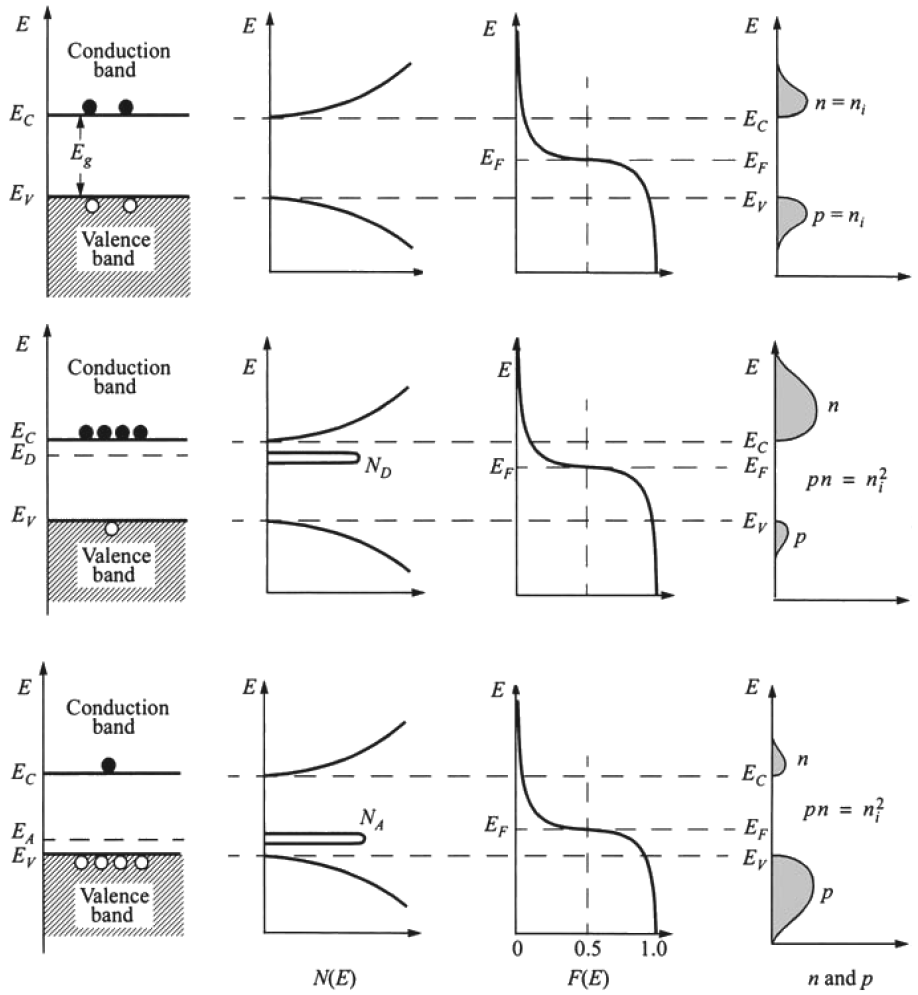

Figure 2.2.: Schematic band diagram: density of states $N(E)$, Fermi-Dirac distribution F(E), and charge carrier concentrations n and p for intrinsic, n-type, and p-type semiconductors (from top to bottom). Adapted from [11].

across the junction increases, the depletion region expands, while the current through the p-n junction remains small. This configuration is referred to as *reverse bias*, which is how silicon sensors are typically operated. When the bias voltage becomes sufficiently large, the depletion region extends to the full thickness of the silicon sensor. Beyond this point, a further expansion of the depletion zone is usually limited by a highly doped p^+ region. The voltage at which the depletion region reaches the full sensor thickness is called the *full depletion voltage* ($W = d$), and is given by:

$$V_{\text{depl}} = \frac{e|\text{N}_{\text{eff}}|d^2}{2\varepsilon_{\text{Si}}\varepsilon_0},$$

neglecting the built-in potential. Here N_A is substituted with $|N_{\text{eff}}|$, replacing the acceptor concentration with the effective space charge density. This proves to be especially useful when dealing with the analysis of irradiated sensors, although it assumes that the effective space charge remains constant throughout the p-type bulk material. In reality, irradiation introduces donor- and acceptor-like defects that do not distribute evenly across

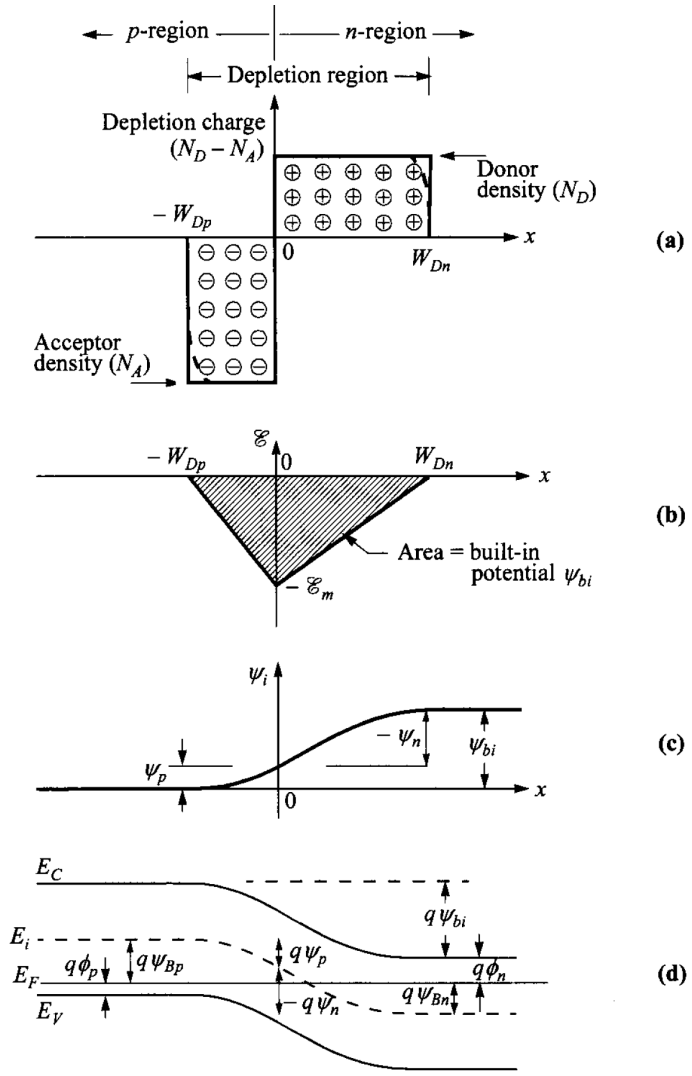

Figure 2.3.: Schematic depiction of the depletion region, electric field, and electric potential (top to bottom) for an abrupt p-n junction in equilibrium. Adapted from [11].

the detector's thickness, leading to a spatially varying effective doping concentration. As a result, the local space charge density becomes non-uniform, and the internal electric field deviates from the simple linear profile expected before irradiation. In many heavily irradiated sensors, this non-uniformity manifests as a double peak structure [13], where enhanced fields develop near the electrodes, while the central region exhibits a reduced field. This complex behavior challenges the conventional definition of a single depletion voltage, since full charge collection may occur even in regions that are not uniformly depleted.

2.2. Energy loss in silicon

The detection of particles relies on the principle that charged particles lose energy as they travel through matter. Part of this energy contributes to the creation of electron-hole

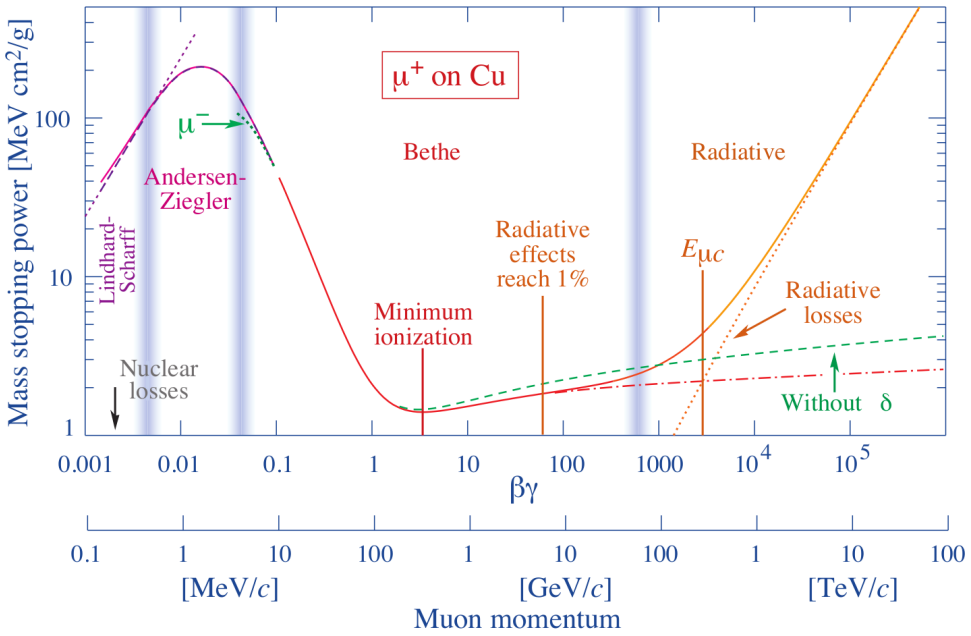

Figure 2.4.: Mass stopping power for antimuons in copper plotted as a function of the antimuon momentum and $\beta\gamma$. Adapted from [15].

pairs in semiconductor detectors, electrons and ions in gaseous detectors, and photons in scintillators, all of which produce detectable signals. A detailed explanation of the interactions between particles and matter is given in [14], with an overview provided in [15] serving as the foundation for this Section.

For charged particles with masses larger than the electron mass m_e, the *Bethe equation* describes the mean energy loss rate, denoted as $\langle -dE/dx \rangle$, also known as the *mass stopping power*, within the range $0.1 < \beta\gamma < 1000$. Here, x represents the distance traveled, and $\beta = v/c$, with v being the particle's velocity and c the speed of light. The Lorentz factor γ is calculated based on the particle's velocity or energy:

$$\gamma = \frac{1}{\sqrt{1-\beta^2}} = \frac{E}{m}\,. \tag{2.2}$$

In this range, energy loss is mainly due to ionization and excitation of atoms in the material. The Bethe equation can be found in [15], and the corresponding energy loss $\langle -dE/dx \rangle$ for antimuons in copper is shown in Figure 2.4. For lower momenta, corrections such as atomic binding energies must be considered, as discussed in [16]. For higher momenta, radiative processes like electron-positron pair production and bremsstrahlung become significant and dominate above a critical energy $E_{\mu c}$, as described in [15]. Both regions are illustrated in the figure, including the density effect correction δ. For $\beta\gamma \approx 3$ the energy loss reaches a minimum, and particles that lose energy at this rate are called Minimum-Ionizing Particles (MIPs). Typically, particle detectors are evaluated based on their performance in detecting MIPs, which produce the smallest possible signals.

The energy loss of a single particle is subject to fluctuations. The corresponding energy loss distributions are known as *straggling functions* and are highly skewed. In practice,

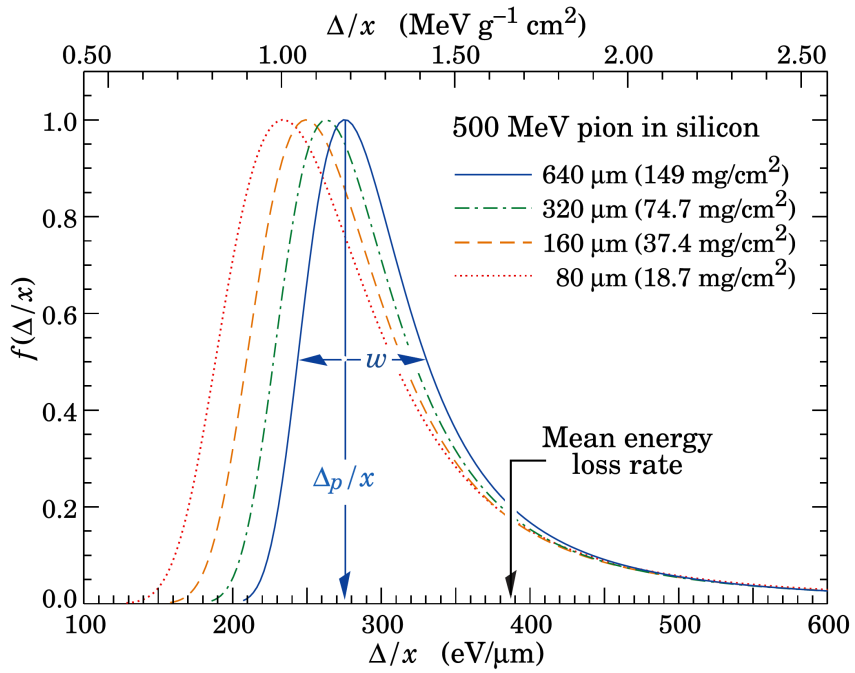

Figure 2.5.: Straggling functions f for 500 MeV pions in silicon with varying thickness x. The energy loss is denoted as Δ, and Δ_p represents the most probable energy loss, while w is the full width at half maximum. The functions are normalized to unity at their maximum value. Adapted from [15].

the mean energy loss rate is of limited use because rare, large energy depositions cause significant fluctuations, especially for small samples, making the measurement sensitive to data cuts [15]. Figure 2.5 shows straggling functions for 500 MeV/c pions passing through silicon of different thicknesses.

In this work, silicon sensors with a thickness of about 150 µm are tested using an electron beam with a momentum of circa 5 GeV/c. For electron momenta greater than a few MeV/c, radiative processes must be considered in energy loss calculations [14]. However, in thin silicon sensors with thicknesses in the order of 100 µm the effect is minor, as explained by Bichsel [17]. This is due to the fact that most of the generated photons are hard and do not interact within the silicon, making their contribution to electron-hole pair generation negligible. Therefore, the energy loss distributions from [17] can be used to estimate the number of electron-hole pairs expected under the specified experimental conditions. The Most-Probable Value (MPV) of the energy loss distributions, denoted as Δ_p, is given by:

$$\Delta_p = d \cdot [190 + 16.3 \ln(d)] \,, \tag{2.3}$$

where Δ_p is in keV, and d is the thickness of the silicon absorber in µm. This value is reported to be accurate within 1% for electrons, pions, and protons with $\beta\gamma > 100$. Additionally, the full width at half maximum of the calculated straggling functions is also reported to agree within 1% for particles at $\beta\gamma > 100$.

Evaluating Equation 2.3 for a thickness of 150 µm results in a most probable energy loss of 40.8 keV. Considering the mean ionization energy in silicon, which is 3.66 eV at room temperature [18], this corresponds to an expected MPV of 11.1×10^3 electron-hole pairs (11.1 ke). In comparison, the specific calculation for a MIP can be obtained from Figure 34.6 in [15], resulting in a most probable energy loss in 150 µm of silicon of about 37.3 keV. Thus, the energy loss for MIPs is approximately 9% lower compared to 5 GeV/c electrons, justifying the usage of this term throughout this work.

Another important aspect of the interaction of charged particles with matter is the angular deflection they experience when passing through material. This net deflection is mainly caused by many small-angle deflections due to Coulomb interactions with nuclei, known as *multiple Coulomb scattering*. Infrequent large-angle deflections create tails in the distribution of scattering angles. Here, a Gaussian approximation is used, following the parametrizations from [19]. A more accurate description of angular distributions is provided by Molière [20] and references in [19]. In the Gaussian model, the distribution of deflection angles in two directions orthogonal to the particle's initial direction has a root mean square (RMS) value given by:

$$\theta_0 = \frac{13.6\,\mathrm{MeV}}{\beta c|\vec{p}|} Z \sqrt{\frac{X}{X_0}} \left[1 + 0.088 \log_{10}\left(\frac{X Z^2}{X_0 \beta^2}\right)\right]. \tag{2.4}$$

In this equation, $|\vec{p}|$ represents the absolute momentum of the incident particle, and Z denotes its charge number. The thickness of the scattering material X is expressed in terms of the corresponding radiation length, X_0, which represents the average distance over which the energy of an electron is reduced to $1/e$ (e being Euler's number) of its initial value due to bremsstrahlung emission [15]. Tabulated values for X_0 can be found in [21].

2.3. Radiation damage in silicon

During operation, particle detectors are exposed to a high flux of particles, which can interact with the detector material and alter its physical properties, potentially impacting its performance. This degradation is known as *radiation damage*. In silicon devices, two types of radiation damage must be addressed: *surface damage* and *bulk damage*.

The mechanisms behind surface damage and its main characteristics are detailed in [22]. Surface damage is caused by the ionizing energy loss of particles and is measured in terms of the *total ionizing dose*. Inside the bulk of silicon, ionizing energy loss leads to the generation of electron-hole pairs, as discussed in Section 2.2. These charge carriers have high mobility in silicon and can be collected by the sensor's electrodes if they are generated within the depletion region. Otherwise, they simply recombine. However, in the silicon dioxide (SiO_2) layer at the surface of silicon sensors, holes have low mobility and those that do not recombine can cause radiation-induced defects, as explained in [22] and [23]. The

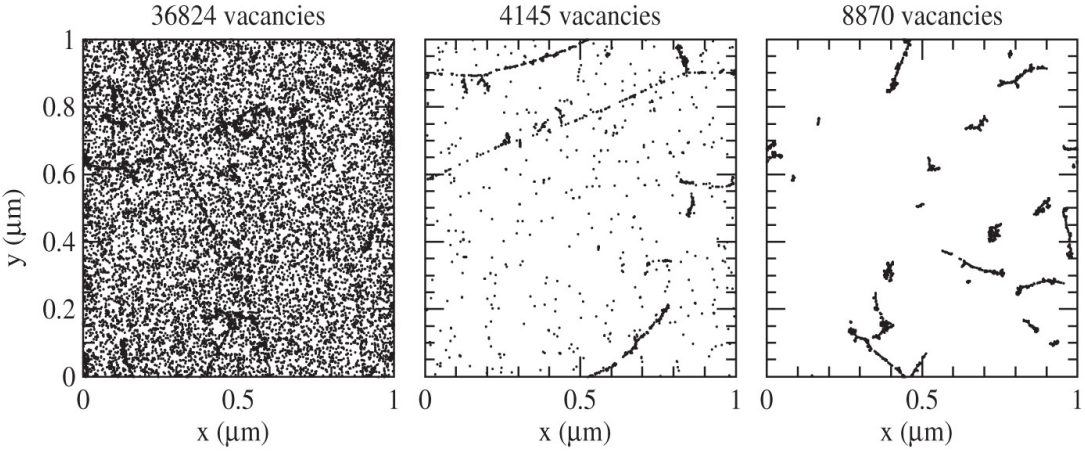

Figure 2.6.: Projected spatial distributions of vacancies over 1 µm in the z-direction. Simulation with a particle fluence of 10^{14} cm^{-2} for 10 MeV protons, 24 GeV/c protons and 1 MeV neutrons. Taken from [29].

generation of the defects begins with the slow transportation of holes toward the Si/SiO_2 interface where some are trapped in long-lived states, such as oxygen vacancies near the interface, leading to an increase in positive oxide charge. Others can create interface traps at the Si/SiO_2 boundary by breaking hydrogen atoms from hydrogen-passivated dangling bonds, in a process involving proton formation. The effects of these processes are discussed in [24] and [25]. The buildup of an oxide charge can cause the formation of an electron accumulation layer between pixel implants in p^+n sensors, which can lead to longer drift times for charge carriers, making them more prone to trapping. This accumulation layer may also short neighboring n^+ implants. Additional surface damage defects and their effects are discussed in [24] and [26]. It is also worth noting that interface traps can increase the leakage current if the adjacent bulk region is depleted. Measurements of this surface generation current on gate-controlled diodes are presented in [27].

The second type of radiation damage, called bulk or displacement damage, is caused by the Non-Ionizing Energy Loss (NIEL) of particles. As discussed in [14], part of the NIEL results in lattice vibrations, which dissipate within the crystal. If the recoil energy from an interaction exceeds a threshold of around 20 eV in silicon [14], a *Frenkel pair* is formed. A Frenkel pair consists of two point defects: a vacancy and an interstitial atom, resulting from a silicon atom being displaced from its original position in the lattice, leading to displacement damage. If the energy transfer is significantly higher, localized clusters of point defects are generated through secondary interactions with displaced atoms. These clusters are reported to range in size from 100 Å to 200 Å for energy transfers around 10 keV [28] and often exhibit line-like shapes (see Figure 2.6).

The displacement damage caused by high-energy particles in silicon depends on the particle type and energy. It is described by the *damage function* $D(E)$, shown in Figure 2.7.

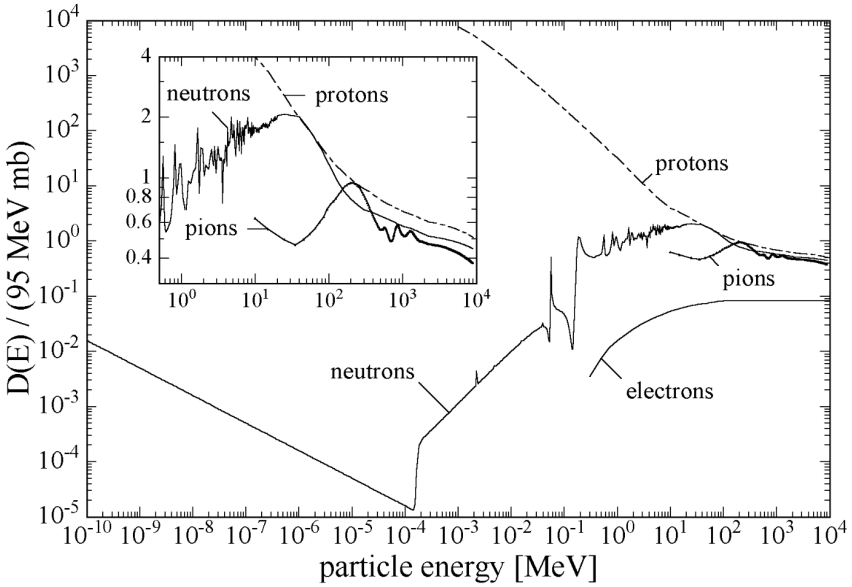

Figure 2.7.: Damage functions $D(E)$ for neutrons, protons, pions and electrons in silicon, taken from [30].

The displacement damage from 1 MeV neutrons is:

$$D_n(1\,\mathrm{MeV}) = 95\,\mathrm{MeV\,mb} \tag{2.5}$$

and it is used to normalize damage functions and radiation fields containing mixed particle types and energies (see Figure 2.7) by introducing a *hardness factor* [30]:

$$\kappa = \frac{\int D(E)\phi(E)\,dE}{D_n(1\,\mathrm{MeV}) \cdot \langle\phi\rangle}\,, \tag{2.6}$$

with $\langle\phi\rangle = \int \phi(E)\,dE$ and $\phi(E)$ being the energy spectrum of the corresponding radiation field. As a result, the 1 MeV *neutron equivalent fluence* is defined as:

$$\phi_{\mathrm{eq}} = \kappa\langle\phi\rangle\,. \tag{2.7}$$

This normalization overlooks the fact that displacement damage is not uniformly distributed, with particles like neutrons generating clusters of displacements. Figure 2.6 illustrates this by showing simulated spatial distributions of vacancies after irradiation with protons of different energies and neutrons. These distributions represent the vacancies immediately after their creation. The generated vacancies and interstitials are mobile at room temperature and may recombine or form long-lived point defects and clusters. Typical defect types include combinations like two vacancies (V_2), a vacancy and an oxygen atom (V-O), or a vacancy and a phosphorus atom (V-P). The simulations in [29] describe the initial creation of vacancies and interstitials, their migration, and their combinations, providing a better understanding of the physics involved. It should also be noted that these defects can break up again, particularly at higher temperatures, leading

to partial recovery of the material properties, in a process known as *annealing*.

Some of these defects or defect clusters are electrically active and introduce additional energy levels into the silicon bandgap, similar to the energy levels introduced by doping. These energy levels can affect the macroscopic properties of the silicon sensor, depending on their position within the bandgap. According to [31], Shockley-Read-Hall statistics can be used to calculate these macroscopic changes if certain defect properties are known, such as their concentration, capture cross sections for electrons and holes, energy levels, and whether they behave like donors or acceptors. Characterization methods like Thermally Stimulated Current (TSC) [32] or Deep-Level Transient Spectroscopy (DLTS) [33] are commonly employed. A summary of the observed macroscopic effects includes:

- **Increased leakage current**: after irradiation, silicon sensors show an increase in reverse (dark) current due to enhanced charge carrier generation. Energy levels near the center of the bandgap are most efficient at generating charge carriers.
- **Donor and acceptor removal**: some defects incorporate the original donor or acceptor atoms, effectively neutralizing the corresponding donor or acceptor levels. This has been identified as a problem in Low Gain Avalanche Diodes (LGADs) [34], as reported in [35].
- **Change in effective space charge**: in addition to donor and acceptor removal, other charged defects form after irradiation, leading to changes in the effective doping concentration (N_{eff}). Due to the leakage current, the local densities of electrons and holes vary with position inside the bulk, affecting trap occupation and space charge distribution. This can lead to the formation of a double junction and an electric field with two peaks at the front and back of the sensor [36]. The changes in effective space charge will be further discussed below.
- **Charge carrier trapping**: Free charge carriers can be captured by defect states, reducing their lifetime and consequently lowering the amount of collected charge. Measurements of trapping times after irradiation with protons, neutrons, and pions are provided in [37]. Fluence and temperature dependencies, as well as annealing behavior, are also discussed.

In principle, the properties of radiation-induced defects can be incorporated into device simulators like Synopsys TCAD [38] to predict the performance of irradiated devices. However, not all defects have been fully characterized, and numerical simulations become very complex as the number of defects increases. As a result, effective models like the Hamburg Penta Trap Model (HPTM) [39] are used to predict the performance of irradiated devices.

As mentioned earlier, the number of initially created point defects scales with the Non-Ionizing Energy Loss, leading to the NIEL hypothesis. This hypothesis suggests that

the number of stable or semi-stable defects formed also scales with the NIEL, implying that certain macroscopic properties should show a linear dependence on ϕ_{eq}. However, this hypothesis is known to have limitations. For instance, some defects are created via second-order processes, resulting in a quadratic fluence dependence [40]. Additionally, different concentrations of certain defects, like E(30 K), have been observed after proton and neutron irradiation [40]. The E(30 K) defect is known to contribute to positive space charge at room temperature. Nonetheless, for observables such as leakage current and effective doping concentrations, linear models are often sufficient for many applications.

2.4. Working principles of silicon pixel sensors

Silicon sensors are an ideal choice for tracking detectors, as they can be segmented with extremely high granularity. In high-energy physics experiments, *hybrid pixel sensors* in particular have been widely adopted for this purpose. In these detectors, the sensor and readout chip are fabricated separately and connected through a *bump-bonding process*. The bumps, approximately 25 µm thick, are usually made from a tin-silver (SnAg) alloy. A schematic of this type of sensor is shown in Figure 2.8.

The sensor consists of an n^+p silicon structure. During operation, a negative bias voltage is applied to the p^+ side of the sensor, referred to as the *backside*. As the bias voltage increases, a depletion region expands from the n^+ doped regions, known as *pixel implants*, into the p-type bulk region. An electric field is established, and at sufficiently high voltage, the depletion region reaches the backside. In practice, the configuration is more complex, often including features such as guard rings and additional implants to ensure inter-pixel isolation. These details, along with other doping combinations such as n^+ implants in n-type material, are discussed thoroughly in [41]. Specific features of the sensors analyzed in this work are described in Section 4.1.

Electron-hole pairs generated by ionizing radiation, as discussed in Section 2.2, are separated by the electric field within the sensor: holes drift towards the backside of the sensor, while electrons move towards the n^+ implants. The movement of these charge carriers induces a current signal in the n^+ pixel implants. Both the drift of charge carriers and the resulting current signal will be further elaborated on later in this Section. The pixel implants are conductively connected to the readout chip via metallization and bump-bonding, as described in sources such as [42]. The current signal is processed within the readout chip and passed through a chain of readout electronics before being stored. The readout system used in this work will be detailed in Section 4.2.

Charge carrier drift in silicon, in presence of a magnetic field, can be described using equations of motion [43]:

$$\frac{d\vec{r}}{dt} = \frac{\mu \left[q\vec{E} + \mu r_H \vec{E} \times \vec{B} + q\mu^2 r_H^2 (\vec{E} \cdot \vec{B})\vec{B} \right]}{1 + \mu^2 r_H^2 |\vec{B}|^2} \tag{2.8}$$

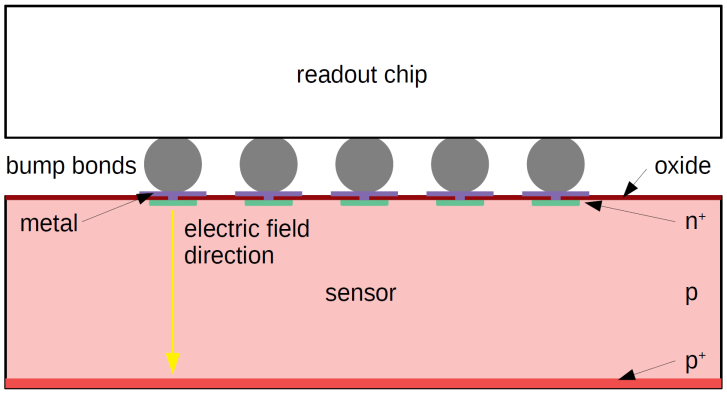

Figure 2.8.: Illustration of an n^+p hybrid pixel assembly.

where the variables include the position $\vec{r}$, the charge q, the Hall factor r_H, and the mobility $\mu(E)$ of electrons or holes. The electric and magnetic fields are denoted by $\vec{E}$ and $\vec{B}$, respectively. The mobility of charge carriers, introduced in [11], is defined as the proportionality constant between drift velocity $\vec{v}_d$ and the electric field:

$$\vec{v}_d = \mu \vec{E} \,. \tag{2.9}$$

At high electric field strengths, mobility becomes a function of the absolute field $|\vec{E}|$, and various parameterizations have been proposed in the literature. In this work, the parameterization presented in [44], which is based on measurements of drift velocity in the <111> crystallographic direction, is used:

$$\vec{v_d} = v_m \frac{\vec{E}/E_m}{\left(1 + \left(|\vec{E}|/E_m\right)^{\beta_m}\right)^{1/\beta_m}} \,. \tag{2.10}$$

The parameters v_m, E_m, and β_m depend on the temperature and the type of charge carrier, and the subscript m is assigned to indicate that these are parameters in the phenomenological equation given in [44], where the explicit values are also provided. Figure 2.9 shows the electron and hole mobilities at -20° C as a function of the electric field.

In the absence of a magnetic field, holes drift in the direction of the electric field, while electrons drift in the opposite direction. When a magnetic field is present, the term $\vec{v} \times \vec{B}$ causes a deflection from these directions, which is quantified by the *Lorentz angle* θ_L as:

$$\tan \theta_L = r_H \mu(|\vec{E}|) B_\perp \,, \tag{2.11}$$

where $B_\perp$ represents the magnetic field component orthogonal to the charge carrier's velocity [41]. Figure 2.10 illustrates the deflection of electrons in a silicon sensor, simulated using Allpix Squared [9]. In the simulation, electron-hole pairs are generated along the z-axis and displaced in the x-direction. The largest displacement, known as the *Lorentz*

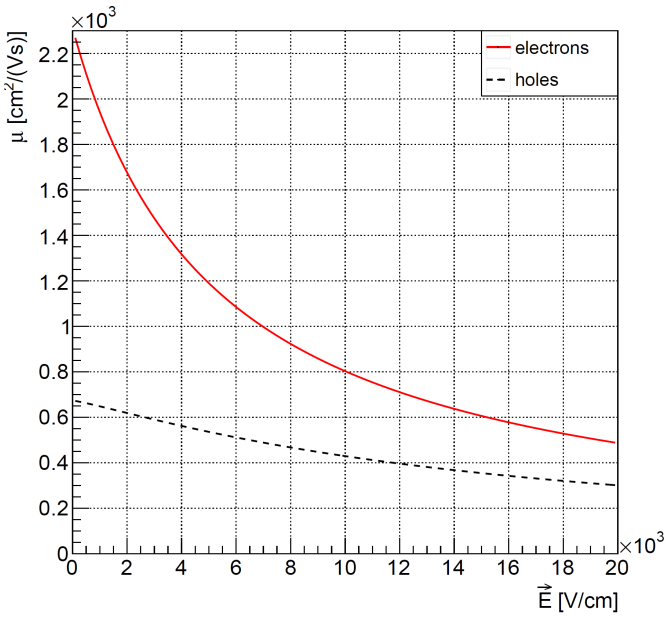

Figure 2.9.: Electron and hole mobilities at $-20°$ C as a function of the electric field obtained using Equation 2.8 and parameters from [44]. Taken from [45].

shift, occurs for electrons generated at the sensor's backside as they drift through its entire thickness.

Assuming a constant electric field, a magnetic field strength of 3.8 T, a sensor thickness of 150 µm, and the mobility parameterization mentioned earlier at a temperature of $-20°$ C, the Lorentz shift is estimated as a function of the electric field using Equation 2.11. The results are shown in Figure 2.10. For an average electric field of approximately 10^4 V/cm, the Lorentz shift is calculated to be 50 µm, while for an average field of approximately 2.6×10^4 V/cm, the shift is about 25 µm. These fields correspond to bias voltages of 150 V and 390 V, respectively, in a sensor of the specified thickness. As discussed later, this calculation is crucial for aligning the Lorentz shift with the pitch of a pixel sensor, where the pitch is defined as the distance between the centers of two adjacent pixel implants.

The transport of charge carriers in silicon is governed not only by drift but also by diffusion. As explained in [41], the diffusion current for electrons and holes can be described using Fick's first law:

$$\begin{aligned} \vec{j}_{e,\text{diff}} &= -D_e \nabla n \\ \vec{j}_{h,\text{diff}} &= -D_h \nabla p \end{aligned} \tag{2.12}$$

Here, $\vec{j}_{e,\text{diff}}$ and $\vec{j}_{h,\text{diff}}$ represent the electron and hole diffusion currents per unit area, D_e and D_h are the respective diffusion constants, and ∇n and ∇p are the gradients of the electron and hole concentrations. The diffusion constants can be derived from the mobility using the Einstein relation:

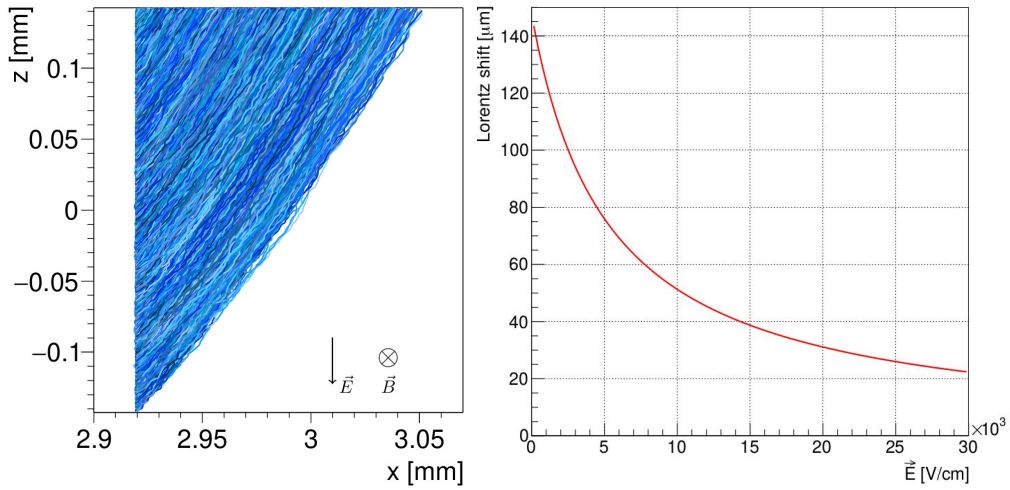

Figure 2.10.: Left: Allpix Squared [9] simulation of electron drift in 300 µm of silicon under the influence of a magnetic field. Electrons are generated along the z-direction at $x = 2.92\,\text{mm}$. The directions of the electric and magnetic fields are indicated in the figure. Taken from [46]. Right: Lorentz shift for electrons drifting through 150 µm of silicon. The directions of the electric and magnetic fields, as well as the shift, correspond to those shown in the figure on the left. The magnetic field is assumed to be 3.8 T, and the electron mobility is consistent with the data in Figure 2.9. The Hall factor for electrons is assumed to be 1.12.

$$D = \mu \frac{k_B T}{e} \,. \tag{2.13}$$

When considering a single charge carrier, it undergoes Brownian motion due to interactions within the material. The probability of finding it at a specific location after a time t follows a Gaussian distribution centered on its initial position, assuming no drift occurs due to an electric field. The width of this Gaussian distribution in one dimension is described by:

$$\begin{aligned} \sigma_{e,\text{diff}} &= \sqrt{2 D_e t} \\ \sigma_{h,\text{diff}} &= \sqrt{2 D_h t} \end{aligned} \tag{2.14}$$

The signal generated in pixel implants is a current induced by the motion of a charge Q within the silicon sensor. This current can be calculated using the Shockley-Ramo theorem [47, 48], as detailed in [49]. With the *weighting field* $\vec{E}_W$, the induced current is given by:

$$j_i = -Q\vec{v} \cdot \vec{E}_W \,. \tag{2.15}$$

The weighting field reflects the geometry of the sensor and accounts for charge collection at a specific electrode. It relates to the *weighting potential* ϕ_W in the same way the electric

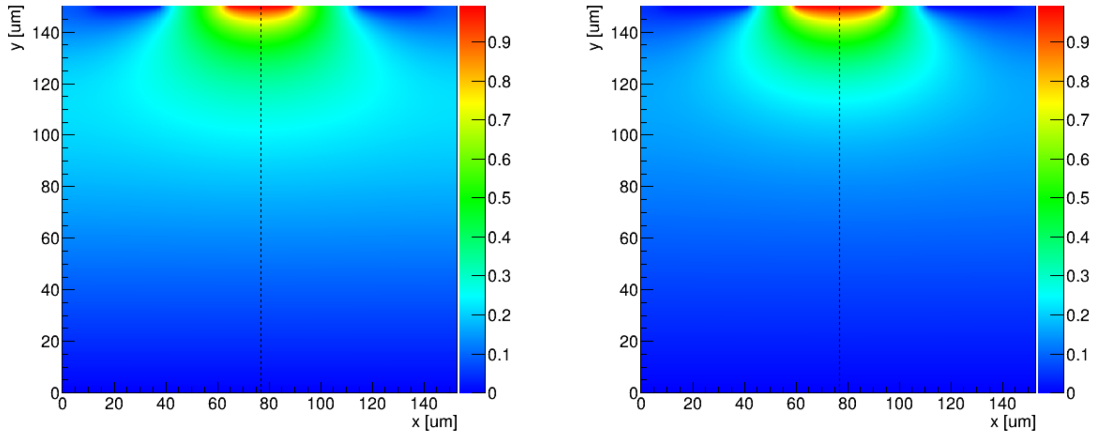

Figure 2.11.: Weighting potential for two strip sensors with a thickness of 150 µm, a pitch of 50 µm, and implant widths of 24 µm (left) and 32 µm (right). The dashed line marks the center of the readout implant at $y = 150$ µm. Taken from [51].

field relates to the electric potential, expressed as $\vec{E}_W = -\nabla\phi_W$. The weighting potential is derived by setting the potential of the electrode of interest to 1 V and all others to 0 V. When charge carrier trapping occurs (see Section 2.2), a charge carrier generated at position $\vec{r}_1$ and trapped at position $\vec{r}_2$ induces the charge:

$$Q_i = Q\left(\phi_W(\vec{r}_2) - \phi_W(\vec{r}_1)\right) . \tag{2.16}$$

For illustration, Figure 2.11 shows the weighting potentials for two strip sensors with different geometries. The potential rises non-linearly near the selected readout electrode. For larger implants, the weighting field is smaller in the sensor's bulk region and increases sharply near the electrodes. In pixel sensors, the rise is even steeper, a phenomenon referred to as the *small pixel effect* [50].

When charge carriers deposited by a single track induce signals in more than one electrode, this phenomenon is known as *charge sharing*. The number of electrodes registering charge above a specific threshold is called the *cluster size*. Charge sharing is influenced mainly by the Lorentz shift and the track angle, as shown in Figure 2.12, with diffusion and the weighting field also contributing.

The cluster size significantly impacts spatial resolution. In the simplest case, where particles hit the sensor uniformly and only one pixel with pitch p registers the signal (firing if the hit is within $\pm p/2$ of the pixel center), the position resolution is given by the square root of the variance of the uniform distribution:

$$\sigma_{\text{bin}} = \frac{p}{\sqrt{12}} , \tag{2.17}$$

commonly referred to as *binary resolution*. However, the assumption of only one pixel firing is often violated, as some particles create a cluster size of two, even when track angles are near normal to the sensor. Assuming such events occur in a region of width s,

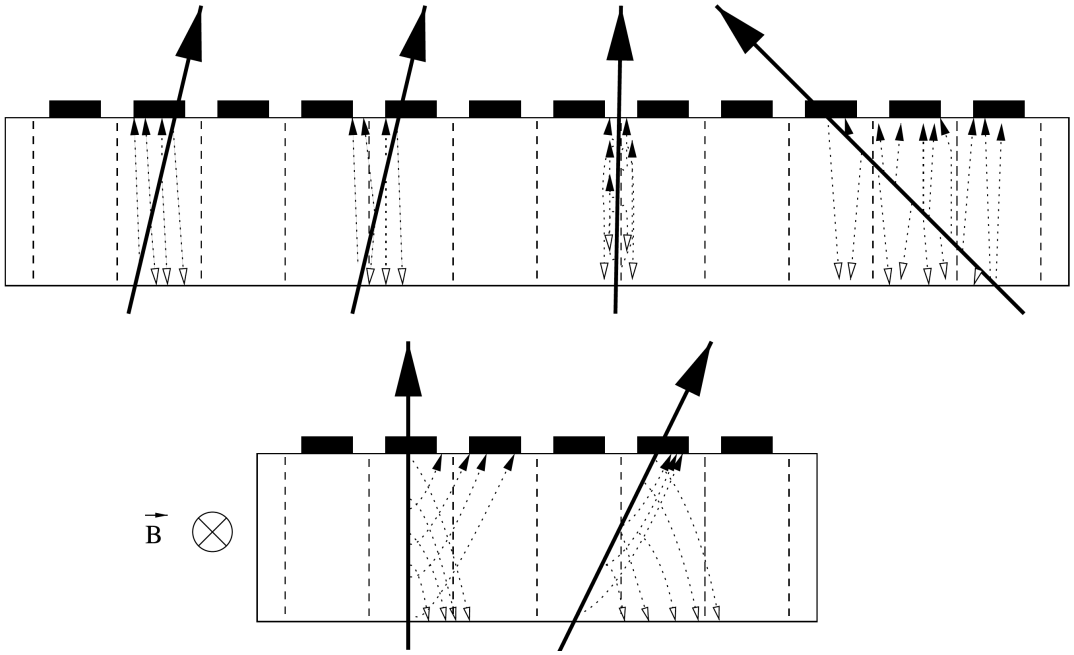

Figure 2.12.: Charge sharing in a silicon sensor for different track angles (solid arrows), shown without (top), and with (bottom) Lorentz shift caused by a magnetic field $\vec{B}$. The black boxes represent n^+ implants collecting electrons (indicated by dashed arrows). Adapted from [41].

the binary readout resolution becomes $(p - s)/\sqrt{12}$ in regions with cluster size one and $s/\sqrt{12}$ in regions with cluster size two [41]. This results in better resolution than predicted by Equation 2.17.

When charge information from each pixel electrode is available, the situation becomes more complex. For cluster sizes greater than one, the additional data can be used to interpolate between the centers of the firing pixels. Various interpolation algorithms are discussed in the literature [52, 53]. Interpolation greatly enhances position resolution, achieving the best results when the cluster size is close to two. This condition is met when $s \approx p$, assuming no threshold effects. Therefore, matching the Lorentz shift to the pixel pitch is beneficial. Similarly, when charge sharing is dominated by the track angle, optimal resolution is achieved for track angles θ satisfying $\tan(\theta) = p/d$, with d being the thickness of the sensor. In this scenario, spatial resolution is primarily limited by readout noise, crosstalk and energy loss fluctuations, as discussed in [54].

2.5. Properties of silicon for the LHC

Silicon pixel sensors play a crucial role in many tracking detectors, used to detect charged particles and determine their trajectories, called *tracks*. Additionally, these sensors can be used to measure the arrival time of charged particles and the energy deposited within the sensor material. In high energy physics experiments, this information is utilized to infer fundamental properties of the collision products, such as the momentum of the charged

particles from the curvature of particle trajectories in a magnetic field.

Particles with sufficiently short lifetimes may decay within the tracking detector, generating secondary vertices, at a distance from the primary vertex known as the *impact parameter*. As lifetimes are a fundamental property of particles and hadrons, impact parameters play an important role in particle identification. In cases where multiple primary collisions, referred to as *pileup*, occur, trajectory and timing information can be used to associate a track with one of the primary vertices. Trajectories are further used to correlate measurements from other sub-detectors, such as calorimeters and muon chambers, as part of particle flow reconstruction [55].

The selection of a detector type and its design are determined by the specific needs of the experiments. Silicon is frequently selected as a base material for tracking detectors due to its properties, meeting many of such requirements. Some of these properties, as outlined in [50] and [56], include:

- **Granularity**: which is the density of readout elements in a plane or volume, determining the ability to resolve individual tracks in high track-density environments, such as high-pileup experiments. It is closely related to spatial resolution.
- **Rate capability**: factor that must be maximized, describing the ability of the detector to handle the frequency of bunch collisions, which limits the available time for signal formation in the sensor and readout processing.
- **Material budget**: factor that must be minimized as it limits track resolution, sprouting from the Coulomb scattering charged particles experience when passing through matter, leading to angular deviations from their original direction.
- **Radiation tolerance**: high-energy physics experiments expose detectors to ionizing and non-ionizing radiation, which causes aging effects in many components. Therefore, detectors must be resilient to these effects over the planned operational period.
- **Cost and scalability**: practical factors such as monetary costs and the scalability of the detector must also be considered.

These properties are influenced not only by the silicon sensors themselves, but also by the design of other components such as the readout chip, data acquisition system, mechanics, and cooling. The following Section will provide an introduction to the Compact Muon Solenoid (CMS) experiment at CERN, where hybrid silicon pixel modules will be operated for the tracking system.

3. The CMS experiment at the LHC

The Large Hadron Collider (LHC) [57, 58] is a particle accelerator with a total circumference of 26.7 km, situated approximately 100 meters underground at CERN. It is capable of accelerating and colliding both protons and heavy ions; however, only proton collisions are relevant to this thesis and will be discussed further.

The LHC features four primary collision points where major experiments are located: ATLAS (A Toroidal LHC ApparatuS) [59] and CMS (Compact Muon Solenoid) [60] are general-purpose detectors used for a broad range of studies; ALICE (A Large Ion Collider Experiment) [61] specializes in heavy-ion physics; and LHCb (LHC beauty) [62] focuses on precision measurements of CP violation and rare b-hadron decays.

In the LHC, particles are accelerated in bunches. Collisions occur at a frequency of 40 MHz, corresponding to an interval of 25 ns between interactions. The mean number of interactions per bunch crossing, commonly referred to as *pileup*, is illustrated in Figure 3.1. The LHC was originally designed to operate at an instantaneous luminosity of 1×10^{34} cm^{-2} s^{-1}. During Run 2, peak luminosities of approximately 2×10^{34} cm^{-2} s^{-1} were achieved, corresponding to a delivered integrated luminosity of about 160 fb^{-1} at $\sqrt{s} = 13$ TeV in both the ATLAS and CMS experiments. Under these conditions, the average pileup was around 37.

To maximize the LHC's discovery potential, a major upgrade known as the High-Luminosity LHC (HL-LHC) is planned for the late 2020s. In the ultimate performance scenario, a peak luminosity of $7.5 \times 10^{34}\,\text{cm}^{-2}\,\text{s}^{-1}$ is foreseen, bringing the expected total integrated luminosity to circa 3000 fb^{-1} and the estimated pileup to 200 [63]. Overall, the HL-LHC operating conditions will be posing major challenges for the experiments. To ensure optimal performance in this demanding environment, the detectors of the main LHC experiments will undergo significant upgrades. This Section outlines the key challenges faced by the CMS detector and the main aspects of its upgrade.

3.1. The CMS detector

The CMS detector is a multi-purpose apparatus [60] designed with multiple subsystems to identify and measure various particle types and their properties. These subsystems are arranged in a layered structure around the beam pipe, as shown in Figure 3.2 and 3.3.

At the core of the detector, the *pixel* and *strip silicon detectors* provide precise tracking capabilities. Surrounding them are the *electromagnetic* and *hadronic calorimeters*,

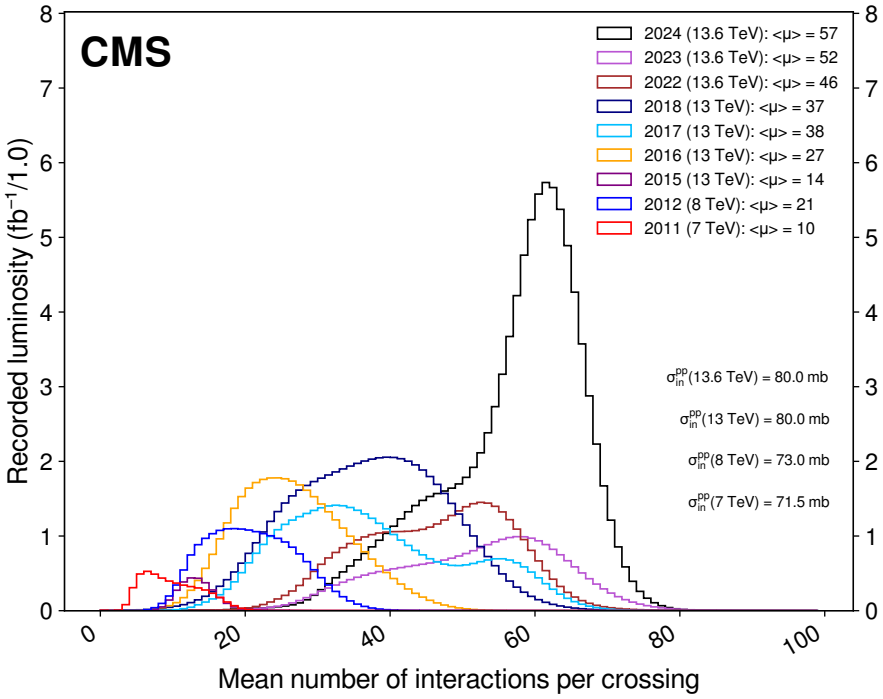

Figure 3.1.: Distribution of the average number of interactions per crossing (pileup) for pp collisions in the years 2011 to 2024. The overall mean values and the minimum bias cross sections are also shown. From [64].

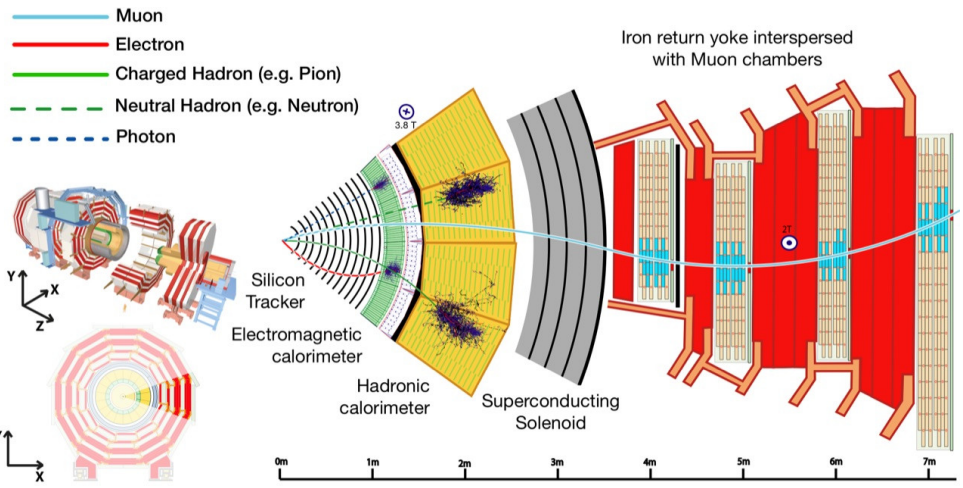

Figure 3.2.: Schematic representations of the CMS experiment. On the left: a three-dimensional expanded view and a front view of the CMS detector, with a highlighted section enlarged on the right. On the right: a detailed slice of the CMS apparatus, showing its main subsystems and the interactions of different particles within the subdetectors. Adapted from [65].

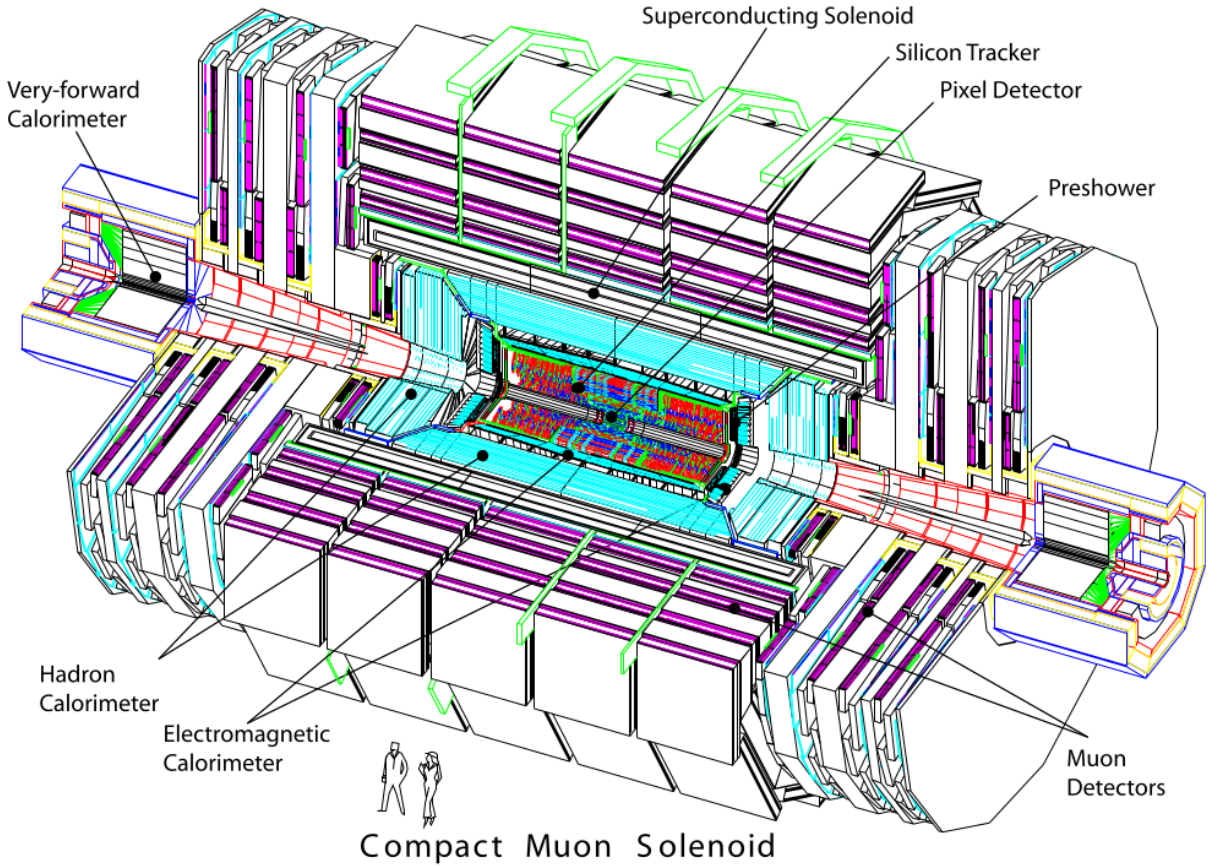

Figure 3.3.: The CMS detector [6].

responsible for measuring energy deposits from electrons, photons, and hadrons. These components are all enclosed within a powerful superconducting solenoid magnet. The outermost layer consists of *muon chambers*, which are embedded within the magnet's return yoke to detect muons efficiently.

Throughout this discussion, the *CMS coordinate system* is used: the origin is defined at the nominal collision point within the detector; the x-axis points radially inward toward the center of the LHC; the y-axis points vertically upward; the z-axis is aligned with the beam direction, pointing toward the Jura mountains. Additional coordinate definitions include the polar angle θ, measured from the z-axis, and the pseudorapidity η, defined as $\eta = -\ln\tan\frac{\theta}{2}$. The azimuthal angle ϕ is measured from the x-axis in the x-y plane, and the radial coordinate r represents the distance from the z-axis in this plane. Below, the key features of all subsystems are summarized. Section 3.2 is dedicated to the current Silicon Tracker.

- The **electromagnetic calorimeter** (ECAL) [66] is designed to measure the energy deposited by electromagnetic showers produced by photons and electrons. It is a homogeneous calorimeter composed of lead-tungstate crystals, emitting scintillation light which is detected using silicon avalanche photodiodes in the barrel and vacuum phototriodes in the endcap. The detector's thickness exceeds $25\,X_0$, ensuring efficient energy containment. A key design requirement of the ECAL was the ability to

detect the Higgs boson decay into two photons ($H \to \gamma\gamma$), leading to the inclusion of a preshower system in front of the endcap to improve the rejection of neutral pion decays ($\pi^0 \to \gamma\gamma$). In test beams, a relative energy resolution of:

$$\left(\frac{\sigma}{E}\right)^2 = \left(\frac{S}{\sqrt{E}}\right)^2 + \left(\frac{N}{E}\right)^2 + C^2 = \left(\frac{2.8\%}{\sqrt{E}}\right)^2 + \left(\frac{12\%}{E}\right)^2 + (0.3\%)^2,$$

was achieved, where S represents the stochastic term, related to shower development, N accounts for noise contributions and C is a constant term influenced by the calibration. The reported values refer to electrons' energy resolution.

- The **hadronic calorimeter** (HCAL) [67] is designed specifically to measure the energy of hadrons with a particular focus on *jets*, collections of hadronic particles that are highly collimated due to the Lorentz boost of the originating quarks or hadronically decaying τ-leptons. This calorimeter is of the sampling type, composed of brass absorbers interleaved with plastic scintillators, and it is divided into a barrel and an endcap section. In the barrel region, the calorimeter is extended with a tail catcher, located outside the solenoid, to further absorb energy from particles that escape the main detector volume. In the forward region, coverage is extended by the hadron forward calorimeter, which uses steel absorbers and quartz fibers. Charged particles passing through the fibers emit Cherenkov radiation, which is used for energy measurement. The depth of the hadronic calorimeter is expressed in nuclear interaction lengths λ_I, which are typically about ten times larger than radiation lengths (as detailed in [15]). Including the tail catcher, the calorimeter reaches a total thickness of 10 to 15 λ_I. The achieved energy resolution of the HCAL is given by:

  $$\left(\frac{\sigma}{E}\right)^2 \approx \left(\frac{a}{\sqrt{E}}\right)^2 + b^2,$$

  where $b = 5\%$ (constant term) and a depends on the detector region: 65% in the barrel, 85% in the endcaps and 100% in the forward calorimeter.

- The **superconducting solenoid** [68] generates the strong bending force required for precise momentum measurements of high-energy charged particles, making it a fundamental element in the detector's design. It consists of a superconducting 12.9 m long niobium-titanium solenoid with an inner diameter of 5.9 m, producing a 3.8 T magnetic field. The magnetic field lines are closed through the return yoke, which is positioned on the outer part of CMS and interleaved with muon chambers.

- The **muon spectrometer** [69] forms the outermost layer of the detector and consists of multiple detection layers embedded within the steel return yoke of the magnet. Most charged particles other than muons are either absorbed in the calorimeters or decay before reaching the muon system. This makes muon identification relatively

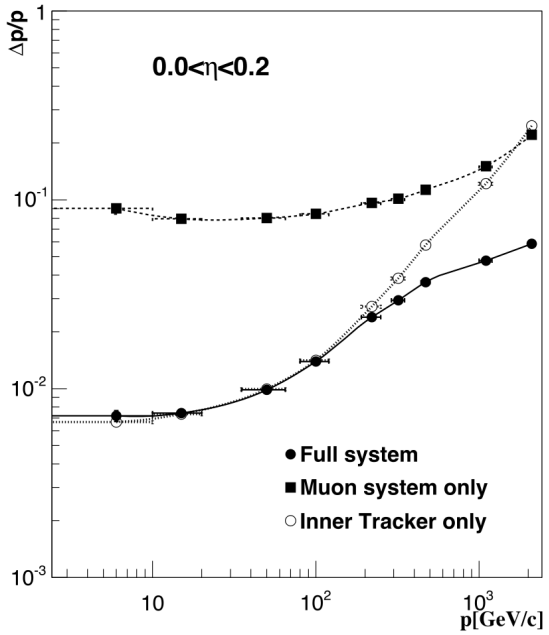

Figure 3.4.: Relative momentum resolution for muons as a function of their momentum. Muons are reconstructed using the muon detectors, the silicon tracker, or a combination of both. The combined reconstruction notably enhances the resolution at high momenta. Figure adapted from [72].

straightforward, making final states containing only muons particularly promising for physics analyses and searches for new phenomena. The system uses various types of gaseous detectors: drift tubes in the barrel region and cathode strip chambers in the endcaps. Both regions are supplemented by resistive plate chambers, which provide dedicated triggering capabilities to enhance the system's responsiveness and coverage. The relative momentum resolution for muons is shown in Figure 3.4.

- The **trigger system** is designed to manage the vast amount of data generated by proton-proton collisions in the LHC. The data rate is reduced from the initial 40 TB/s by a factor of circa 10^6 in a two-step process: the Level-1 (L1) Trigger [70] and the High-Level Trigger (HLT) [71]. The L1 Trigger consists of custom-designed, programmable electronics that process data with coarse segmentation from the calorimeters and muon system. The HLT is a software-based system that has access to the full detector readout, allowing it to perform more complex event reconstruction and selection before final storage.

3.2. The Phase-1 silicon Tracker

The tracking system [73, 74] plays a crucial role in precisely measuring the trajectories of charged particles and reconstructing both primary interactions and secondary vertices. Since charged hadrons make up approximately two-thirds of the particles produced in

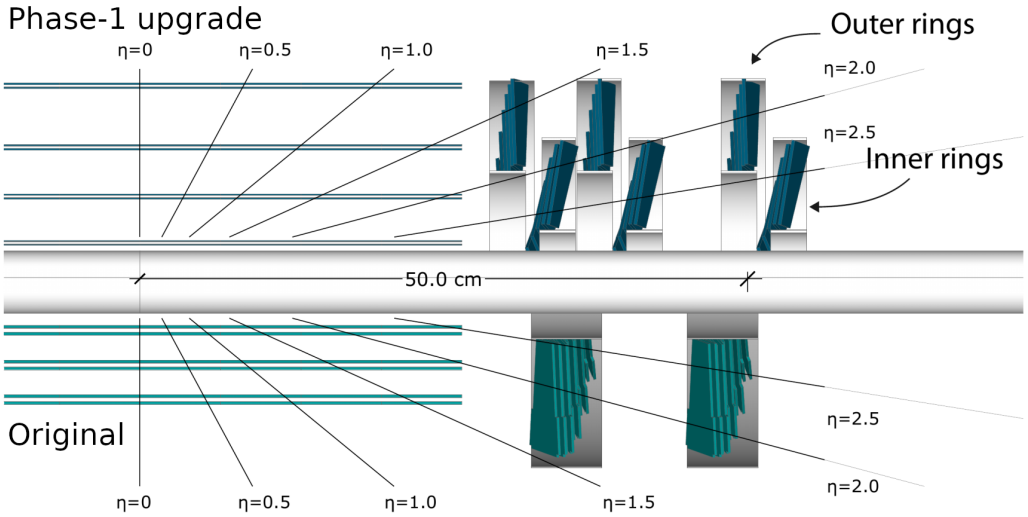

Figure 3.5.: Longitudinal view comparing the layout of the Phase-1 pixel detector, with the original detector layout used up to and including the 2016 data-taking period [75].

proton-proton collisions, their accurate reconstruction is essential for the experiment's physics program. Additionally, identifying secondary vertices is key for processes such as b-quark hadronization, where jets originate from decaying b-hadrons. Positioned closest to the interaction point, the tracking system operates in an environment with high particle flux, leading to significant radiation damage over time. To fulfill its purpose, the detector must maintain high resolution in position and momentum measurement, as well as high reconstruction efficiency. It also requires fine granularity to keep low occupancy per bunch crossing. To meet these demanding requirements, the tracking system is entirely silicon-based: the innermost layers consist of pixel sensors, while strip sensors form the outer layers.

- The **strip detector** forms the outer component of the tracking system, extending the coverage beyond the pixel detector and enabling precise momentum and trajectory reconstruction over a large volume. It provides up to 10 measurement points per track and covers the pseudorapidity range $|\eta| < 2.5$.

  The detector comprises four main substructures: the Tracker Inner Barrel (TIB), comprising four layers; the Tracker Outer Barrel (TOB), surrounding the TIB with six layers; the Tracker Inner Disks (TID) and Tracker Endcaps (TEC) consisting respectively of three and nine disks per side.

  The provided spatial resolution ranges from 20 to 50 µm in the transverse plane and 200 to 500 µm along the longitudinal direction, depending on the strip pitch and the number of fired strips [76].

- The **pixel detector** is the innermost component of the tracking system, positioned closest to the beam pipe and the interaction point. It consists of a barrel section (BPIX) and two endcaps in the forward region (FPIX).

The pixel sensors are manufactured using n-in-n technology, featuring n-type implants in an n-type substrate with a p-doped backside. They are 285 µm thick, with pixel cell dimensions of 100×150 µm^2, providing similar track resolution in both r-ϕ and z directions.

The original (Phase-0) pixel detector was designed to operate at the LHC's initial luminosity of 10^{34} cm^{-2} s^{-1} and was installed at the beginning of data-taking in 2010. The primary motivation for the upgrade was to enable efficient tracking performance at instantaneous luminosities reaching 2×10^{34} cm^{-2}s^{-1}, twice the original design luminosity of the LHC, and to compensate for the accumulated radiation damage reducing hit efficiency [77]. The Phase-1 Upgrade introduced an additional pixel layer in the barrel region and an extra disk per endcap, closer to the beam pipe to improve the measurement of the interaction vertices. A comparison of the original and upgraded pixel detectors is shown in Figure 3.5.

In the Phase-0 BPIX detector, the fitted width of the residual distribution, quantifying the difference between the measured hit position and the reconstructed track position, was 13.27 µm in r-ϕ and 34.08 µm in z. In the Phase-1 detector, these values improved to 9.5 µm (r-ϕ) and 22.2 µm (z) [75].

3.3. The Phase-2 Upgrade of the Tracker

Under the HL-LHC operating conditions, the increased event pileup and radiation exposure will pose significant challenges for all experiments, which will have to undergo major upgrades to function effectively in this demanding environment.

The tracker system currently operating in CMS, described in Section 3.2, was designed to maintain high efficiency under instantaneous luminosities up to 10^{34} cm^{-2} s^{-1}, with an average pileup of 20 and an integrated luminosity of 500 fb^{-1}, after being introduced as a replacement for the original detector, which had to be retired due to dynamic inefficiencies in the readout chip at high rates. Since detector performance beyond 1000 fb^{-1} won't meet the requirements outlined in [78], hindering effective b-tagging and impact parameter resolution, the tracker system will be replaced for HL-LHC operation.

The Phase-2 Tracker will consist of two silicon-based subsystems: the Outer Tracker (OT), which will feature strip and macro-pixel sensors, and the Inner Tracker (IT), composed of pixel sensors, as shown in Figure 3.6. The number and arrangement of layers have been optimized to ensure robust and reliable tracking performance. This design offers several key advantages: it maintains performance even in the event of a layer failure, enables track finding at the Level-1 trigger stage, and supports pixel-based track seeding, which enhances the overall quality and efficiency of track reconstruction.

While IT modules will be accessible for replacement during routine shutdowns, no maintenance is planned for the OT. The expected maximum fluence for different tracker

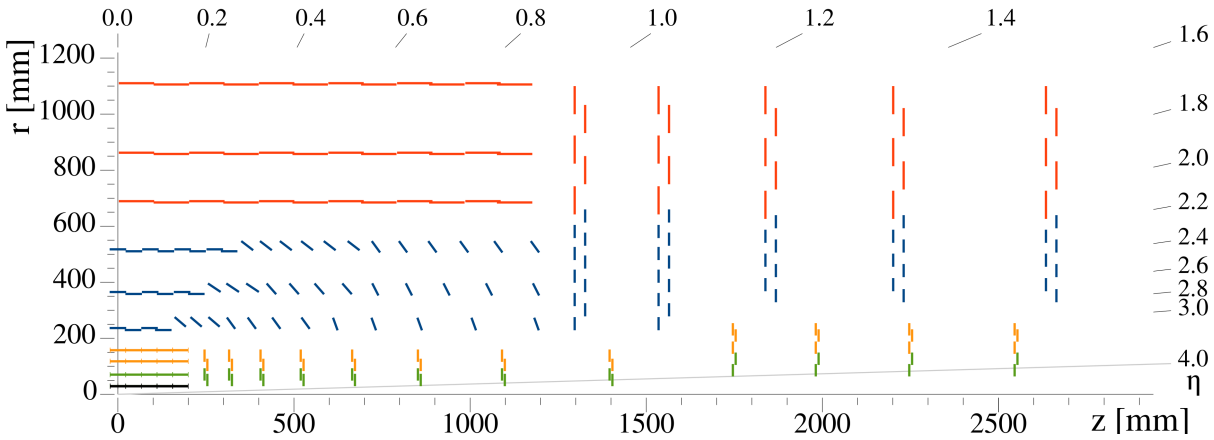

Figure 3.6.: Cross-sectional view of one quarter of the tracking system for the Phase-2 upgrade of the CMS detector. Pixel modules equipped with two and four readout chips are indicated by green (and black, for 3D sensors) and yellow lines, respectively. Modules based on strip and macro-pixel sensors are shown in blue, while two strip sensors appear in red. Taken from [56].

Region or component	Max. fluence [$n_{eq}\,cm^{-2}$]	r [mm]	z [mm]
IT barrel layer 1	2.3×10^{16}	30	0
IT barrel layer 2	5.0×10^{15}	61	0
IT barrel layer 3	2.0×10^{15}	104	0
IT barrel layer 4	1.5×10^{15}	146	89
IT forward, ring 1	1.0×10^{16}	51	252
OT PS modules	9.6×10^{14}	218	129
OT 2S modules	3.0×10^{14}	676	2644

Table 3.1.: Maximum expected fluence for selected tracker detector regions or components. Values correspond to 3000 fb^{-1} of pp collisions at $\sqrt{s} = 14$ TeV, assuming a total cross section (σ_{pp}) of 80 mb. The listed positions in r and z indicate where the highest fluence levels are reached for each respective region or component type. Adapted from [56].

components is summarized in Table 3.1, with the innermost IT regions experiencing fluences as high as 2.3×10^{16} $n_{eq}\,cm^{-2}$. Fluence variations along z are moderate since particle fluence depends primarily on the radial distance r.

This Section outlines the key features of the planned upgrade of the CMS Tracker.

3.3.1. The Outer Tracker

The design of the Outer Tracker (OT) has been heavily influenced by the need to contribute to the L1 event selection. To achieve this, the OT must self-select information at each bunch crossing, relying on local data reduction performed by the front-end electronics. This is accomplished using p_T-modules, which can filter out signals from particles below a predefined transverse momentum threshold.

The concept, illustrated in Figure 3.7, is based on the p_T-dependent bending of charged particles in the transverse plane under the 3.8 T magnetic field of the CMS solenoid.

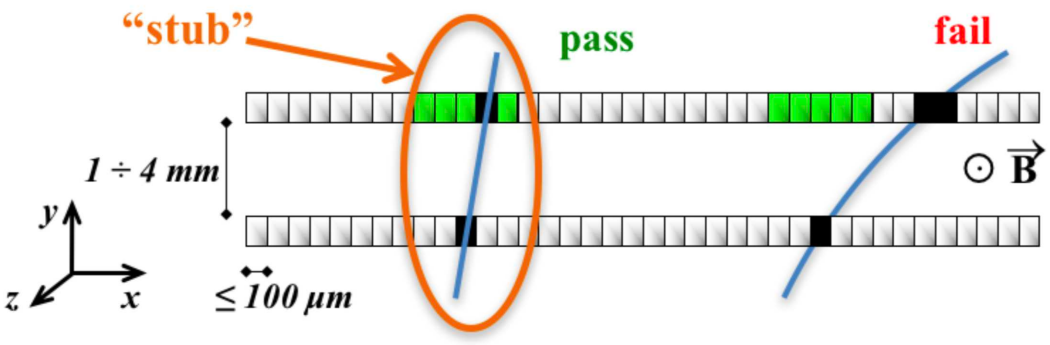

Figure 3.7.: Diagram illustrating the p_T-module concept. Signals from closely spaced sensors are correlated to reject low-p_T particles, with the green-highlighted channels representing the selection window for an accepted stub. Source [56].

Each so called p_T-module consists of two closely spaced single-sided sensors read out by a common set of front-end ASICs. By correlating signals from both sensors, the system selects hit pairs called *stubs* that are consistent with particles above the chosen p_T threshold. By applying a minimum p_T threshold of approximately 2 GeV, this approach reduces data volume by an order of magnitude, allowing stub transmission at 40 MHz. The p_T-modules are designed in different configurations: single-strip sensors and macro-pixel sensors will be used in the three innermost OT layers; two-strip sensors will be installed in the three outermost OT layers. More technical details about these modules can be found in [56].

3.3.2. The Inner Tracker

Due to its proximity to the interaction point, the Inner Tracker must endure the most extreme conditions within the CMS detector. It consists of a four-layer barrel section (Tracker Barrel Pixel Detector, TBPX), eight small forward double-disks (Tracker Forward Pixel Detector, TFPX), and four large endcap disks (Tracker Endcap Pixel Detector, TEPX) on each side of the TBPX. Two types of modules will be used: 1×2 modules (two chips arranged in a one-by-two layout, green and black in Figure 3.6) and 2×2 modules (four chips in a two-by-two configuration, yellow in Figure 3.6). In the TBPX, pixel modules are arranged in ladders that are staggered in radius to ensure overlap in the r-ϕ direction. In the TFPX and TEPX, modules are arranged in concentric rings. Each double-disc consists of two overlapping discs to ensure coverage in both r and r-ϕ. Each disc is further divided into two D-shaped halves, called *dees*. The system's coverage extends up to $|\eta| \approx 4$ to align with the calorimeter coverage. A perspective view of the IT components is shown in Figure 3.8, supplementing Figure 3.6.

The pixel sensors will have six times finer granularity compared to the current pixel tracker, with pitches of $25 \times 100\,\mu m^2$ and a thickness of 150 µm (with the long side along z in the barrel and along r in the endcaps). To maintain good spatial resolution

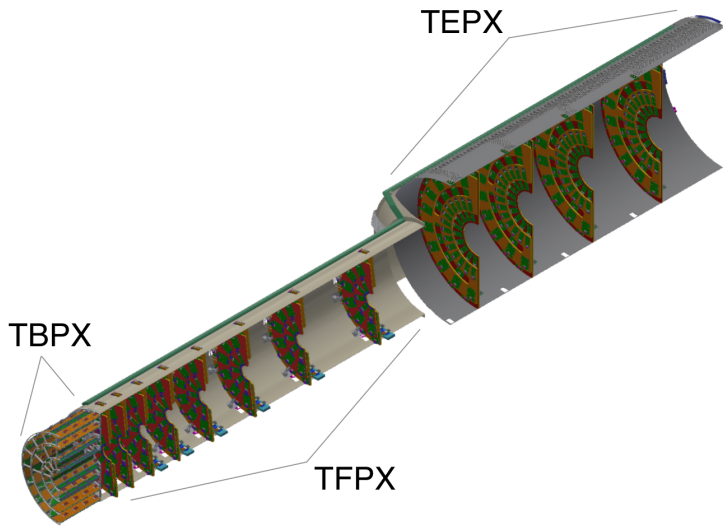

Figure 3.8.: Perspective view of one-quarter of the Inner Tracker, displaying the TBPX ladders along with the TFPX and TEPX dees within the supporting structures. Pixel modules are represented in orange for TBPX and in green for TFPX and TEPX. The dees are shown as red and orange surfaces [56].

over time despite radiation damage, n-in-p type silicon pixel sensors will be used. These improvements will enhance two-track separation and impact parameter resolution, leading to better b-tagging and more precise reconstruction of hadronic τ decays in boosted jets. The readout chips, designed by the RD53 collaboration [79] (a joint ATLAS-CMS effort), will be implemented in a 65 nm CMOS technology, optimized for its pixel segmentation.

The baseline technology for the outer three layers of the TBPX and TFPX rings is planar pixel sensors, as these regions will experience neutron equivalent fluences up to 1×10^{16} cm^{-2}. For the innermost TBPX layer, 3D sensors will be employed, as their lower power consumption facilitates cooling and reduces the risk of thermal runaway. These assemblies are described in Chapter 4.

The pixel detectors of the IT will be subjected to doses of up to 1.2 Grad, a hadron fluence reaching 2.3×10^{16} $\mathrm{n_{eq}\,cm^{-2}}$ over 3000 fb^{-1} and a pileup of up to 200, with hit rates approaching 3 GHz/cm^2 in the inner layers under the most demanding scenarios. They will be powered in a serial approach, amounting to ≈ 50 kW of power in the entire pixel detector. To keep the modules at the foreseen operating temperature of -20° C, an evaporative CO_2 cooling system will be employed, aiming for temperatures of about -35° C in the cooling pipes in contact with the carbon fiber support structure.

The upgraded detector is required to preserve the track and vertex finding performance of Phase-1 under the more challenging Phase-2 conditions. Figure 3.9 shows two examples comparing the performance of the Phase-1 and Phase-2 tracker in simulation. For high track densities, a significant improvement of the tracking efficiency is expected. The same holds for the impact parameter resolution for all track pseudorapidities.

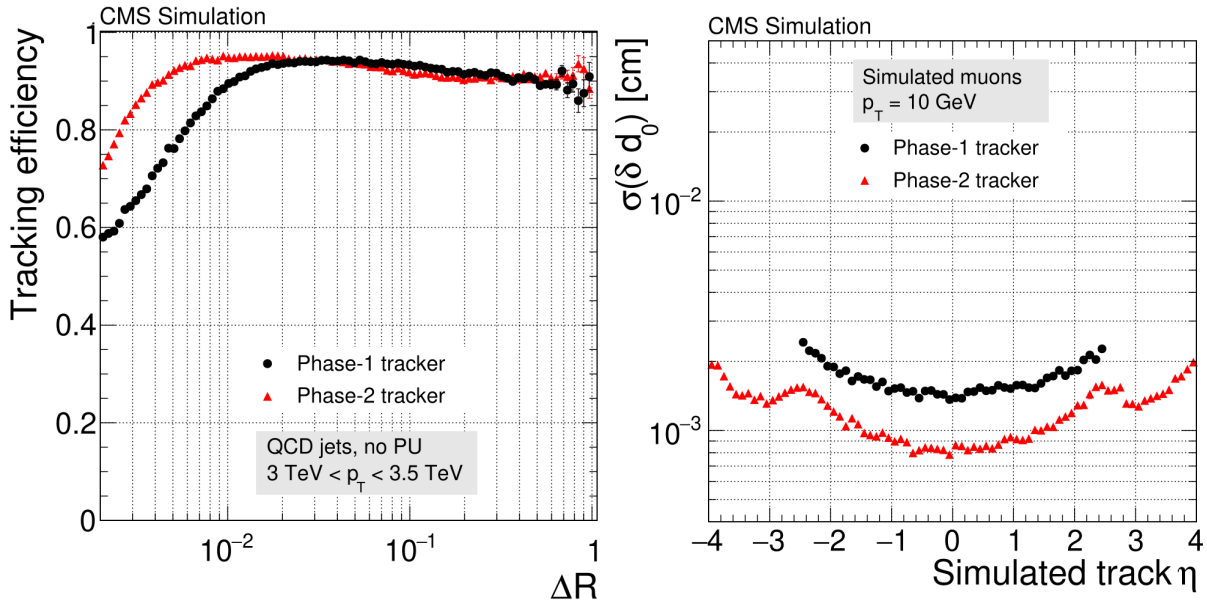

Figure 3.9.: Simulated tracking efficiency as a function of the distance to the nearest neighboring track, defined as $\Delta R = \sqrt{\Delta\eta^2 + \Delta\phi^2}$, is shown on the left for QCD jets in the transverse momentum range of 3 to 3.5 TeV. Pileup events are not included in this simulation. On the right, the transverse impact parameter resolution is presented as a function of the track pseudorapidity η, evaluated for isolated muons with a transverse momentum of 10 GeV. Taken from [56].

4. Sensor design and readout chip architecture

Fine-pitch planar silicon pixel sensors with a nominal active thickness of 150 µm are the baseline choice for the entire pixel detector, except for the innermost TBPX layer, where 3D sensors will be installed. In this Chapter, planar and 3D pixel sensors for the IT will be described, together with two iterations of their readout chip counterparts and the tuning procedure for module operation.

4.1. Sensor design

Planar sensors

An overview of the first production of Hamamatsu Photonics (HPK) sensors is provided in [80]. This study focuses on planar sensors featuring a *bitten* design with pitch sizes of 25×100 µm^2, compatible with the RD53A [81] and the RD53B_CMS (also called CROC or CROCv1) [82] readout chips, which will be described later in this Chapter.

Figure 4.1 presents the top view and cross-section of the pixel layout. The latter is obtained cutting along the red line reported on the top view. The peculiar placement of the bumps is due to the different aspect ratios between the pixels of the sensor (25×100 µm^2) and the readout chip (50×50 µm^2), which causes the passivation opening to be positioned between adjacent rows. This introduces a capacitive coupling, known as *crosstalk*, between neighboring pixels. The bitten design owes its name to the shape of the n^+ implant (shown in green) which wraps around the metallization under the bump, preventing overlaps and thereby reducing crosstalk to levels compliant with CMS requirements, as discussed in Chapter 5.

The sensors are n^+p type with a nominal active thickness of 150 µm. They are produced on 6-inch wafers with a resistivity ranging from 3 kΩ·cm to 8 kΩ·cm and an oxygen concentration between 1×10^{16} cm^{-3} and 6.5×10^{17} cm^{-3} [83]. Capacitance-voltage measurements revealed a bulk doping concentration of about 4.4×10^{12} cm^{-3}, and the full depletion voltage was found to be between 55 V and 75 V. During the production, wafers are mechanically thinned from the backside after the processing of the front side. The p^+ implantation on the backside is carried out following the thinning process.

Positive charges present in the oxide layer at the sensor surface cause electron accu-

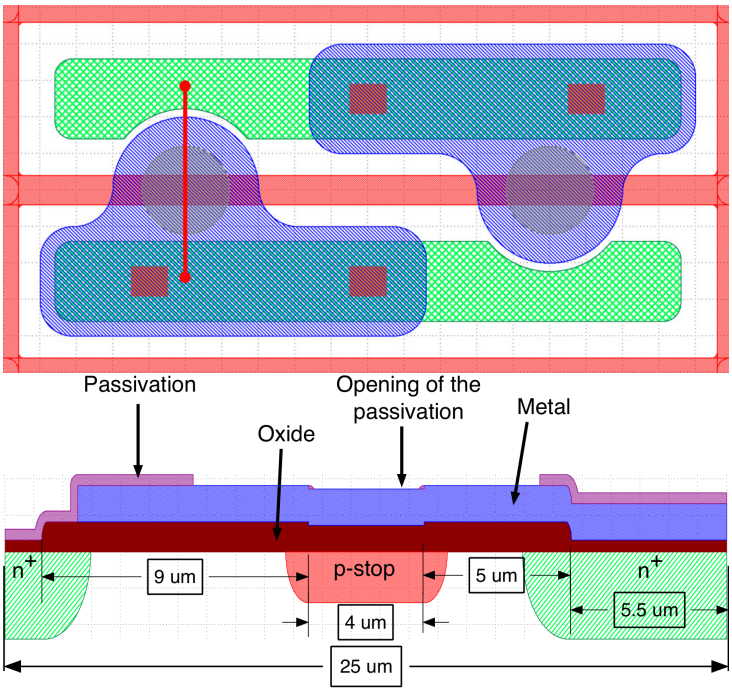

Figure 4.1.: Top and cross-sectional view of the pixel sensor layout with a pitch of 25×100 µm^2. Colors are consistent between the two figures.

mulation in the adjacent silicon bulk. Since electrons are the majority carriers in the n^+ implants, this accumulation layer can create an electrical short between neighboring n^+ implants. To prevent this, a p-doped region is added to maintain inter-pixel isolation. For the sensors under study, pixels are isolated using the p-stop technique, which introduces an additional p^+ implant between pixels, as shown in the cross-section of Figure 4.1.

3D sensors

The thermal behavior of the first layer in the barrel section has been thoroughly simulated using Ansys Fluent [84], considering both planar and 3D sensors across various fluence levels and power consumption scenarios. Figure 4.2 presents the results of the thermal simulation at an equivalent fluence of 2×10^{16} cm^{-2}, a level anticipated after roughly seven years of HL-LHC operation. Thermal runaway in pixel sensors is a self-reinforcing process where a temperature rise increases leakage current, which generates more heat and further raises the temperature. This cycle can lead to excessive noise, instability, or sensor damage if not properly managed. For the planar sensor modules, the temperature required to avoid thermal runaway is well below the minimum achievable coolant temperature. In contrast, the 3D sensors exhibit a safety margin of more than 10°C in the low power consumption scenario, and around 4°C in the high power case. For this reason, 3D sensors were chosen for the innermost layer of the barrel in the CMS detector.

The 3D sensors will be manufactured by Fondazione Bruno Kessler (FBK) [85]. A sketch of the sensor design can be seen in Figure 4.3.

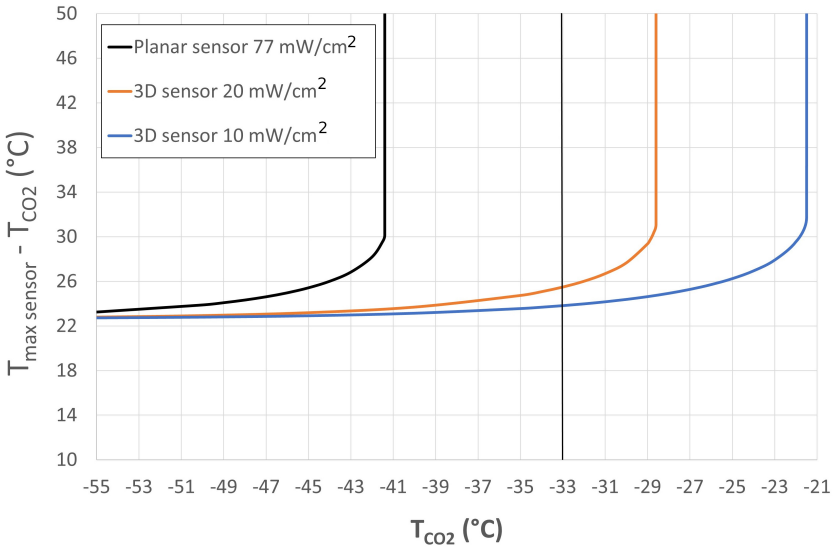

Figure 4.2.: Thermal simulation results for planar (black) and 3D (orange/blue) pixel sensor modules in the innermost layer of the barrel are shown. The comparison is based on a simulated fluence of 2×10^{16} $n_{eq}cm^{-2}$, assuming operating voltages of 600 V for planar sensors and 140 V for 3D sensors. The minimum temperature achievable by the coolant at the module location is indicated by a vertical black line at $T_{CO_2} = -33°C$. Taken from [86].

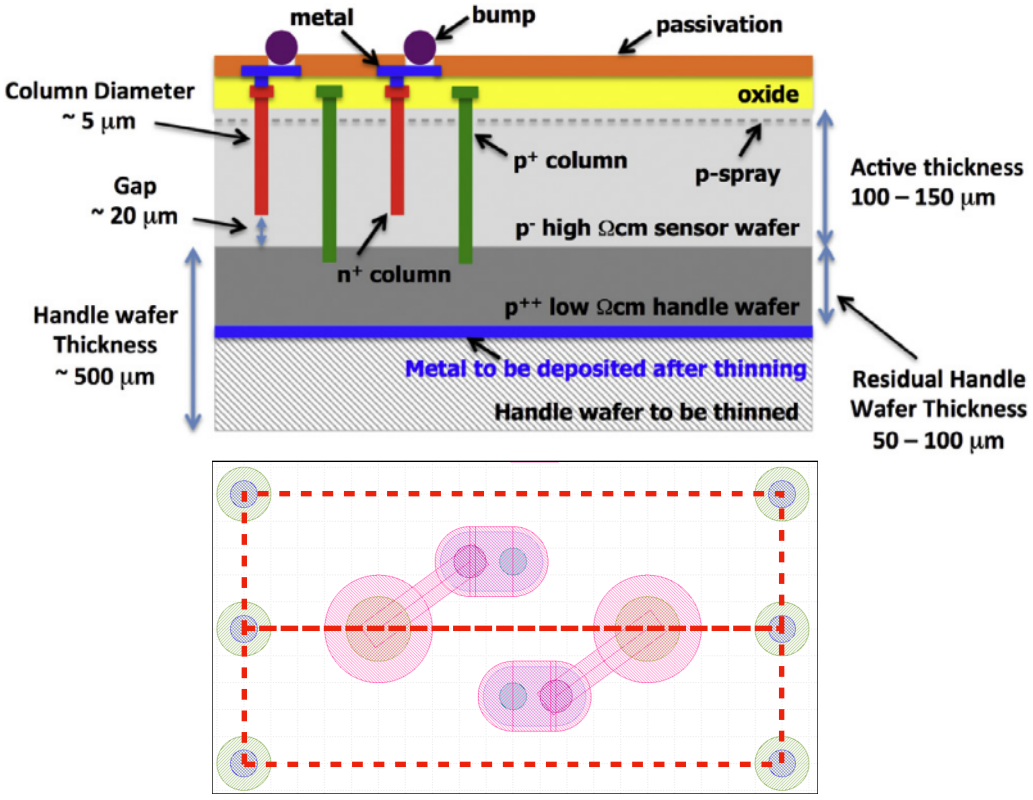

Figure 4.3.: Top: cross-sectional view of an FBK 3D sensor, showing the high-resistivity and low-resistivity layers, the p^+ ohmic columns and n^+ junction columns [87]. Bottom: top view of two neighboring pixel cells, each measuring 25×100 μm^2, outlined by dotted rectangles. The routing from the bump pads to the junction columns (blue circles) is shaded in pink [87]. Taken from [86].

The silicon wafers are composed of two layers, bonded together using the direct wafer bonding technique developed by IceMOS [88]. The high-resistivity layer has a nominal thickness of 150 µm and a resistivity of circa 3 kΩ·cm, while the low-resistivity layer measures about 100 µm and has a resistivity ranging from 0.1 to 1 Ω·cm. The columnar electrodes are fabricated using a single-sided deep reactive-ion etching process and extend vertically through the bulk, perpendicular to the sensor surface. The n^+ junction columns connect the sensor to the ASIC via the bumps. These have a diameter of 5 µm, and contact the highly doped p^+ region close to the backside metallization. The pixels are electrically isolated using the p-spray technique, which is a continuous deposition of low dose p-dopant on the sensor surface. As for planar sensors, a special routing was adopted in order to match the pitch of the readout chip, as shown in Figure 4.3 (bottom). Further information on the performance of 3D sensors can be found in [86].

4.2. Readout chip designs

The readout chips under study have been designed by the CERN RD53 Collaboration, established in 2013 to develop pixel readout chips for the Phase-2 upgrades of the ATLAS and CMS experiments. Among the many requirements that can be found in Table 1 of [82], the new pixel detectors will require readout electronics capable of operating in an extremely harsh radiation environment, withstanding a total ionizing dose of up to 1 Grad. Additionally, they will need to handle high hit rates of 3.5 GHz/cm^2, support high data rate readout at 5 Gb/s, maintain power consumption below 1 W/cm^2 and be compatible with serial powering, an innovative approach designed to reduce cabling and minimize the material budget.

RD53A was the first half-scale demonstrator, and is shown mounted on its PCB in Figure 4.4 (left). Submitted in 2017, it featured a 400×192 pixel matrix for a total area of 20×11.6 mm^2, two distinct pixel readout architectures to determine the most suitable implementation for the final production chips, and three different analog front-end designs: the linear, the differential and the synchronous front-ends [89]. RD53A has been extensively tested over several years for verification of the overall architecture, as well as for the qualification of various pixel sensors. Based on test results and specific requirements, ATLAS and CMS selected different front-ends for their chips: the differential and the linear, respectively. The corresponding pre-production chips were named RD53B_ATLAS (ItkPixV1) and **RD53B_CMS** (**CROCv1**), and were submitted in March 2020 and June 2021. They were the first full-size readout chips, with matrices featuring 400×384 and 432×336 pixel, respectively, for a total area of 20×21 mm^2 and 21.6×18.6 mm^2. A sensor-readout chip assembly in its CMS flavour, mounted on a PCB card, is shown in Figure 4.4 (right).

The production chips, RD53C_ATLAS (ItkPixV2) and RD53C_CMS (CROCv2), were later submitted in March 2023 and October 2023. For this reason, they are not part of

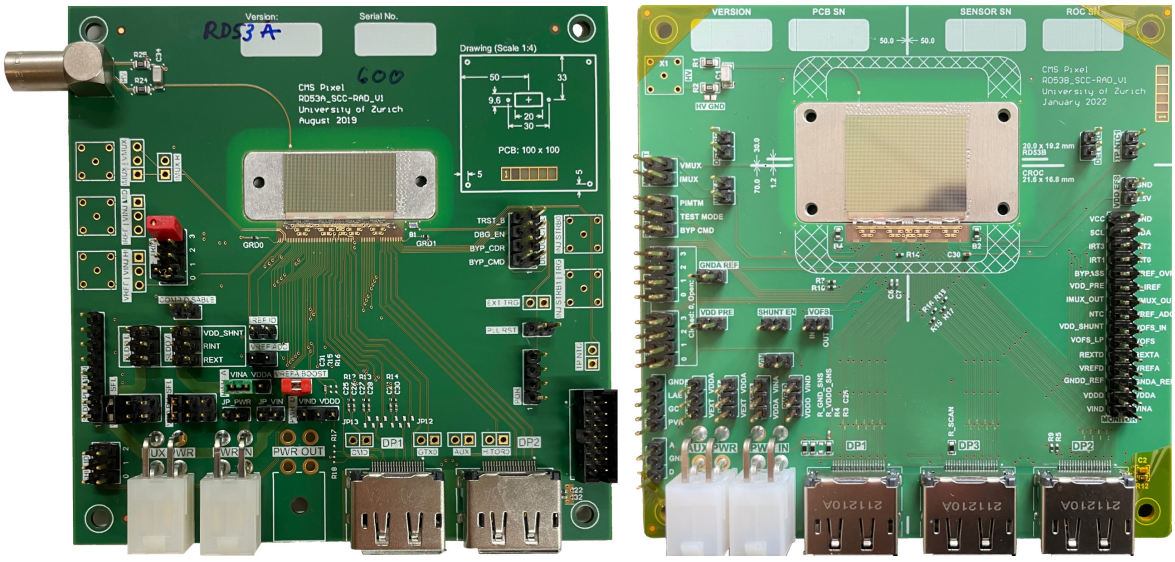

Figure 4.4.: Side by side comparison of the RD53A (left) and RD53B_CMS (right) single chip assemblies mounted onto their relative PCBs.

this study. Further details about the layout and the common RD53 floor plan can be found in [82].

4.2.1. Analog Front-End

The Analog Front-End (AFE) plays a crucial role in converting radiation-induced charge signals into a digital form suitable for further processing. Most AFEs have three building blocks: the preamplifier, the comparator and the Time-to-Digital Converter (TDC). The preamplifier shapes the fast current pulses originating from the movement of carriers in the sensor into smoother voltage signals, which are easier to sample. The output of the preamplifier is then compared to a threshold, which must be as uniform as possible across pixels in the matrix, by a fast comparator, to suppress noise-induced signals. Lastly, pulses exceeding the threshold are digitized by the TDC.

In the case under study, the RD53A and RD53B versions of the linear front-end share a common architecture, illustrated in Figure 4.5. They implement a shaper-less analog processor, consisting of a charge-sensitive amplifier (CSA or preamplifier) driving a threshold discriminator, which is used for time-over-threshold (ToT) conversion of the input signal amplitude. The readout channel includes a tuning DAC for threshold equalization and a calibration circuit that generates a test signal through an injection capacitor connected to the CSA input.

Preamplifier

As previously mentioned, the preamplifier is the analog block responsible for the amplification of the fast current signals generated by the collection of e^-/h^+ pairs in the pixels of the sensor. In the specific architectures under examination, it consists of a low-noise CSA

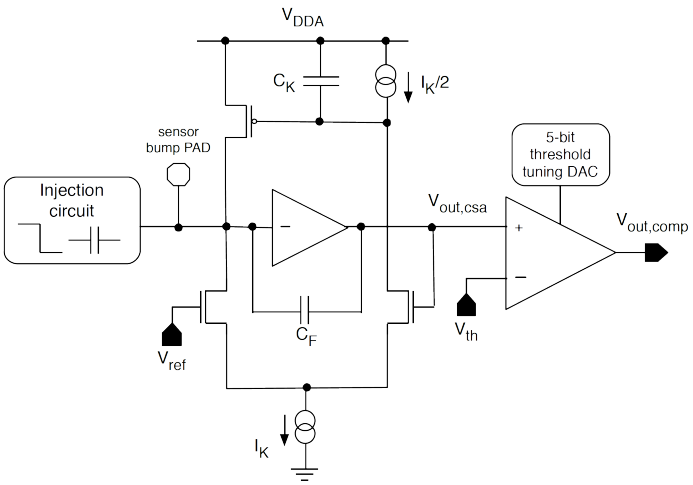

Figure 4.5.: Simplified schematic of the linear AFE for both iterations of the chips [91].

featuring a gain stage with a *Krummenacher* feedback network, responsible for the linear discharge of the integrated pulse and partially compensating for the additional leakage current induced by radiation damage [90]. The linearity of the feedback ultimately results in a proportionality between the charge deposited in the pixel and the duration of the output signal. The CSA's gain stage utilizes a folded cascode architecture, with the input branch biased at 3 µA and the cascode branch at 200 nA. Circuit simulations show a DC gain of circa 76 dB and a cut-off frequency of 140 kHz. The *charge sensitivity*, which is the ability of the preamplifier to convert an input charge signal into an output voltage signal, was designed to be close to 25 mV/ke$^-$ for both the RD53A and RD53B_CMS linear front-ends.

Threshold Discriminator and Tuning DAC

The block diagram of the threshold discriminator (or comparator) integrated into the RD53A and RD53B versions of the linear front-end is shown in Figure 4.6. It consists of a transconductance stage, where the output current is determined by the difference between the signal from the preamplifier ($V_{\mathrm{o,csa}}$) and the global threshold (V_{th}). This stage is followed by a transimpedance amplifier (TIA), based on a slightly modified version of the Träff amplifier [92]. The output of the TIA is processed by a pair of inverters, operating in the digital domain, ensuring sharp transitions and stable logic levels for the comparator output signal. Local threshold tuning is achieved by adjusting a DC current, I_{trim}, generated by an in-pixel threshold tuning DAC. This DAC is controlled by the trimming DAC (TDAC) digital input, which has a resolution of 4 bits in RD53A and 5 bits in RD53B. The specific implementation of the transimpedance stage and the tuning DAC differs between the two front-end versions and is discussed in Section 4.2.2. When the signal at the preamplifier output exceeds the pixel threshold, the comparator generates a positive output step, indicating the detection of a significant event. As $V_{\mathrm{o,csa}}$ drops back below the threshold level, the comparator output toggles again, defining a

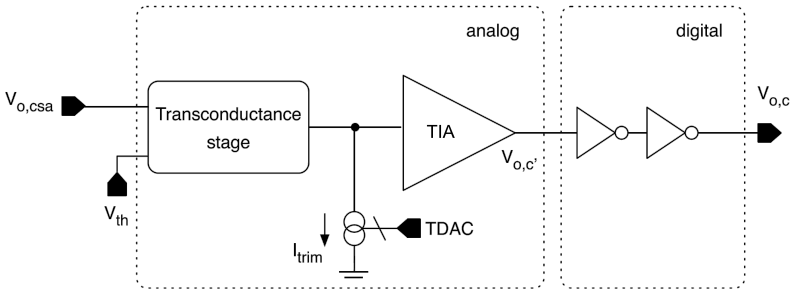

Figure 4.6.: Simplified schematic of the comparator in both iterations of the chip [91].

ToT interval that is proportional to the input signal amplitude. The digital-like output of the comparator is subsequently processed by a 4-bits TDC, that quantifies the duration of the ToT with respect to a 40 MHz clock.

4.2.2. Front-End optimization

While the RD53A chip demonstrated excellent performance in testing, several improvements and design corrections were implemented in the second-generation RD53B chip [93]. In particular, two drawbacks associated with the linear front-end emerged during the characterization of RD53A: an excessively large time-walk, and highly non-linear input-output response of the in-pixel TDAC circuit at higher TDAC values for irradiated modules operated at low temperatures.

The term *time-walk* refers to the variation in the detection time of a pulse depending on its amplitude. This originates from the fact that pulses with higher amplitudes cross the threshold earlier than those with smaller amplitudes generated at the same time. This effect needs to be corrected to accurately associate events with the correct bunch-crossing. The linear front-end in RD53A exhibited significant time-walk, with signals originating from an injected charge of 30 ke^- crossing the threshold (set at 1000 e^-) circa 40 ns earlier than those originating from an injected charge of 1 ke^-. This is much larger than the peaking time of the preamplifier, which is about 20 ns in simulations, indicating a significant time-walk contribution from the comparator. The comparator design has been revised in RD53B_CMS, as shown in Figure 4.7. Specifically, the revised front-end incorporates a modified version of the RD53A TIA: upon further investigation, it was discovered that the diode-connected transistors M_{1b} and M_{2b} in the RD53A design limited the current in the inverter amplifier and prevented the gain stage from operating in the linear region for a broad range of the input current $i_{\text{in,TIA}}$. This led to a slow comparator response, negatively impacting time-walk performance. In the RD53B_CMS version, the diode-connected transistors have been removed and instead M_5 sets the gain stage's static current at $\sim$200 nA. Figure 4.9 (left) shows the simulated time-walk for the two linear front-ends as a function of the input charge, ranging from 1 ke^- to 30 ke^-. The simulation, with a threshold set to 1 ke^-, indicates a significant reduction in time-walk in the RD53B_CMS front-end: circa 25% for small input signals, going from 40 to 30 ns.

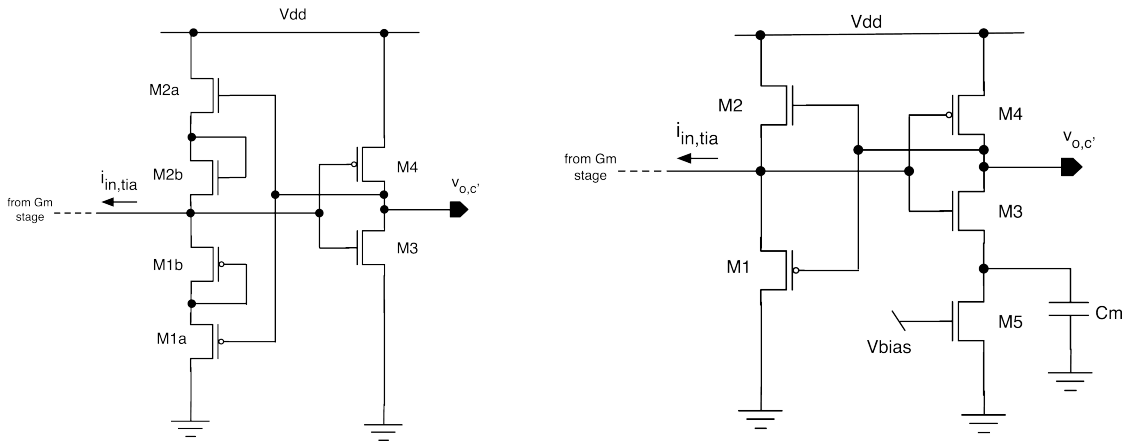

Figure 4.7.: Comparator design in the RD53A (left) and RD53B_CMS (right) readout chips [91].

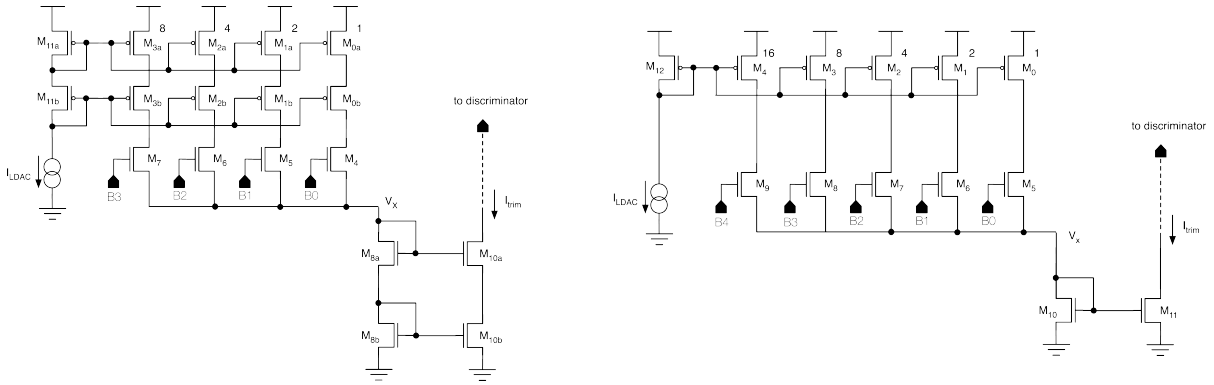

Figure 4.8.: TDAC circuit design in the RD53A (left) and RD53B_CMS (right) readout chips [91].

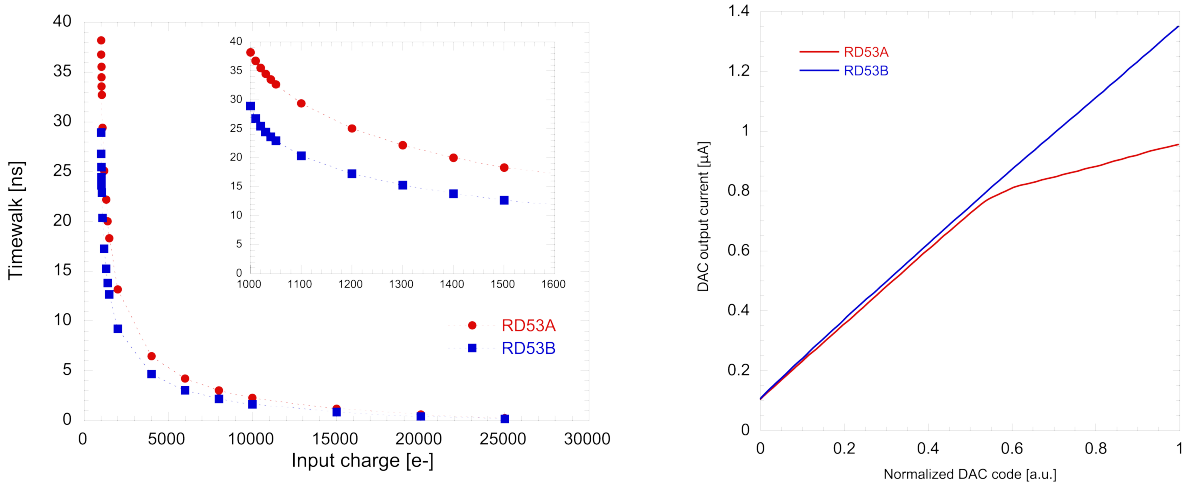

Figure 4.9.: Left: simulated time-walk for RD53A (red) and RD53B_CMS (blue). Right: input-output characteristic of the TDAC circuit as a function of the normalized TDAC code [91].

The threshold tuning capabilities of the linear front-end have also been enhanced with a new in-pixel TDAC design. The RD53A linear front-end featured a 4-bit binary-weighted

current DAC with cascoded current mirrors, while the RD53B_CMS version includes a more compact, 5-bit DAC with regular current mirrors in the same binary-weighted architecture. The TDAC circuit's output node, which generates a current I_{trim}, is connected to the output of the transconductance stage of the comparator, as shown in Figure 4.8. Figure 4.9 (right) illustrates the simulated I_{trim} current as a function of the normalized TDAC input code for both versions of the TDAC circuits, with I_{LDAC} current set to 30 µA. Thanks to this novel architecture, the dynamic range of the TDAC circuit in the latest iteration of the chip had a two-fold increase, going from about 1700 e^- for RD53A to circa 3400 e^- for RD53B_CMS.

4.3. Module tuning

To ensure the uniformity of the response by all channels in the matrix and to disable faulty pixels, each module must be tuned. This is achieved by means of the injection circuit, whose purpose is to inject a well-defined amount of charge into specific pixels, emulating the signals generated by incident ionizing particles. This allows for calibration and testing of various aspects of the module's performance, such as the linearity and uniformity of the pixels' response across the matrix. The tuning procedure consists of three main steps: the tuning of the global threshold, the equalization and the masking.

4.3.1. Global threshold tuning

The term *global threshold* refers to the DC voltage input of the comparator (V_{th} in Figure 4.6), which is common for all pixels in the matrix. This parameter is tuned by iteratively injecting pulses into each pixel, with a magnitude corresponding to the target threshold. The optimal value is found by performing a binary search, adjusting the DC threshold voltage of the comparator until an average occupancy of 50% is achieved within the matrix.

4.3.2. S-curve method and threshold equalization

To measure the thresholds of the pixels in the matrix, the S-curve method is used. In this process, pixels are injected with a specific number of pulses of increasing amplitudes. At every step, the *detection efficiency* is measured, which is the ratio between the amount of detected pulses and the total number of issued pulses. The point corresponding to a 50% detection efficiency in the S-shaped curve that originates from this process represents the pixel's threshold.

The equalization procedure serves to narrow the dispersion of the thresholds after the global threshold tuning. This makes use of the TDAC circuit, which can apply small variations on the common DC voltage input of the comparator in the ranges specified

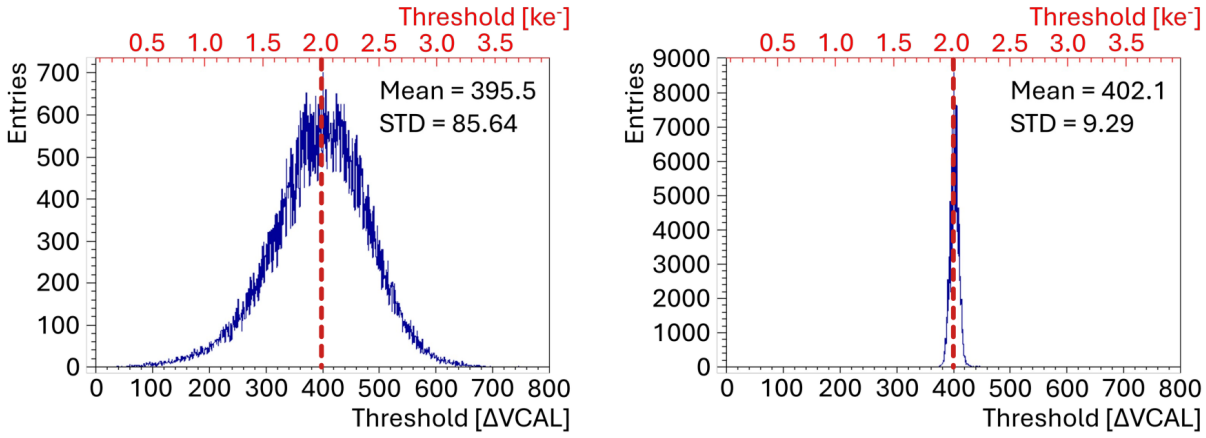

Figure 4.10.: Distribution of the thresholds before (left) and after (right) the equalization process, with a target threshold of 2000 e^- (red dashed line). The upper axis shows the approximate values in e^-.

in Section 4.2.1, to minimize the difference between the individual pixel's and the target threshold. During the tuning of the global threshold, the TDAC codes of all pixels are initialized to the same value. The best TDAC code is assigned during the equalization procedure, by repeatedly measuring each pixel's threshold for different TDAC values, ultimately assigning the one that brings the pixel's threshold closest to the targeted value. The difference between the dispersion of the thresholds distribution before and after the equalization can be appreciated in Figure 4.10.

4.3.3. Faulty pixels

To conclude the tuning procedure, faulty channels must be disabled. It is important to distinguish between two types of faulty pixels: noisy and stuck pixels. A pixel is referred to as *noisy* when its occupancy is greater than a specified value ($f_{\text{occ}}^{\text{noise}}$). These can be identified by disabling the injection, issuing a number of triggers (N_{trig}) and counting the amount of hits (N_{hits}) recorded by each individual pixel: all channels with $N_{\text{hits}} > N_{\text{trig}} \cdot f_{\text{occ}}^{\text{noise}}$ are then automatically disabled. Stuck pixels on the other hand, measure a number of hits that is below a predefined fraction ($f_{\text{occ}}^{\text{stuck}}$) of the number of pulses being injected (N_{pulses}): all pixels with $N_{\text{hits}} < N_{\text{pulses}} \cdot f_{\text{occ}}^{\text{stuck}}$ at the end of the injection cycle are disabled. Each module must satisfy two primary requirements: first, the total number of masked pixels should not exceed 1% of the overall pixel count, and second, the average noise hit occupancy of unmasked pixels must remain below 10^{-6}. This limit represents 1% of the minimum simulated average occupancy expected in the IT for physics cases as, e.g. top quark pair production [56]. In the case under examination, the occupancy threshold to classify a pixel as noisy was set to $f_{\text{occ}}^{\text{noise}} = 10^{-4}$, and $f_{\text{occ}}^{\text{stuck}} = 0.9$.

This concludes the tuning procedure, which must take place before data taking – both in the laboratory and at the test beam facilities. The process can be repeated iteratively to tune a module to lower thresholds, starting from high threshold settings.

5. Crosstalk and timing

The pixel detectors of the CMS Inner Tracker play a crucial role in precise position measurement of traversing ionizing particles. Crosstalk is among the numerous phenomena having a detrimental impact on the tracking performance, and its mitigation is therefore essential to achieve high-level tracking capabilities.

In this chapter, the correlation between crosstalk and the timing of the readout for RD53A and RD53B_CMS is investigated. Measurements were done by means of the integrated charge injection circuit, pulsing controlled signals in individual pixels and observing the responses in their neighbours. The impact of different readout schemes was systematically explored. A simulation was realized to reproduce the observed intra-bunch-crossing variation of the detection efficiency of pulsed signals.

A correlation between the timing of the readout and the magnitude of the crosstalk has been observed, with the latter exhibiting a clear minimum within the bunch-crossing time frame. This phenomenon, which was neither observed nor exploited during the chip design phase, provides evidence that the requirement of maintaining crosstalk below 10% is already met by the current iterations of the readout chip.

List of Own Contributions The author's contributions to the results presented in this chapter include:

- The identification of the correlation between the timing of the readout and the measured crosstalk levels.
- The optimization of the procedure employed to evaluate crosstalk with RD53B_CMS assemblies.
- Together with Prof. Luigi Gaioni and Prof. Mauro Dinardo, the modeling of the simulation used to reproduce the observed threshold oscillation in RD53B_CMS assemblies.

This work was developed in collaboration with Prof. Mauro Dinardo and Prof. Luigi Gaioni.

5.1. Crosstalk in RD53 readout chips

Crosstalk is a phenomenon wherein signals originating from one pixel intrude upon and affect adjacent channels due to capacitive coupling. In the case under exam, the presence of crosstalk arises from the diverse geometry of the sensor and chip pixel designs in the hybrid module [94], as shown in Figure 4.1. This configuration results in capacitive couplings that differ depending on the pixel being examined: pixels with the closest proximity between their two metal layers have the highest TCAD-simulated inter-pixel capacitance (14 fF) and are referred to as *coupled pixels*, while pixels with the second closest metal layers arrangement have a simulated inter-pixel capacitance of 6.5 fF and are referred to as *uncoupled pixels*.

The working principles of the AFE for RD53A and RD53B_CMS have been introduced in Section 4.2.1. Hits are read out on the rising edge of a 40 MHz clock, in a configuration called *synchronous mode*. The delay between the injection and the effective readout of the hit is commonly referred to as *timing of the readout* and is regulated by a register called `CAL_EDGE_FINE_DELAY`. In this Section, the impact of this parameter within the tuning procedure will be discussed.

5.2. Readout timing

The probability p of detecting a hit is a function of the threshold of the comparator V_{th}, of the delay between the injection and the moment of the sampling Δt, and the injected charge Q, as shown in Figure 5.1. The first step of the tuning procedure, described in Section 4.3, is the tuning of the global threshold, which is carried out for a specific delay, iteratively injecting a well-defined amount of charge and changing the DC voltage input of the comparator. It is crucial to notice that the detection probability varies as a function of the delay between the injection and the readout Δt.

Figure 5.2 (left) shows the simplified representation of the output of the preamplifier for an injected charge Q, the sensing edge of the readout-clock (CLK) and the best interpolated global threshold (THR). In this configuration and assuming a noise-less signal, the pulse of charge Q is the smallest detectable signal: the trailing edge of an early signal and the leading edge of a late one of the same charge are both below the threshold during the sampling. This behaviour is shown in Figure 5.2 (center). If $Q^{'}$ and $Q^{''}$ are the smallest detectable charges for a late and an early signal respectively, then the following relation applies: $Q^{'} > Q^{''} > Q$. A graphical representation can be found in Figure 5.2 (right). The charge required to sample a signal varies as a function of the delay: it has a clear minimum for the delay t_0, it increases linearly for early signals with $t_1 < t_0$ as a function of the Krummenacher current and increases exponentially for late signals with $t_1 > t_0$ due to time-walk effects, with the profile shown in Figure 5.3 (left).

The probability of detecting a signal is oscillating with a period of 25 ns, and the

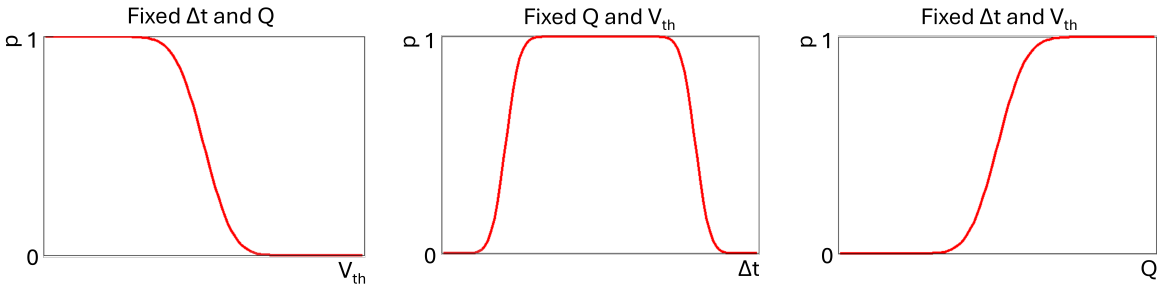

Figure 5.1.: Detection probability as a function of the threshold of the comparator V_{th}, the timing of the readout with respect to the injection Δt and the injected charge Q. Adapted from [95].

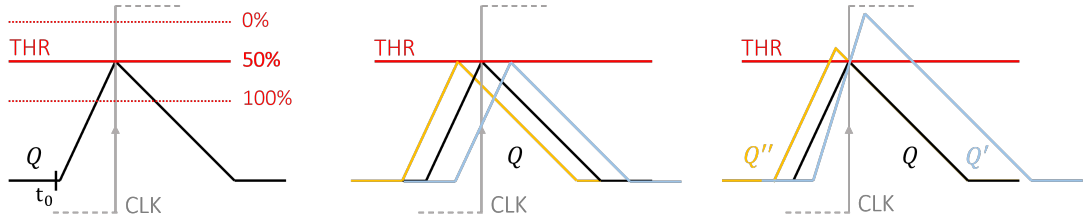

Figure 5.2.: Binary search of the optimal global threshold (left) corresponding to Q and representation of the smallest detectable charges for in-time (Q), early (Q'') and late (Q') signals (center, right).

intrinsic variation of the threshold is given by the intersection of the curves representing the detection probability for each bunch-crossing. The final oscillation of the *effective threshold* is highlighted in red in Figure 5.3 (right). Focusing on the intersection of the curves within one bunch-crossing, it is possible to appreciate that the minimum of the curve corresponds exactly to the charge Q to which the module was tuned. Hence, signals smaller than the set threshold, as for example noise hits, are rejected.

Choosing a delay $t_1 \neq t_0$ for the readout causes a shift in the expected set threshold: the DC voltage input of the comparator is shifted downwards to match the 50% detection efficiency criteria, making Q no longer the smallest detectable charge. If the readout is fixed at a time $t_1 > t_0$, the smallest detectable signal corresponds to the late signal of charge Q' and if $t_1 < t_0$ to the early signal of charge Q'', as can be seen in Figure 5.4. The curve in Figure 5.5 (left) shows that the smallest detectable charge at the time t_1

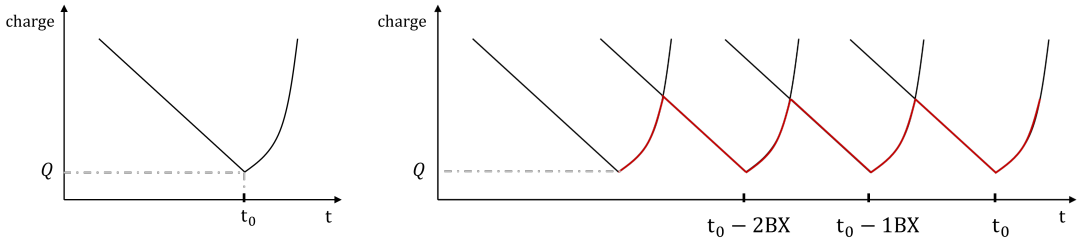

Figure 5.3.: Minimum detectable charge as a function of the timing of the readout for 1 bunch-crossing and N bunch-crossings.

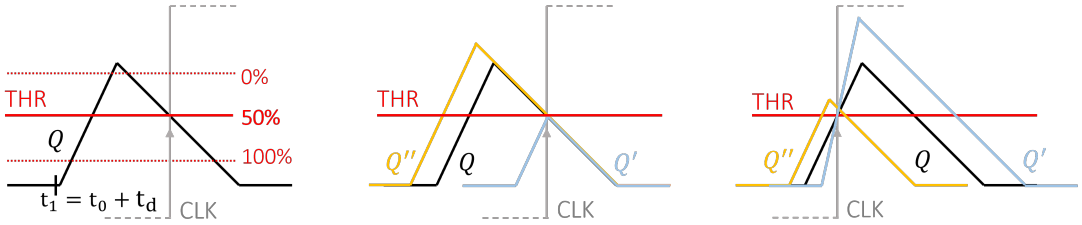

Figure 5.4.: The binary search results in a smaller value for the optimal global threshold if the delay is set incorrectly, as can be seen by comparing the representations on the left in this Figure and Figure 5.2. The smallest detectable signal becomes the late-signal Q' if the delay $t_1 > t_0$ or Q'' if the delay $t_1 < t_0$, with t_0 being the optimal delay.

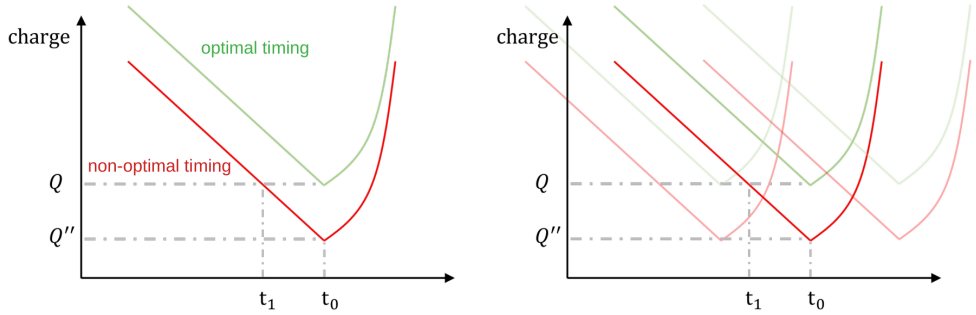

Figure 5.5.: Minimum detectable charge as a function of the timing of the readout for 1 (left) and N (right) bunch-crossings, for a chip tuned to a threshold Q at the optimal delay t_0 (green curve) and a non-optimal delay t_1.

is still Q, but the smallest detectable charge within the entire bunch-crossing time frame corresponds to Q'', obtained for the best delay t_0. Hence, asynchronous hits corresponding to a charge lower than the set threshold can still be detected and digitized by the front-end, instead of being rejected. This concerns noise hits or hits originating from particle interactions in un-bunched beams (e. g. beams at the DESY or SPS test beam facilities). It is fundamental to mention that in the final experiment, the phasing of the clock will match the best fine delay chosen for the tuning, such that the region associated with the highest efficiency will be exactly the one associated with the lowest threshold.

In summary, the oscillation of the measured effective threshold within the bunch-crossing is to be expected and depends on the shape of the signal. Tuning the chip using the correct setting for the delay is crucial to set the highest DC voltage as the input of the comparator, leading to the smallest detectable signal being equal to the set threshold within the entire 25 ns time frame and to the rejection of all asynchronous hits below the set threshold. This analysis applies for signals of all shapes: by setting the correct delay, it is always possible to appreciate the full, periodical oscillation of the effective threshold within the bunch-crossing and the presence of a clear minimum associated with the lowest effective threshold, although the shape of the oscillation and the location of the minimum may change. This is the case for signals associated with crosstalk, as will be discussed in Section 5.4.

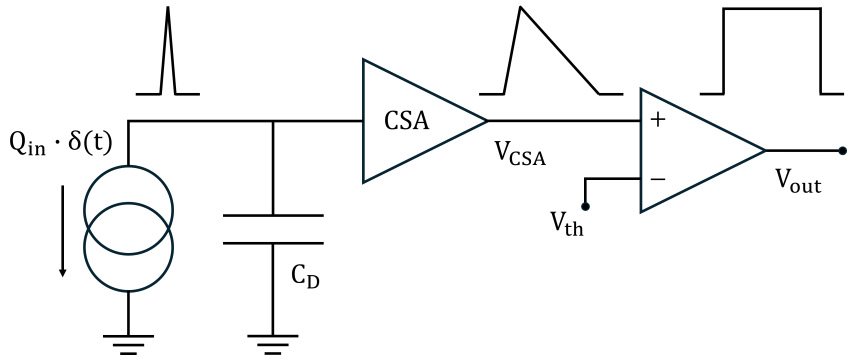

Figure 5.6.: Schematics of the simulated circuit. The input pulse is simulated as a Dirac-delta like signal ($Q_{in} \cdot \delta(t)$) and the detector with a capacitance $C_D = 50\,\text{fF}$. The output of the charge sensing amplifier (V_{CSA}) is compared to the threshold V_{th}, resulting in the comparator output V_{out}.

5.3. Simulation: timing of the readout and effective threshold

To understand the behavior observed in Figure 5.3, a simulation has been realized together with Prof. Luigi Gaioni and Prof. Mauro Dinardo, using the Spectre [96] simulator within the Cadence [97] framework. The effective threshold has been studied as a function of the time at which the charge injection takes place at the input of the front-end. The simulated structure includes a CSA whose output is fed to a comparator, as shown in Figure 5.6. In the simulated structure, the detector is modelled by means of a current source delivering Dirac-delta like pulses, $Q_{in} \cdot \delta(t)$, together with a detector capacitance C_D, connected to ground. The CSA input signal is converted into a voltage signal, V_{CSA}, which is then compared with a global threshold, V_{th}, resulting in a digital pulse at the comparator output, V_{out}. The detector capacitance C_D was set to 50 fF.

The RD53A and RD53B_CMS versions of the linear AFE have been simulated. In order to evaluate threshold variations with the injection time, the following procedure has been adopted: an input charge of 1000 e^- has been injected at the absolute time $t = 50\,\text{ns}$, and the global threshold has been tuned in order to achieve a valid signal (i. e. the minimum signal detectable by the subsequent digital logic) at the output of the comparator. The signals (V_{CSA} and V_{out}) resulting from one test injection are shown in Figure 5.7, for RD53A and RD53B_CMS.

The optimal time at which the comparator output can be sampled ensuring maximum rejection of spurious jittering effects and noise hits lies in the center of the originating step-like signal. For RD53A, the optimal sampling time is found around 104 ns, hence 54 ns after the injection, as shown in Figure 5.7 (left); for RD53B_CMS, an optimum value close to 86 ns has been obtained. This is related to the partial re-design of the comparator stage in RD53B_CMS, carried out with the goal of improving the time-walk performance, that translated to a faster and narrower response of the threshold discriminator.

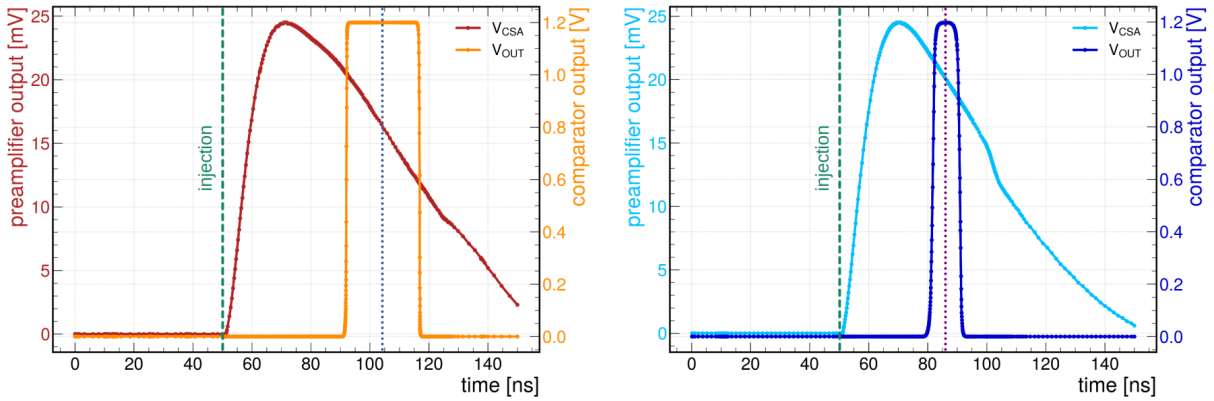

Figure 5.7.: V_{CSA} and V_{out} for RD53A (left) and RD53B_CMS (right). The injection takes place at $t = 50$ ns. The optimum time for the readout is highlighted with a dotted line, and corresponds to 104 ns and 86 ns, respectively.

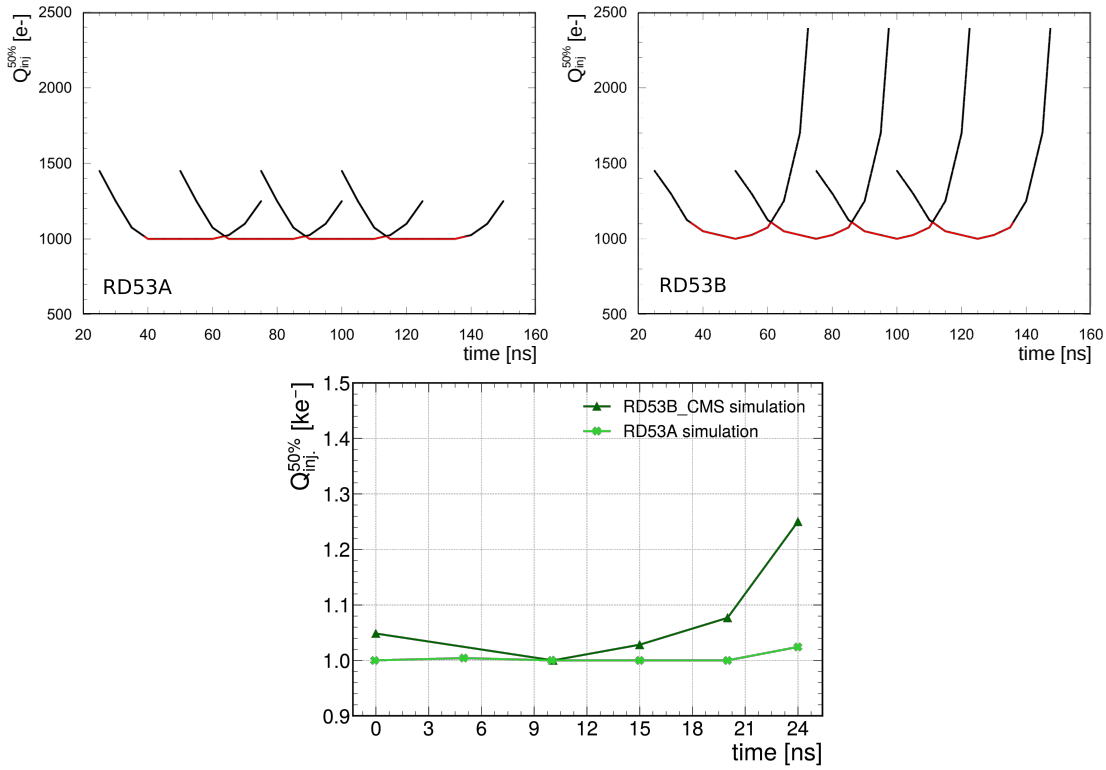

Figure 5.8.: Top: effective threshold as a function of the injection time, evaluated for RD53A (left) and RD53B_CMS (right) for multiple bunch-crossings. The red curve results from the intersection between the individual curves. Bottom: simulated effective threshold for RD53A and RD53B_CMS for one bunch-crossing.

As a next step, the time at which the charge injection occurs has been made to vary between 25 ns and 75 ns, and the input charge needed to sample a digital "1" at the optimal sample times discussed in Section 5.2 has been evaluated. This makes it possible to determine the effective threshold as a function of the time at which injection takes place.

Extending the analysis to multiple bunch-crossings, the curves in Figure 5.8 (top) can be obtained. In these plots, the effective threshold is the curve marked in red resulting from the intersection between the individual curves, with a period equal to 1 bunch-crossing. For this simple simulation, the final minimum-to-maximum amplitude variation (from now on, *min-to-max*) corresponds to circa 20 e^- for RD53A and 100 e^- for RD53B_CMS. By simulating just one bunch-crossing, the curves shown in Figure 5.8 (bottom) are obtained. In this case, the min-to-max variation is 25 e^- for RD53A and 240 e^- for RD53B_CMS.

To interpret the curves in Figure 5.8, it is important to recall that the RD53A chip exhibits a longer comparator output duration compared to the RD53B_CMS chip, when injected with the same amount of charge (see Figure 5.7). As a result, the readout window for detecting a signal with RD53A is wider, and hits can still be successfully registered even if the sampling time deviates from the optimal point. Conversely, the RD53B_CMS chip features a faster and sharper comparator response, and while this is beneficial for minimizing time-walk, it makes the chip more sensitive to the timing of the readout, as hits must be detected in a narrower readout window. This feature is reflected in the min-to-max variation of the effective threshold observed for the two chips: RD53A shows minimal dependence on the sampling time within the 25 ns bunch-crossing period, while RD53B_CMS chip displays a relevant variation over the same time frame.

In conclusion, the variation of the detection efficiency as a function of the timing of the readout is an intrinsic feature of the AFEs under exam, and is more pronounced in the RD53B_CMS version of the chip, due to its faster and sharper comparator response. This analysis applies to the detection of both injected signals and crosstalk-induced signals, as discussed in the next Section.

5.4. Crosstalk measurements and readout timing

The signals read out from the injected pixels and those induced by crosstalk differ in timing and shape. Hence, the associated detection efficiencies oscillate with diverse amplitudes and minima.

In pixel detectors, crosstalk can be measured by means of the injection circuit. The RD53A and RD53B_CMS readout chips have been tested, both bonded to an HPK sensor with the bitten design and $25 \times 100\,\mu m^2$ pixels. Different settings for the biasing of the preamplifier and the speed of the discharge were explored. Both modules were tuned following the procedure described in Section 4.3 to a threshold of $1000\,e^-$, keeping the optimal setting for the timing of the readout. All channels with a noise occupancy higher

than $f_{\text{occ}}^{\text{noise}} = 10^{-4}$ were masked.

To quantify crosstalk, a series of steps are undertaken. First, the charge corresponding to a 50% detection efficiency is measured: this corresponds to the effective threshold of the injected pixels $Q_{\text{sig,inj}}^{50\%}$. Next, the charge corresponding to a 50% detection efficiency in coupled pixels ($Q_{\text{XT,coup.}}^{50\%}$) is determined: this process entails injecting a pixel while reading out the pixel with the highest capacitive coupling to it. $Q_{\text{XT,uncoup.}}^{50\%}$ for uncoupled pixels is determined following the same procedure as for coupled pixels, but reading out the pixel with the second highest capacitive coupling to the injected one. These quantities are usually referred to as *effective thresholds* of the *coupled* or *uncoupled* pixels. It must be noted that $Q_{\text{XT,coup.}}^{50\%}$ and $Q_{\text{XT,uncoup.}}^{50\%}$ are much larger than $Q_{\text{sig,inj}}^{50\%}$, given that the signal being detected is just a fraction of the charge injected in the neighbouring pixel. All hits are read out in synchronous mode and in 1 bunch-crossing.

These measurements are repeated varying the delay of the readout, and for the AFE settings reported in Table 5.1. This study focuses on two registers, determining the biasing current of the preamplifier and the speed of the discharge of the preamplifier's output signal via the Krummenacher current. Increasing the DAC value of the register responsible for the preamplifier's bias current resulted in an increase from circa 3 µA to 3.5 µA. The setting for the Krummenacher discharge resulted in an average ToT = 5.3 for an injected charge of 6000 e^- when initialized to 29 and 70 DAC units for RD53A and RD53B_CMS, respectively, and an average ToT = 2 when increased to 70 and 180 DAC units. With an increased Krummenacher current in fact, the return to baseline of the preamplifier's signal is faster. It is important to mention that the granularity of the delay differs for the two iterations of the chip: it is 1.56 ns for RD53A (16 steps in the 25 ns bunch-crossing) and 0.78 ns for the RD53B_CMS (32 steps). The crosstalk (XT) can then be calculated as follows:

$$\text{XT}_{\text{un/coupled}} = \frac{Q_{\text{sig,inj}}^{50\%}}{Q_{\text{XT,un/coup.}}^{50\%} + Q_{\text{sig,inj}}^{50\%}} \tag{5.1}$$

	Configuration	PA bias [DAC]	I Krumm. [DAC]
RD53A	default	350	29
	high PA bias	400	29
	fast discharge + high PA bias	400	70
RD53B_CMS	default	300	70
	high PA bias	450	70
	fast discharge + high PA bias	450	180

Table 5.1.: Settings used to evaluate crosstalk for different configurations of the AFE.

	XT coupled [%]				XT uncoupled [%]			
	best delay	average	min	max	best delay	average	min	max
RD53B	4.68	8.93	4.66	15.36	2.57	3.48	2.56	5.71
RD53A	14.22	14.07	13.72	14.33	4.43	4.65	4.41	4.93

Table 5.2.: Measured crosstalk values for best delay, average, minimum, and maximum for the two chip iterations, tuned using the default settings.

5.4.1. Crosstalk measurements with the injection circuit

The effective threshold (normalized to the set target threshold in the following plots) exhibits the expected oscillating behaviour with a clear minimum for most front-end configurations, as shown in Figure 5.9. These results must be compared with the simulation targeting a single bunch-crossing, shown in Figure 5.8 (bottom). For the default settings, there is a qualitative agreement between the simulation and the results obtained by means of the injection circuit: the 50 e^- and 500 e^- min-to-max variation of the measured effective threshold for RD53A and RD53B_CMS, respectively, is circa two times larger than the corresponding min-to-max values obtained with the simulation.

Different AFE settings were explored, to evaluate the dependence of the intra-bunch-crossing threshold variability from other parameters, which were not part of the aforementioned simulation. Increasing the biasing of the preamplifier had a negligible impact on RD53B_CMS, while it induced an increase of the effective threshold towards higher delays for RD53A. A faster discharge caused a shift of the minimum towards higher delays for both chips. These effects are not accounted for by the simple examples introduced in Section 5.2, and will require further studies.

A similar variability of the effective threshold can be observed when measuring crosstalk-induced hits on the coupled and uncoupled pixels, as shown in Figure 5.10. A substantial difference between the two iterations of the chips is the phase relationship between the oscillation of the effective threshold of the injected pixels and those of the coupled and uncoupled pixels. As it can be seen from the comparison of Figures 5.9 and 5.10 (left), the curves describing the variation of the effective threshold of the injected pixels and those of coupled and uncoupled pixels for the RD53B_CMS chip are in anti-phase. This is not the case for the curves obtained for RD53A, whose respective minima fall inside the same bunch-crossing and which feature just a minor phase shift, as can be seen from Figures 5.9 and 5.10 (right). If these oscillations are in anti-phase, the measured crosstalk exhibits a clear minimum within the bunch-crossing time frame; if instead the oscillations are in phase or have minimal phase shift, crosstalk levels remain stable within the bunch-crossing. The two different cases are observed for RD53B_CMS and RD53A, respectively.

Despite the observed fluctuations, the only value that must be quoted for the effective crosstalk at the LHC is that obtained for the best time delay, or in a small interval around it. In fact, this is the region that will be selected for the readout in the final experiment,

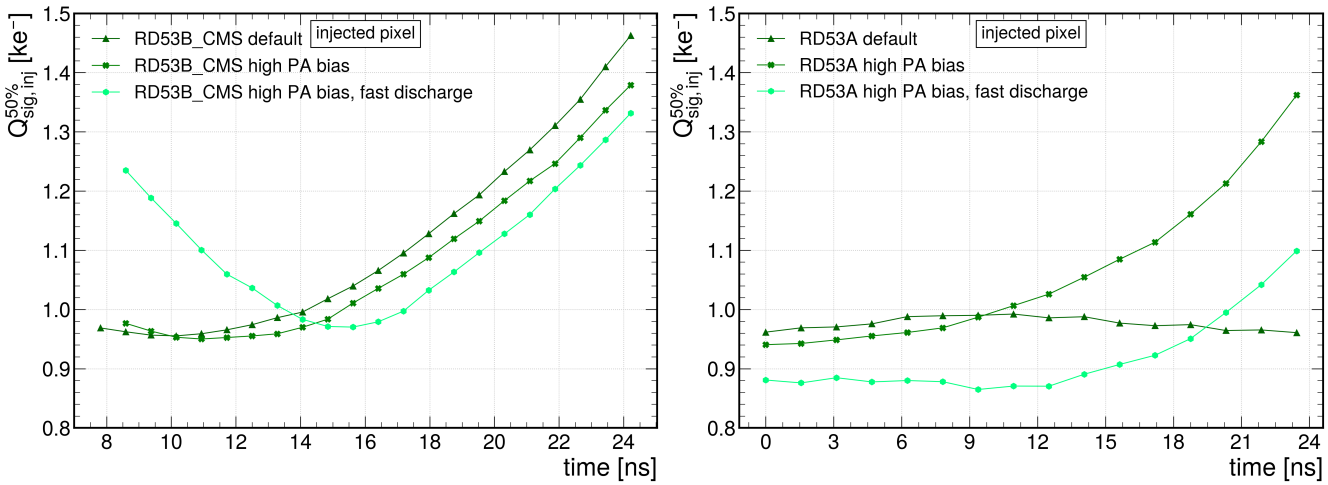

Figure 5.9.: Measured charge corresponding to the effective threshold for RD53B_CMS (left) and RD53A (right). The results are in agreement with the simulation shown in Figure 5.8. The values used for the high preamplifier (PA) bias and for the fast discharge are given in Table 5.1.

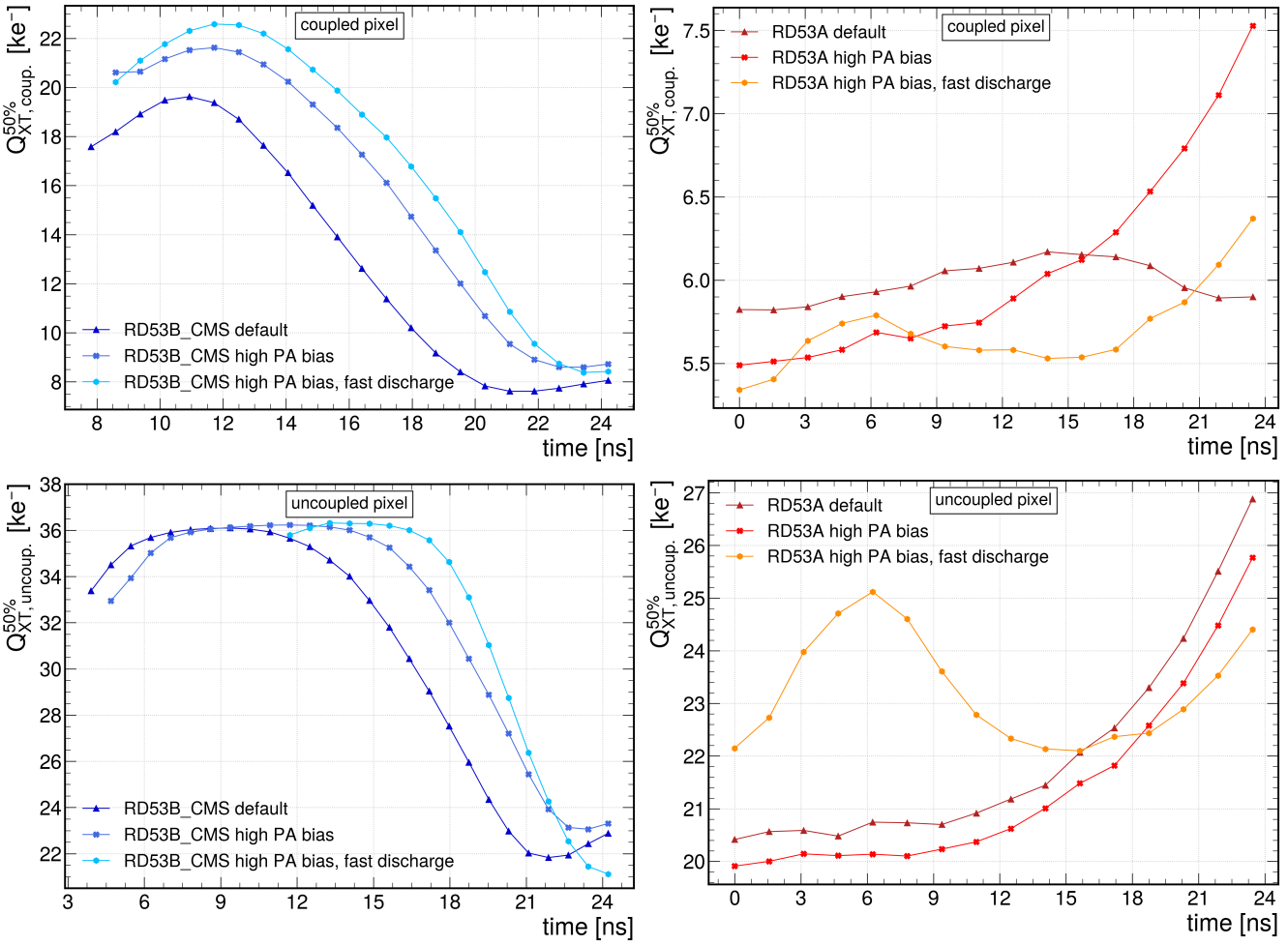

Figure 5.10.: Measured charge corresponding to the effective threshold of coupled (top) and uncoupled (bottom) pixels, for RD53B_CMS (left) and RD53A (right). The values used for the high preamplifier (PA) bias and for the fast discharge are given in Table 5.1.

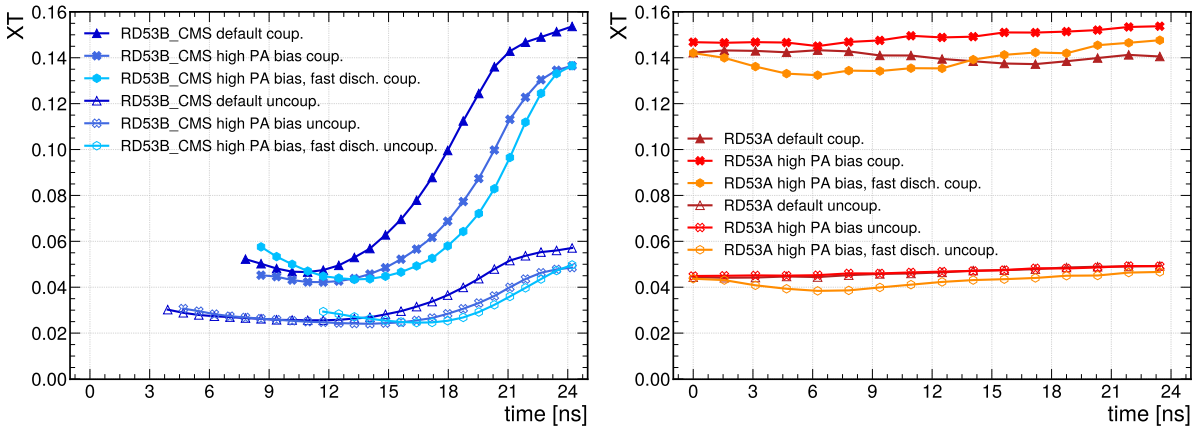

Figure 5.11.: Crosstalk values, calculated using Eq. 5.1, for coupled and uncoupled pixels (closed and open symbols) in the two iterations of the chip, for default and high bias settings of the preamplifier and the Krummenacher current (see Table 5.1).

as it is associated with the lowest threshold and therefore the highest efficiency. For asynchronous beams (e.g. the DESY or SPS test beams) however, the final crosstalk value that needs to be taken into account is an average on the entire 25 ns. A summary of the relevant crosstalk values measured for the default setting of the chips can be found in Table 5.2. For the last iteration of the chip, crosstalk levels remain below 10% for all explored AFE settings at the respective optimal readout times, as shown in Figure 5.11.

5.5. Conclusions

This study investigated the correlation between the effective threshold, crosstalk and the timing of the readout in RD53A and RD53B_CMS chips, connected to HPK sensors with a bitten design and pixel size of $25 \times 100\,\mu m^2$. By using an integrated charge injection circuit to inject controlled signals into individual pixels and observing the responses in neighboring pixels, crosstalk levels for different configurations of the analog front-ends have been evaluated.

Both iterations of the chip displayed an oscillating behavior of effective thresholds as a function of the time delay between the injection and the readout, and a strong correlation was observed between readout timing and crosstalk magnitude for RD53B_CMS. The fluctuations of the effective threshold for injected and coupled pixels are in anti-phase, resulting in a pronounced minimum of crosstalk within the 25 ns bunch-crossing; in contrast, RD53A showed only a minor phase shift between these oscillations, leading to more stable crosstalk levels.

Simulations confirmed the experimental observations, proving that, due to the architecture of the AFEs, the effective threshold of the injected pixel changes with a periodicity of 25 ns. The min-to-max variations of the simulated effective thresholds are circa half of the ones measured with the injection circuit, displaying however a qualitative agreement,

with RD53B_CMS reporting a more relevant variation within the bunch-crossing with respect to RD53A.

In the region centered around the best delay $t_0 = 10.14 \pm 0.78$ ns, the final evaluated crosstalk for RD53B_CMS assemblies tuned using the default settings is $4.6\% - 4.8\%$ for the coupled pixels and 2.6% for uncoupled pixels. For RD53A, the crosstalk is stable and independent of the timing of the readout at an average of 14.1% for coupled pixels and 4.6% for uncoupled pixels. For the latest iteration of the chip and for all the AFE settings explored, crosstalk levels remain below 10% as per requirement of the CMS collaboration.

During operation, each module will be tuned using the optimal delay parameter, ensuring that the smallest charge detectable by the readout corresponds to the set threshold. The latency of each module will be chosen accordingly, such that the selected readout phase coincides with the region of maximum detection efficiency, which, by design, is associated with the lowest effective threshold. This configuration, corresponding to the optimal delay determined during tuning, will be maintained throughout operation. The tuning procedure will be repeated periodically over the lifetime of the modules. Preliminary measurements on irradiated assemblies indicate that the overall shape of the threshold oscillation is preserved for accumulated fluences up to $1 \times 10^{16}\,\mathrm{cm}^{-2}$, suggesting that the optimal-delay tuning strategy remains applicable under HL-LHC operating conditions.

6. Experimental setup for test beam measurements

The purpose of test beam measurements is to evaluate detector components under conditions that closely resemble those in a high-energy physics experiment. Key beam parameters such as particle type, momentum, time structure, and intensity must be selected to match the requirements of the specific tests being conducted.

For tracking detector components, the beam momentum is typically set either near the minimum of the ionizing energy loss curve to study the detector's performance with the smallest possible signal, or at the highest available energies to minimize the impact of multiple Coulomb scattering. Depending on the goals of the test, additional equipment such as scintillators, beam telescopes, or magnets may be used to provide trigger signals, precise reference tracks, or controlled magnetic fields.

The test beam measurements presented in this work were carried out at beam line 21 (TB21) of the DESY II synchrotron. The following Sections provide an overview of the beam line, its infrastructure, and the data acquisition software framework. Additionally, specific aspects of the setup used for measurements involving the RD53B_CMS readout chip are discussed in detail.

List of Own Contributions The author's contributions to the results presented in this chapter include:

- Preparing and conducting test beam measurements.
- Data quality assessment during test beam measurements.
- Characterization, calibration, and optimization of the tuning of sensor modules in the laboratory and at the test beam facility.

This work was developed in collaboration with Dr. Massimiliano Antonello, Dr. Annika Vauth, Dr. Jörn Schwandt, Dr. Georg Steinbrück and Chin-Chia Kuo.

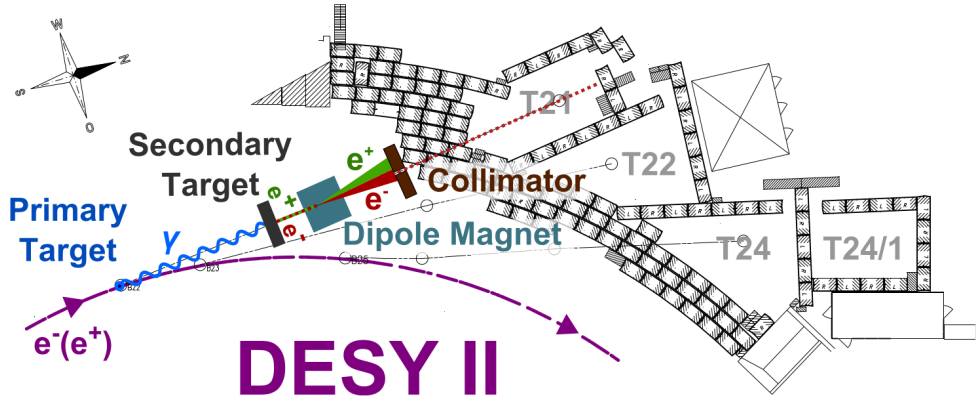

Figure 6.1.: Test beam generation for beam line 21. From [98].

6.1. The DESY II test beam facility

At the core of the DESY II test beam facility is the DESY II synchrotron, the successor to the original accelerator that gave the Deutsches Elektronen-Synchrotron (DESY) its name. The synchrotron has a radius of 46.6 m and a total circumference of 292.8 m. It accelerates either positrons or electrons to serve the PETRA III facility as well as three test beam areas: TB21, TB22, and TB24. While a comprehensive description of the DESY II Test Beam Facility can be found in [98], this Section provides a summary of the elements most relevant to this work, with particular emphasis on the EUDET-type Pixel Beam Telescope DATURA.

Beam line

Electron or positron bunches, pre-accelerated to a momentum of 0.45 GeV/c, are injected into DESY II and further accelerated to momenta of up to 6 GeV/c. Typically, each electron bunch undergoes two acceleration cycles before being dumped, spending a total of 160 ms in the synchrotron.

The process of producing a beam from these bunches, illustrated in Figure 6.1 for beam line 21, begins with the generation of photons via bremsstrahlung. To achieve this, a 7 µm thick carbon wire is inserted into the DESY II beam orbit. The wire causes the bunch to gradually lose intensity while producing photons at a rate of about 1.02 MHz, as each revolution in the synchrotron takes approximately 0.98 ms. These photons exit the vacuum system tangentially to the DESY II ring through an aluminum window.

Just beyond this point, a secondary target converts the photons into electron-positron pairs before they enter another vacuum section. The available targets are made of either aluminum or copper, and come in various thicknesses ranging from 1 mm to 5 mm. For the measurements discussed here, a 5 mm thick copper target was used to maximize the electron yield.

A dipole magnet with a maximum field strength of 1.38 T then separates the resulting particles by momentum and charge. The magnetic field can be tuned so that a primary

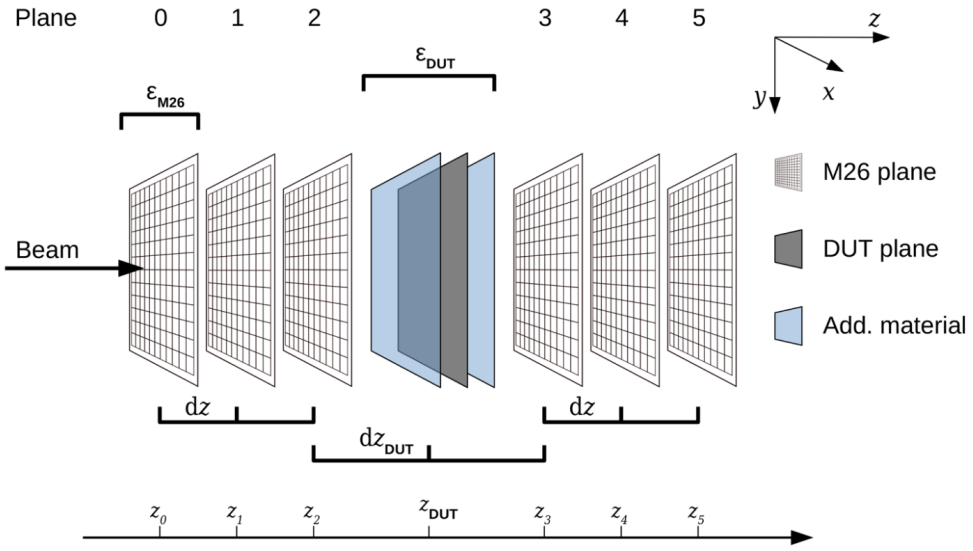

Figure 6.2.: Example setup for test beam measurements using the DATURA beam telescope. The telescope planes are separated by a uniform distance dz. The distance between the DUT and the nearest telescope plane is dz_{DUT}. The material budgets of a MIMOSA26 plane and the DUT, defined as in [99], are indicated by ϵ_{M26} and ϵ_{DUT}, respectively. From [99].

collimator, made of 100 mm thick tungsten, selects particles (electrons or positrons) with chosen momenta between 1 GeV/c and 6 GeV/c.

Test beam measurements take place in designated areas known as *test beam zones*. Within these areas a secondary collimator, positioned as the final element before the beam exits the vacuum system, shapes the beam before it reaches the experimental setup. Various collimators with aperture sizes ranging from 5×5 mm^2 to 20×20 mm^2 are available, allowing for adjustment of the beam profile. The momentum spread of the beam is influenced by the widths of both the primary and secondary collimators, and typically lies around 0.16 GeV/c.

Once inside the test beam area, the beam passes through the experimental setup, which may include scintillators, several planes of a beam telescope, and the detector components under test. After traversing the setup, the beam is absorbed in a combination of lead blocks and a concrete wall.

For safety, a beam shutter connected to an interlock system can block the beam, enabling secure access to the area when needed. A spill counter inside the synchrotron and a beam monitor positioned ahead of the secondary collimator provide real-time information on the accelerator's operational status and the particle rate within the test beam area.

Beam telescope

A beam telescope is an essential tool for studying the spatial resolution of tracking detector modules in high-energy physics, as it provides the reference measurements needed to reconstruct particle trajectories. Since the hit resolutions of these modules are typically

on the order of a few micrometers, the beam telescope must offer a track resolution of similar or better precision.

At TB21, the DATURA beam telescope serves this purpose. It is a EUDET-type pixel telescope composed of six individual planes, each equipped with a MIMOSA26 sensor. A comprehensive description and performance evaluation of the telescope is provided in [99]; a brief overview is presented here.

The MIMOSA26 sensor [100] is a monolithic active pixel sensor fabricated using the AMS 350 nm CMOS process, featuring a pixel pitch of 18.4 × 18.4 µm^2. The sensor consists of 1152 columns and 576 rows, covering a total area of 21.2 × 10.6 mm^2. Its average physical thickness is 54.5 ± 3.6 µm. Readout is performed using a rolling-shutter method with an integration time of 115.2 µs. The sensor provides binary hit information for each pixel. For particles impinging perpendicularly, the intrinsic hit resolution of a single plane was measured to be 3.24 ± 0.9 µm, using a threshold set at six times the pixel noise level. Each of the six MIMOSA26 sensors is mounted on an aluminum frame and covered with a 50 µm thick kapton foil for light shielding. The total material budget of one telescope plane amounts to 7.6 × 10^{-4} X_0, with material properties and radiation lengths taken from [15]. The aluminum frames are water-cooled and maintained at 18°C. In typical operation, the telescope is configured such that three sensor planes form a triplet, as shown in Figure 6.2: one triplet is placed upstream and the other downstream of the Device Under Test (DUT).

The track resolution of the beam telescope at the DUT position depends on several factors, as shown in Figure 6.3: the spacing between telescope planes (dz), the distance from the DUT to the nearest upstream plane (dz_{DUT}), and the material budget of the DUT (ϵ_{DUT}, defined as in [99]). The minimal material budget of the DUT setup is determined by the combined contributions of the thickness of the sensor and readout chip, and it is approximately 0.0097, based on values from [15]. The minimum distance dz_{DUT} is circa 7 cm, due to mechanical constraints of the setup. Even when using the minimal values for dz_{DUT} and ϵ_{DUT}, the track resolution is found to be better with larger spacings. This justifies the average spacing of circa 12 cm between the MIMOSA26 telescope planes used throughout the data taking.

The track resolution is also influenced by the momentum of the particles in the beam. A momentum of circa 5.2 GeV/c is chosen as a compromise, balancing a sufficiently high particle rate with good tracking precision.

Additional infrastructure

In addition to the particle beam and beam telescope, further infrastructure is required to study tracking detector modules for high-energy physics experiments. One essential component is the trigger system, which initiates the readout sequence when a relevant event occurs. What qualifies as “relevant” depends on the context of the experiment.

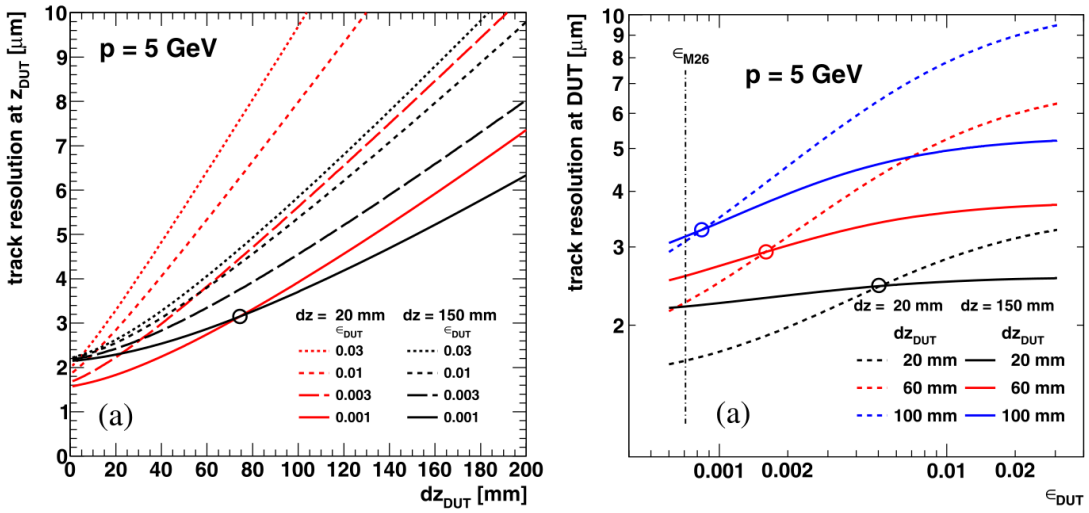

Figure 6.3.: Track resolution of the DATURA beam telescope at the DUT position for two telescope triplet spacings dz, predicted using the General Broken Lines formalism [101]. The resolution is shown as a function of the DUT position (left) and as a function of the DUT material budget (right). From [99].

For the measurements discussed here, an event is considered relevant if a particle passes through a defined acceptance window that covers the active area of the DUT.

To generate a trigger signal, two scintillators are used, each with an acceptance area of 10×20 mm^2. These scintillators are connected to photomultiplier tubes (PMTs) via light guides. The PMT outputs are sent to a Trigger Logic Unit (TLU), which supplies the necessary voltage to the PMTs, and processes their signals by applying discrimination and configurable logic, such as AND/OR, to up to four inputs. It then outputs a trigger signal using NIM/TTL standards.

An important feature of the TLU is its handshake mechanism. This system allows an operation mode in which no new trigger signals are sent until all the detector components have processed the readout from previous events. To achieve this, each component can send a busy signal to the TLU, which can temporarily block further triggers until the busy signal is clear, once all components completed their readout. More details about the TLU and the handshake mechanism are provided in [102].

The test beam setup also includes two linear stages and one rotational stage, which allow for precise positioning of the DUT. The linear stages enable vertical and horizontal movement with a precision of 0.1 µm and are mainly used to center the DUT relative to the beam axis. The rotational stage, with an angular precision of 50 µrad, allows the DUT to be tilted with respect to the beam direction, making it possible to study detector performance as a function of particle incidence angle.

Software

An essential component of test beam measurements is the software framework used for data acquisition from both the beam telescope and the other detector systems. The

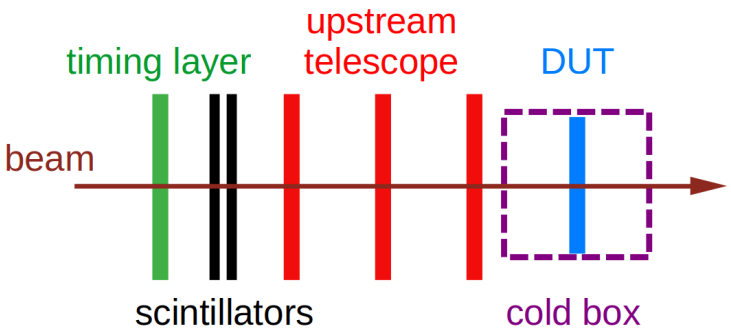

Figure 6.4.: Detector arrangement used for the test beam measurements of CMS pixel assemblies. The three telescope planes, the timing layer and the DUT are represented in red, green and blue respectively. The DUT is encapsulated in the cold box, when tested at cold.

EUDAQ2 framework (from now on, simply EUDAQ) [99, 103], originally developed for EUDET-type beam telescopes, is designed to handle the telescope readout and TLU control, and supports integration with additional devices. In the measurements presented here, EUDAQ is used to control and acquire data from the beam telescope as well as the DUT and the time reference plane, which are described in more detail later in this Chapter.

To integrate a detector into the EUDAQ framework, a producer is required to serve as the interface between the detector's data acquisition system and the EUDAQ Run Control. The producer receives commands from the Run Control and transmits data to a Data Collector, which can merge data from all connected detectors and store it on disk.

The EUDAQ Run Control acts as a user interface, allowing users to configure the detectors and manage the start and end of data acquisition runs. In addition, EUDAQ offers online monitoring capabilities and gathers log messages from all integrated devices to support data quality assessment.

6.1.1. Measurement setup for RD53B_CMS pixel sensors

The setup for test beam measurements with RD53B_CMS assemblies is tailored to the conditions and infrastructure of the DESY II test beam facility, particularly the beam telescope described in Section 6.1. For the measurements presented here, electrons with a momentum of 5.2 GeV/c are selected using the primary collimator. These electrons enter the TB21 area and pass through the detector setup, which is illustrated in Figure 6.4.

The trigger scintillators are positioned upstream of the setup, facing the incoming beam. The beam telescope is arranged with three MIMOSA26 sensors positioned in front of the DUT, with a distance of circa 12 cm between planes. In the measurements presented here, only the forward triplet is used, as the presence of a cooling copper layer in the *cold box* (described later in this Section) scatters the electrons, impeding track reconstruction. Due to the presence of this cooling system, the minimum distance between the DUT and

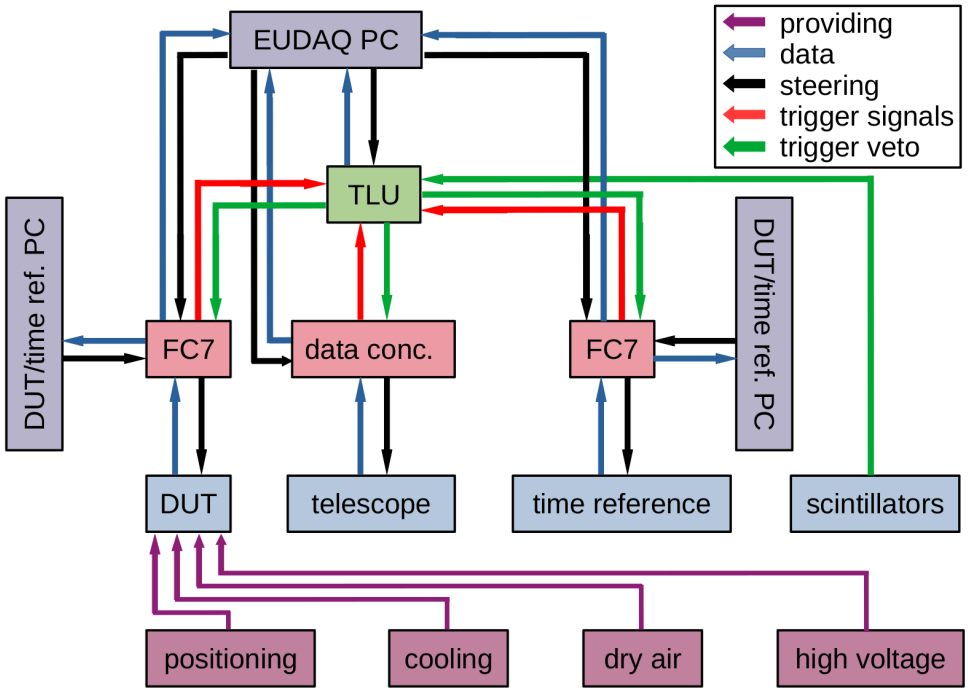

Figure 6.5.: Simplified block diagram of the test beam setup, where each block represents a physical device and is color-coded by type: PCs (gray), trigger system components (green), data acquisition systems (light red), detectors (light blue), and environmental control devices (purple). Arrows illustrate the direction of signal flow or control interactions between the components.

the closest telescope plane is approximately 7 cm, when the assemblies are tested at cold.

As the MIMOSA26 sensors have a relatively long integration time of 115.2 µs, another RD53B_CMS single chip module with pixel pitches of 50 × 50 µm^2 is used as a *time reference plane*, to select tracks that are in sync with the DUT's readout window. This time reference plane is installed at vertical incidence, before the first beam telescope plane.

Figure 6.5 presents a simplified block diagram of the setup, illustrating how the various detectors are integrated into a system of interconnected devices and how these devices interact or influence one another. Certain operating conditions must remain stable throughout a run or across multiple runs; these are referred to as *environmental control parameters*. For clarity, the block diagram only includes the environmental control system associated with the DUT. A photograph of the actual detector setup is provided in Figure 6.6. In the diagram, the devices are grouped by their function.

DUT control parameters

The DUT requires active cooling to maintain the leakage current below 10 nA per pixel (as per CMS requirement). To achieve this, a two-stage cooling system is employed. The first stage consists of a silicon oil chiller, set to circa −25° C, which cools a U-shaped copper structure inside the cold box. The second stage uses two Peltier elements, operating at 5 W to 7 W, in direct thermal contact with the copper bridge that is contacting the aluminium

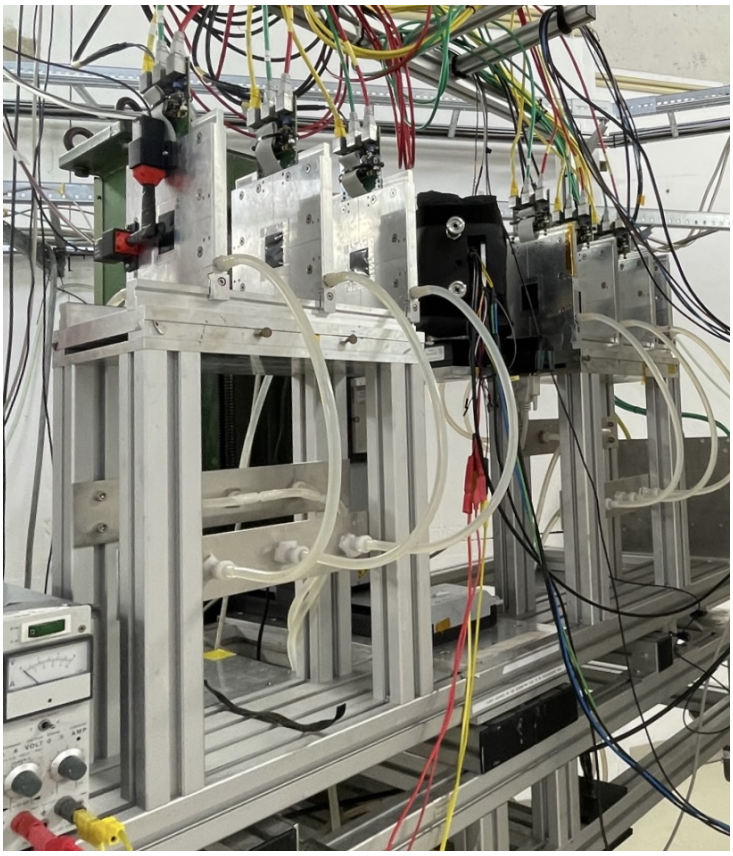

Figure 6.6.: Photograph of the test beam setup at TB21. Visible in the image are the MIMOSA26 planes and the cold box, wrapped with ArmaFlex foam.

layer glued to the DUT assembly, as shown in Figure 6.7. To ensure thermal isolation and avoid condensation, the copper support structure is enclosed in an aluminium container, referred to as the cold box, insulated with ArmaFlex foam and flushed with dry air. To minimize material in the beam path, the box is designed with a kapton opening in the front. While the DUT temperature is not measured directly, thermistors placed on the copper bridge indicate it is circa $-20°$ C.

Accurate positioning of the DUT is also essential, as it must be aligned within the 10×20 mm^2 acceptance window defined by the trigger scintillators in order to benefit from the available particle rate. The DUT is mounted on the two linear stages to allow precise adjustments in the x- and y- directions.

High voltage for the pixel sensor is supplied by a Keithley 2470 high voltage sourcemeter, located in the beam area and controlled remotely. The bias current is monitored for every run to ensure it remains below the aforementioned limit.

Once the environmental control parameters are set to the desired values and no further human interaction in the test beam area is required, the beam interlock is activated. The data-taking run is then initiated after the tuning of the reference module and the DUT, by starting the data acquisition software on the EUDAQ computer. The EUDAQ computer runs the EUDAQ framework (see Section 6.1), which manages the readout and control of the six MIMOSA26 telescope planes, the TLU, the time reference plane and the DUT.

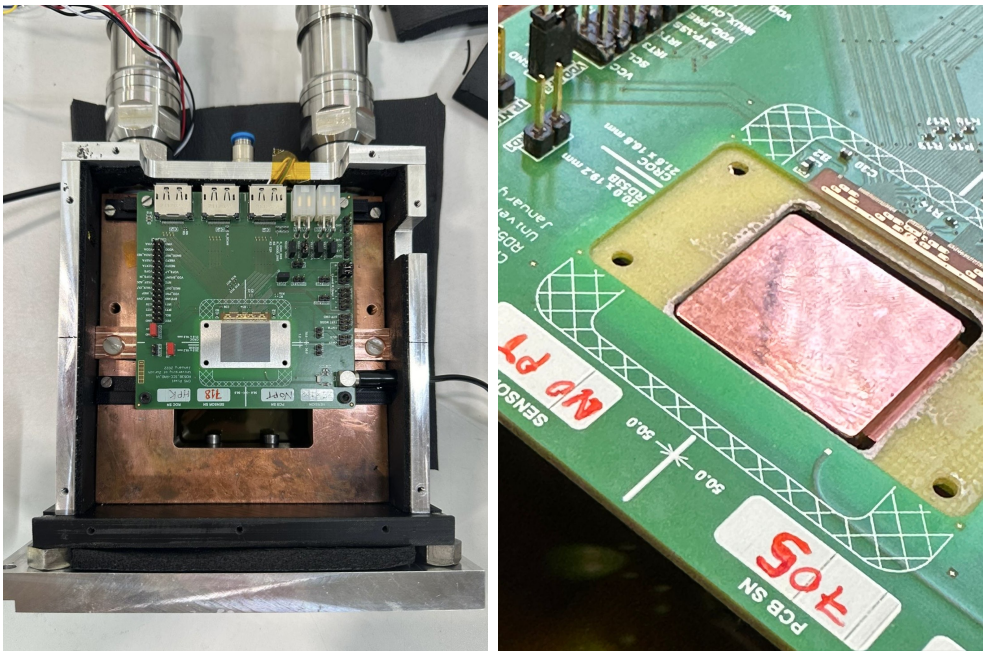

Figure 6.7.: Left: top view of the cold box. The assembly and the associated PCB rest on a copper bridge, screwed to a copper U-shaped element, kept cold by the fluid pumped from the chiller. Two Peltier elements are located where the copper bridge contacts the copper U. Right: protruding copper bridge element, visible behind a virgin PCB before the gluing of the assembly.

Data acquisition and tuning of the RD53B_CMS chip is done with the Ph2_ACF [104] readout system, which includes a custom designed base board and a commercial FPGA, called FC7 [105]. The RD53B_CMS chip supports up to 4 lanes of data transfer with a rate of 1.28 Gbit/s. The FC7 base board provides data transfer for up to 20 lanes, with a matching rate of 1.28 Gbit/s. The connection from the RD53B_CMS chip to the FC7 is done via a display port cable to provide a high rate transfer at a low cost. In order to carry out measurement with the RD53B_CMS chip, the sensor-readout chip assembly is wirebonded to a PCB (also known as Single Chip Card, SCC). The PCB provides necessary connectors for communication with the chip and biasing of the sensor.

During data taking, each time an electron passes through the setup, the PMTs generate a signal that is sent to the TLU, which checks coincidence conditions and makes trigger decisions. Operating in handshake mode, the TLU processes the signal and forwards it to the data acquisition systems only when all devices are ready, as determined by their busy signals (see Section 6.1). The data acquisition systems then initiate the readout sequence for their respective detectors and send the recorded data to the corresponding computers.

6.1.2. Assemblies under study and irradiation

Two non-irradiated and one irradiated assembly have been thoroughly studied for this work, and are listed in Table 6.1. All DUTs featured a bitten design, with pixel pitches of $25 \times 100\,\mu m^2$. A range is specified for the accumulated equivalent fluence of the irradiated

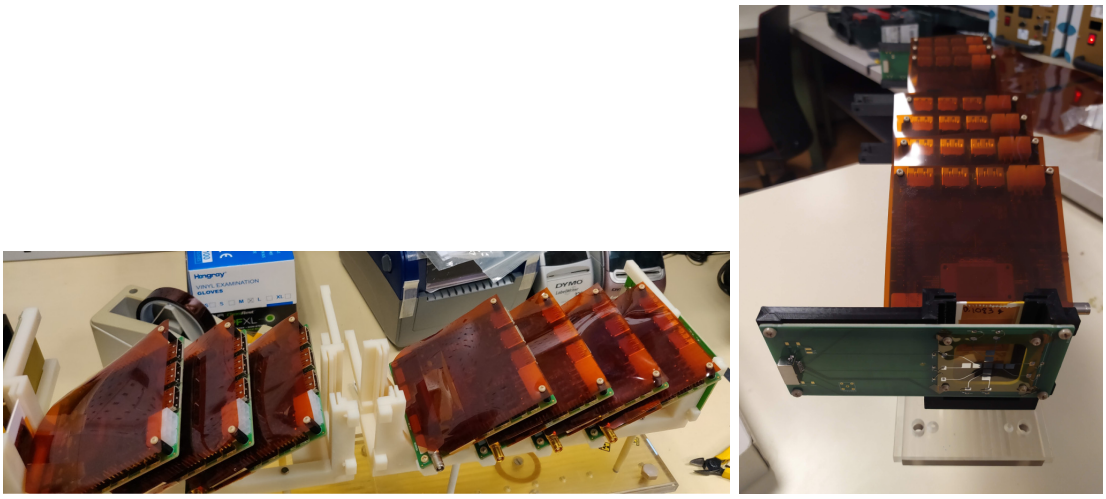

Figure 6.8.: Support structure used during the irradiation campaigns at the CERN PS-IRRAD, with modules tilted by 30° as viewed from the longitudinal direction.

assembly, as it has been irradiated inhomogeneously. Module number 702 was used as timing reference module.

Name	Type	Pitch	Status	Equivalent fluence
702	default	$50 \times 50\,\mu m^2$	non-irradiated	-
705	bitten	$25 \times 100\,\mu m^2$	non-irradiated	-
707	bitten	$25 \times 100\,\mu m^2$	irradiated	1×10^{16} cm^{-2} – 4.8×10^{15} cm^{-2}
718	bitten	$25 \times 100\,\mu m^2$	non-irradiated	-

Table 6.1.: List of modules tested or used in this work.

Irradiated samples

Module 707 was irradiated with protons to study the impact of radiation damage on its performance. Irradiation was carried out at the CERN PS-IRRAD facility using protons with a beam momentum of 24 GeV/c (corresponding κ-factor ≈ 0.62 [106]). The beam at the CERN PS-IRRAD has an approximately Gaussian profile, with a full width at half maximum of about 14.5 mm in the horizontal direction and 6.5 mm in the vertical direction.

A dedicated support structure, shown in Figure 6.8, was developed to ensure uniform irradiation across the modules, holding them at a 30° tilt in the vertical plane, and rotating them around a horizontal axis aligned with the beam direction. To expose the entire horizontal width of the modules, the support was moved along a 26 mm path. Beam alignment with respect to the module position was verified using a laser, as illustrated in Figure 6.9 (left).

Before irradiation, the modules were coated with parylene to protect the wirebonds. Additionally, aluminum foils were placed behind selected modules to enable precise fluence

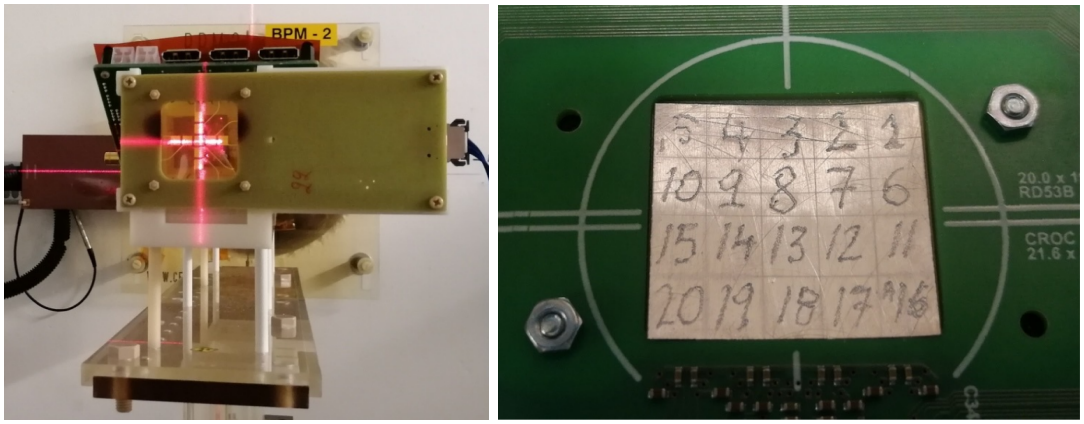

Figure 6.9.: Laser-aided beam alignment process (left) and an aluminum foil attached to the back of an RD53B_CMS assembly, used for post-irradiation dose profiling.

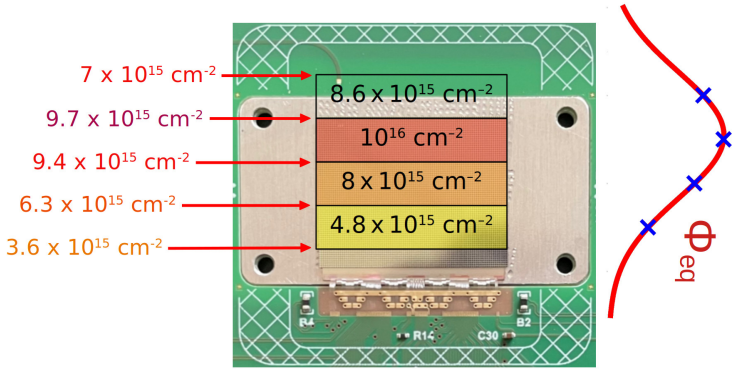

Figure 6.10.: Results of the analysis of the aluminium foils for the irradiated assembly, and extrapolated fluence profile. The estimated RD53B_CMS position is lower with respect to the aluminium foils, as the sensors had a 30° tilt during irradiation.

measurement, as shown in Figure 6.9 (right). After irradiation, the foils were sectioned into smaller pieces, and the activity of each piece was measured via spectroscopy. The overall uncertainty in the fluence determination was estimated to be circa 7%. The irradiation was performed at room temperature, as the devices were unpowered, and afterwards the samples were stored at low temperature to prevent annealing.

Due to a misalignment of the support table with respect to the beam, the modules were not irradiated uniformly, but with a gradient going from the bottom to the top of the matrix, in direction of the columns. Analysing the aluminium foils, it emerged that the equivalent fluence profile on the surface of the sensor ranged from 4.8×10^{15} cm^{-2} to 1×10^{16} cm^{-2}, respectively, as depicted in Figure 6.10.

Given the presence of this gradient, three horizontal sections of 100 rows each have been studied separately to evaluate their performance as a function of the accumulated radiation damage. Throughout this work, it is assumed that the inhomogeneous total ionizing dose accumulated by the readout chip had a negligible impact on the operation of the assemblies.

7. Analysis of test beam data

The main observables needed to characterize the pixel assemblies are the position resolution and the hit efficiency, that are extracted from test beam measurements using accurate reconstruction and careful selection of particle tracks.

The following Sections describe the track reconstruction process for the detector setup outlined in the previous chapter, beginning with the identification of individual pixel hits and their clustering. These pixel clusters indicate potential particle intersections with the detector planes and serve as the basis for building track candidates. Through an iterative alignment procedure, the reconstructed tracks are used to refine the alignment of the setup, leading to improved track quality. Once alignment is optimized, the definitions and reconstruction methods for position resolution, hit efficiency, and other relevant observables are presented. The Section concludes with a set of selection criteria designed to isolate track candidates most likely associated with genuine particle interactions, thereby minimizing background contributions in the analysis.

List of Own Contributions The author's contributions to the results presented in this chapter include:

- Together with Dr. Massimiliano Antonello, the optimization of the set of cuts used for data selection, and of the routine used to reconstruct test beam data at the DESY II test beam facility.
- The in-depth study of the effect on the relevant observables of the individual cuts and the cut-flow, for both non-irradiated and irradiated assemblies.

This work was developed in collaboration with Dr. Massimiliano Antonello, Dr. Annika Vauth, and Chin-Chia Kuo.

7.1. Track reconstruction and setup alignment

The analysis of test beam data in this work is done using Corryvreckan, a flexible and modular software framework designed for the reconstruction and analysis of test beam and laboratory data. More information on the software can be found in [107].

The specific procedure used in this work for the analysis of the test beam data can be summarized as follows:

- Clustering
- Prealignment of the telescope planes
- Prealignment of the DUT
- Track reconstruction
- Telescope alignment
- Alignment of the DUT
- Evaluation of the observables

In the following Section, a detailed description of each of these steps will be given.

Clustering and position reconstruction

The first step in the reconstruction process is the identification of the pixels that registered charge deposited from the impinging ionizing radiation. When a trigger signal is issued, the responses of pixels that recorded a hit are stored. As the tuning is performed before data taking, all detector planes are able to suppress most noise-induced hits. These pixels are then grouped into a cluster using a clustering algorithm. After clustering, the position where the particle crossed the detector plane is reconstructed based on the cluster information. This reconstructed position is subsequently used in the overall track reconstruction.

The clustering algorithm begins with a single pixel and continues adding neighboring pixels that meet the clustering criteria. When no additional pixels can be added to the current cluster, the algorithm moves on, skipping any pixel already included in a cluster. This process repeats until all eligible pixels have been grouped into clusters.

The *clustering condition* is defined as:

$$|\Delta i| \leq 1 \quad \text{and} \quad |\Delta j| \leq 1, \tag{7.1}$$

where Δi and Δj represent the differences in column and row indices between any pixel already in the cluster and any unassigned neighboring pixel.

For a given cluster, the cluster position x_{cl} (and analogously y_{cl}) is calculated as:

$$x_{\text{cl}} = p_x \cdot \frac{\sum_{k=0}^{N-1} Q_k \cdot i_k}{\sum_{k=0}^{N-1} Q_k}, \tag{7.2}$$

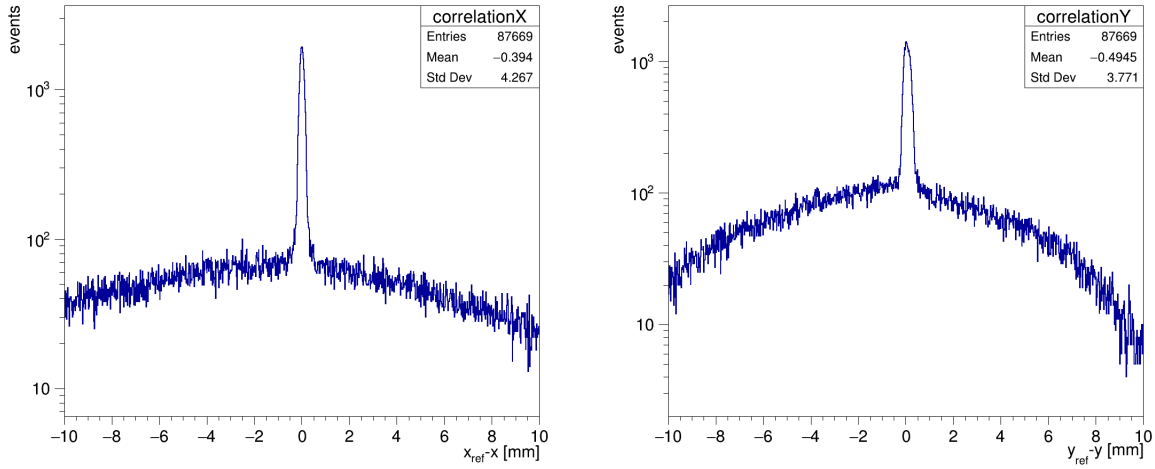

Figure 7.1.: Correlations in the x- and y-directions between the reference plane and the DUT.

where p_x is the pixel pitch in the x-direction, N is the total number of pixels in the cluster, i_k is the column index of the k-th pixel, and Q_k is the pixel charge introduced in Section 7.2.1. This method is commonly known as the *weighted mean* or *center-of-gravity* algorithm. The *cluster charge* is defined as the sum over the charges of all pixels in a cluster. For the purpose of telescope alignment, Q_k is taken to be the number of neighboring pixels, as MIMOSA26 readout chips only have binary readout.

Prealignment

The starting point for the alignment of the detector planes is given by the measurements taken by hand during the installation of the setup. In the software, these parameters are first refined using correlation values between the detectors and a reference plane (prealignment) and then iteratively with tracks (alignment).

The prealignment procedure relies on identifying the most frequently observed spatial offset between the individual detectors of the setup and the telescope plane closest to the DUT, also called the *reference plane*. The prealignment of the DUT, for example, is achieved by collecting cluster pairs from the DUT and the reference plane, with timestamps belonging to the same event. For each pair, the spatial differences in the x- and y-directions are calculated and filled into correlation histograms, such as the ones shown in Figure 7.1. These histograms reflect how the DUT and reference detector are spatially correlated, with a high concentration of entries indicating a common offset. The bin with the highest number of entries is interpreted as the most probable relative shift between the two detectors. The corresponding x- and y-offsets are then taken as the prealignment corrections to be applied to the DUT. This approach assumes that the correct alignment will produce the sharpest and most populated correlation peak, and is particularly effective in situations with high statistics and a dominant single alignment solution.

Track reconstruction

The track reconstruction procedure begins by identifying clusters on each detector plane. To ensure these originate from the same particle, clusters are required to have been recorded in the same event for all detectors. The track reconstruction starts by selecting pairs of clusters on the first and last telescope planes, and using them to seed a straight-line trajectory. This initial track is then extrapolated to the positions of the remaining detectors in the setup.

At each detector plane, the algorithm searches for additional clusters that lie close to the extrapolated trajectory. Spatial proximity is evaluated using elliptical cuts that reflect the detector's resolution in each coordinate. If a cluster satisfies these constraints and is the closest candidate, it is added to the track. The procedure continues iteratively, plane by plane. Once all suitable clusters have been associated, the track is fitted accounting for scattering. Tracks that pass quality criteria, such as a minimum number of associated clusters and acceptable χ^2 values (see Section 7.3.3), are retained. The final tracks are stored for further analysis, and their parameters are used to fill histograms related to residuals, track angles, and resolution, providing detailed diagnostics on the tracking performance.

Alignment of the telescope planes

The alignment of the telescope in Corryvreckan is performed by adjusting the relative positions and orientations of the individual planes. This is essential for achieving optimal track reconstruction and for ensuring that the *residuals*, which are the differences between measured and predicted hit positions, are minimized across all sensors. Two example distributions of the residuals in the x- and y-directions for the first telescope plane are shown in Figure 7.2. The method implemented here is based on the well-established Millepede algorithm [108], which solves a large system of linear equations to simultaneously determine the best alignment parameters for all planes.

The process begins by collecting reconstructed tracks throughout the data run. These tracks are stored and later used to define equations that relate residuals to shifts and rotations of the detectors. All three rotational parameters are investigated for the alignment procedure, together with x and y. The z-direction is excluded from the alignment, as the divergence of the beam is too small to be able to reconstruct this parameter correctly. Each track is checked for completeness (i. e. whether it has hits on all necessary planes) and then contributes two equations (one for x and one for y) for each cluster.

Millepede then constructs a system of equations that describe how small changes in alignment parameters influence the residuals. Using an iterative procedure, it solves this system, applies corrections to the geometry, and refits the tracks with updated detector positions. This cycle is repeated until the alignment parameters converge below a defined threshold.

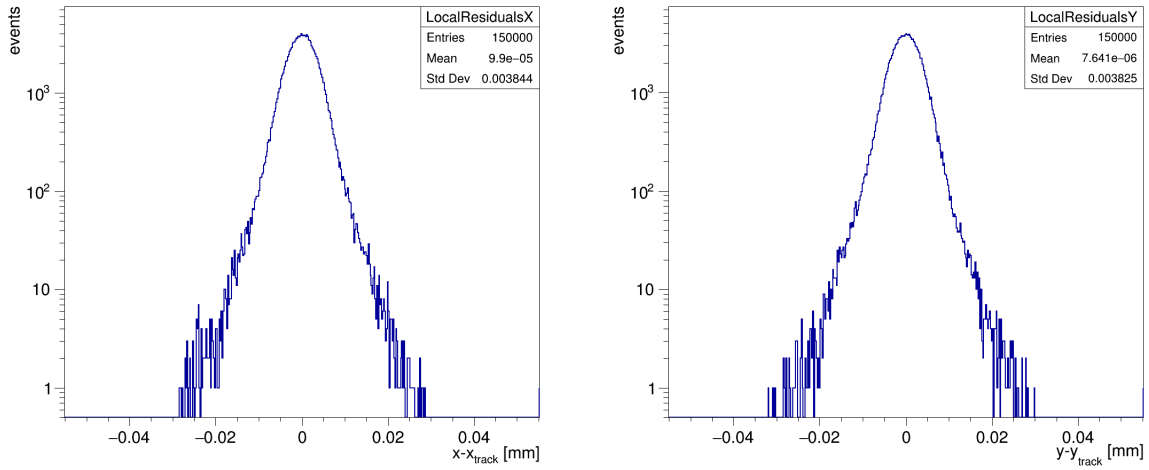

Figure 7.2.: Distributions of the residuals in the x- and y-directions for the first telescope plane.

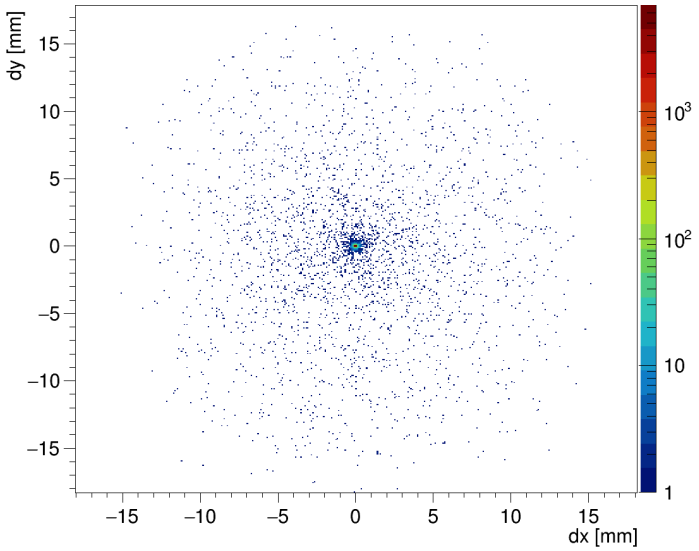

Figure 7.3.: Normalized 2D distance between tracks and centers of the clusters.

The output is a set of optimized shifts and rotations for each plane, which improves the spatial consistency of the track fits and minimizes the overall residuals.

Association of the DUT-clusters to tracks

Once the tracks have been reconstructed and the telescope has been aligned, tracks need to be associated to the DUT. This step is crucial for later performance studies, such as efficiency and resolution, as it links the predicted particle trajectory with the actual sensor response.

For each event, tracks are associated to spatially compatible clusters on the DUT. The association is done with respect to the center of the cluster, and the spatial compatibility is evaluated using a configurable elliptic cut. Each cluster passing all criteria is associated with the track. Throughout the process, the spatial offsets between track intercepts and clusters are monitored and stored, as shown in Figure 7.3.

Alignment of the DUT

The alignment of the DUT in Corryvreckan is done by minimizing the spatial residuals between reconstructed tracks and the associated clusters on the DUT. The underlying idea is to iteratively refine the position and orientation of the DUT such that the average distance between predicted track intercepts and the hit positions measured from the clusters is minimized, improving the geometrical alignment within the overall detector system.

The core of the alignment procedure uses a minimization routine (based on the MINUIT algorithm [109]) that iteratively adjusts the DUT's orientation and position along x- and y-directions to reduce the total residual χ^2, defined as the weighted sum of squared residuals:

$$\chi^2 = \sum_{\text{tracks}} \sum_{\text{clusters on DUT}} \left[\frac{\left(x_{\text{track}} - x_{\text{cluster}}\right)^2}{\sigma_x^2} + \frac{\left(y_{\text{track}} - y_{\text{cluster}}\right)^2}{\sigma_y^2} \right],$$

where σ_x^2 and σ_y^2 are the binary limits in the x and y pitch directions, $(x_{\text{cluster}}, y_{\text{cluster}})$ are the coordinates of the center of the clusters calculated with the weighted mean algorithm, and $(x_{\text{track}}, y_{\text{track}})$ are the coordinates of the associated hit positions, extrapolated on the surface of the DUT from the reconstructed telescope tracks. The χ^2 is often scaled by the number of degrees of freedom, defined as the difference between the number of measurements and the number of fit parameters (five, in the case under exam: x, y, and the three rotational angles). An example distribution is shown in Figure 7.9 (left).

This minimization is repeated over several iterations, and the shifts in translation and rotation are tracked to monitor convergence. Once the telescope and the DUT are aligned and the tracks are reconstructed, the relevant observables can be evaluated.

7.2. Definition of observables

To characterize the performance of the investigated pixel assemblies, the efficiency and the spatial resolution are evaluated. In addition, other observables such as cluster size and collected charge offer deeper insight into the underlying physics of the sensors, such as charge sharing, noise, and the impact of radiation damage.

7.2.1. Charge

The total collected charge at the readout electrodes of a silicon sensor can decrease following exposure to particle radiation, as discussed in Section 2.3. Since charge collection directly influences detector performance, studying its degradation as a function of neutron equivalent fluence is of particular interest.

The output of the readout chip is expressed in terms of a 4-bits Time-over-Threshold

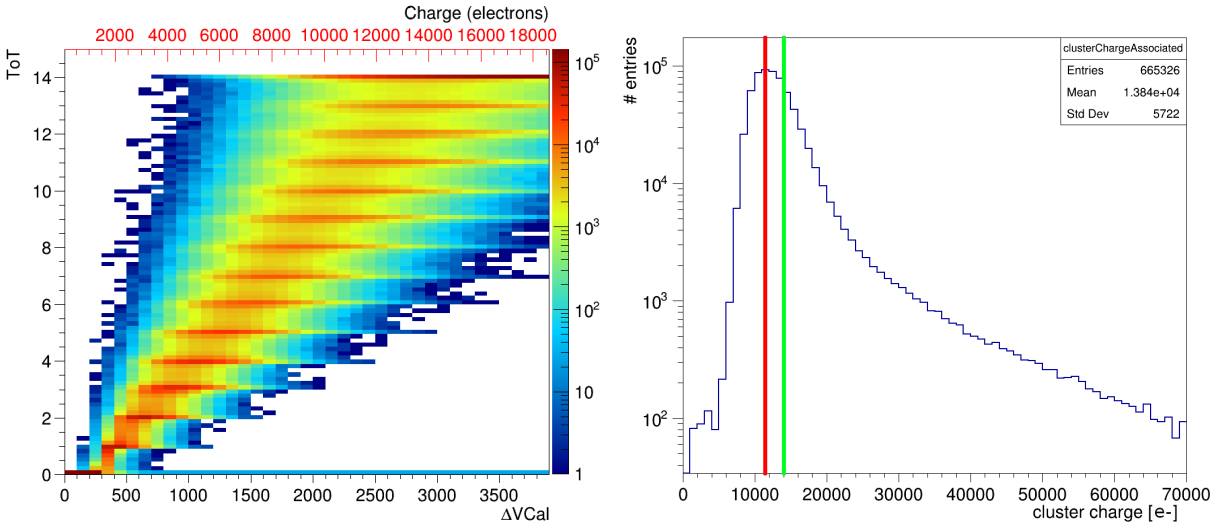

Figure 7.4.: Left: ToT output for different injected charges for all pixels in the matrix. Right: final cluster charge distribution. The mean value is marked in green, and the MPV is marked in red.

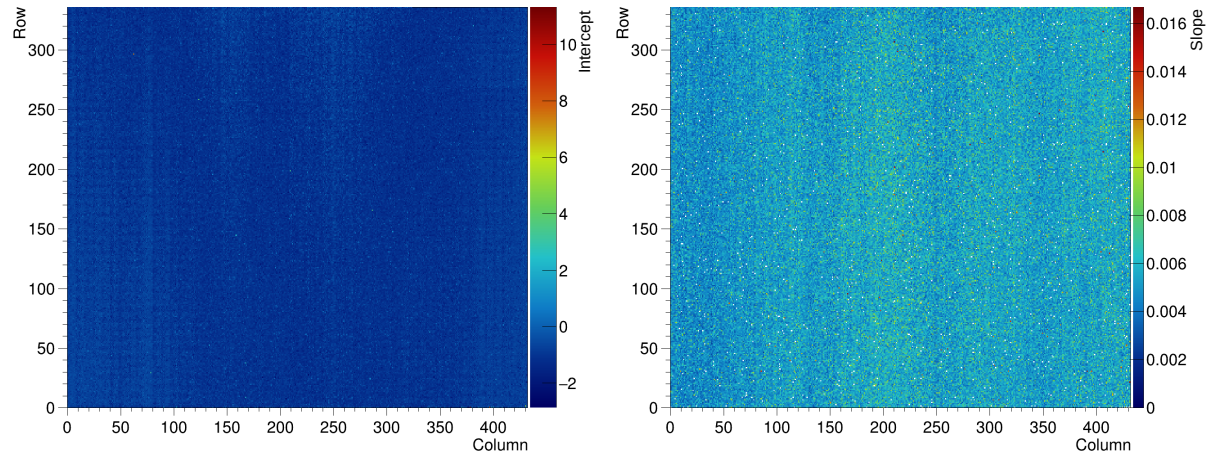

Figure 7.5.: 2D maps of the interpolated intercept (left) and slope (right) values.

(ToT, see Section 4.2.1). The valid values range from 0 to 14, as value 15 is used to signal a faulty output. To map each pixel's ToT into the corresponding amount of electrons, a calibration scan is launched at the end of every tuning procedure. The output for the entire matrix can be seen in Figure 7.4 (left). This plot is obtained by injecting each pixel with an increasing amount of charge and storing the corresponding responses in terms of ToT. Each pixel's response is then fit, and the parameters for the slope and intercept are stored. On average, the interpolated lines intersect the x-axis at a charge corresponding to the set threshold. The maps for interpolated intercepts and slopes can be seen in Figure 7.5. An example of the final cluster charge distribution obtained after data taking with a calibrated module can be seen in Figure 7.4 (right). The mean value and the MPV of the distribution are marked in green and red, respectively.

7.2.2. Noise

As the neutron equivalent fluence increases, the leakage current in the silicon sensor also rises. This leads to an increase in shot noise, which contributes to the overall noise of the sensor module. Although the leakage current can grow by several orders of magnitude, the resulting increase in noisy pixels remains largely independent of the applied bias voltage (see Figure 8.6). Consequently, the leakage current is considered a subdominant factor, and the observed noise increase is primarily attributed to radiation-induced effects in the readout chip.

Noisy pixels are masked during the tuning procedure, before data taking, following the procedure outlined in Section 4.3.3. They are identified by disabling the internal injection, issuing a number of triggers N_{trig} and counting the number of hits recorded by each of the pixels N_{hits}. Channels with an occupancy greater than the pre-defined threshold $f_{\text{occ}}^{\text{noise}} > N_{\text{hits}}/N_{\text{trig}}$ are disabled. Throughout this work, $f_{\text{occ}}^{\text{noise}} = 10^{-4}$.

7.2.3. Hit efficiency

The *hit efficiency* of the DUT is defined as:

$$\epsilon_{\text{hit}} = \frac{N_{\text{track}}^{DUT}}{N_{\text{track}}},$$

where N_{track} is the total number of selected telescope tracks, and N_{track}^{DUT} refers to the subset of tracks that are matched with a corresponding hit in the DUT. This is usually corrected for the amount of pixels that have been disabled at the end of the tuning procedure with a factor called *acceptance*, defined as:

$$\alpha = 1 - \frac{N_{\text{masked}}}{N_{\text{total}}},$$

where N_{total} and N_{masked} are the total amount of pixels available in the entire matrix or in a specific region of interest, and the total amount of masked pixels in the same region.

The matching between telescope tracks and DUT hits is carried out by applying a cut on the radial distance r_{min} between the expected impact positions obtained by projecting the reconstructed tracks onto the DUT surface (x_{tel}, y_{tel}) and the centers of the associated clusters on the DUT ($x_{\text{min}}, y_{\text{min}}$):

$$r_{\text{min}} = \sqrt{(x_{\text{min}} - x_{\text{tel}})^2 + (y_{\text{min}} - y_{\text{tel}})^2} < \text{spatial cut}.$$

Details concerning the chosen value for the spatial cut are discussed in Section 7.3.1. The uncertainty on the efficiency is determined using a Clopper–Pearson [110] confidence interval at the one-sigma level, an approach recommended by the Particle Data Group [111]. Analogous to a Gaussian standard deviation, this corresponds to the central 68.3% interval of the binomial distribution for the measured efficiency. However, unlike

the Gaussian approximation, it properly accounts for the bounded nature of probabilities between 0 and 1. For high statistics, its uncertainty can be approximated with the one of a binomial distribution:

$$\sigma_\epsilon = \sqrt{\frac{\epsilon\,(1-\epsilon)}{N_{\text{track}}}},$$

where ϵ_{hit} is the hit efficiency and N_{track} is the total number of selected telescope tracks.

7.2.4. Spatial resolution

In this work, the term *spatial resolution* refers to the uncertainty associated with the measurement of the hit positions in the investigated assemblies, commonly referred to also as *single-plane resolution* or *hit resolution*.

The resolution in the x- and y-directions is calculated starting from the distributions of the residuals:

$$x_{\text{res}}^{\text{DUT}} = x_{\text{cluster}}^{\text{DUT}} - x_{\text{tel}}^{\text{DUT}}, \quad y_{\text{res}}^{\text{DUT}} = y_{\text{cluster}}^{\text{DUT}} - y_{\text{tel}}^{\text{DUT}},$$

where $x_{\text{cluster}}^{\text{DUT}}$ is the position of the center of the cluster calculated with the weighted mean algorithm, and $x_{\text{tel}}^{\text{DUT}}$ is the position of the associated hit, obtained by projecting the tracks reconstructed with the telescope planes on the DUT surface. As the discussion is confined to the DUT, and to prevent the notation from becoming needlessly cumbersome, the superscript "DUT" will henceforth be omitted. The discussion below focuses on the y-direction, though the same method applies to the x-direction.

Beyond careful selection of the tracks considered in the analysis, two main challenges must be addressed: consistently quantifying the width of the distributions of the residuals, and disentangling the combined contributions from the telescope and the DUT. The analysis procedure outlined in the following is designed to resolve these challenges.

Any method used to quantify the width of this distribution should satisfy the following three requirements:

- It should account for the non-Gaussian nature of the distribution at incidence angles near 0°, which arises from physical effects such as energy loss and multiple Coulomb scattering, both contributing to pronounced tails. Additionally, the method should be sensitive to possible asymmetries in the distribution, which may result from biases in the reconstruction algorithm.

- It should maintain compatibility with other publications, which often report spatial resolution in terms of the standard deviation σ of a Gaussian fit.

- It should offer stability, particularly against outliers caused by δ-electrons or variations in the applied track selection criteria.

To fulfill these requirements, the width of the residual distribution is determined using a *truncated RMS*, denoted as $\mathrm{RMS}_{\mathrm{trc}}(y_{\mathrm{res}})$ and $\mathrm{RMS}_{\mathrm{trc}}(x_{\mathrm{res}})$. For a Gaussian distribution, the RMS is equal to the standard deviation σ, ensuring compatibility with commonly reported values in the literature without assuming a specific distribution shape. To reduce the impact of outliers, the RMS is computed iteratively by excluding values outside the range $\pm 4 \cdot \mathrm{RMS}_{\mathrm{trc}}$. This procedure converges quickly and retains more than 99.7% of the events in the residual distributions for the datasets analyzed. For the sake of notational simplicity, we define:

$$\sigma_{\mathrm{res,y}} := \mathrm{RMS}_{\mathrm{trc}}(y_{\mathrm{res}}), \quad \sigma_{\mathrm{res,x}} := \mathrm{RMS}_{\mathrm{trc}}(x_{\mathrm{res}}).$$

The finite telescope resolution introduces an uncertainty on the predicted positions x_{tel} and y_{tel}, which in turn contributes to the overall width of the residuals, so that:

$$\sigma^2_{\mathrm{res,y}} = \sigma^2_{\mathrm{hit,y}} + \sigma^2_{\mathrm{tel,y}}, \quad \sigma^2_{\mathrm{res,x}} = \sigma^2_{\mathrm{hit,x}} + \sigma^2_{\mathrm{tel,x}}\,,$$

where σ_{hit} and σ_{tel} represent the contributions of the DUT and the telescope to the final width of the distribution of the residuals. To quantify these contributions, $\sigma_{\mathrm{res,y}}$ and $\sigma_{\mathrm{res,x}}$ are evaluated for a specific subset of events, which must fulfill the set of requirements discussed in detail in [112]. First, they must originate from particles impinging on the DUT at vertical incidence. Then, they must be associated to clusters of size two in the column or the row direction. Last, to avoid including crosstalk-induced events in the final set of data, for the asymmetry of the charge distribution it must apply that $|\eta_y| < 0.3$, with the parameter for asymmetry η_y defined as:

$$\eta_y = \frac{Qx_2 - Qx_1}{Qx_1 + Qx_2}. \tag{7.3}$$

For this specific subset of events, the contribution of the telescope to the overall width of the residuals distribution remains unchanged, while the contribution of the DUT becomes negligible, as the spatial resolution of segmented silicon detectors at the boundary between pixels is less than 1 µm [112]. More specifically, for $|\eta_y| \approx 0$ the charge in the two pixels is approximately the same, and the simulated $\sigma_{\mathrm{hit,y}} < 150\,\mathrm{nm}$, while for $|\eta_y| \approx 0.3$ the contribution is circa 0.4 µm. An example of the residual's distribution associated to these events is shown in Figure 7.6.

The effective telescope resolution (also known as *track position resolution* σ_{tpr}, when evaluated on this subset of events) can then be calculated as:

$$\sigma^2_{\mathrm{res,y}}\big|_{\mathrm{tpr}} = \sigma^2_{\mathrm{hit,y}}\big|_{\mathrm{tpr}} + \sigma^2_{\mathrm{tel,y}}\big|_{\mathrm{tpr}} \approx \sigma^2_{\mathrm{tel,y}}\big|_{\mathrm{tpr}} =: \sigma^2_{\mathrm{tpr,y}}\,,$$

where the subscript *tpr* indicates the above-mentioned bundle of conditions that these events must fulfill. This can then be scaled to correct the extrapolated width of the

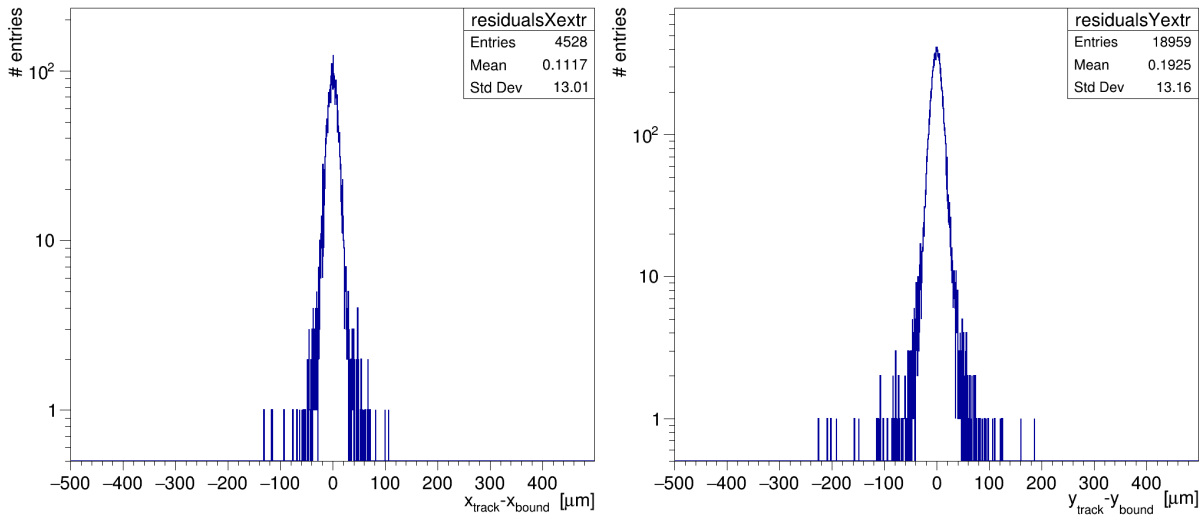

Figure 7.6.: Residuals in the x- and y-directions for the subset of events described in the text.

DUT's residual distributions as a function of the angle θ, as:

$$\sigma^2_{\mathrm{tpr,y}}(\theta) = \sigma^2_{\mathrm{tpr,y}} \frac{\cos(\theta_0)}{\cos(\theta)},$$

with θ being the angle between the versor perpendicular to the surface of the sensor and the beam, and θ_0 being the angle obtained when aligning the DUT to achieve an almost vertical incidence of the particles on the assembly, used to calculate $\sigma_{\mathrm{tpr,y}}$. The factor $\cos(\theta)$ accounts for the fact that $\sigma_{\mathrm{tel,y}}$ is calculated in the global coordinate system, whereas $\sigma_{\mathrm{hit,y}}$ is expressed in the local DUT coordinate system. The uncertainty on this parameter is then calculated as:

$$\mathrm{err}_{\mathrm{tpr,y}}(\theta) = \mathrm{err}_{\mathrm{tpr,y}} \frac{\cos(\theta_0)}{\cos(\theta)}.$$

Once the track position resolution is determined, the resolution of the DUT can be calculated as:

$$\sigma_{\mathrm{hit,y}} = \sqrt{\sigma^2_{\mathrm{res,y}} - \sigma^2_{\mathrm{tpr,y}}}.$$

The statistical uncertainty on $\sigma_{\mathrm{hit,y}}$ is obtained by propagating the statistical uncertainties on both $\sigma^2_{\mathrm{res,y}}$ and $\sigma^2_{\mathrm{tpr,y}}$. It is important to note that $\sigma_{\mathrm{tpr,y}}$ is an *effective resolution*, and it is always greater than the nominal telescope resolution $\sigma_{\mathrm{tel,y}}$. This is due to several reasons. First, the nominal telescope resolution quoted e. g. in [99] is calculated using both the three upstream and the three downstream telescope planes, whereas in this work only the upstream planes could be used, due to the presence of the cold box (see Section 6.1.1). The cold box also imposed a minimum separation of 7 cm between the last telescope plane and the DUT. Moreover, a 20 mm thick layer of foam and a 150 µm thick layer of kapton were standing between the last telescope plane and the DUT for thermal

isolation, introducing additional scattering. Finally, the assumption that the contribution of the DUT to the width of the residuals is negligible is formulated assuming a perfectly flat device, while the assemblies under study are bowed with a sagitta of circa 20 µm.

7.2.5. Cluster size

The cluster size is a simple yet informative observable that reflects the effects of charge sharing, a process that significantly influences spatial resolution. As introduced in Section 7.1, the term "cluster" refers to a group of neighboring pixels that exceed the threshold and are likely associated with the passage of a particle. These pixels are grouped using a clustering algorithm that applies the condition specified in Equation 7.1.

For any given cluster, the *cluster size* is defined as the total number of pixels it contains. Additionally, two related quantities, $cluster^{r-\phi}_{size}$ and $cluster^{z}_{size}$, are often used. These represent (in the specific case under study) the projections of the cluster size along the row and column directions, respectively.

7.3. Selection criteria

The methods and algorithms used to reconstruct telescope tracks and to derive observables to characterize the pixel sensors can be influenced by background effects, that are difficult to model or fully correct for. For instance, noisy pixels or fragmented clusters may mimic genuine particle hits in the beam telescope planes. In some cases, combinations of such spurious hits, whether entirely fake or partially real, may satisfy the track reconstruction criteria, leading to the formation of fake tracks.

To minimize the impact of such artifacts on the reconstructed observables, and improve the reliability of the measurements, a series of selection cuts are applied to the reconstructed data. A complete summary of these criteria is provided in the following Section, and the impact on the collected statistics is shown in Table 7.1 and Table 7.2 for a non-irradiated and an irradiated assembly, when the cuts are applied individually and one after the other.

7.3.1. Time-reference link and spatial cuts

The MIMOSA26 sensors used in the beam telescope operate with an integration time of 115.2 µs. In comparison, the signal shaping time of the RD53B_CMS readout chips is on the order of a few microseconds. At the TB21 beamline, the particle rate typically exceeds $(115.2\,\mu s)^{-1} = 8.7\,kHz$, meaning that multiple particles may pass through the setup's acceptance during a single readout cycle of the MIMOSA26 sensors.

In most cases, only one of these particles is responsible for generating the trigger signal and falls within the effective integration window of the RD53B_CMS. The remaining

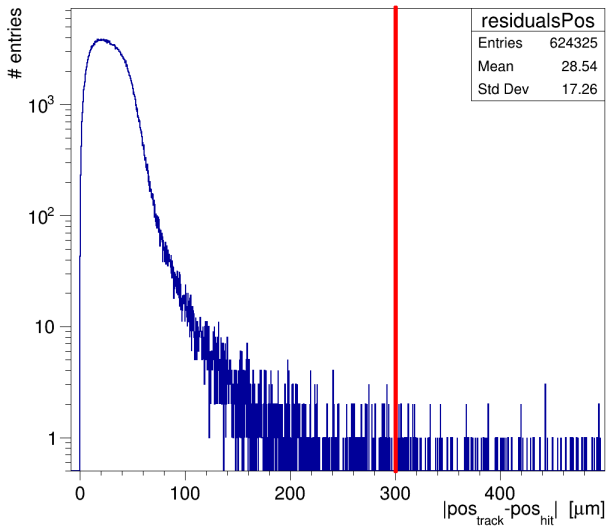

Figure 7.7.: Absolute distance between the clusters' centers and the reconstructed track positions on the DUT surface. In red, the spatial cut at 300 µm for the DUT.

tracks, caused by additional particles, are recorded by the beam telescope but cannot be associated with any meaningful measurement in the DUT. If not properly accounted for, these pileup tracks could introduce false zero-efficiency entries, among other inaccuracies.

To exclude them, all reconstructed telescope tracks are matched to hits in the time reference plane, and must fall within a well defined radius from the associated clusters recorded on its surface. Since the time reference plane and the assemblies under test share the same readout chip, this serves as a reliable means of verifying whether a track is time-correlated with the DUT.

The matching process involves calculating the intersection point between each telescope track and the time reference plane. The residuals between the projected track position and the cluster position in the time reference plane, denoted as $x_{\text{res}}^{\text{REF}}$ and $y_{\text{res}}^{\text{REF}}$, are then calculated. A telescope track must satisfy the following conditions:

$$|x_{\text{res}}^{\text{REF}}| \leq 250\,\mu\text{m}, \quad |y_{\text{res}}^{\text{REF}}| \leq 250\,\mu\text{m}.$$

A similar relation applies also when the tracks are then paired to the DUT:

$$|x_{\text{res}}^{\text{DUT}}| \leq 300\,\mu\text{m}, \quad |y_{\text{res}}^{\text{DUT}}| \leq 300\,\mu\text{m}.$$

This can be justified looking at the absolute distance between the track and hit in local coordinates. An example for the DUT is shown in Figure 7.7.

The impact of these cuts executed individually and one after the other on the distribution of the residuals in the y-direction for a run taken at vertical incidence with a non-irradiated module is shown in Figure 7.10 (a), Figure 7.10 (b) and Figure 7.11(b), respectively, and in Figure 7.12 (a), Figure 7.12 (b) and Figure 7.13(b), for the section irradiated to 8×10^{15} cm^{-2}.

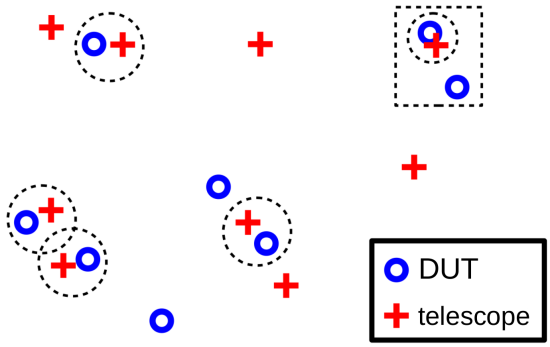

Figure 7.8.: Pairing of cluster centers (blue circles) and track positions reconstructed on the DUT's surface (red crosses), adapted from [45].

Among all cuts that will be discussed, the one on the time-reference link is found to have the second largest single cut impact on the retained event statistics, cutting circa 68% of the initial number of events for the non-irradiated module and 44% for the irradiated assembly. This is primarily due to the fact that the majority of recorded events are not in-time with the readout window of the DUT, and are therefore discarded. The spatial cut on the DUT has the largest impact when executed as a single cut on the initial statistics (69% and 44% of the events, respectively, for the non-irradiated and the irradiated assemblies), and the second largest effect for the non-irradiated assembly when executed in the cut-flow after the time-reference link (9% for the non-irradiated and 7% for the irradiated modules), as it efficiently rejects a significant fraction of noise-induced hits.

7.3.2. Residual pairing

To evaluate the spatial resolution of the detectors, residuals are computed between the position measurements obtained from two different devices. However, ambiguities can arise when more than one position measurement is recorded in at least one of the devices. This can happen, for instance, if multiple particles traverse the setup during the integration time of one or both sensors, or if noise fluctuations mimic particle hits. An example of such a situation is shown in Figure 7.8.

The core challenge lies in determining which of these measurement pairs are produced by the same particle. One approach to resolve ambiguities is to form pairs of measurements that satisfy the following criteria:

1. The measurement j on device 1 is the closest to measurement k on device 2.

2. The measurement k on device 2 is the closest to measurement j on device 1.

Only measurement pairs meeting both conditions simultaneously are accepted. These mutually closest pairs are indicated with dotted circles in Figure 7.8. The impact of this cut executed alone and after the two cuts presented in the previous Section is shown

for the non-irradiated assembly in Figure 7.10 (c) and Figure 7.11 (c), respectively, and in Figure 7.12 (c) and Figure 7.13 (c) for the irradiated one. The impact of this cut is relatively minor, reducing the overall statistics in the cut-flow of 2-3% for both the non-irradiated and the irradiated modules, as the majority of noise-induced hits are already removed by the spatial cut on the DUT. It nevertheless serves as a further refinement, acting within the 300 µm circular window associated to the previous cut.

7.3.3. Charge and χ^2 cuts

Particle hits with large energy depositions are typically associated with the production of δ-electrons, and can lead to significantly increased residual values. This occurs because the additional charge generated by δ-electrons may distort the charge distribution, shifting the reconstructed cluster position away from the true trajectory of the primary particle. These rare but substantial energy depositions have a pronounced impact on the RMS of the distributions of the residuals. In this analysis, a cut is applied to exclude events with large cluster charges (circa 5.4% of the total events) from the evaluation of the efficiency and the resolution. This threshold is chosen so that events associated to a charge greater than 1.5 times the mean value of the cluster charge distribution are excluded, as shown in 7.9 (left). The impact of this cut on the non-irradiated module can be seen in Figure 7.10 (d) and Figure 7.11 (d) when applied alone and after the other cuts, respectively. For the irradiated assembly, the impact is shown in Figure 7.12 (d) and Figure 7.13 (d). This cut brings the event sample size close to the final statistics employed for the evaluation of the observables, cutting circa 6% (9%, for the irradiated assembly) of the event statistics in the cut-flow.

Last, a cut is applied on the tracks that still have a relatively high χ^2 after applying all the other cuts, more specifically for tracks with $\chi^2/\text{ndof} \geq 5$, as shown in Figure 7.9 (right). This cut has minimal impact on the final statistics, as it can be seen from Figure 7.10 (e) and Figure 7.11 (e), for the non-irradiated module, and Figure 7.12 (e) and Figure 7.13 (e) for the irradiated one, reducing the final statistics of circa 1%. It is however crucial to remove the events poorly matched to the reconstructed tracks.

Single cuts	No cuts	Reference	DUT	Res. Pair.	Q	χ^2
Non-irradiated	2356k	760k	733k	2053k	2203k	2327k
(Reduction statistics)		(-67.7%)	(-68.9%)	(-12.9%)	(-6.5%)	(-1.2%)
8×10^{15} cm^{-2}	426k	238k	238k	384k	387k	419k
(Reduction statistics)		(-44.1%)	(-44.1%)	(-9.9%)	(-9.1%)	(-1.6%)

Table 7.1.: Impact on the total statistics of the spatial cuts for the reference module and DUT (Section 7.3.1), the residual pairing (Section 7.3.2), the cluster charge and the χ^2 (Section 7.3.3), applied individually, for the non-irradiated and irradiated assemblies.

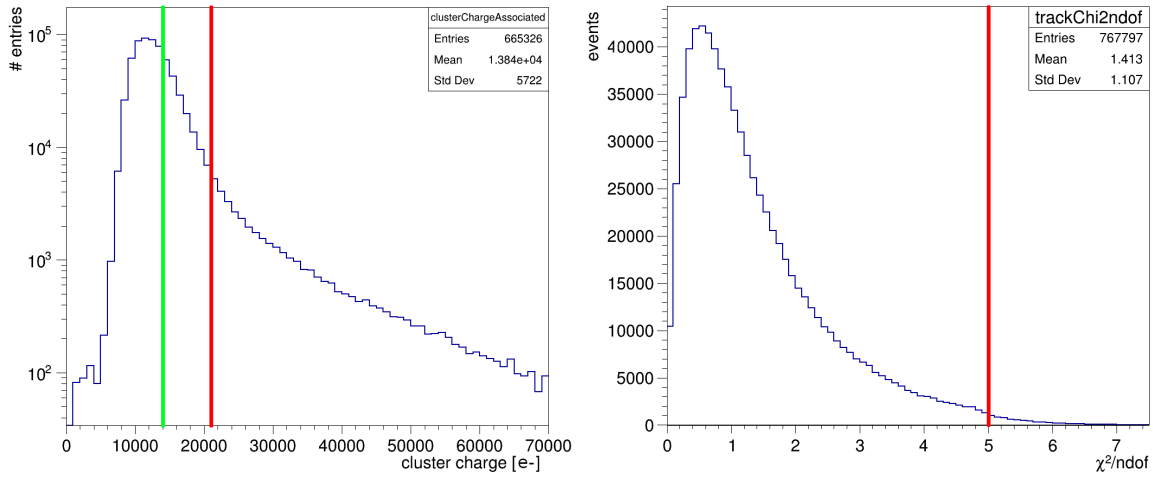

Figure 7.9.: Left: distribution of the clusters charges. The mean of the distribution is marked by the green line. The cut, applied at 1.5 times the mean of the histogram, is marked by the red line. Right: χ^2/ndof for the reconstructed tracks. The cut is represented by the solid red line.

Cut flow	No cuts	Reference	DUT	Res. Pair.	Q	χ^2
Non-irradiated	2356k	760k	691k	671k	629k	624k
(Reduction statistics)		(-67.7%)	(-9.1%)	(-2.9%)	(-6.3%)	(-0.8%)
8×10^{15} cm^{-2}	426k	238k	222k	217k	198k	196k
(Reduction statistics)		(-44.1%)	(-6.7%)	(-2.3%)	(-8.8%)	(-1.0%)

Table 7.2.: Impact on the total statistics of the spatial cuts for the reference module and DUT (Section 7.3.1), the residual pairing (Section 7.3.2), the cluster charge and the χ^2 (Section 7.3.3), applied one after the other, for the non-irradiated and irradiated assemblies.

7.4. Conclusions

This chapter has presented the reconstruction of tracks in the beam telescope and the alignment procedure for the detector planes, the definition of observables in the DUT, and the event selection criteria applied throughout the analysis.

Within the selection cuts, the time-reference link proved to be the most impactful, followed by the spatial cut on the DUT. The sequential application of all described cuts significantly reduced statistics on the tails of the distribution of the residuals, but minimally affected the central region, while improving the reliability of extracted observables.

In the next Chapter, these observables will be evaluated for non-irradiated and irradiated modules tuned to different angles, biased with different voltages and being traversed by the electrons of the beam at different incidence angles.

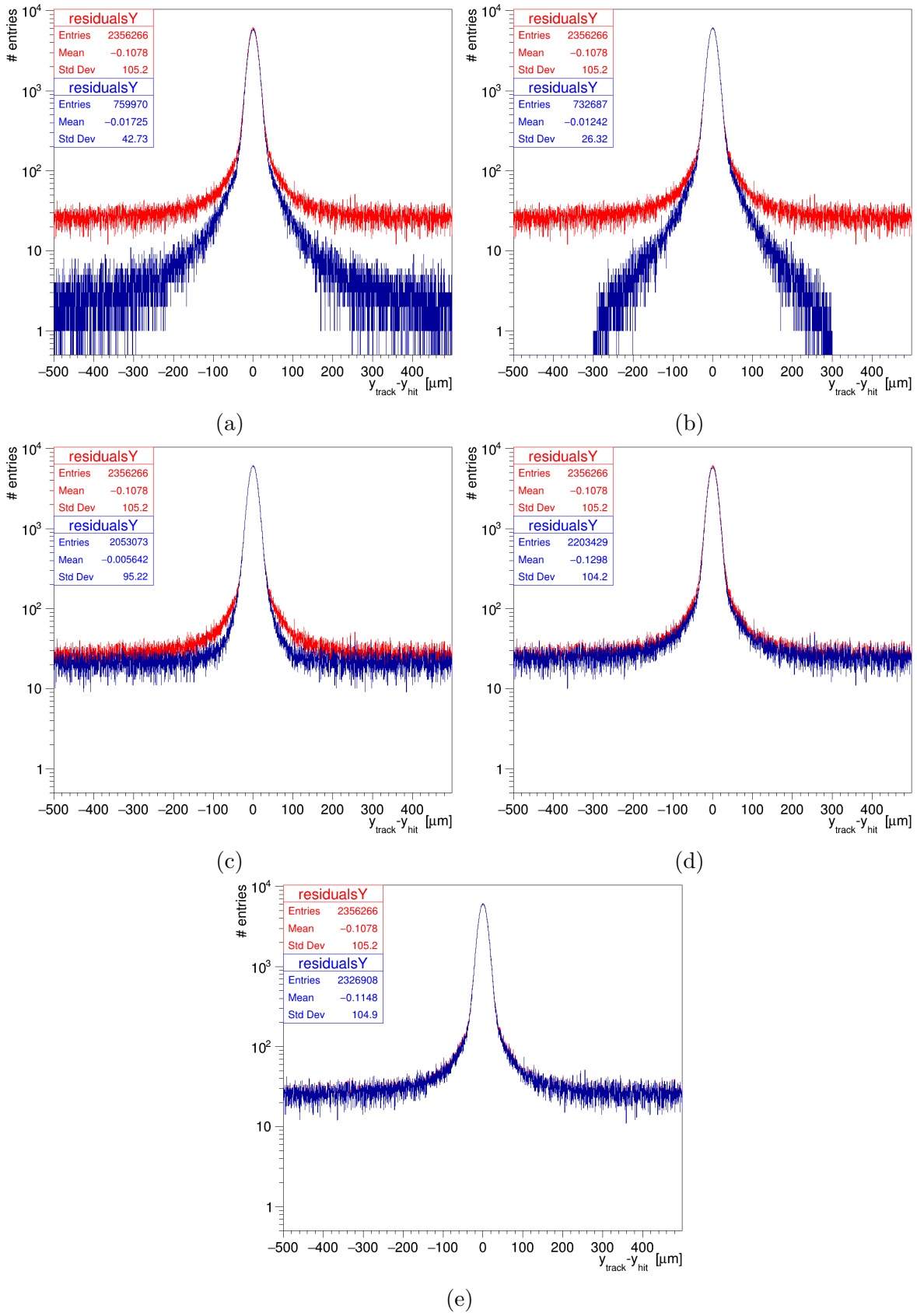

Figure 7.10.: The distribution of the residuals obtained without any cut is shown in red. In blue, the impact of the individual cuts for the time-link of the reference module (a), the spatial cut on the DUT (b), residual pairing (c), charge (d) and χ^2/ndof (e) on a non-irradiated module biased to 120 V at vertical incidence.

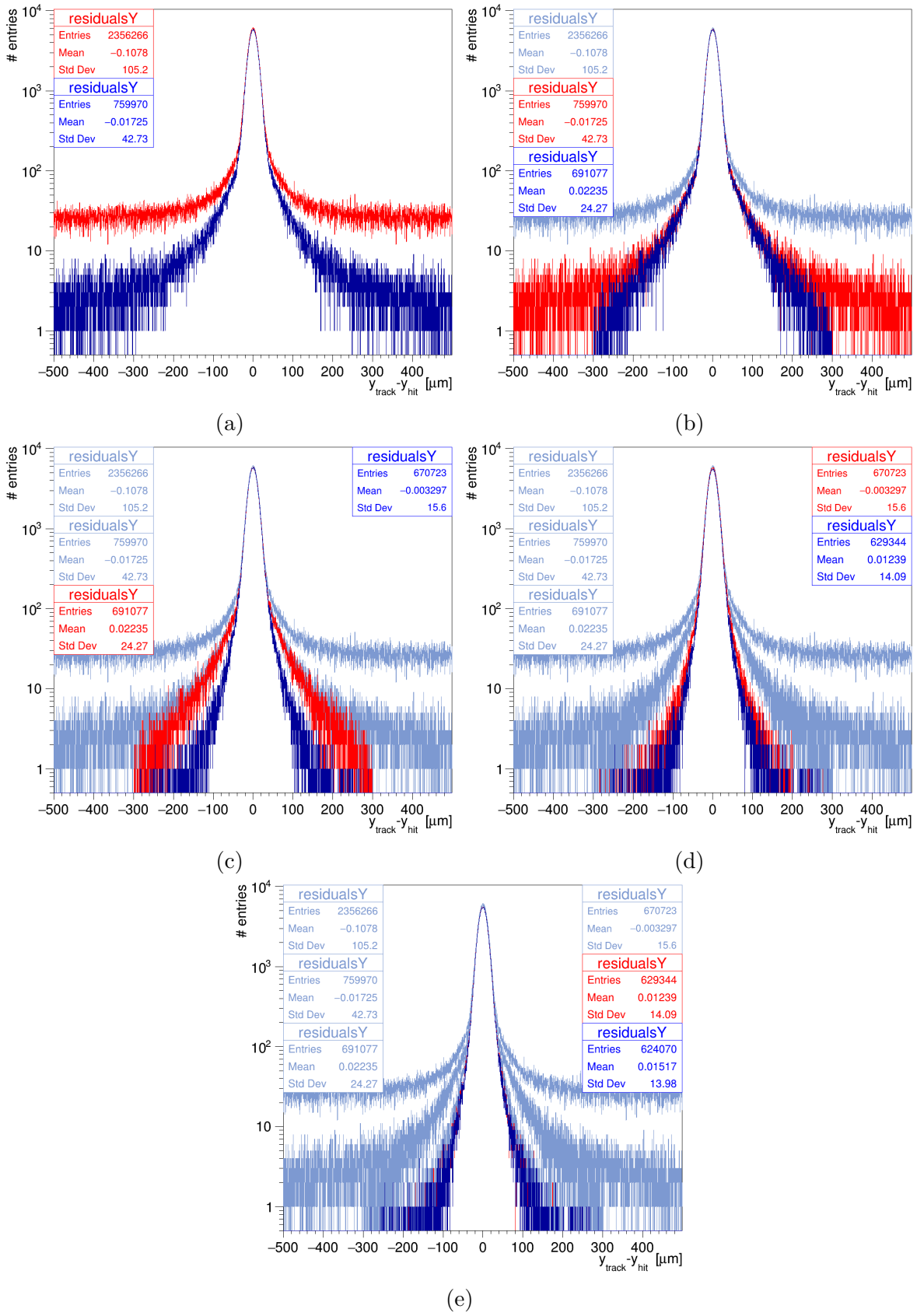

Figure 7.11.: Impact of the cumulative application of the cuts for the time-link of the reference module (a), the spatial cut on the DUT (b), residual pairing (c), charge (d) and χ^2/ndof (e) on a non-irradiated module biased to 120 V at vertical incidence. The $(n-1)^{th}$ cut is shown in red, and the n^{th} cut in blue. Previous cuts are represented in gray.

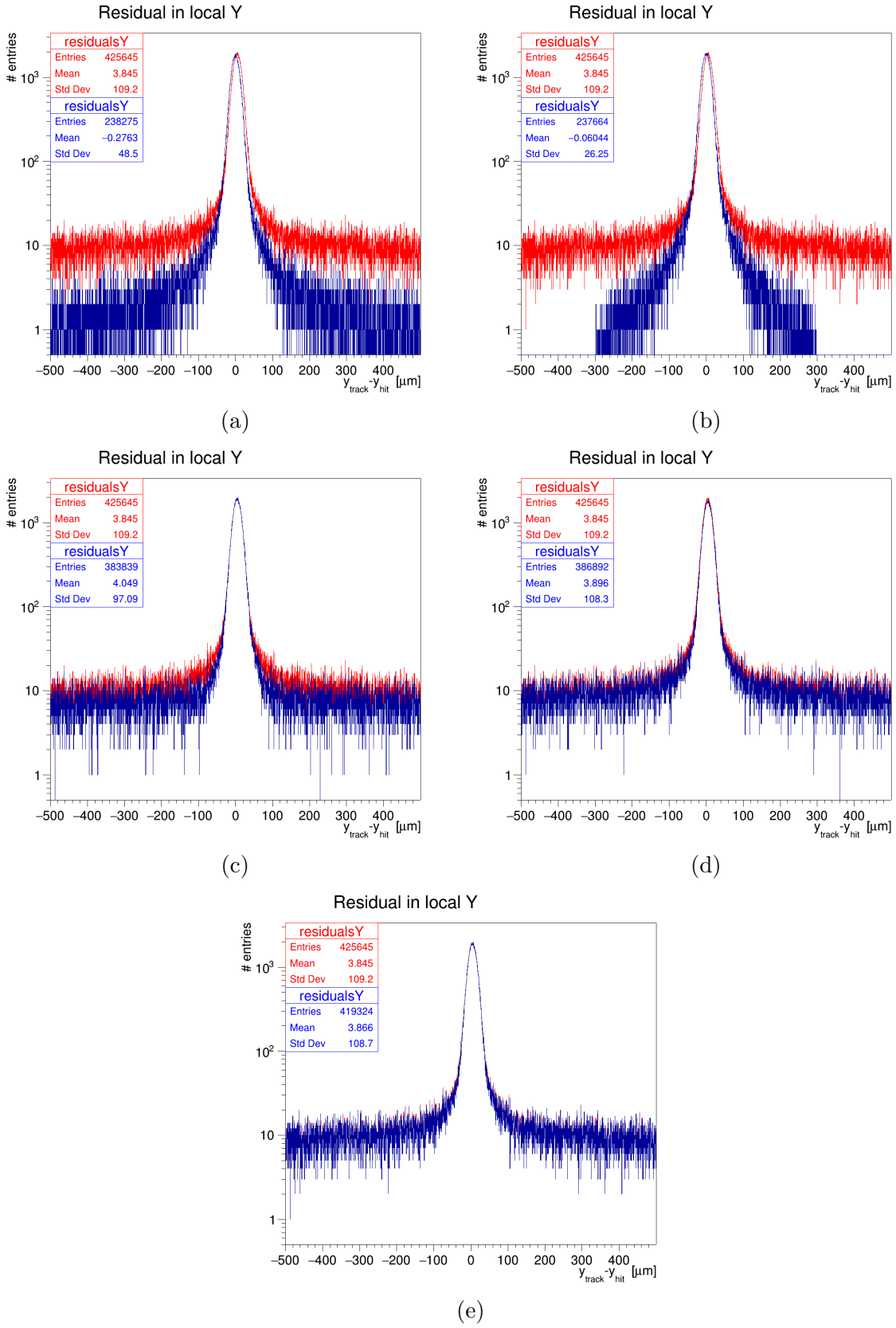

Figure 7.12.: The distribution of the residuals obtained without any cut is shown in red. In blue, the impact of the individual cuts on the section irradiated to 8×10^{15} cm^{-2} biased to 600 V at vertical incidence for the time-link of the reference module (a), the spatial cut on the DUT (b), residual pairing (c), charge (d) and χ^2/ndof (e).

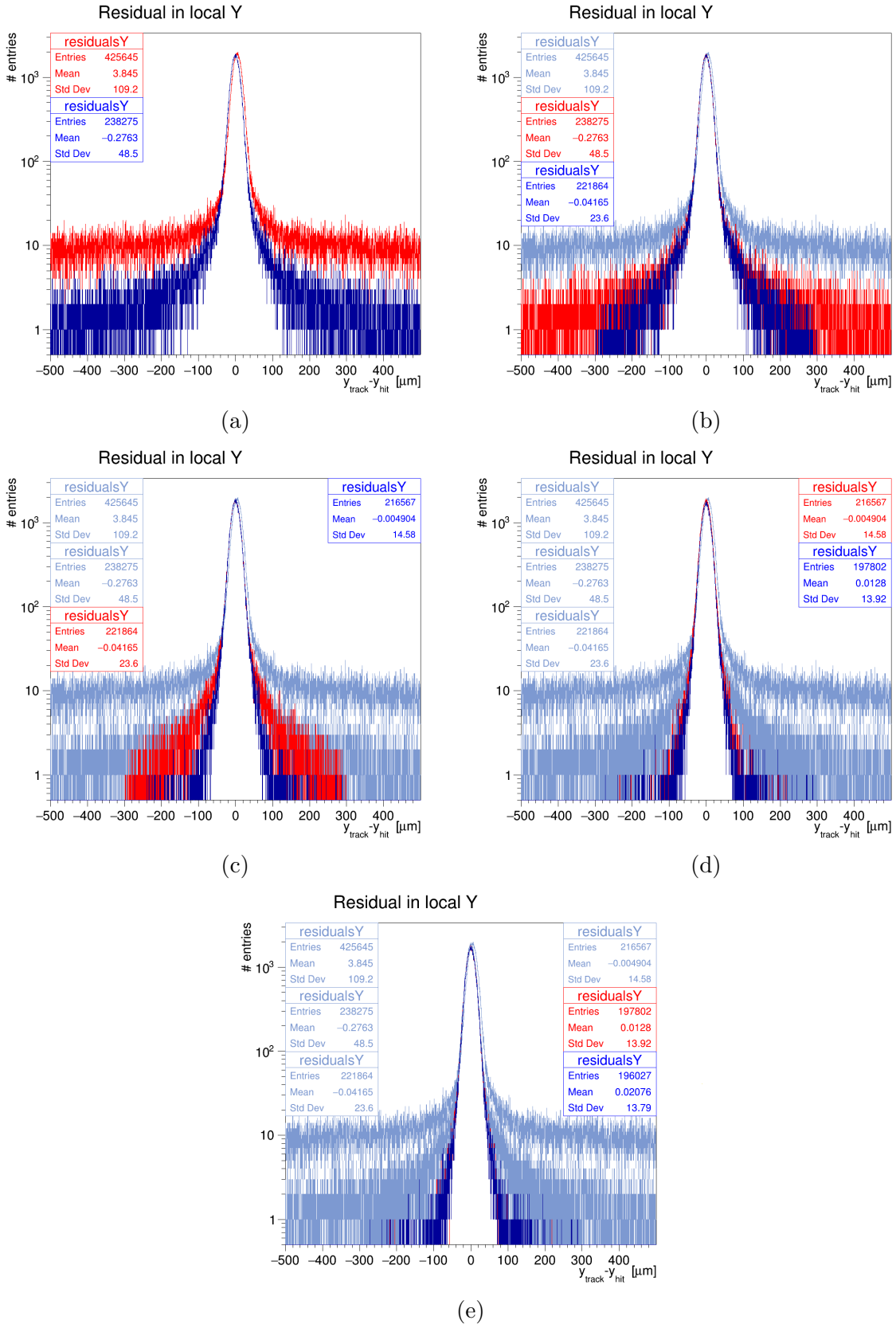

Figure 7.13.: Impact on the section irradiated to 8×10^{15} cm^{-2} biased to 600 V at vertical incidence of the cumulative application of the cuts for the time-link of the reference module (a), the spatial cut on the DUT (b), residual pairing (c), charge (d) and χ^2/ndof (e). The $(n-1)^{th}$ cut is shown in red, and the n^{th} cut in blue. Previous cuts are represented in gray.

8. Characterization of RD53B_CMS assemblies in test beams

This chapter presents the results of test beam measurements performed with planar HPK sensors featuring a bitten design, paired with RD53B_CMS readout chips, developed for the CMS Phase-2 Upgrade. First, the requirements that these assemblies must fulfill are outlined. Then the results obtained for both non-irradiated and proton-irradiated samples tuned to different thresholds are discussed, with particular focus on hit efficiency, spatial resolution and charge collection efficiency. These results demonstrate that pre-production assemblies already satisfy the CMS performance requirements.

List of Own Contributions The author's contributions to the results presented in this chapter include:

- Comprehensive analysis of the presented test beam measurements.
- Quality assessment of the analyzed data with respect to alignment and the corrections applied to reconstructed quantities.
- Investigation of the systematic effects.

This work was developed in collaboration with Dr. Massimiliano Antonello, Dr. Annika Vauth, and Chin-Chia Kuo.

8.1. Requirements

A comprehensive list of the requirements that must be fulfilled by the detectors under study can be found here [56, 113]. For this work, the focus lied on the parameters listed in Table 8.1.

Crosstalk and the associated requirement have been discussed Chapter 5. The requirement for the $\epsilon_{\text{hit}} \times \alpha$ stems from the need of keeping the detection efficiency above 99% when reconstructing particle hits with three out of four detector layers in the Inner Tracker. This requirement is twofold, depending on the irradiation level: for modules

irradiated up to $\phi_{eq} = 5 \times 10^{15}\,\mathrm{cm}^{-2}$, the efficiency times acceptance must be greater than 99%; for modules irradiated to higher fluences, it must be greater than 98%, in both cases keeping the bias voltage below 600 V, to avoid thermal runaway.

The spatial resolution must remain below the binary limit [50], which is given by the pitch/$\sqrt{12}$, corresponding to circa 7.2 µm and 28.9 µm in the short and long pitch directions, respectively. The amount of masked pixels must be less than 1% of the total amount of pixels in the module (see requirement for $\epsilon_{\mathrm{hit}} \times \alpha$), and the average noise occupancy of the remaining enabled pixels must remain below 10^{-6}. This limit represents 1% of the minimum simulated average occupancy expected in the IT for physics cases as, e. g. top quark pair production [56].

In the following Sections, these observables will be evaluated, demonstrating that the assemblies under study already fulfill the requirements needed to be employed in the Inner Tracker of the CMS detector during the HL-LHC.

Parameter	Requirement (planar sensors)
crosstalk	$< 10\%$
$\epsilon_{\mathrm{hit}} \times \alpha$ before irradiation	$> 99\%$
$\epsilon_{\mathrm{hit}} \times \alpha$ at $\phi_{eq} \leq 5 \times 10^{15}\,\mathrm{cm}^{-2}$	$> 99\%$ for V $\leq$ 600 V
$\epsilon_{\mathrm{hit}} \times \alpha$ at $\phi_{eq} > 5 \times 10^{15}\,\mathrm{cm}^{-2}$	$> 98\%$ for V $\leq$ 600 V
σ_{hit}	$<$ pitch $/\sqrt{12}$
masked pixels, avg. noise occupancy	$< 1\%$, $< 10^{-6}$

Table 8.1.: List of requirements under evaluation for this work. Adapted from [56, 113].

8.2. Non-irradiated assemblies

The characterization of non-irradiated pixel modules tuned to different thresholds provides an initial and valuable understanding of the properties of the investigated assemblies. This Section begins with measurements of the efficiency times acceptance and concludes with the evaluation of the spatial resolution, studied as a function of the bias voltage and of the particles' incidence angle, respectively.

8.2.1. Hit efficiency

Measurements of the efficiency times acceptance were taken for bias voltages ranging from 5 V to 350 V, keeping the module at $-20°$ C and perpendicular to the beam. The assembly was tuned to three different thresholds: 1000 e^-, 1200 e^- and 1500 e^-.

The dependence of the $\epsilon_{\mathrm{hit}} \times \alpha$ on V_{bias} as a function of the set threshold can be seen in Figure 8.1. The requirement of keeping the efficiency above 99% is reached with a

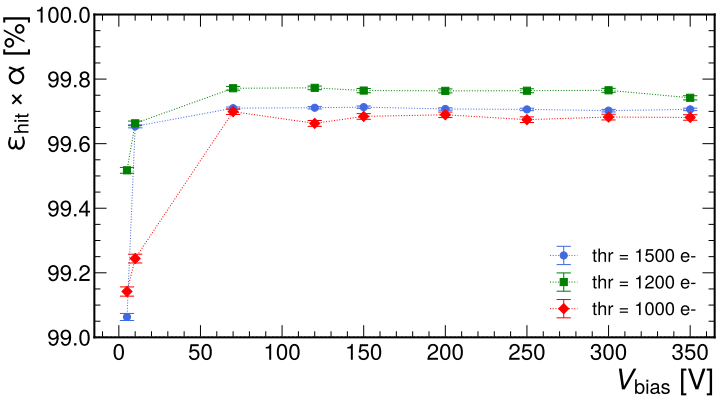

Figure 8.1.: $\epsilon_{\text{hit}} \times \alpha$ for a non-irradiated module tuned to three different thresholds as a function of the bias voltage. The three thresholds are represented in red (1000 e^-), green (1200 e^-) and blue (1500 e^-).

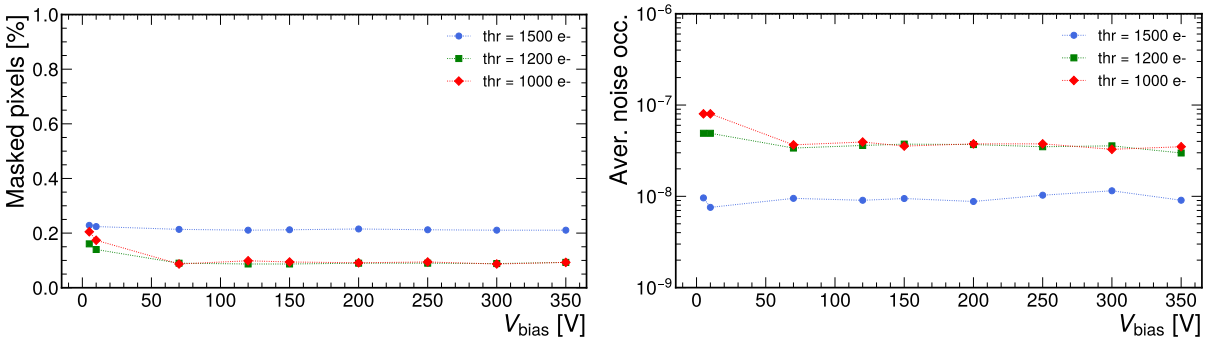

Figure 8.2.: Percentage of masked pixels (left) for the non-irradiated assembly and average noise occupancy after masking (right).

minimal bias voltage of 5 V, and all curves saturate for $V_{\text{bias}} \geq 70$ V, indicating complete sensor depletion. Although small bias voltages would be sufficient for all three thresholds to reach the efficiency benchmark, and would be preferable from the perspective of power consumption, in practice higher voltages are required to enter the regime of mobility saturation, thereby reducing the Lorentz angle in the magnetic field of CMS. This consideration is particularly relevant for sensors with a $25 \times 100\,\mu m^2$ pixel pitch, where limiting charge sharing along the 25 µm direction is crucial, as discussed in Section 2.4. The amount of masked pixels remained below the 1% threshold for all investigated bias voltages, while keeping the average noise occupancy of the remaining enabled pixels $< 10^{-6}$, as shown in Figure 8.2. A summary of all results can be found in Table 8.2.

These findings are consistent with results documented in the literature. Studies performed on 3D sensors reported a final hit efficiency of 98.5%, exceeding the requirement of 97%, for bias voltages above 5 V [114]. For the previous iteration of the readout chip (RD53A) coupled to the same sensor design, an efficiency of 99% was achieved at a bias voltage of 10 V [115]. For planar pixel sensors with pitches of 50×50 µm^2 coupled to the RD53B_ATLAS readout chip, an efficiency of 99.7% was obtained at a bias voltage of 20 V [116]. In all the cases discussed above, the efficiency attained the corresponding

benchmark values already at bias voltages below the depletion point, and subsequently saturated once the applied voltage exceeded the depletion voltage.

8.2.2. Spatial resolution

Beyond the hit efficiency, the spatial resolution is a central performance metric for the investigated pixel modules. It is defined as the single-plane resolution, and it is extrapolated following the procedure detailed in Section 7.2.4. It depends on both operational conditions and sensor properties, such as the track incidence angle, the applied bias voltage, the set threshold and the radiation damage. Measurements were taken for three different thresholds, investigating angles ranging from 0° to circa 15°, keeping a constant bias voltage of 120 V and a temperature of −20° C.

The evaluation of the spatial resolution proceeded in three main stages: first, the width of the distributions of the residuals was quantified, using the truncated RMS method; second, the contribution of the telescope to the measured residuals was evaluated, using the events outlined in Section 7.2.4; last, the two contributions were subtracted in quadrature, to obtain the DUT's spatial resolution. Figure 8.3 shows the distributions of the residuals for the three thresholds under exam, obtained for vertical incidence and at the optimal angle. The evolution of the truncated RMS values, derived from these distributions, across the complete angle scan is summarized in Figure 8.4 (a,b). Focusing on the y-direction (also referred to as r-ϕ, in the CMS coordinate system), the width of the residuals' distributions reaches a minimum around $\theta \approx 7.7°$. This angle is associated to a relevant percentage of two-pixels clusters, enabling charge-weighted interpolation between adjacent pixels, as it can be seen in Figure 8.4 (c) and Table 8.3. For larger angles, the charge starts spreading across multiple pixels, and the resolution degrades. In this regime, fluctuations in energy loss also become more pronounced [54]. At smaller angles, single-pixel clusters dominate, preventing interpolation and causing the resolution to approach the binary limit of $p/\sqrt{12} \approx 7.2\,\mu\text{m}$. In both limits, biases from the reconstruction algorithm (Equation 7.2) become more significant [117].

The contribution of the telescope $\sigma_{\text{tpr}}^{r-\phi}$, extrapolated from DUT data, is evaluated following the guidelines introduced in Section 7.2.4. The associated distributions of the residuals as a function of the set threshold can be seen in Figure 8.4 (e), and the values used to extrapolate the spatial resolution from the distributions of the residuals across the complete angle scan are reported in Figure 8.4 (f).

Once the contribution of the telescope for each incidence angle is evaluated, the spatial resolution $\sigma_{\text{hit}}^{r-\phi}$ can be calculated subtracting it in quadrature from the truncated RMS values of the corresponding residuals' distributions. The curves associated to the three threshold settings can be seen in Figure 8.4 (g,h). For the non-irradiated module under exam, the resolution depends on the chosen threshold only in the in the x-direction (also referred to as z, adopting the CMS coordinate system), with higher thresholds resulting in higher spatial resolutions. This is due to the fact that the average projected cluster size

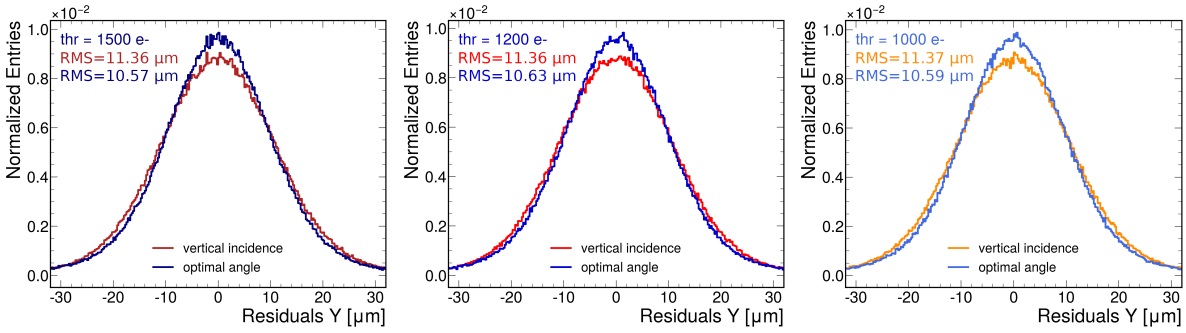

Figure 8.3.: Distribution of the residuals in the 25 µm direction at vertical incidence and at optimal angle for a non-irradiated assembly tuned to 1500 e^-, 1200 e^- and 1000 e^-.

in this direction is smaller, and hence more sensitive to the impact of higher thresholds, further reducing the number of cluster size two events for each data set, as discussed in Section 7.1. For the three investigated thresholds of 1000 e^-, 1200 e^-, and 1500 e^-, the best resolutions in the r-ϕ direction are observed between 7.7° and 9.6°, and read:

$$3.05\,\mu\text{m} \pm 0.18\,\mu\text{m}, \quad 3.35\,\mu\text{m} \pm 0.16\,\mu\text{m}, \quad 3.08\,\mu\text{m} \pm 0.18\,\mu\text{m}. \tag{8.1}$$

Consequently, the minimum is observed near the Lorentz angle expected in the barrel region of the CMS pixel detector, as discussed in Section 2.4. The quoted uncertainties are purely statistical, while systematic contributions are addressed in Section 8.5. A summary of all results can be found in Table 8.4.

In the literature, measurements on 3D pixel sensors reported a spatial resolution of 2.5 µm at an incidence angle of approximately 10° [114], measured at a temperature of −10° C. For the RD53A readout chip, coupled to planar sensors with a bitten design, a spatial resolution of 2.15 µm was measured at circa 9° [115, 118], at room temperature.

The observed discrepancy can be understood as a consequence of the sensor behavior at low temperatures. For temperatures approaching −20° C, a fraction of pixels exhibits thresholds that deviate significantly from the nominally tuned target value. To recover these pixels, the dynamic range of the TDAC circuit must be extended. Since the TDAC circuit has a fixed number of bits, this necessarily reduces the granularity with which individual pixel thresholds can be adjusted, as discussed in Section 4.2. The result is a broader threshold distribution across the pixel matrix.

A wider spread in threshold values directly impacts the dispersion of the ToT response for a given injected or collected charge, as the ToT depends on the effective threshold of each pixel. Given that the precision with which the cluster center can be reconstructed is determined by the relative ToT values of the pixels forming the cluster, a broader ToT distribution translates into a less precise position interpolation, and thus a degradation of the spatial resolution. It follows that, in this particular case, a dependence of the spatial resolution on the operating temperature is expected.

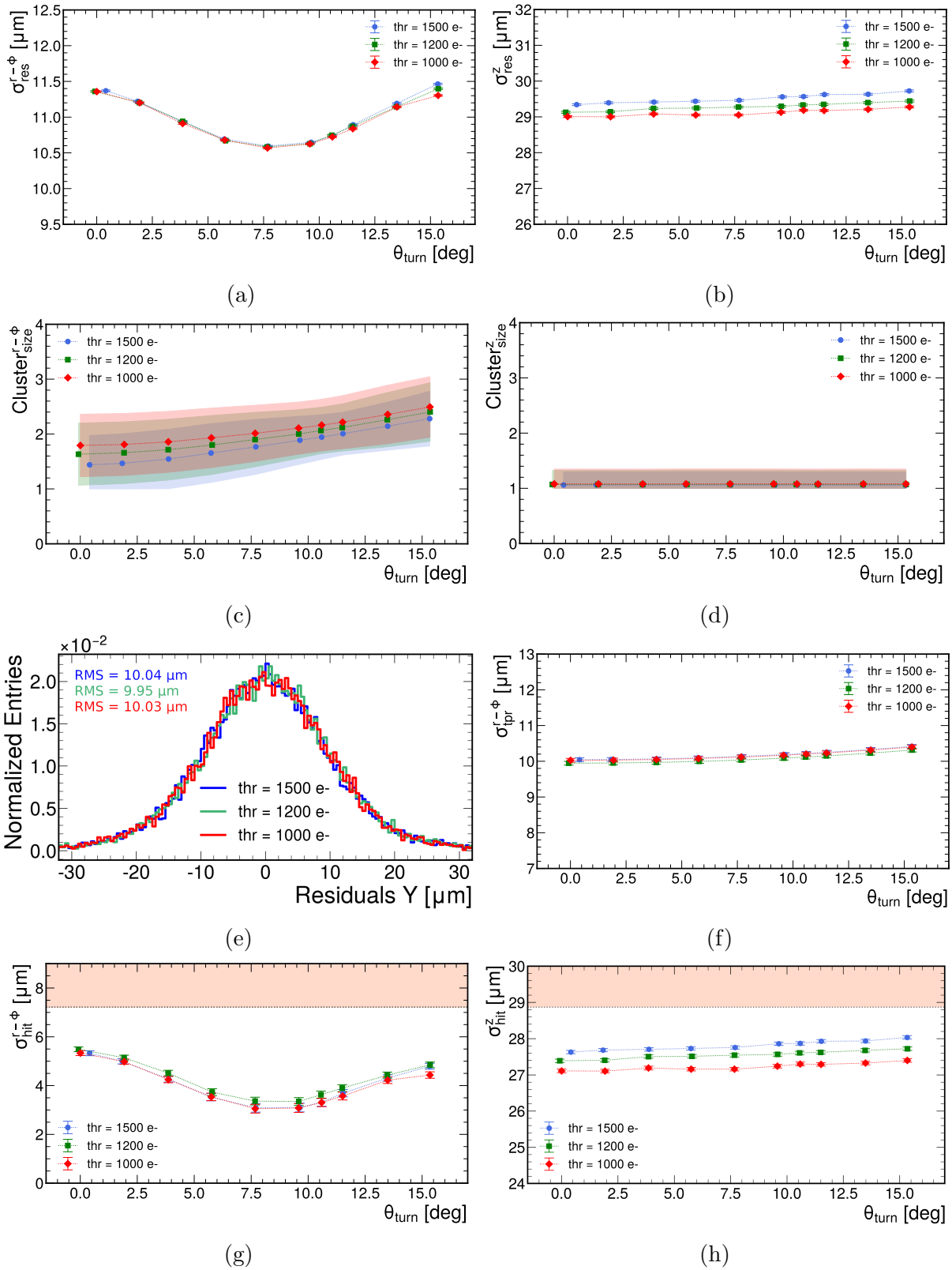

Figure 8.4.: Residuals in the 25 µm (a) and 100 µm (b) directions. Cluster sizes in the 25 µm (c) and 100 µm (d) directions. (e) Residuals' distributions of the events used for the extrapolation of the telescope's contribution to the DUT's spatial resolution. Extracted telescope resolutions as a function of the track incidence angle (f). Measured spatial resolution for the three thresholds under study (1000 e^-, 1200 e^-, and 1500 e^-) in the 25 µm (g) and 100 µm (h) directions, represented in red, green and blue, respectively.

8.3. Irradiated assemblies

A hybrid pixel assembly was irradiated with 24 GeV/c protons at PS-IRRAD. The profile of the accumulated equivalent fluence measured circa $4.8 \times 10^{15}\,\mathrm{cm}^{-2}$ at the bottom of the pixel matrix, $8 \times 10^{15}\,\mathrm{cm}^{-2}$ in the middle and $1 \times 10^{16}\,\mathrm{cm}^{-2}$ at the top. Further details are provided in Section 6.1.2. This Section begins with measurements of hit efficiency and spatial resolution studied as a function of the bias voltage and particle's incidence angle, respectively, for the above-mentioned different irradiation levels. It concludes with measurements of the charge collection efficiency and studies of the radiation-induced signal losses registered by the pixels of a cluster.

8.3.1. Hit efficiency

Measurements of the efficiency times acceptance were taken for bias voltages ranging from 200 V to 800 V, keeping the module at -20° C and perpendicular to the beam. Each section of the assembly was tuned to three different thresholds: 1000 e^-, 1200 e^-, and 1500 e^-. This Section focuses on the results obtained for a threshold of 1200 e^-. The main results for all thresholds are summarized in Table 8.2 and the associated plots can be found in Appendix A.

Figure 8.5 shows the $\epsilon_{\mathrm{hit}} \times \alpha$ as a function of the applied bias voltage V_{bias} for the three sections of the module associated to the above-mentioned equivalent fluences and for a non-irradiated assembly, all tuned to a threshold of 1200 e^-. The bias voltages required to reach $\epsilon_{\mathrm{hit}} \times \alpha > 99\%$ (for $\phi_{eq} \leq 5 \times 10^{15}\,\mathrm{cm}^{-2}$) and $\epsilon_{\mathrm{hit}} \times \alpha > 98\%$ (for $\phi_{eq} > 5 \times 10^{15}\,\mathrm{cm}^{-2}$) are approximately 350 V, 450 V and 500 V for the lowest to highest fluence, respectively, illustrating the degradation of the assembly's performance with increasing accumulated fluence. Both the total number of masked pixels and the average noise occupancy after masking remained below the respective limits of 1% and 10^{-6}, as shown in Figure 8.6.

Focusing on the highest fluence, the dependence of $\epsilon_{\mathrm{hit}} \times \alpha$ on the applied threshold and the corresponding fraction of masked pixels can be observed in Figure 8.7. At higher bias voltages, the increased number of masked pixels associated with a threshold of 1000 e^- leads to a reduction in $\epsilon_{\mathrm{hit}} \times \alpha$, resulting in values consistently below those obtained for the 1200 e^- threshold. This trend is observed across all investigated fluences, and the maximum $\epsilon_{\mathrm{hit}} \times \alpha$ fulfilling all CMS requirements is always achieved for a threshold of 1200 e^- at a bias voltage of 600 V. A summary of all results can be found in Table 8.2.

These findings are in agreement with the results reported in the literature. Studies performed on 3D sensors irradiated to an equivalent fluence of 1×10^{16} cm^{-2} reached the required hit efficiency of 97% at 100 V, and a maximum efficiency of 98% at 150 V [114], the highest bias voltage that could be applied on these assemblies at the LHC. For RD53A chips coupled to planar sensors with a bitten design, the benchmark efficiency of 98% was achieved at a bias voltage of 450 V [115], for an assembly irradiated to 1.2×10^{16} cm^{-2}.

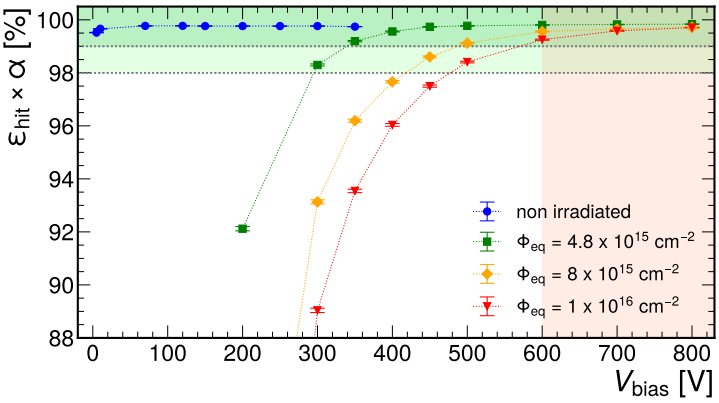

Figure 8.5.: $\epsilon_{\text{hit}} \times \alpha$ as a function of the bias voltage for the non-irradiated assembly and three sections of the irradiated module with corresponding average equivalent fluences of 4.8, 8 and $10 \times 10^{15}\,\text{cm}^{-2}$ tuned to a threshold of 1200 e^-.

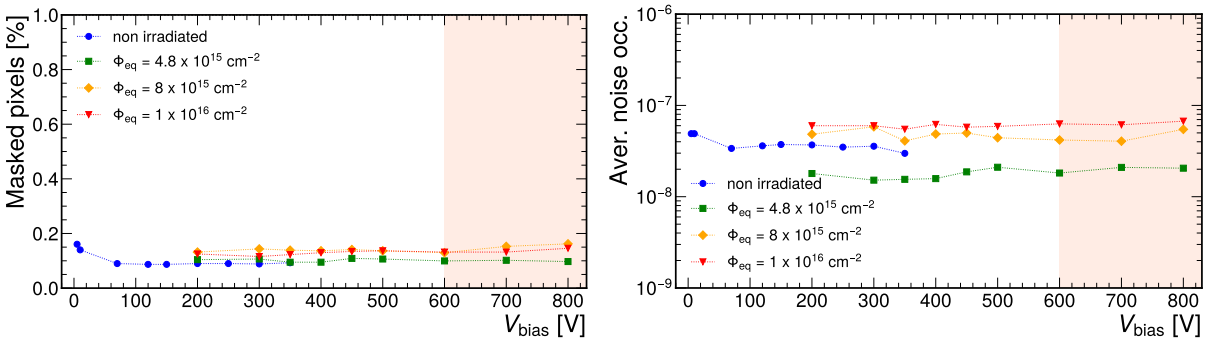

Figure 8.6.: Percentage of masked pixels (left) and average noise occupancy after masking (right) for the non-irradiated and irradiated assemblies under study, tuned to a threshold of 1200 e^-, as a function of the bias voltage.

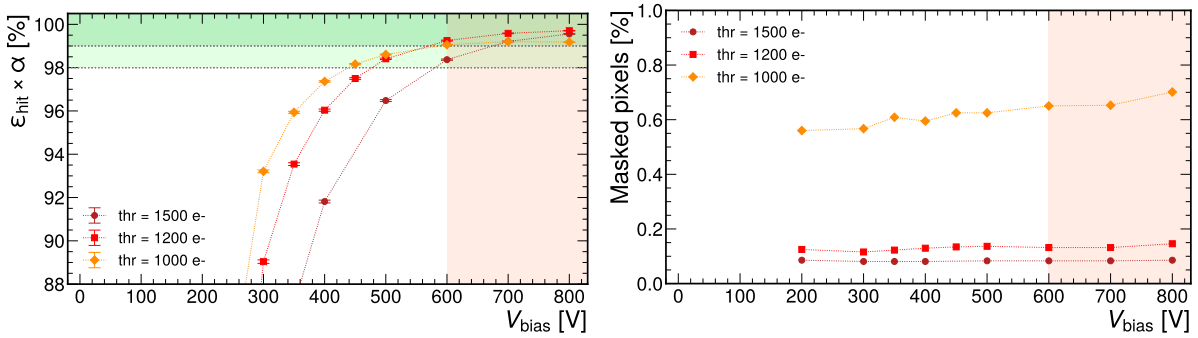

Figure 8.7.: Left: $\epsilon_{\text{hit}} \times \alpha$ as a function of the bias voltage for the section with an average equivalent fluence of $1 \times 10^{16}\,\text{cm}^{-2}$ tuned to three different thresholds. Right: Corresponding percentages of masked pixels.

ϕ_{eq} [cm^{-2}]	Maximum $\epsilon_{hit} \times \alpha$ [%]	V_{bias} [V]	Threshold [e$^-$]
non-irradiated	99.70	70	1000
	99.77		1200
	99.71		1500
4.8×10^{15}	99.60	600	1000
	99.81		1200
	99.81		1500
8×10^{15}	99.32	600	1000
	99.56		1200
	99.22		1500
1×10^{16}	99.06	600	1000
	99.25		1200
	98.37		1500

Table 8.2.: Maximum efficiency times acceptance as a function of threshold and accumulated equivalent fluence. For all cases under exam, the maximum $\epsilon_{hit} \times \alpha$ is found for a threshold of 1200 e$^-$ and a bias voltage of 600 V.

It should be noticed, however, that this value was not scaled for the acceptance. For the ATLAS planar pixel sensors with pitches of 50×50 µm^2 coupled to RD53B_ATLAS, an efficiency of 98.1% was obtained at 400 V, for a module irradiated to 4.3×10^{15} cm^{-2} [116].

8.3.2. Spatial resolution

The reconstruction of the spatial resolution follows the procedure described in Section 7.2.4 and is consistent with the approach used for the non-irradiated samples. All measurements were performed at $V_{bias} = 600$ V, and at a temperature of $-20°$ C.

The dependence of the truncated RMS of the distributions of the residuals on the track incidence angle, as a function of the accumulated fluence, is shown in Figure 8.8 and Figure 8.9 (a,b). Focusing on the r-ϕ direction, the width of the residual distributions $\sigma_{res}^{r-\phi}$ reaches its minimum at angles larger than the one measured for the non-irradiated module. This shift toward higher optimal angles is a consequence of radiation-induced damage, which reduces the effective active depth of the sensor by creating regions in the sensor's bulk with a near-zero electric field [119, 120, 39]. As a result, the projected cluster size decreases with increasing fluence, and a significant fraction of two-pixel clusters is only achieved at larger incidence angles, as illustrated in Figure 8.9 (c).

The contribution of the telescope is evaluated as for the non-irradiated module. The corresponding residual distributions are shown in Figure 8.9 (e), and the values used to extrapolate the spatial resolution from the distributions of the residuals across the complete angle scan are reported in Figure 8.9 (f). Due to limited statistics, the extrapolated contribution for the highest fluence appears slightly larger than for the other cases. This has only a minor impact on the final spatial resolution and represents an unavoidable

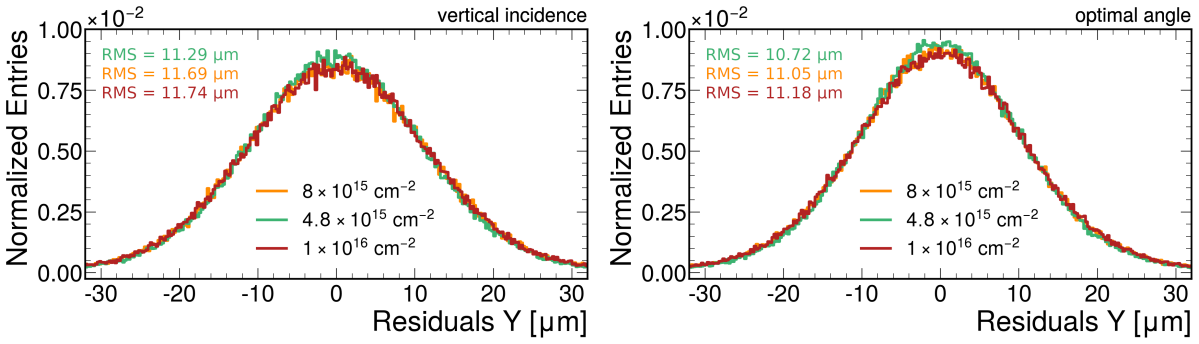

Figure 8.8.: Distribution of the residuals in the 25 µm direction at vertical incidence (left) and at optimal angle (right) as a function of fluence.

trade-off when estimating the telescope contribution using DUT data alone.

Once the contribution of the telescope for each incidence angle is evaluated, the spatial resolution can be calculated. Figure 8.9 (g,h) presents the spatial resolution as a function of the track incidence angle for both non-irradiated and irradiated assemblies. As for the residuals, the overall shape of the resolution curve changes, with the minimum shifting towards larger angles. The best resolution $\sigma_{\text{hit}}^{r-\phi}$ degrades from 3.35 µm for the non-irradiated sample to:

$$4.09\,\mu\text{m} \pm 0.26\,\mu\text{m}, \quad 4.55\,\mu\text{m} \pm 0.28\,\mu\text{m}, \quad 3.46\,\mu\text{m} \pm 0.42\,\mu\text{m}, \tag{8.2}$$

for $4.8 \times 10^{15}\,\text{cm}^{-2}$, $8 \times 10^{15}\,\text{cm}^{-2}$, and $1 \times 10^{16}\,\text{cm}^{-2}$, respectively. These minima are observed at incidence angles of 9.8°, 12.6°, and 14.5°. The quoted uncertainties are purely statistical, while systematic effects are discussed in Section 8.5. As noted earlier, the decrease of the resolution values at the highest fluence is to be attributed to the estimation of the telescope's resolution, which is sensitive to the limited event statistics.

For the lowest fluence, a similar trend is observed, as shown in Figure 8.10. Here, the position of the minimum resolution is influenced by threshold effects, which impact the fraction of two-pixel clusters, shifting the optimal incidence angle towards larger values. The respective minima for thresholds of $1000\,\text{e}^-$, $1200\,\text{e}^-$, and $1500\,\text{e}^-$ are observed at 8.7°, 9.8°, and 10.7°, respectively. A summary of all results can be found in Table 8.4.

These results are consistent with the literature. Measurements on 3D pixel sensors irradiated to an equivalent fluence of 1×10^{16} cm^{-2} have reported a spatial resolution of 3.5 µm at an incidence angle of approximately 11° [114], measured at a temperature of −30° C. For RD53A paired with a sensor featuring a bitten design, a spatial resolution of 4.2 µm was measured at an angle of circa 6.5° [115, 118], for an assembly irradiated to a fluence of 1.2×10^{16} cm^{-2} and kept at a temperature of circa −20° C. The reason for the observed shift of the angle corresponding to the minimum towards smaller angles in this case is not yet fully understood. This behaviour may indicate limitations of the used reconstruction algorithm, potentially influenced by backscattering effects in the experimental setup.

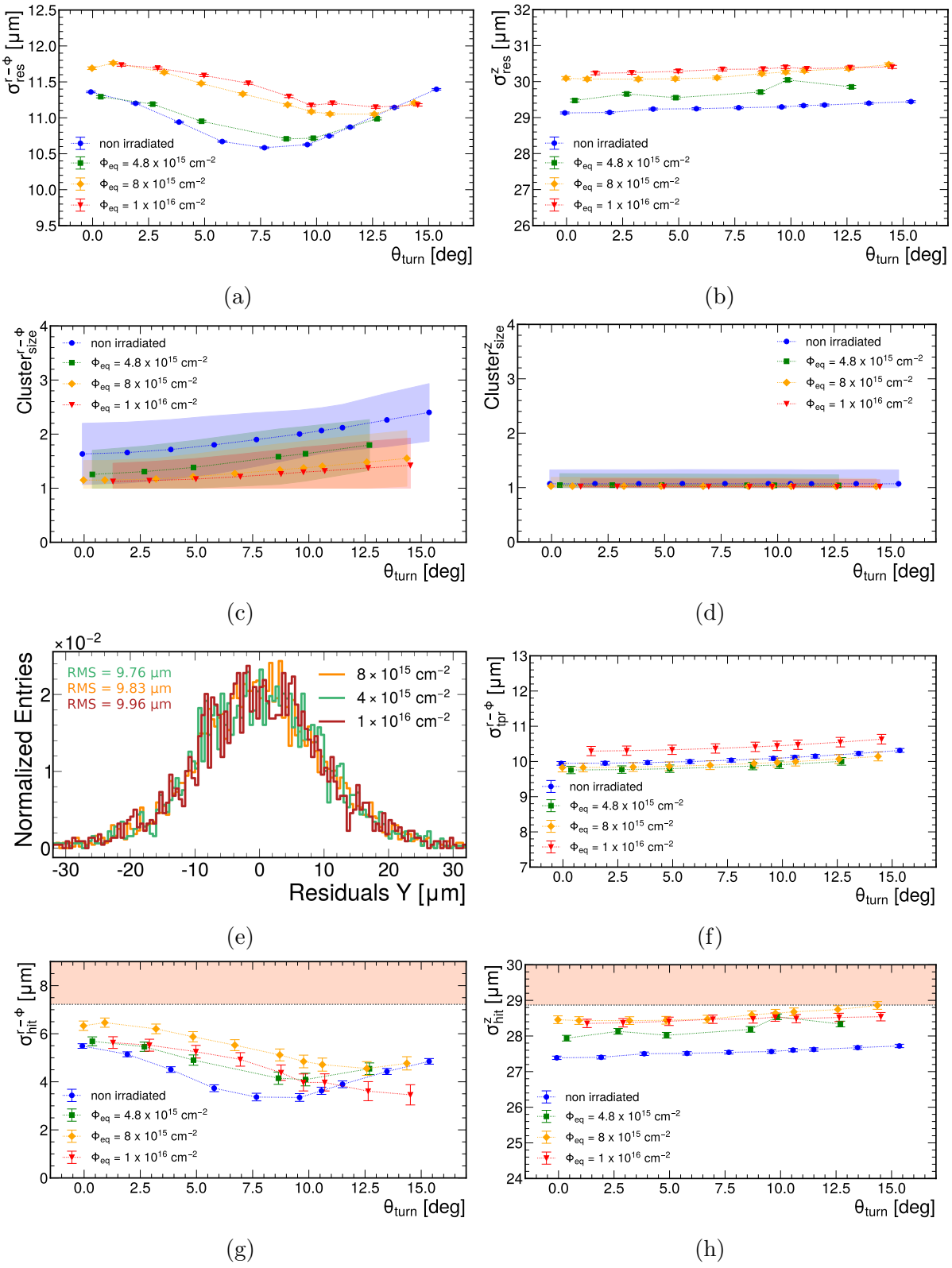

Figure 8.9.: Residuals in the 25 µm (a) and 100 µm (b) directions. Cluster sizes in the 25 µm (c) and 100 µm (d) directions. (e) Residuals' distributions of the events used for the extrapolation of the telescope's contribution to the DUT's spatial resolution. (f) Extracted telescope resolutions as a function of the track incidence angle. Measured spatial resolution in the 25 µm (g) and 100 µm (h) directions for the three fluences under study and a non-irradiated assembly.

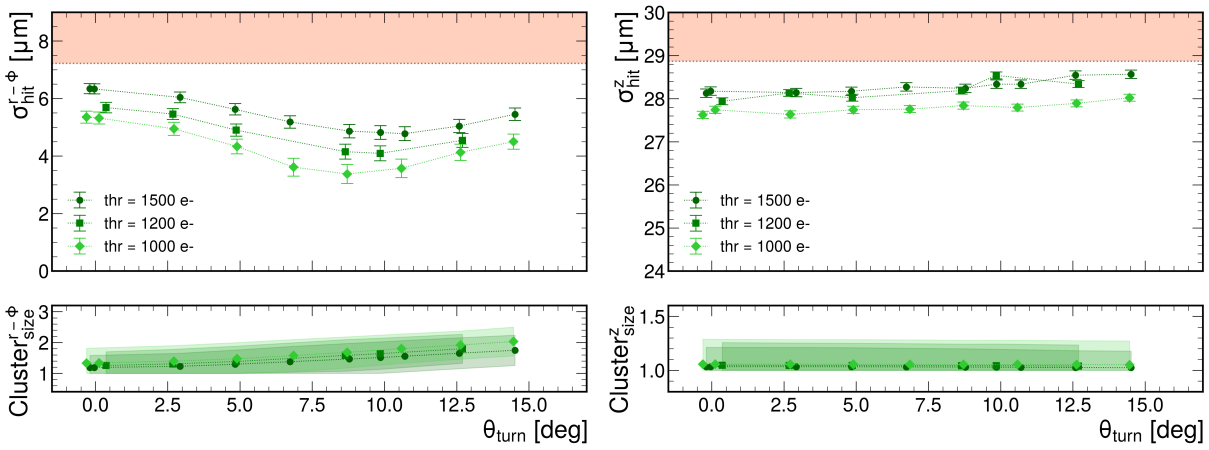

Figure 8.10.: Spatial resolution and corresponding projected cluster size in the 25 µm (left) and 100 µm (right) directions as a function of the track incidence angle, measured for different thresholds for a section with an equivalent fluence of $4.8 \times 10^{15}\,\mathrm{cm}^{-2}$.

ϕ_{eq} [cm^{-2}]	Minimum $\sigma^{r-\phi}_{hit}$ [µm]	Angle [°]	Threshold [e^{-}]
non-irradiated	3.05 ± 0.18	7.67	1000
non-irradiated	3.35 ± 0.16	9.59	1200
non-irradiated	3.09 ± 0.18	7.70	1500
4.8×10^{15}	3.38 ± 0.34	8.72	1000
4.8×10^{15}	4.09 ± 0.26	9.85	1200
4.8×10^{15}	4.78 ± 0.24	10.7	1500
8×10^{15}	4.11 ± 0.30	12.58	1000
8×10^{15}	4.55 ± 0.28	12.58	1200
8×10^{15}	4.86 ± 0.24	14.39	1500
1×10^{16}	3.68 ± 0.34	14.50	1000
1×10^{16}	3.46 ± 0.42	14.52	1200
1×10^{16}	5.67 ± 0.29	14.46	1500

Table 8.4.: Best spatial resolution $\sigma^{r-\phi}_{hit}$ as a function of threshold and accumulated equivalent fluence.

8.4. Charge collection efficiency

The previous Sections have shown that both the hit efficiency and the spatial resolution of the investigated pixel modules degrade progressively with increasing fluence. These macroscopic performance metrics provide valuable information on the detector's operational limits; however, they do not directly address the microscopic mechanism responsible for such degradation. In silicon sensors, radiation damage manifests primarily through

ϕ_{eq} [cm^{-2}]	1-pixel cls.	2-pixels cls.	Mean cls.	Thr. [e$^-$]	Angle [°]
non-irradiated	57.9%	40.3%	1.44	1500	0
	26.8%	69.8%	1.77		7.7 (σ_{hit}^{min})
	41.0%	54.9%	1.63	1200	0
	9.3%	81.4%	2.00		9.6 (σ_{hit}^{min}, ref.)
	28.5%	64.1%	1.79	1000	0
	11.9%	75.4%	2.01		7.7 (σ_{hit}^{min})
4.8×10^{15}	74.9%	24.7%	1.26	1200	0
	42.7%	56.4%	1.58		9.6 (σ_{hit}^{min} non-irr.)
	37.4%	61.5%	1.64		9.9 (σ_{hit}^{min})
8×10^{15}	85.2%	14.7%	1.15	1200	0
	66.4%	33.3%	1.34		9.6 (σ_{hit}^{min} non-irr.)
	52.4%	47.0%	1.48		12.6 (σ_{hit}^{min})
1×10^{16}	87.5%	12.4%	1.13	1200	0
	73.7%	26.1%	1.27		9.6 (σ_{hit}^{min} non-irr.)
	58.2%	41.4%	1.42		14.5 (σ_{hit}^{min})

Table 8.3.: Occurrence of single- and two-pixel clusters for the three investigated thresholds. For the non-irradiated module, results are shown at vertical incidence and at the angle of minimum resolution. For the irradiated sections, results are given at vertical incidence, at the angle corresponding to the minimum of the resolution of the non-irradiated module, and at the angles of the respective resolution minima.

the creation of defect states in the crystal lattice, which act as trapping centers for charge carriers. This process reduces the amount of charge that is ultimately induced on the electrodes, thereby lowering the signal-to-noise ratio and increasing the likelihood that the signal will fall below the discriminator threshold. As a result, both efficiency and resolution are adversely affected.

In order to gain a deeper understanding of this degradation and to establish a direct link between microscopic radiation damage and macroscopic detector performance, the charge collection efficiency (CCE) is measured, which quantifies the fraction of the charge generated by a traversing particle that is successfully collected by the readout electrodes.

In this work, the CCE was evaluated by measuring the MPV of the charge distributions as a function of bias voltage for both the non-irradiated and the irradiated modules, each tuned to three different thresholds (1000 e$^-$, 1200 e$^-$ and 1500 e$^-$). An example of cluster charge distributions for the non-irradiated module and the three fluences under exam is shown in Figure 8.11 (left). The discussion presented here focuses on a threshold of 1200 e$^-$, while results for thresholds of 1000 e$^-$ and 1500 e$^-$ are summarised in Table 8.5.

For the non-irradiated module, the measured collected charge saturates at the depletion voltage of 70 V, reaching a value of 10500 e$^-$, as it can be seen from the blue curve in Figure 8.12 (left). This value is used as a reference for the evaluation of the CCE.

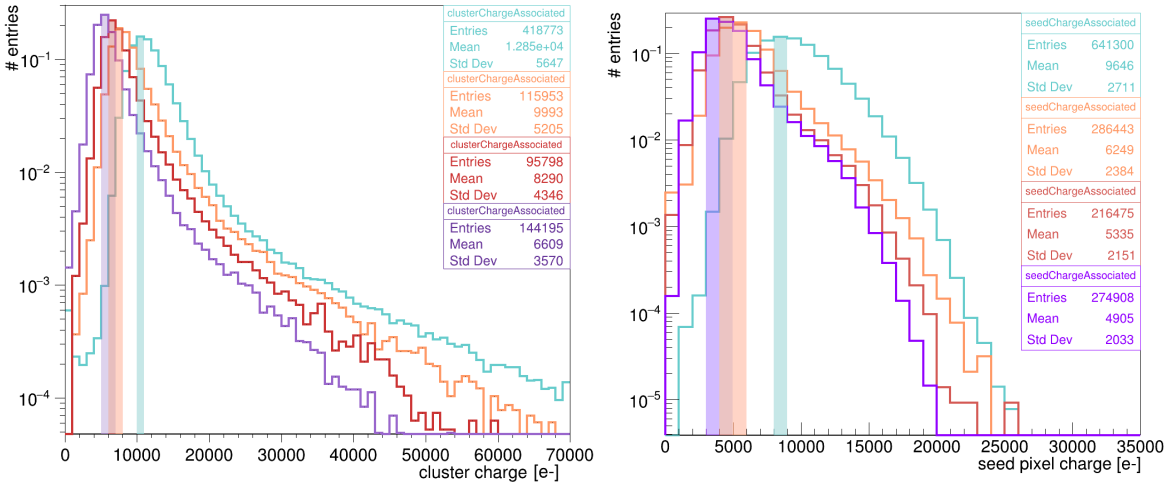

Figure 8.11.: Cluster (left) and seed (right) charge distributions for the non-irradiated assembly (blue) and the fluences under exam: $4.8 \times 10^{15}\,\mathrm{cm}^{-2}$ (orange), $8 \times 10^{15}\,\mathrm{cm}^{-2}$ (red) and $1 \times 10^{16}\,\mathrm{cm}^{-2}$ (purple). The MPVs have been highlighted. Modules were tuned to 1200 e^{-} at the 600 V.

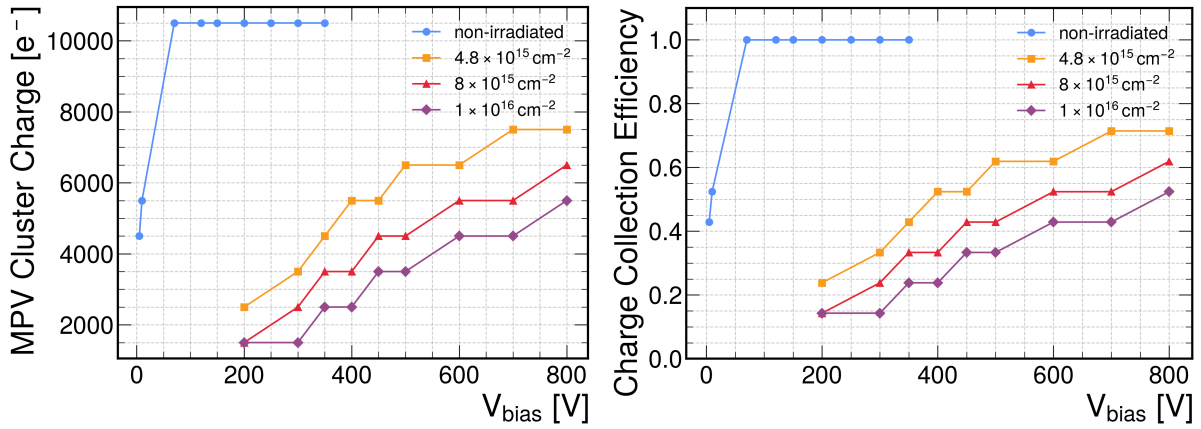

Figure 8.12.: Left: MPV of the cluster charge distribution versus bias voltage for the non-irradiated module (blue curve) and the three sections of the irradiated module (yellow, red and purple curves for increasing fluences). Right: the MPV is normalized, obtaining the charge collection efficiency (CCE).

Applying the same procedure to the three sections of the irradiated module reveals a clear reduction of the collected charge with increasing average equivalent fluence. Normalising these MPVs to the reference obtained for the non-irradiated module yields the CCE curves presented in Figure 8.12 (right). For the investigated fluences, the CCE increases approximately linearly with bias voltage and shows no sign of saturation within the voltage range under study. This behaviour stands in marked contrast to the non-irradiated module, where the CCE rapidly saturates after depletion.

The absence of saturation in irradiated modules reflects the fact that even at the highest applied bias voltages, trapping continues to limit the collected charge. The observed linear trend suggests that increasing the electric field through higher bias voltages partially

ϕ_{eq} [cm^{-2}]	$Q_{\text{MPV}}^{\text{non-irrad.}}$ [e$^-$]	Threshold [e$^-$]	Q_{MPV} [e$^-$]	CCE
4.8×10^{15}	10500	1000	6500	0.62
	10500	1200	6500	0.62
	9500	1500	6500	0.68
8×10^{15}	10500	1000	5500	0.52
	10500	1200	5500	0.52
	9500	1500	5500	0.58
1×10^{16}	10500	1000	4500	0.43
	10500	1200	4500	0.43
	9500	1500	4500	0.47

Table 8.5.: MPV of the charge distributions and CCE for different fluences and thresholds. The MPV of the charge distribution for the irradiated sections is taken at 600 V. The normalization for the CCE is performed with respect to the MPV of the non-irradiated assembly at 70 V for the corresponding threshold. The coarse binning (1000 e$^-$) of the charge distributions prevents a more granular definition of the MPVs.

mitigates the effects of trapping, but cannot fully restore the efficiency to pre-irradiation levels.

8.4.1. Radiation damage and threshold effects

The histograms in Figure 8.11 show a reduction of the MPVs of the cluster and seed charge distributions, induced by the accumulated radiation damage. This shift is caused by the radiation-induced defects, trapping part of the moving carriers, and reducing the overall induced signal. The impact is twofold: while seed pixels still register signals above threshold, albeit smaller, the signals of edge pixels may drop below the threshold, preventing hit detection. Consequently, the reduction in the MPV observed for the seed pixel is inherently limited to, and cannot exceed, the reduction seen in the MPVs of the full cluster charge distributions.

To quantify the signal loss caused exclusively by the radiation damage, the MPVs of the seed charge distributions obtained for different fluences can be compared. The signal loss relative to the one registered for the non-irradiated module can be quantified as follows:

$$\text{reduction}_{\text{seed}} = \frac{Q_{\text{seed}}^{\text{non-irr.}} - Q_{\text{seed}}^{\text{irr.}}}{Q_{\text{seed}}^{\text{non-irr.}}}, \quad \text{reduction}_{\text{cluster}} = \frac{Q_{\text{cluster}}^{\text{non-irr.}} - Q_{\text{cluster}}^{\text{irr.}}}{Q_{\text{cluster}}^{\text{non-irr.}}}. \tag{8.3}$$

The result obtained for the different fluences under study can be seen in Figure 8.13. The signal loss registered for the cluster charge increases from 43.5% to 60.9% for the two limit fluences under study. The signal loss measured exclusively on the seed pixel is smaller than the one measured for the cluster, as expected, increasing from 35.3% to 58.8% for the investigated fluence range. The difference between the relative signal loss measured

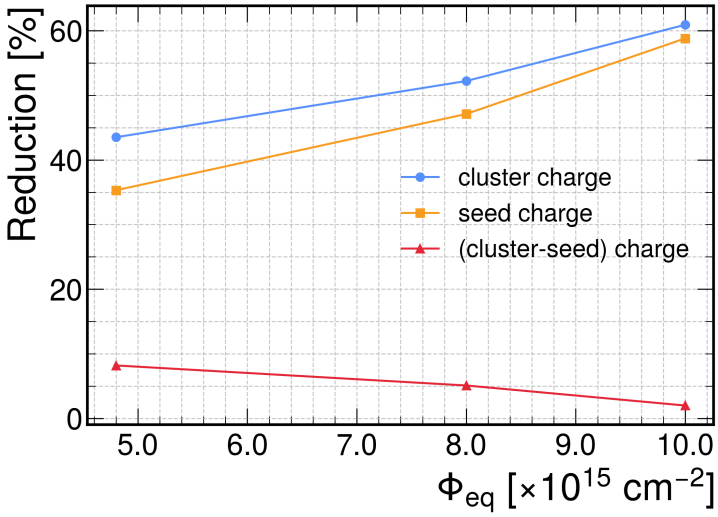

ϕ_{eq} [cm^{-2}]	red$_{cluster}$ [%]	red$_{seed}$ [%]	Δred [%]
4.8×10^{15}	43.5	35.3	8.2
8.0×10^{15}	52.2	47.1	5.1
1.0×10^{16}	60.9	58.8	2.1

Figure 8.13.: Reduction of the MPVs of the cluster (blue) and seed charge (yellow) distributions relative to the values of the non-irradiated assembly, for the three investigated fluences, evaluated at optimal angle. The difference is plotted in red.

for the cluster and the seed can be ascribed to the additional charge that is lost by edge pixels with signals below threshold. It decreases as a function of fluence, as the fraction of single-pixel clusters increases with the accumulated radiation damage, as reported in Table 8.3. Since the granularity of the binning is too coarse to appreciate the variations of the radiation-induced relative signal loss for different thresholds, the results reported in Table 8.3 apply for all investigated thresholds.

8.5. Systematic uncertainties

The conclusions of this work rely on the comparison of hit efficiencies and spatial resolutions for different irradiation levels and threshold configurations, as presented in the previous Sections. The previously quoted uncertainties are purely statistical and typically negligible. This Section focuses on the evaluation of systematic uncertainties affecting the reported results, as well as their sensitivity to the applied selection criteria.

It was shown that the $\epsilon_{hit} \times \alpha$ is particularly sensitive to the threshold. On top of this, two main factors influence this observable: the fluence ϕ_{eq} to which the module was exposed, and its annealing state. For proton-irradiated modules, the fluence uncertainty is estimated to be 7 % in the beam spot region. These uncertainties are not propagated to the hit efficiency, as the dependence of charge collection on fluence varies with the type and combination of bulk and implant doping, as shown in [121], and has not been

ϕ_{eq} [cm^{-2}]	Angle	Charge cut	Spatial cut	RMS cut	Alignment
non-irradiated	0°	0.2	0.0	6.6	0.0
		-0.5	0.0	-3.9	0.0
	9.5°	4.3	0.0	8.4	0.0
		-3.7	0.0	-5.0	0.0
	15°	3.0	0.0	8.0	0.6
		-2.4	0.0	-4.8	0.0
8×10^{15}	0°	-0.4	0.0	5.0	0.0
		-0.2	0.0	-2.8	0.0
	9.5°	-0.1	0.6	6.0	0.5
		-0.5	0.3	-2.8	0.4
	15°	0.7	-0.9	5.8	-0.5
		-1.8	-1.1	-3.2	-0.3

Table 8.6.: Systematic effects on the resolution in r-ϕ for fresh and irradiated sensors at different angles.

characterized for the sensors studied here.

The annealing state of the sensors is estimated to correspond to a few days at room temperature, accumulated during irradiation, shipment, and handling. Studies of the annealing behavior of sensors with n-type implants and p-type bulk [122] indicate that it depends on fluence, thickness, and substrate type, but the exact behavior is unknown for the sensors investigated in this work. Due to the limited number of modules with comparable irradiation conditions, a quantitative assessment of these effects is not possible.

Systematic effects on the spatial resolution and $\epsilon_{\text{hit}} \times \alpha$ were evaluated for a subset of the measurements presented in this work. This subset includes three track incidence angles for the non-irradiated module and the section irradiated to $\phi_{\text{eq}} = 8 \times 10^{15}\,\text{cm}^{-2}$. The investigated angles, along with the results of the systematic studies, are summarized in Table 8.6. Given that the maximum variation of the uncertainty of the $\epsilon_{\text{hit}} \times \alpha$ was $< 0.02\%$, it is not reported in the Table.

To assess the impact of the alignment precision, the module was forcefully located in two specific configurations during the reconstruction. Knowing the uncertainty of the spatial alignment parameters σ_x and σ_y, the assembly was first aligned in position (x', y'), with $x' = x + \sigma_x$ and $y' = y + \sigma_y$, corresponding to a movement towards the top left corner, and then in (x'', y''), with $x'' = x - \sigma_x$ and $y'' = y - \sigma_y$, corresponding to a movement towards the bottom right corner. For every iteration, the spatial resolution was recalculated, and the RMS of these values relative to the unperturbed measurement is reported in the last column of the table. The effect is negligible, with maximum variations around $\theta = 15°$ of 0.6 % and 0.5 % observed for the non-irradiated and the irradiated modules, respectively.

Additional systematic effects are related to the reconstruction procedure. The charge cut (see Section 7.3.3) is varied such that all clusters with charges greater than $Q_{\text{MPV}} \cdot 1.7$ and $Q_{\text{MPV}} \cdot 1.3$ are excluded, instead of the nominal $Q_{\text{MPV}} \cdot 1.5$. This resulted in maximum

variations of 4.3% for the non-irradiated assembly at optimal angle, and 1.8% for the irradiated one at 15°.

When the spatial cut (see Section 7.2.4) is modified by ±10 %, the impact is negligible before irradiation, and reaches variations of up to 1.1% for the irradiated module at 15°.

Finally, the truncated RMS is recalculated discarding values outside $\pm 5 \cdot \mathrm{RMS}_{\mathrm{trc}}$ and $\pm 3 \cdot \mathrm{RMS}_{\mathrm{trc}}$, instead of the nominal $\pm 4 \cdot \mathrm{RMS}_{\mathrm{trc}}$. This cut has the largest influence, leading to reductions of up to 5 % and increases of up to 8.4 % around $\theta \approx 9.5°$.

The relative decreases and increases in the spatial resolution resulting from these variations are summarized in Table 8.6. It should be noted that the variations of the cuts are chosen arbitrarily to provide an estimate of the sensitivity.

8.6. Conclusions

The central outcomes of this work are the performance results of the planar sensor developed for the Phase-2 Upgrade of the CMS pixel detector, as presented in the preceding Sections. Initial conclusions can already be drawn from the measurements performed on the non-irradiated sensor modules:

- At the optimal track incidence angles, hit resolutions of:

  $$3.05\,\mu\mathrm{m} \pm 0.18\,\mu\mathrm{m}, \quad 3.35\,\mu\mathrm{m} \pm 0.16\,\mu\mathrm{m}, \quad 3.08\,\mu\mathrm{m} \pm 0.18\,\mu\mathrm{m}$$

  were achieved for an assembly operated at a bias voltage of 120 V and tuned to thresholds of 1000 e^-, 1200 e^- and 1500 e^-, respectively. Results can be seen in Figure 8.4 (g,h).

- The benchmark value of 99% for the $\epsilon_{\mathrm{hit}} \times \alpha$ is already reached for bias voltages as low as 5 V. The results of the efficiency measurements as a function of the bias voltage and the set threshold are shown in Figure 8.1.

Finally, this work presents a series of measurements on proton-irradiated sensor modules. Since radiation damage in the CMS pixel detector is dominated by charged particles, these results are of highest relevance. The main conclusions from these measurements are:

- The investigated sections of an irradiated assembly with measured accumulated equivalent fluences of $4.8 \times 10^{15}\,\mathrm{cm}^{-2}$, $8 \times 10^{15}\,\mathrm{cm}^{-2}$, and $1 \times 10^{16}\,\mathrm{cm}^{-2}$ achieve the corresponding efficiency benchmarks at bias voltages below 600 V, as shown in Figure 8.5. This indicates that planar sensors with a bitten design can be operated in layers two to four of the CMS pixel detector, and the forward and endcap disks, where a maximum equivalent fluence of 1×10^{16} cm^{-2} is expected.

- The spatial resolution at the optimal angle degrades to:

$$4.09\,\mu\text{m} \pm 0.26\,\mu\text{m}, \quad 4.55\,\mu\text{m} \pm 0.28\,\mu\text{m}, \quad 3.46\,\mu\text{m} \pm 0.42\,\mu\text{m}$$

  for increasing fluences. The angle scan presented in Figure 8.9 (g,h) shows a shift of the optimal angle to larger values for higher fluences, which can be explained by the increased charge trapping and the presence of low field regions induced by the accumulated radiation damage.

The charge collection efficiency was measured as a function of the accumulated fluence, for a range of bias voltages of 200 V to 800 V. The values obtained for the irradiated sections of the assemblies never reach saturation, as trapping continues to limit the collected charge even at the highest applied bias voltages. The observed linear trend suggests that increasing bias voltages partially mitigates these effects, but cannot fully restore the efficiency to pre-irradiation levels.

Relative signal losses due to the accumulated radiation damage and threshold effects were decoupled, studying the reduction of the MPVs of the seed and cluster charge distributions. A discrepancy of 8.2% was measured for the lowest fluence, corresponding to the additional fraction of charge that is lost by edge pixels with signals below threshold. The difference decreases as a function of fluence, due to the increase of the fraction of single-pixel clusters.

Systematic effects were assessed by varying alignment parameters, spatial and charge cuts, and the truncated RMS definition. The sensitivity of the spatial resolution to these variations was generally below 5%, with the largest variations observed around 9.5°. The efficiency results were found to be robust against these systematics, with variations below 0.02%.

These findings provide strong evidence that planar pixel sensors with this design can meet the demands of the HL-LHC environment.

9. Simulation of RD53B_CMS planar pixel assemblies

The simulation of the measurements presented in this work serves two main objectives: first, by comparing the simulated results to the experimental data in terms of the previously defined observables, the simulation procedure can be validated; second, it allows the identification and evaluation of systematic effects, ensuring that they are either well understood and included in the simulation, or negligible. Once validated, the simulation framework can be employed to predict the sensor performance under a broader range of conditions, such as larger track incidence angles. This is particularly valuable, as test-beam campaigns are resource-intensive in terms of both cost and time, and can realistically cover only a limited set of operational scenarios. Consequently, a robust simulation provides an essential tool for extending the predictive capabilities beyond what can be achieved with measurements alone.

The simulation is performed in Allpix Squared [9], used to model the response of the pixel sensors, the operation of the readout chip and the properties of the test beam setup. A direct comparison between simulation and measurement is presented in Section 9.1.6.

List of Own Contributions The author's contributions to the results presented in this chapter include:

- Simulation of non-irradiated and irradiated assemblies as a function of the track angle and bias voltage.
- Adding effects of the readout chip (digitization) to the simulation framework.
- Reconstruction of the relevant observables from the simulation.
- Validation of the simulated results with measurements for non-irradiated sensors.

This work was developed in collaboration with Dr. Annika Vauth, and Dr. Jörn Schwandt.

9.1. Simulation of pixel sensors

Allpix Squared is a versatile simulation framework developed to provide a user-friendly environment for simulating the performance of semiconductor detectors, covering the full chain from the interaction of ionizing particles with the sensor material to the digitization of signals in the readout electronics. The framework relies on established external packages to perform key tasks in the simulation chain. In particular, Geant4 [123] is used to model the passage of particles through matter and simulate the generation of charge carriers in the sensor. It is designed in a modular fashion, to facilitate the integration of specialized detector models and separate the core functionalities from the implementation of individual simulation modules.

In this work, Allpix Squared has been employed not only to model the behavior of the device under test, but also to reproduce the complete test beam environment. This comprehensive approach enables a consistent and realistic simulation of the full experimental setup. The following Sections will outline the basic functionality of the most relevant modules used to describe the charge deposition, transport and collection in the sensor, and to model the digitization of the charge operated in the readout chip.

9.1.1. Charge deposition

The detection of a charged particle in a silicon detector begins with its passage through the sensor material and the associated energy loss, which leads to the creation of electron–hole pairs, commonly referred to as *charge deposition*.

This process constitutes the starting point of the full Allpix Squared simulation chain, as it determines the spatial and energetic characteristics of the primary charge carriers that will subsequently undergo drift, diffusion, and collection before being digitized by the readout electronics.

Upon initialization, the software defines sensitive detector volumes (typically the active regions of the silicon sensors) to record the energy depositions within them. Each detector is assigned a set of physical parameters, such as the energy required to generate an electron-hole pair (3.66 eV for silicon [18]) and the corresponding Fano factor (0.115, in [124]).

The trajectory of the primary electron and of the secondary generated electrons and photons are then simulated, together with the associated energy deposited in the sensitive volumes. The expected number of carriers created in every step is calculated by dividing the deposited energy by the average creation energy of the material. The final number of carriers is drawn from a Gaussian distribution centered at the calculated mean value, with a variance proportional to the product of the mean and the Fano factor, to capture the fluctuations of the number of generated carriers due to the energy partitioning between ionization and other processes such as phonon excitation. Negative outcomes are

excluded, and the result is rounded to yield a discrete integer count. Following each event, the deposited charges are propagated. To maintain physical accuracy while ensuring computational efficiency, the software imposes step size and time cutoffs for the propagation of secondary particles. The maximum step length within the sensitive volume is set to 1 µm, to resolve fine-grained features of the charge deposition profile.

In the case under study, the source is defined as a collimated beam of 5.2 GeV/c electrons, with an angular spread matching the one at the DESY II test beam facility.

9.1.2. Charge transport

Allpix Squared simulates the propagation of charged carriers, including drift, diffusion, recombination, trapping and detrapping of electrons and holes after energy deposition by an incident particle. This process is crucial for converting physical charge deposition into signals that can be read by the detector electronics.

The spatially dependent electric field is provided by Dr. Jörn Schwandt and obtained from TCAD simulations; an example for different bias voltages is shown in Figure 9.1. Carrier mobilities follow the parametrization introduced in Section 2.4. The numerical integration of the trajectories is carried out with a 5^{th}–order Runge–Kutta algorithm with adaptive step sizes ranging from 0.1 ps to 250 ps. At each integration step, several physical processes are accounted for. Diffusion is modeled by adding a random displacement sampled from a Gaussian distribution, with its width determined by the local field and temperature via the Einstein relation. Trapping and detrapping are similarly modeled using probabilities and trapping times. If the integration time limit is reached or the carrier exits the sensor volume or enters an implant, the propagation is halted.

The module also includes a detailed implementation of the Van Overstraeten–de Man impact ionization model [125]. When enabled, new secondary charge carriers may be created during transport, with positions and generation depths tracked and plotted. These secondary carriers are recursively propagated, up to a configurable maximum level to prevent infinite multiplication chains.

9.1.3. Charge collection

The movement of electrons and holes within the silicon sensor induces a current on its electrodes. Since the carrier drift times in silicon (typically on the order of a few nanoseconds) are much shorter than the integration time of the preamplifiers in the readout chip (approximately 200 ns), simulating the detailed transient pulse shapes of the induced signals is not necessary when modeling non-irradiated modules, and charge trapping can be neglected. In a physical pixel sensor, the electric signal induced by a charge cloud in the readout electrode is not perfectly localized. Due to capacitive coupling, a fraction of the signal can be transferred to adjacent pixels. This is implemented in the software by using

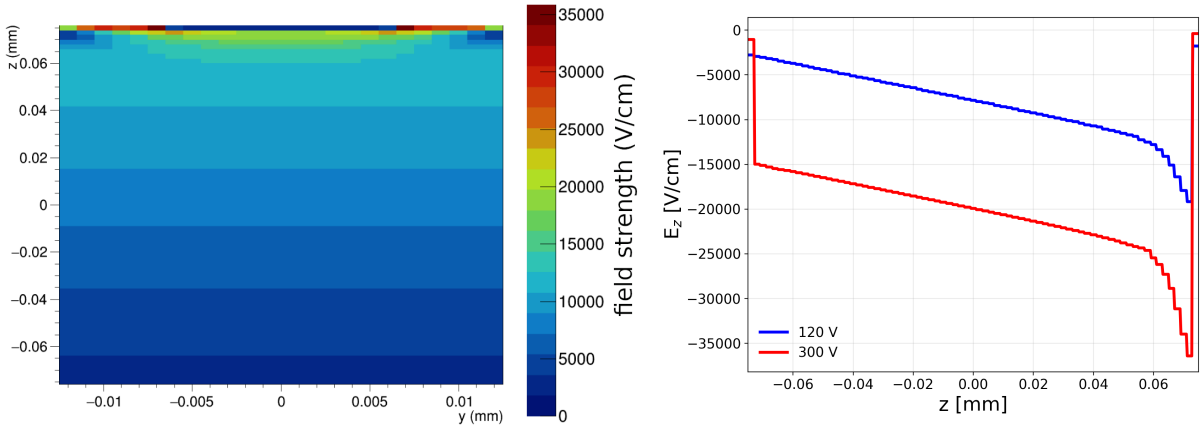

Figure 9.1.: Left: electric field used in the simulation for a bias voltage of 120 V in the y-z direction. Right: z-component of the electric field calculated at the center of the pixel for bias voltages of 120 V and 300 V.

capacitive coupling matrices that determine how much charge is shared across the matrix of pixels via crosstalk.

When the charge cloud has reached the proximity of the surface (a distance of 5 µm from the upper boundary, in the case under study), the software locates the nearest pixel and distributes the charge across that pixel and its neighbors according to the specified coupling matrix. The charge assigned to each pixel is computed by multiplying the original charge by the coupling factor defined in the matrix. These values are then accumulated in a map, ensuring that multiple contributions to the same pixel are summed.

9.1.4. Digitization

Modeling the properties of the readout chip is crucial to transform the analog signals induced on the sensor electrodes into digitized pixel hits. This process includes amplification, noise modeling, threshold discrimination, and digitization.

In addition, various aspects of electronic signal degradation and uncertainty are incorporated. One of the first such effects is electronic noise, which is modeled as a Gaussian fluctuation and added to the input charge. This step emulates the intrinsic noise of the preamplifier and subsequent analog electronics. The charge, now affected by noise, is then passed through the comparator and is subjected to threshold discrimination. In practice, the detection threshold in a readout chip is not a fixed value but fluctuates slightly from event to event due to noise and thermal effects. To mimic this behavior, the module smears the configured threshold value by drawing a per-event threshold from a Gaussian distribution with a user-defined width. Only charges that exceed this smeared threshold value are retained for further processing, while those below it are discarded.

For simulations that aim to reproduce the quantization behavior of analog-to-digital converters (ADCs) or time-to-digital converters (TDCs), the module includes support for QDC and TDC digitization. In the case under study, the output of the comparator is

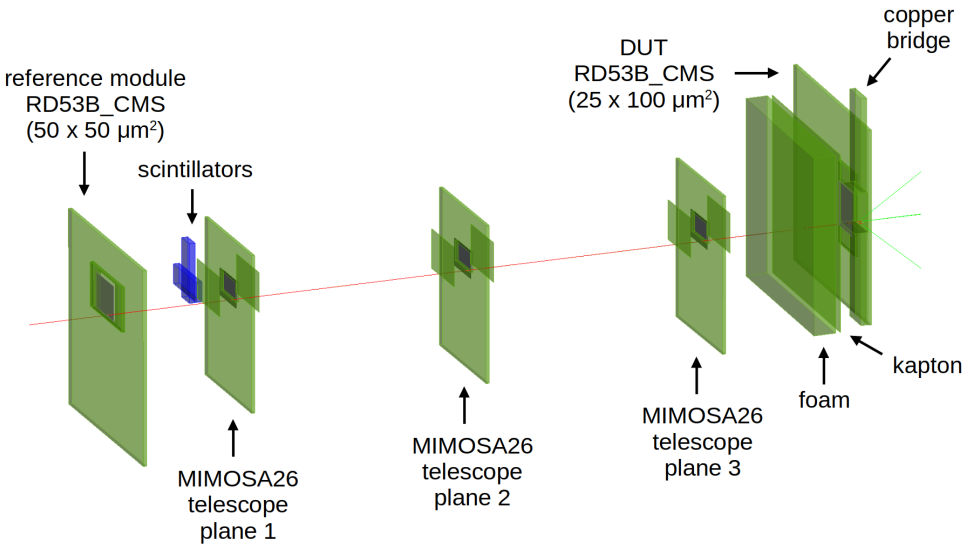

Figure 9.2.: Simulated setup used at the DESY II test beam facility.

stored directly in electrons.

9.1.5. Geometry

The last step of the simulation is the description of the geometry of the system under exam. This work focused on data taking with RD53B_CMS modules at the DESY II test beam facility. The simulated setup reproduced the two upstream scintillators, the timing reference module (an RD53B_CMS assembly with pixel pitches of $50 \times 50\,\mu m^2$), the DUT and the telescope planes.

The geometrical details concerning the segmentation of the silicon sensors, their depth, the dimension of the bumps connecting them to the readout chip (for the RD53B_CMS assemblies), and the PCBs used for support were modeled and used as starting points for the simulation. The three upstream MIMOSA26 detectors were modeled according to the known geometry and operational parameters documented in [126]. The kapton foils protecting each telescope plane were also included in the simulation, together with the protecting foam and kapton layers in front of the DUT. A rendering of the final environment can be seen in Figure 9.2. All the parameters describing the sensors under study can be found in Appendix C, together with examples of the geometry and configuration files used in this simulation.

9.1.6. Comparison with test beam data

The parameters from Table 9.1 were taken as the baseline description of the analog front-end of the DUT. The reported values for the threshold, the associated smearing and the electronic noise were measured for the non-irradiated assembly before data taking at the test beam, and are shown in Figure 9.3. Crosstalk levels were obtained as the average of the values measured for the 25 ns readout cycle, as detailed in Chapter 5. A systematic

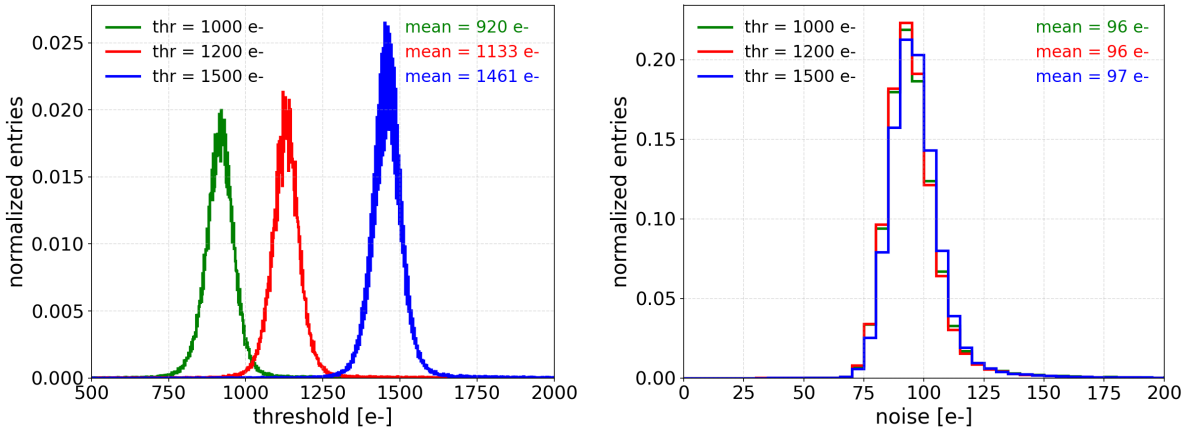

Figure 9.3.: Normalized threshold and noise distributions for the non-irradiated assembly biased to 120 V, measured before beam test data taking. The set thresholds are 1000 e^- (green), 1200 e^- (red), and 1500 e^- (blue).

study was conducted to investigate the impact of these parameters on the simulated cluster size, cluster charge and seed charge, and the results are collected in Appendix B. In the following Sections, the optimization of the simulation for a module tuned to 1200 e^- will be discussed.

9.2. Non-irradiated assemblies

The tuning of the simulation relied on the direct comparison with experimental measurements obtained at vertical incidence, where systematic effects from track inclination are minimal. A comparison between simulated and real test beam data obtained at vertical incidence and at optimal angle can be found in Figure 9.4. The plots for the cluster size in the 25 µm direction (Figure 9.4 (a,b)) indicate that the simulation reproduces the test beam data not only in terms of the mean value, but also with respect to the relative frequencies of the different cluster sizes. The agreement persisted across the entire angular scan: Figures 9.5 (a,b) illustrate the comparison for all runs in the scan, covering the full range of track angles, with the simulation consistently reproducing the measured cluster size. The distributions of the simulated and measured cluster charge (Figure 9.4 (c,d)) share the same MPV, and have similar mean values, with discrepancies below 1000 e^-. It should be noted, however, that the mean is particularly sensitive to small differences in the tails of the distribution. The most pronounced difference arises in the seed charge

Thr. $\pm$ $\sigma_{\text{Thr.}}$ [e^-]	Noise [e^-]	XT [uncoupled, coupled]
920 $\pm$ 71	96	
1133 $\pm$ 70	96	3.5%, 8.9%
1461 $\pm$ 75	97	

Table 9.1.: Simulation parameters for the DUT at different nominal threshold settings.

distributions, shown in Figure 9.4 (e,f). While both simulation and test beam data exhibit the same most probable value, the simulation shows an extended high-charge tail, whereas the test beam distribution is truncated. This truncation originates from the limited dynamic range of the ToT-to-electron calibration, introduced in Section 7.2.1: in the simulation the seed charge can take arbitrary values, but in the test beam data the maximum measurable charge is constrained by the ToT saturation at 14, and thus by the corresponding upper bound in electrons. In practice, this discrepancy affects only a small fraction of the events (fewer than 5%) which are anyway excluded from the final subset of events used to calculate the relevant observables by the cut on cluster charge described in Section 7.3.3. Consequently, the impact on the results presented here is negligible.

In principle, to reproduce the discrete mapping of ToT values to electrons observed in test beam measurements, the intercept and slope parameters obtained for each pixel from the electrons-to-ToT calibration (see Section 7.2.1) could be provided as inputs to the simulation. In this approach, the number of electrons collected by each pixel would first be mapped to the corresponding integer ToT value, and then converted back into the equivalent number of electrons associated with that integer ToT. While this method would more closely reflect test beam data, it would also introduce additional computational overhead and complexity. Moreover, most of the contributions to the cluster and seed charge arising from the tails of the distributions would in any case be removed from the final statistics. For these reasons, this approach was not pursued within the scope of this work.

Examining the distributions of the residuals from track reconstruction, it becomes apparent that the simulated residual distributions exhibit a smaller RMS value compared to those measured in the test beam, as it can be seen in Figures 9.5 (c,d) for vertical incidence and optimal angle, and in Figures 9.5 (e,f) for the entire angle scan. This discrepancy is expected. Certain effects that broaden the residuals in real data, such as the threshold oscillations described in Section 5.2 or small-scale mechanical deformations of the sensor surface (bowing), are not included in the simulation model. To prove that the track position resolution method [112] used to disentangle the telescope's contribution from the measured residuals is robust, these additional broadening effects should appear as an increased RMS of the distributions used to extrapolate the telescope's resolution for real test beam data, when compared to the ones obtained for the simulation. Indeed, as illustrated in Figures 9.5 (g,h), the distributions used to extrapolate the intrinsic telescope resolution in the simulation appear systematically narrower than their counterparts from the measured data. The larger value of the extrapolated simulated telescope resolution with respect to, for instance, the one reported in [99], can be attributed to several experimental constraints. First, the presence of the cold box limited the track reconstruction to only the three upstream telescope planes. In addition, the material budget between the last telescope plane and the DUT was increased by the 20 mm thick foam layer and the protective kapton foil, both of which introduced additional multiple scattering. Finally,

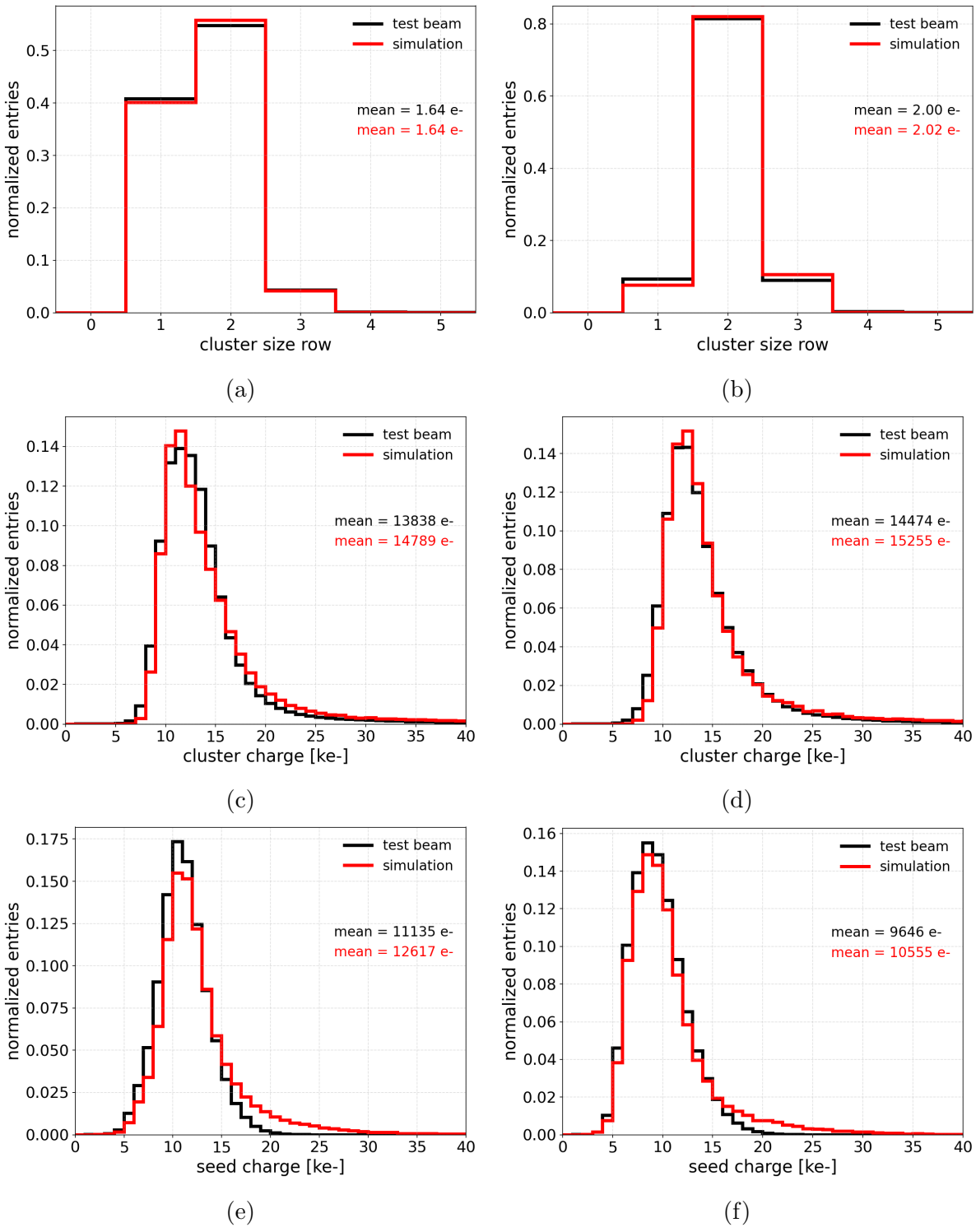

Figure 9.4.: Comparison between test beam data (black) and simulation (red) for cluster size in the 25 µm direction, cluster charge and seed charge at vertical incidence (left) and at optimal angle (right).

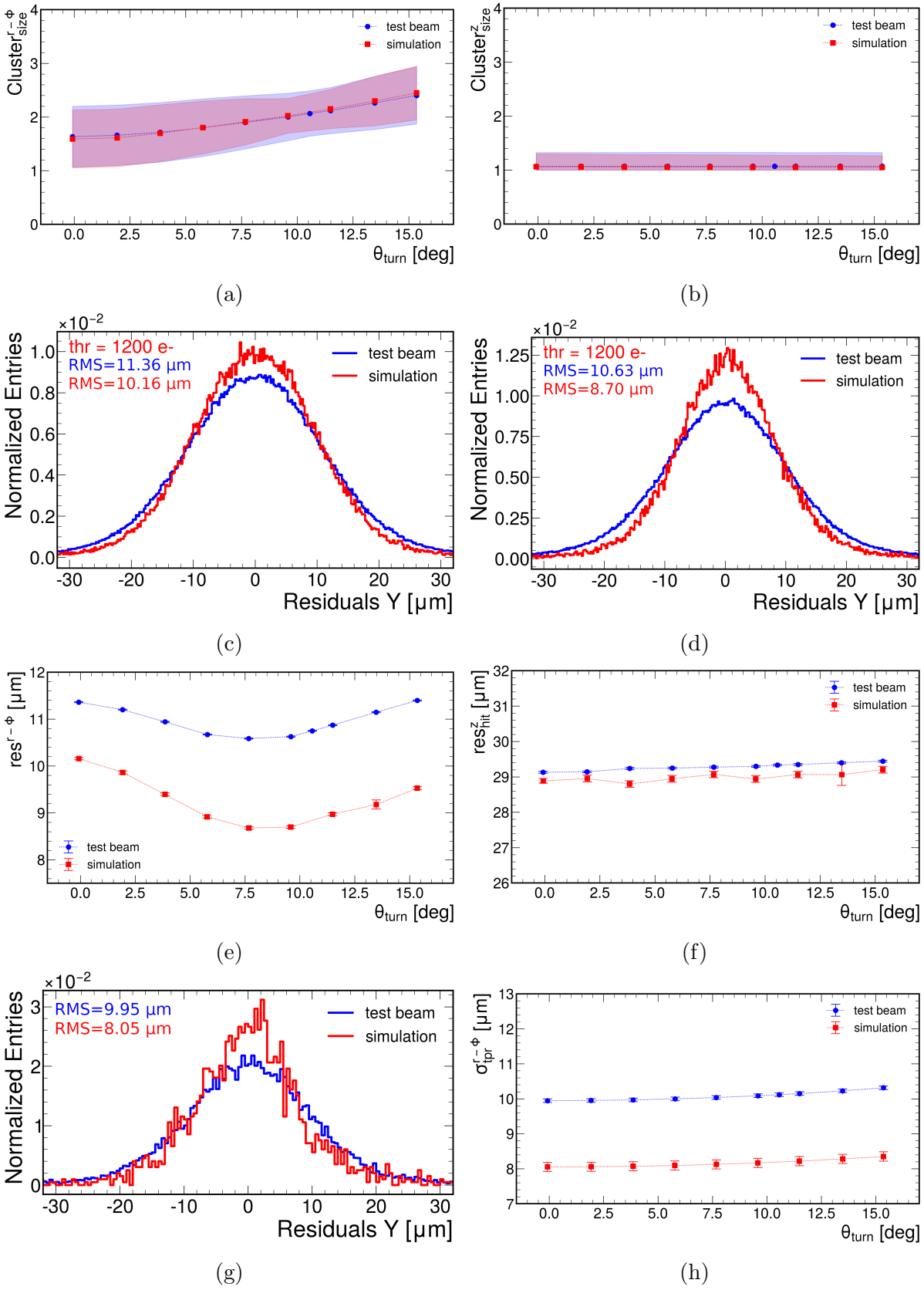

Figure 9.5.: Average cluster size and spread in the 25 µm (a) and 100 µm (b) directions. Distributions of the residuals in the 25 µm direction at vertical incidence (c), and optimal angle (d). Measured values for the residuals as a function of the angle in the 25 µm (e) and the 100 µm (f) directions. Distribution of the residuals of the events used to extrapolate the telescope's resolution (g), and calculated values as a function of the angle (h).

the DUT could not be positioned closer than 7 cm to the last telescope plane, further degrading the achievable pointing resolution.

Lastly, when the DUT resolution is calculated by subtracting in quadrature the telescope resolution from the RMS of the DUT residuals, the values obtained from the simulation and from the experimental data are in close agreement, as shown for the three thresholds under study in Figure 9.6 and Table 9.2. In all cases, the simulated resolutions are comparable with the ones measured in the test beam, measuring $3.05\,\mu m \pm 0.18\,\mu m$, $3.35\,\mu m \pm 0.16\,\mu m$, $3.06\,\mu m \pm 0.18\,\mu m$, for thresholds of 1000 e^-, 1200 e^-, and 1500 e^-, respectively. Differences range from $0.33\,\mu m$ to $0.48\,\mu m$, which remain within the combined uncertainties. The resolution minima occur at the same angle for both test beam data and simulation.

Using the tuning of the simulation established for the angle scan, it was possible to extend the study to the bias scan by substituting the electric field profile corresponding to each applied bias voltage. This approach allows the simulation to reproduce the detector response under varying bias conditions without further adjustment of other simulation parameters. The same pixels masked during real data taking were disabled for the simulation.

The comparison between test beam measurements and simulation results for all three thresholds is shown in Figure 9.7. In both cases, the efficiency saturates at the same bias voltage of 70 V, corresponding to the depletion voltage of the device. At the lowest bias voltage of 5 V, a small but measurable inefficiency is observed in both simulation and data. The only noticeable deviation is found for the configurations with threshold of $1000\,e^-$ and $1200\,e^-$, where the simulated efficiencies are systematically higher ($\approx$0.2% on average) than the ones obtained from the test beam data.

A quantitative comparison of the efficiencies extracted from the test beam measurements and from the simulation for all thresholds and bias voltages is presented in Table 9.3. Overall, the agreement is satisfactory, indicating that the tuning derived from the angle scan provides a robust description of the sensor response also in the bias scan configuration.

In the literature, the Allpix Squared framework has been extensively employed to model silicon detectors in realistic test beam environments, with simulated observables directly compared to experimental measurements. In [9], the performance of the software was validated using Timepix3 ASICs bump-bonded to n-in-p silicon sensors with thicknesses of 50 µm and 100 µm. The study demonstrated good agreement between simulation and data for cluster size, cluster charge, and residuals. In particular, for the 100 µm thick sensor, the cluster size was accurately reproduced except for very large clusters, likely originating from delta electrons. Similarly to the case examined in this work, small discrepancies were observed for the tails of the charge distributions at high charges, while the most probable value, where most of the statistics lie, was consistently well reproduced. While in [9] the agreement between simulation and real test beam data extends also to

Thr. [e$^-$]	$\sigma_{\text{hit}}^{\text{r}-\phi}$ test beam [µm]	$\sigma_{\text{hit}}^{\text{r}-\phi}$ simulation [µm]	$\lvert\Delta(\sigma_{\text{hit}}^{\text{r}-\phi})\rvert$ [µm]	θ [°]
1000	3.05 ± 0.18	2.72 ± 0.41	0.33	7.7 ($\sigma_{\text{hit}}^{\text{min}}$)
1200	3.35 ± 0.16	2.99 ± 0.37	0.36	9.6 ($\sigma_{\text{hit}}^{\text{min}}$)
1500	3.09 ± 0.18	2.61 ± 0.42	0.48	7.7 ($\sigma_{\text{hit}}^{\text{min}}$)

Table 9.2.: Test beam and simulation results at the corresponding resolution minima.

the distribution of the residuals, a situation more akin to that observed here is described in [127] for the FEI4B chip coupled to a 200 µm thick n^+-in-n planar silicon sensor. In this article, the mismatch between simulation and data was attributed not only to the absence of detector-related effects in the simulation, such as misalignments and inefficiencies, but also to a larger simulated cluster size (which is not observed in this study), positively biasing the cluster position reconstruction algorithm. A further example is provided in [128], where 100 µm CMOS pixel sensors with a small collection electrode design were investigated. In this case, a minor mismatch in the cluster charge distribution was reported at low charges (the high-charge tail is truncated in the comparison), traced back to small differences in the simulated cluster size of small clusters. Importantly, the simulated and measured resolutions, compared as a function of threshold, showed excellent agreement, with deviations not exceeding 0.3 µm, a discrepancy comparable to the ones presented in this work. Likewise, the simulated and measured efficiencies as a function of threshold differed by less than 1%, a level of agreement comparable to the one reported here.

Threshold [e$^-$]	$\epsilon_{\text{hit}} \times \alpha$ test beam [%]	$\epsilon_{\text{hit}} \times \alpha$ simulation [%]	$\lvert\Delta(\epsilon_{\text{hit}} \times \alpha)\rvert$ [%]	V_{bias} [V]
1000	99.70	99.86	0.16	
1200	99.77	99.83	0.06	70
1500	99.71	99.69	0.02	

Table 9.3.: Comparison between measured and simulated efficiency times acceptance at the depletion voltage.

9.3. Irradiated assemblies

While the simulation of non-irradiated modules within the Allpix Squared framework has reached a stage of maturity where key observables can be reproduced with satisfactory accuracy, the same cannot yet be said for irradiated sensors. The simulation of such devices presents a significantly more challenging problem, both from the standpoint of input parameterisation and from the standpoint of module implementation within the current version of Allpix Squared.

The fundamental complication is that the radiation damage sustained by the sensor bulk alters not only the effective doping concentration and electric field profile, but also

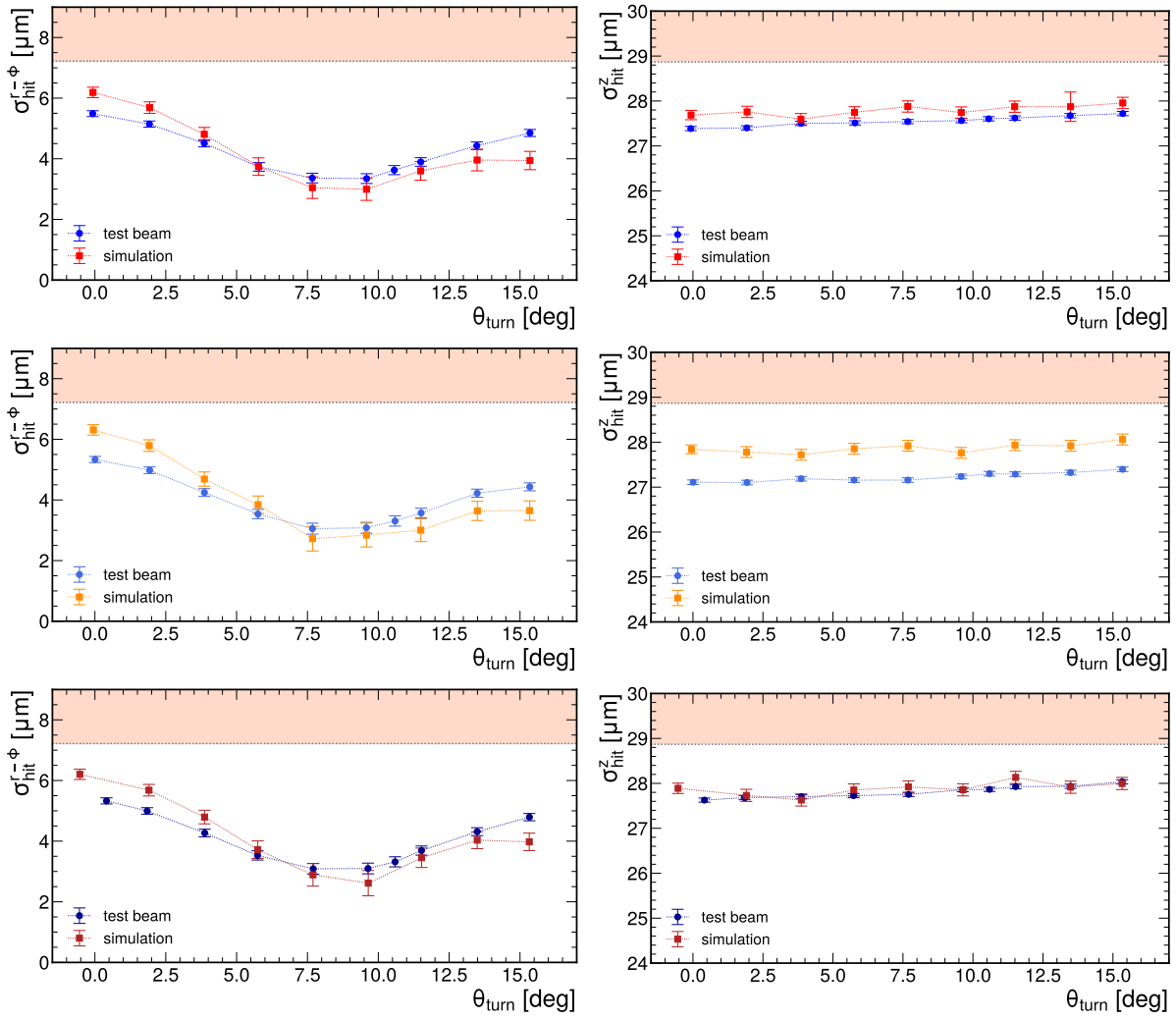

Figure 9.6.: Resolution of the simulated (red) and real test beam data (blue) for the investigate angle range and thresholds of 1000 e^- (top), 1200 e^- (middle) and 1500 e^- (bottom). Binary limits are marked by the pink bands at the top of each plot.

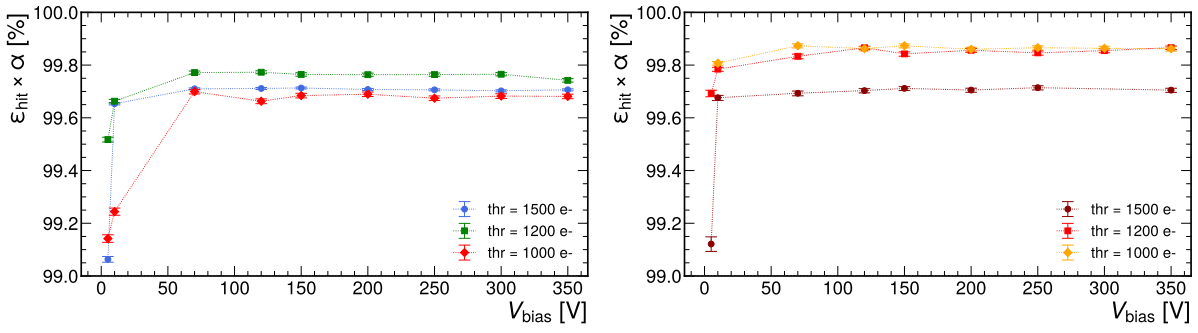

Figure 9.7.: Efficiency times acceptance for test beam data (left) and simulation (right) for thresholds of 1000 e^-, 1200 e^-, and 1500 e^-.

introduces trap states that capture and, in some cases, subsequently release charge carriers. These effects must be explicitly accounted for if one aims to reproduce the charge collection behaviour observed in test beam measurements. In practice, the simulation of irradiated devices requires as input:

1. The electric field within the sensor bulk for the relevant fluence and bias voltage.
2. The weighting field for the electrode geometry under study, or the implementation of the mirror charge method to account for the charge induced by trapped particles on the electrodes [47, 48].
3. The trapping and de-trapping times for both electrons and holes at the given fluence, bias, and temperature.

In this work, they are provided by TCAD simulations performed by Dr. J. Schwandt, using the Hamburg Penta Trap Model (HPTM), described in detail in [39] and compared with other models in [115]. The electric and weighting fields are computed directly from the device geometry and biasing conditions. Trapping times can, in a first approximation, be taken as constant across the volume for a given fluence and temperature, although in reality these times depend on the distribution of trap states in the bulk and can vary with local electric field.

In irradiated sensors, the electric field typically develops a distinctive shape, shown for the z-component of the simulated electric field in Figure 9.8 (right): two maxima, one at the n^+ readout side and one at the p^+ back, separated by a low-field region near mid-thickness. This phenomenon, discussed in [119, 120, 39], arises because radiation-induced deep donors/acceptors create a non-uniform effective space-charge $\rho_{\text{eff}}(z)$: electrons drifting to the n^+ side leave behind net negative charge near the front, while holes drifting to the p^+ side leave net positive charge near the back. The result is space-charge of opposite sign at the two surfaces and hence two depletion fronts, with a reduced field in the middle. The front peak is larger, as the n^+ side features a higher implantation density, steepening the potential drop; the p^+ back is typically more lightly doped and shares less of the drop. As fluence increases, the concentration of radiation defects grows roughly $\propto$ fluence, so $|\rho_{\text{eff}}(z)|$ near the surfaces increases, pushing the two depletion fronts further inward and depressing the mid-plane field, while the fixed bias constraint $\int_0^d E_z(z)\,dz \approx 600$ V forces the ends to compensate with higher peaks. Consistent with this picture, for $\phi_{\text{eq}} = 4.8$, 8, and 10×10^{15} cm^{-2} at 600 V, the $E_z(z)$ curves show two maxima at the electrodes with the n^+ maximum dominant; as ϕ_{eq} increases the end-peaks rise and sharpen, and the central minimum widens and drops toward lower values, indicating a progressively more pronounced low-field region that limits charge collection from the bulk.

The parameters from Table 9.4 were taken as the baseline description of the analog front-end of the irradiated DUT. The reported values for the threshold, the associated smearing and the electronic noise were measured before data taking at the test beam,

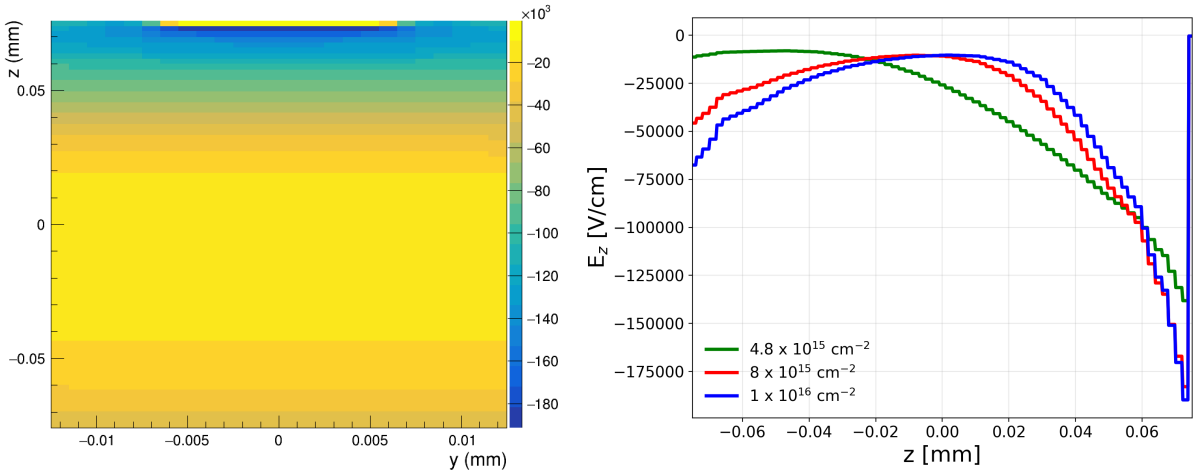

Figure 9.8.: Left: electric field used in the simulation of a module irradiated to an equivalent fluence of 4.8×10^{15} cm^{-2} for a bias voltage of 600 V in the y-z direction. Right: z-component of the electric field calculated at the center of the pixel for simulated modules irradiated to equivalent fluence of 4.8×10^{15} cm^{-2}, 8×10^{15} cm^{-2} and 1×10^{16} cm^{-2}, for a bias voltage of 600 V.

and are shown in Figure 9.9. A systematic study was conducted to evaluate the impact of trapping times on the simulated cluster size, cluster charge and seed charge, and the results are collected in Appendix B.

ϕ_{eq} [cm^{-2}]	Thr. $\pm$ $\sigma_{\text{Thr.}}$ [e$^-$]	Noise [e$^-$]	$\sigma_{\text{e}^-}/\sigma_{\text{h}^+}$ [ns]	XT
4.8×10^{15}	1180 $\pm$ 84	119	0.6222 / 1.909	
8×10^{15}	1185 $\pm$ 114	131	0.2928 / 0.893	3.5%, 8.9%
1×10^{16}	1202 $\pm$ 133	142	0.2292 / 0.702	

Table 9.4.: Simulation parameters for the DUT at different nominal threshold settings.

Simulating irradiated modules requires additional physics processes to be modelled compared to non-irradiated ones. In particular, when carriers are trapped before reaching the electrodes, their motion up to the trapping point still induces a measurable transient signal on the readout electrodes, which must be included to obtain realistic values of the total collected charge. Moreover, in regions close to the electrodes where the electric field is extremely high (greater than 10^5 V/cm), impact ionisation can occur, generating additional charge carriers that further modify the induced signal. The computation of the induced charge necessarily involves the weighting field, as described in Section 2.4.

Within Allpix Squared, the charge transport from the point of generation to the readout is conceptually split into two stages:

- **Propagation**: the drift and diffusion of carriers through the sensor bulk, including effects such as trapping.
- **Transfer**: the conversion of the induced charge into the signal domain of the readout electronics.

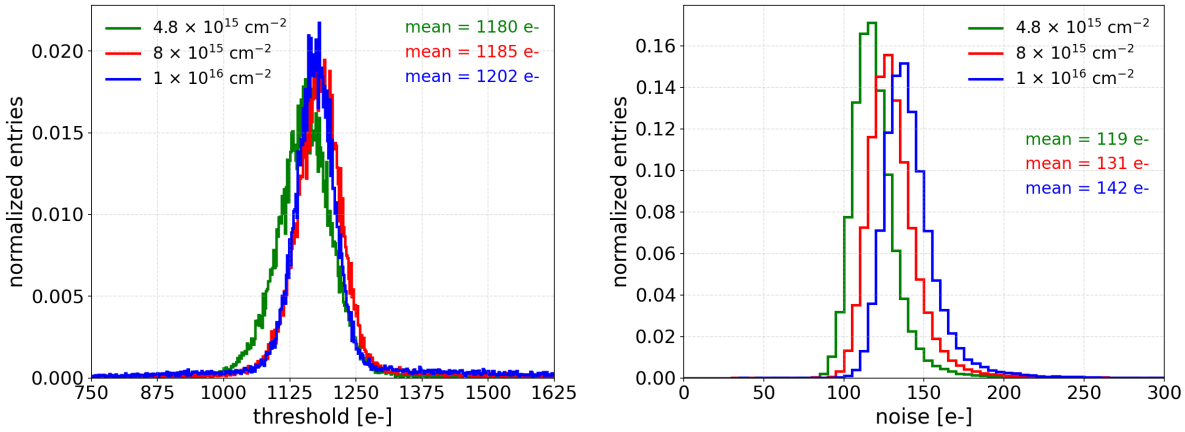

Figure 9.9.: Normalized threshold and noise distributions for the irradiated sections of the assembly, biased to 600 V, measured before beam test data taking. The respective equivalent fluences are 4.8×10^{15} cm^{-2} (green), 8×10^{15} cm^{-2} (red), and 1×10^{16} cm^{-2} (blue).

Correspondingly, two classes of modules are relevant:

- for the propagation stage: `GenericPropagation`, `TransientPropagation`.
- for the transfer stage: `InducedTransfer`, `CapacitiveTransfer`.

At present, three possible combinations of these modules can be considered for the simulation of irradiated sensors, each with its own strengths and limitations. The associated results can be seen in Figure 9.10.

GenericPropagation + CapacitiveTransfer The `GenericPropagation` module is the default choice for non-irradiated sensors. It computes the motion of carriers through the bulk, including drift, diffusion, and trapping, but does not model the induction of charge on the electrodes by carriers that are trapped before arrival. Consequently, only the charge that physically reaches the electrodes is counted towards the total collected signal. Crosstalk effects can still be modelled afterwards by using `CapacitiveTransfer`. While this approach is sufficient for non-irradiated devices, where trapping is negligible, it leads to a significant underestimation of both the cluster size and the total cluster charge for irradiated devices, precisely because trapped carriers are ignored. The results are shown in red in Figure 9.10.

GenericPropagation + InducedTransfer By retaining `GenericPropagation` for the transport stage, and replacing `CapacitiveTransfer` with `InducedTransfer`, trapped carriers are partially recovered via a simplified induction model: the induced charge is computed as the product of the transported charge and the difference in weighting potential between the start and end positions of each carrier. While this restores some of the missing charge, it is a coarse approximation, as it neglects the full trajectory of the

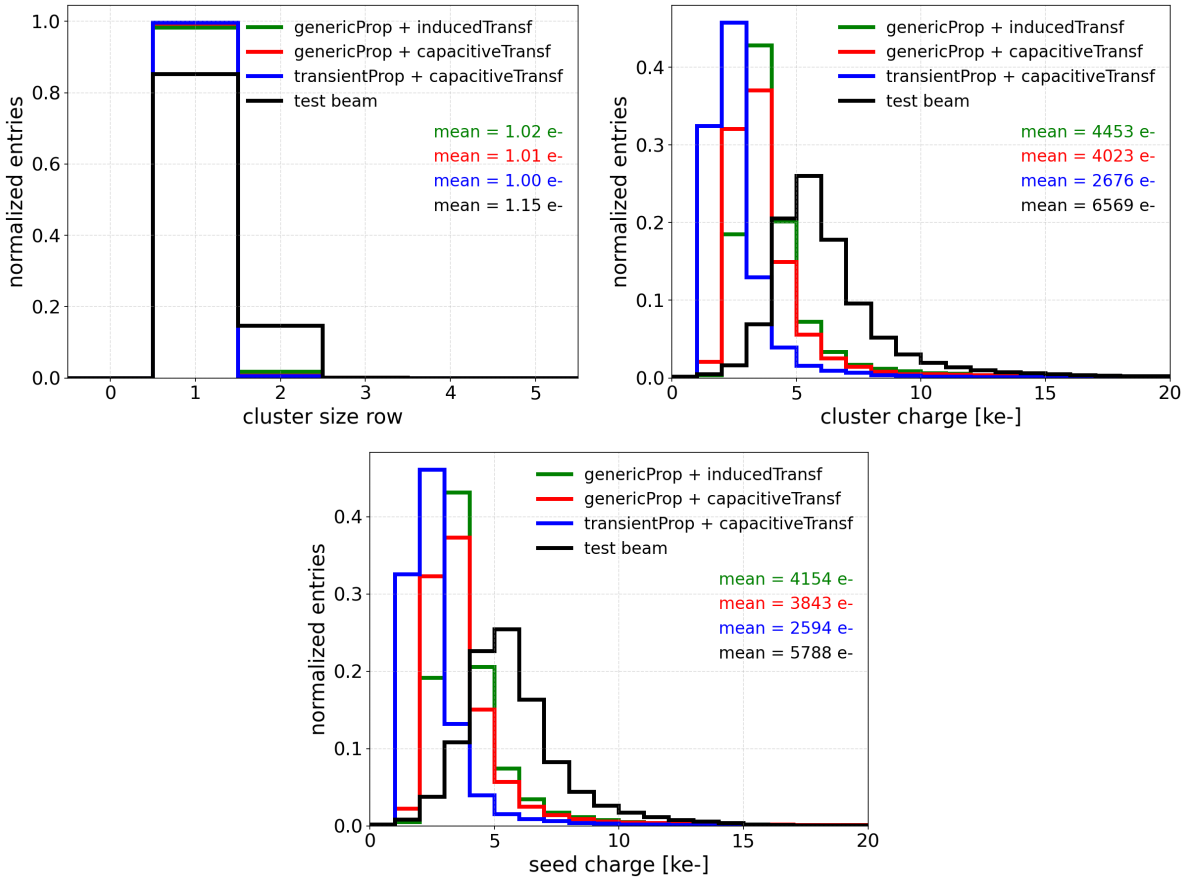

Figure 9.10.: Cluster size, cluster charge and seed charge for the three simulation methods under study and test beam data (black). The combination of `GenericPropagation` and `CapacitiveTransfer` can be seen in red; `GenericPropagation` and `InducedTransfer` in blue; `TransientPropagation` and `CapacitiveTransfer` in green.

carrier and therefore does not reproduce the pulse shape. Moreover, the current implementation of `InducedTransfer` is incompatible with the modelling of crosstalk, meaning that inter-pixel charge sharing effects due to capacitive coupling cannot be simulated with this approach. However, crosstalk only has a minor (circa 1%) impact on the main observables, as characterized in Figure B.5 in Appendix B. In terms of reproducing the average cluster size and charge, this configuration currently gives the best results among the available options, shown in green in Figure 9.10.

TransientPropagation + CapacitiveTransfer Another possible approach is to replace `GenericPropagation` with `TransientPropagation`. This module computes the induced charge at every step along the carrier trajectory, using the local weighting field. This allows both the total induced charge and the full electrode pulse shapes to be obtained. In principle, adding `CapacitiveTransfer` after `TransientPropagation` should yield a simulation that includes both induction and crosstalk. In practice, however, this combination produces average cluster sizes and charges that are smaller than those obtained

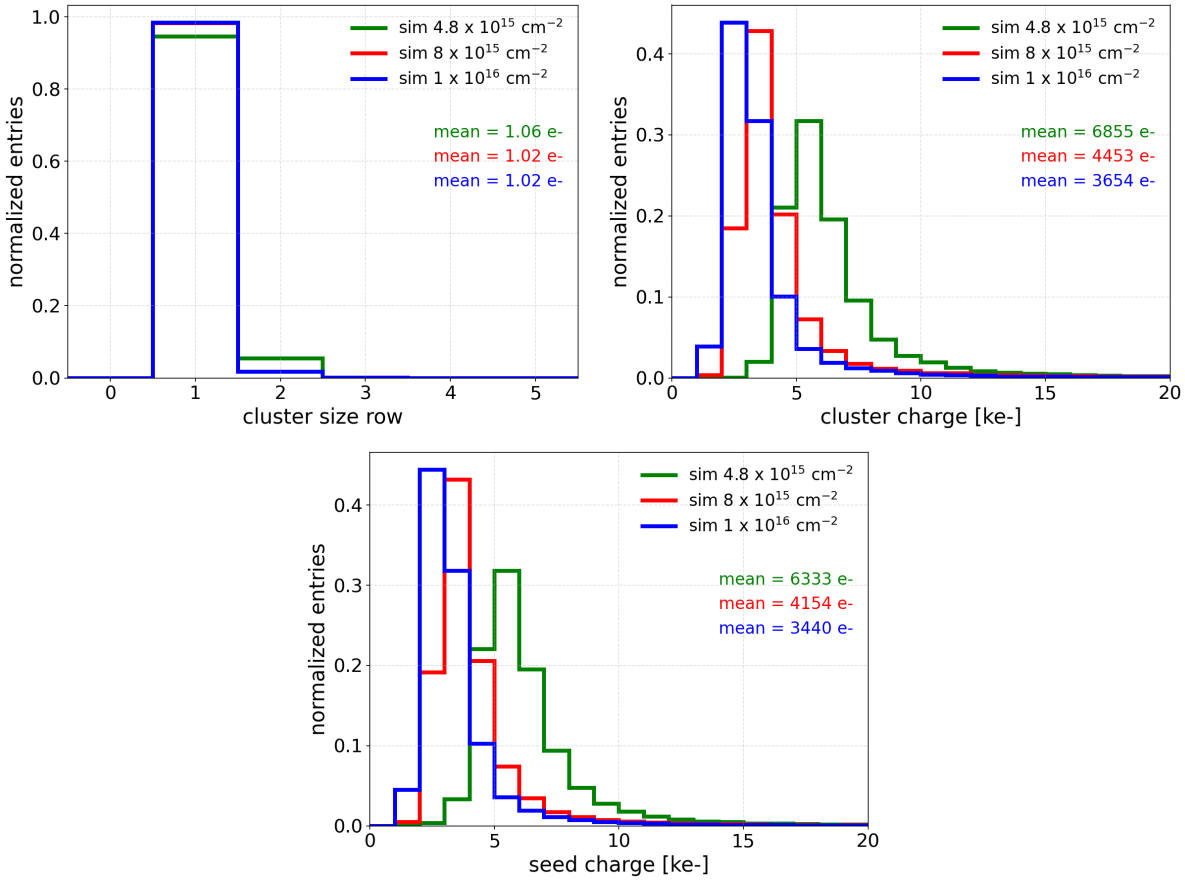

Figure 9.11.: Normalized cluster size, cluster charge and seed charge for equivalent fluences of 4.8 (green), 8 (red), and 10 × 10^{15} cm^{-2} (blue), simulated using `GenericPropagation` and `InducedTransfer`.

with `GenericPropagation + InducedTransfer`, for reasons not yet understood. This issue has been reported to the Allpix Squared development community, but no definitive explanation has yet been found. The method is also significantly more computationally demanding, with a large (almost tenfold) increase in runtime relative to the other two approaches. Results are shown in blue in Figure 9.10.

Given these discrepancies in such fundamental observables, it is not currently possible to simulate irradiated modules with the same level of agreement achieved for non-irradiated devices. Once the causes of this mismatch will be identified, the same validation procedure used for non-irradiated modules can be applied.

Just as an exercise, it is possible to simulate all fluences using the `GenericPropagation` with `TransientPropagation` method. The results are shown in Figure 9.11. The mean cluster size, cluster charge and seed charge decrease as a function of fluence. This is in agreement with the expectations (as documented e. g. in [121, 129]), as increased radiation damage results in higher trapping levels, and an increased signal loss.

To evaluate if an erroneous evaluation of the accumulated equivalent fluence could be at the root of the observed discrepancies, the results obtained for the section irradiated to 8 × 10^{15} cm^{-2} and the simulation performed for an equivalent fluence of 4.8 × 10^{15} cm^{-2}

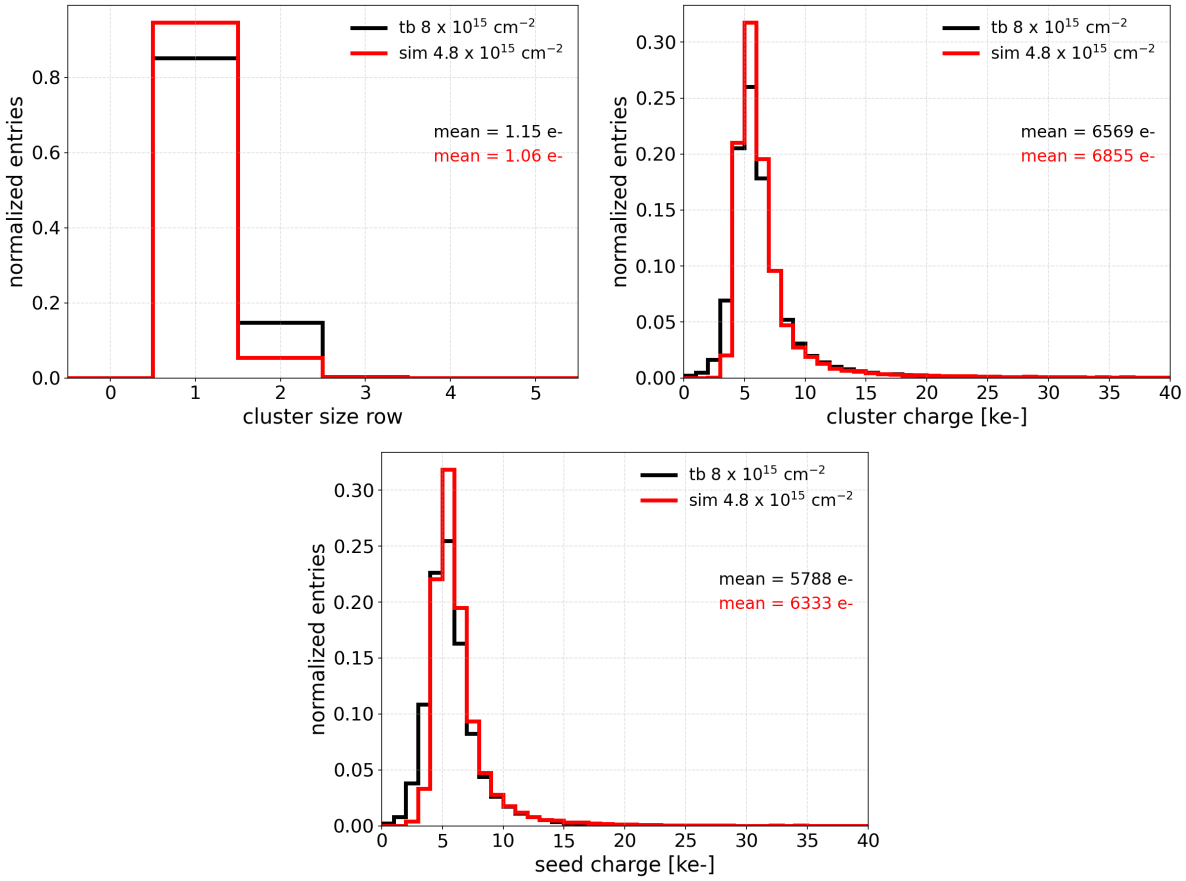

Figure 9.12.: Normalized cluster size, cluster and seed charge for test beam data collected with the section irradiated to 8×10^{15} cm^{-2} (black) and for a simulated $\phi_{\text{eq}} = 4.8 \times 10^{15}$ cm^{-2} (red).

can be compared. Even when an apparent match between the mean cluster and seed charge values of the simulated and measured data is achieved, it becomes clear from Figure 9.12 that this agreement is only superficial, as the mean cluster size predicted by the simulation remains significantly lower than the one observed in the measured data.

9.4. Conclusions

This chapter has demonstrated the capability of the Allpix Squared framework to reproduce the performance of the non-irradiated planar pixel assemblies under realistic test beam conditions. By modelling the device under test and the upstream telescope planes, it was possible to reproduce the full beam test environment in simulation, allowing for a direct comparison with experimental data.

Starting from measured operational parameters for the DUT and telescope, the simulation was tuned using a single dataset at vertical incidence. Distributions for the cluster and seed charge and cluster size were well reproduced in both peak position and shape, with only minor deviations in the high-charge tail due to ToT saturation in real test beam data. Since these events are rare and excluded by the charge cut, they had a negligible

impact on the analysis.

The residual distributions from the simulation were consistently narrower than those from the experimental data. This difference could be attributed to real-world effects absent from the simulation, such as threshold fluctuations and sensor bowing, which contributed additional broadening in the measurements. Importantly, the methodology used to extract the telescope's resolution from the data correctly accounted for these additional effects, such that when the DUT resolution is computed by subtracting the telescope contribution in quadrature, the results from simulation and experiment are in close agreement across all threshold settings. This confirms both the robustness of the resolution extraction method and the reliability of the simulation chain for non-irradiated devices.

In contrast, the simulation of irradiated modules remained limited by the current state of the software, specifically by the modelling of induced signals from trapped carriers.

In summary, the presented results validate the simulation strategy for non-irradiated sensors and highlight the specific developments needed to extend this capability to irradiated devices, paving the way for reliable, simulation-based performance predictions over a sensor's operational lifetime.

10. Conclusions

The studies presented in this thesis were conducted in the context of the Phase-2 Upgrade of the CMS detector, motivated by the forthcoming High-Luminosity LHC. During this phase, the CMS experiment will undergo a substantial upgrade, including a complete replacement of the current pixel detector with the Inner Tracker, designed to operate reliably under unprecedented radiation levels and particle densities. This worked focused on the study of the hybrid planar pixel assemblies designed for this upgrade.

In Chapter 5, the correlation between the timing of the readout, crosstalk and the effective threshold of the assemblies has been investigated, for both the half-size demonstrator (RD53A) and the pre-production (RD53B_CMS) readout chips. Measurements were done by means of the integrated charge injection circuit, and revealed a strong dependence of crosstalk on the timing of the readout within the bunch crossing time-frame. By optimizing the delay between the injection and the readout, crosstalk levels as low as 4.7% (capacitively coupled pixels) and 2.6% (uncoupled pixels) were measured for RD53B_CMS. This is well below the 10% threshold set by CMS requirements. Assemblies equipped with the RD53A readout chip exhibited stable, albeit higher, crosstalk levels: 14.1% and 4.4% for coupled and uncoupled pixels, respectively, when evaluated for the optimal timing of the readout. Additionally, the variation of the effective threshold within the bunch-crossing time frame was measured using the integrated injection circuit, and simulated using the Cadence framework. The simulated effective thresholds showed minimum-to-maximum variations roughly half as large as those measured with the injection circuit, while still exhibiting a qualitative agreement.

Test beam results obtained before and after the irradiation of the pixel modules are discussed in Chapter 8. A range of parameters was systematically explored during the measurements. These included the bias voltage applied to the sensor, the incidence angle of the beam particles, and the front-end threshold settings. All assemblies were tested at their final foreseen temperature of -20° C to replicate the realistic operating conditions at the HL-LHC. Data was collected using the Ph2_ACF framework [104] and analysed using Corryvreckan [107]. A tailored set of selection cuts, described in Chapter 7, was defined to extract a high-quality and reliable subset of events, used to extrapolate the values of the observables under study.

For the non-irradiated assembly, the spatial resolution and the efficiency (corrected for the number of noisy pixels) were measured for three different thresholds corresponding to 1000 e^-, 1200 e^-, and 1500 e^-. The extrapolated spatial resolution was $3.1\,\mu m \pm 0.2\,\mu m$

for the highest and lowest threshold settings, and 3.4 µm ± 0.2 µm for a threshold of 1200 e^-. The hit efficiency exceeded the 99 % benchmark at a bias voltage of 5 V. After irradiation to average equivalent fluences of 4.8×10^{15} cm^{-2}, 8×10^{15} cm^{-2}, and 1×10^{16} cm^{-2}, the fluence-dependent efficiency benchmarks were reached for bias voltages in the range of 400 V – 500 V, and the best efficiencies were registered for a threshold of 1200 e^- and a bias voltage of 600 V for all investigated fluences. The spatial resolution degraded after irradiation, reaching minima of circa 4 µm for the different fluences and thresholds under exam. It remained nevertheless below the binary limits, fulfilling the CMS requirement. The angles for which the minima of the spatial resolutions have been observed increased with fluence and threshold, due to charge trapping induced by the accumulated radiation damage reducing the average event cluster size, and threshold effects. The charge collection efficiency (CCE) was studied as a function of the accumulated fluence. Measurements showed that for the non-irradiated assembly, the CCE reached 100% for all bias voltages greater or equal to the full depletion voltage, while for irradiated modules it increased linearly with bias voltage, decreasing with fluence from 62% to 43% for a threshold of 1200 e^- at the reference voltage of 600 V, and did not exhibit saturation within the accessible voltage range. By studying the CCE separately on the seed pixel and the clusters, it was possible to decouple the signal loss due to radiation damage and threshold effects.

To complement the experimental results, a dedicated simulation of the non-irradiated assemblies was performed using the Allpix Squared framework [126], as described in Chapter 9. By modelling the device under test and the telescope planes, and tuning the model to real datasets, it was possible to simulate the full test beam environment. The results successfully reproduced key observables such as cluster size, charge distributions, efficiency and resolution. The average difference between the simulated and the measured spatial resolution and efficiency was found to be 0.4 µm and 0.1%, respectively. This validates the framework also as a predictive resource for exploring detector response under conditions not directly accessible to test beam campaigns.

A. Appendix: Analysis of test beam data

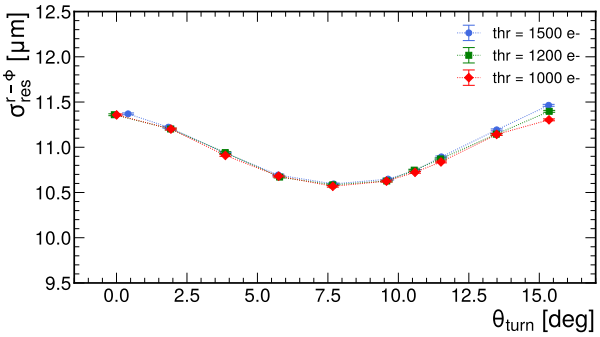

(a) Residuals in the 25 µm direction.

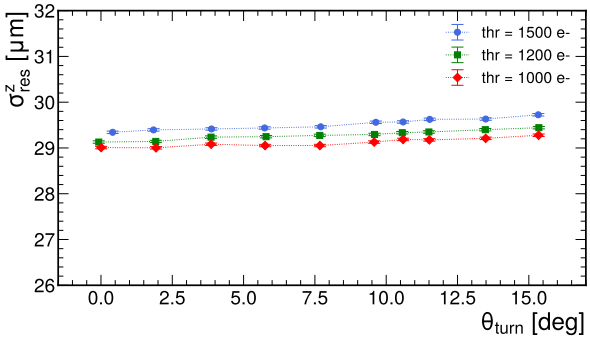

(b) Residuals in the 100 µm direction.

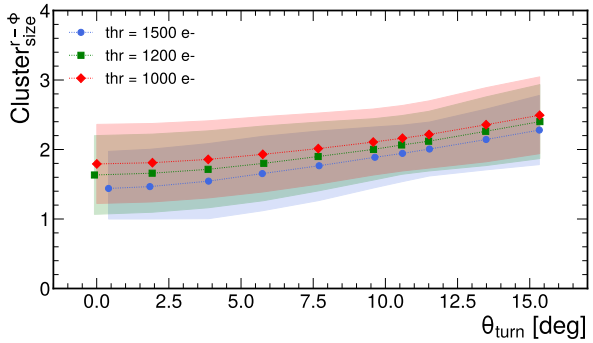

(c) Cluster size in the 25 µm direction.

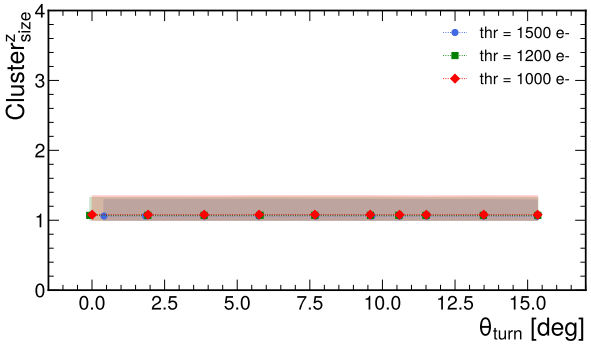

(d) Cluster size in the 100 µm direction.

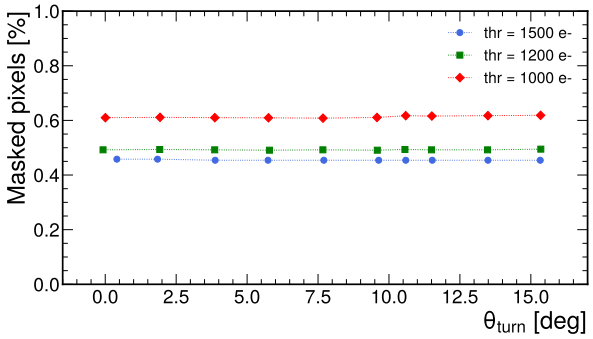

(e) Masked pixels.

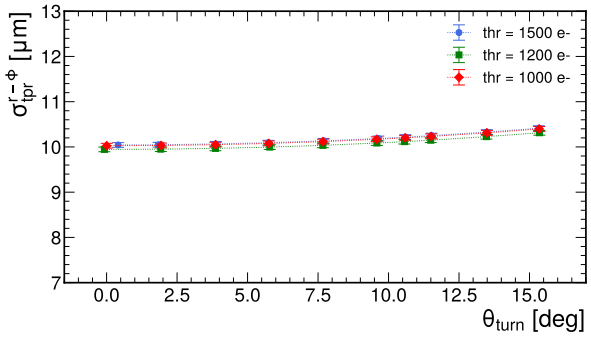

(f) Extracted telescope resolutions.

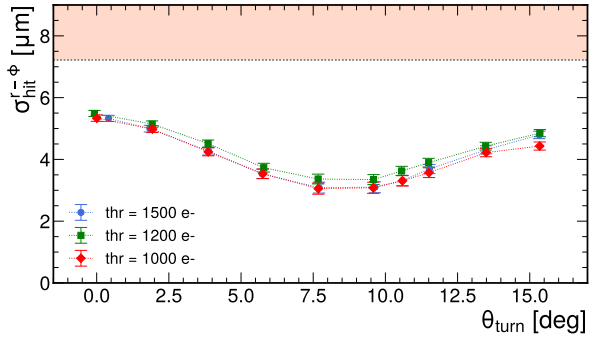

(g) Spatial resolution in the 25 µm direction.

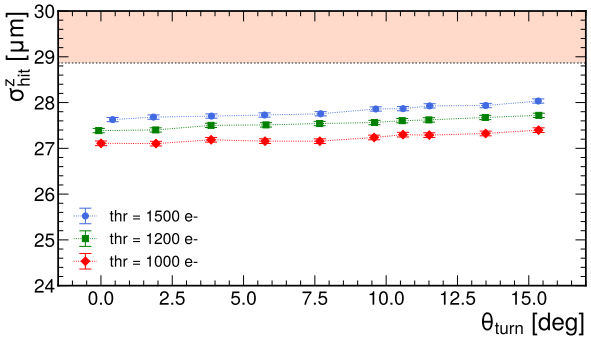

(h) Spatial resolution in the 100 µm direction.

Figure A.1.: Results of an angle scan for a non-irradiated assembly cooled to -20°C, tuned to 1000 e^- (red), 1200 e^- (green), and 1500 e^- (blue).

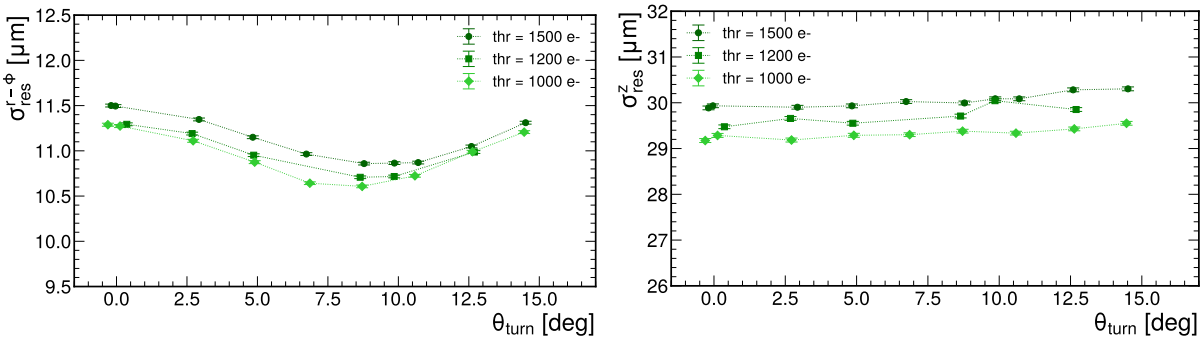

(a) Residuals in the 25 µm direction.

(b) Residuals in the 100 µm direction.

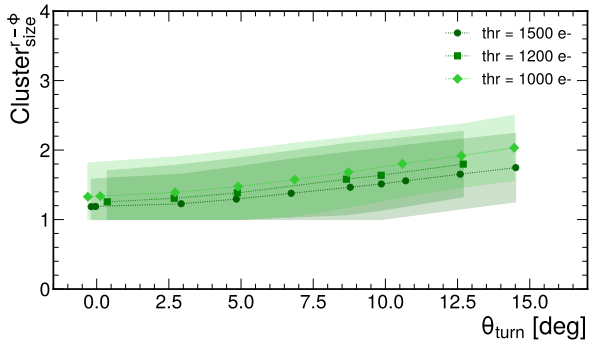

(c) Cluster size in the 25 µm direction.

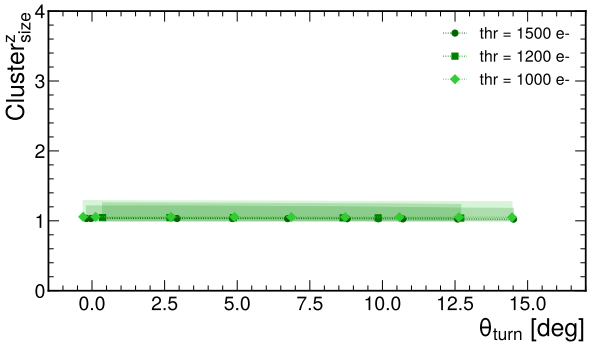

(d) Cluster size in the 100 µm direction.

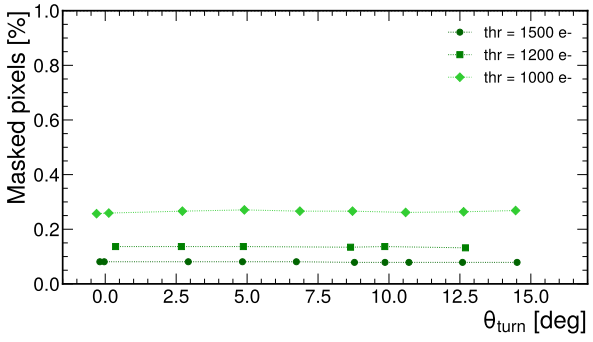

(e) Masked pixels.

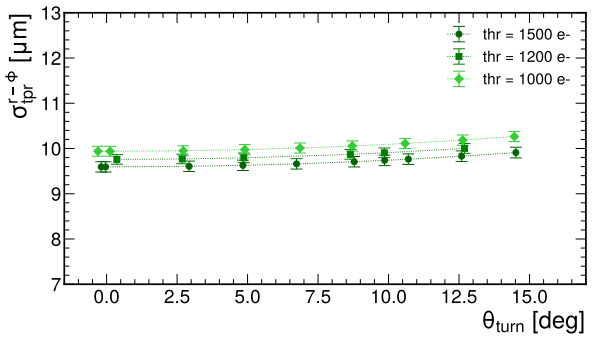

(f) Extracted telescope resolutions.

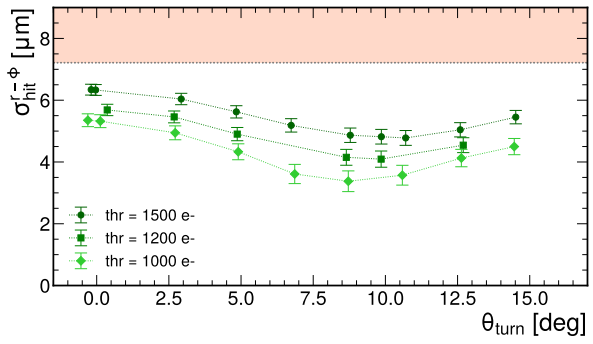

(g) Spatial resolution in the 25 µm direction.

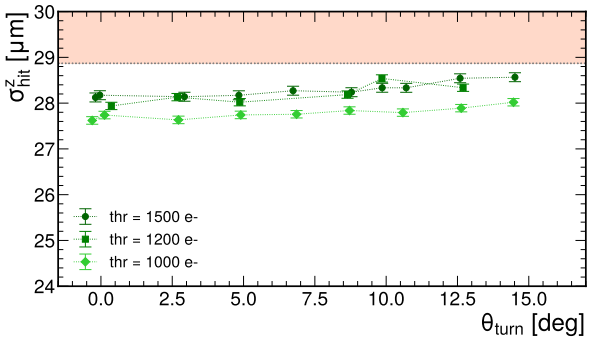

(h) Spatial resolution in the 100 µm direction.

Figure A.2.: Results of an angle scan for a section irradiated to $4.8 \times 10^{15}\,\mathrm{cm}^{-2}$, cooled to -20°C, tuned to 1000 e^- (red), 1200 e^- (green), and 1500 e^- (blue).

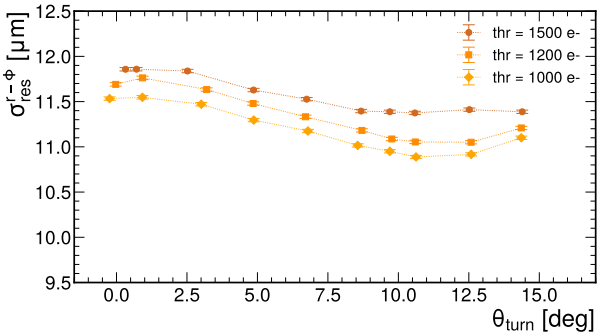

(a) Residuals in the 25 µm direction.

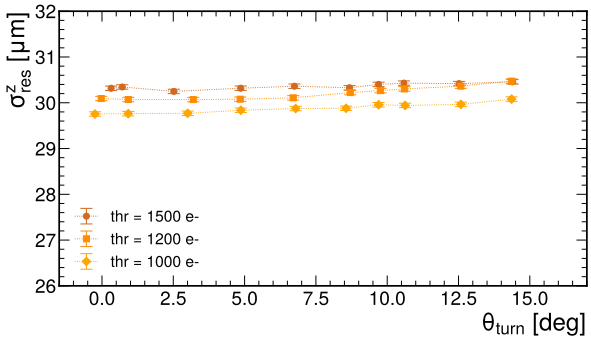

(b) Residuals in the 100 µm direction.

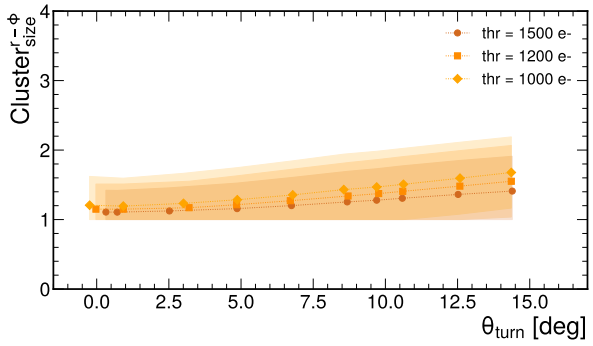

(c) Cluster size in the 25 µm direction.

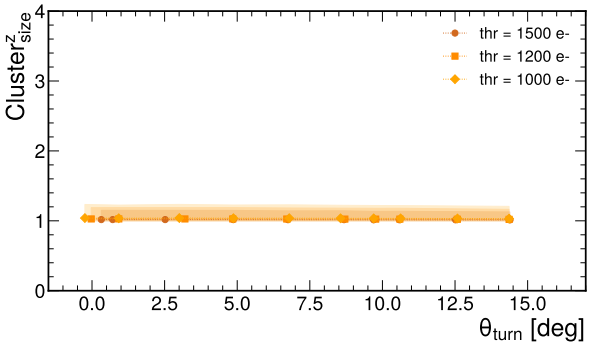

(d) Cluster size in the 100 µm direction.

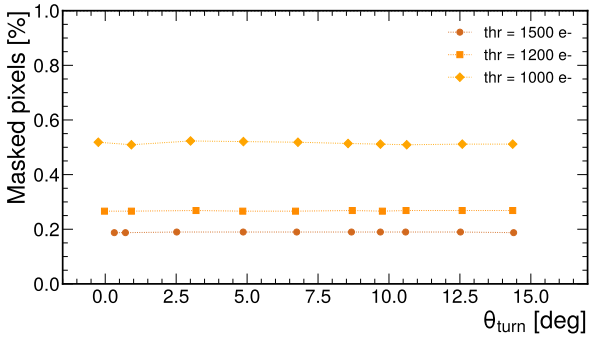

(e) Masked pixels.

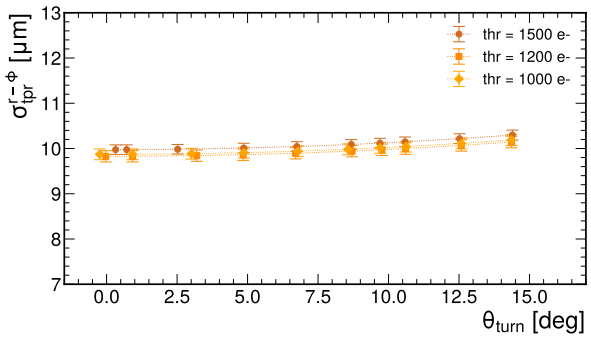

(f) Extracted telescope resolutions.

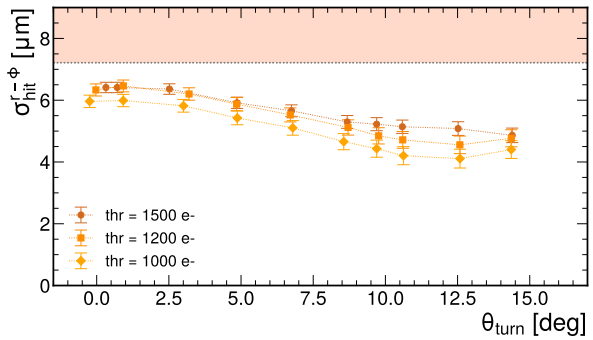

(g) Spatial resolution in the 25 µm direction.

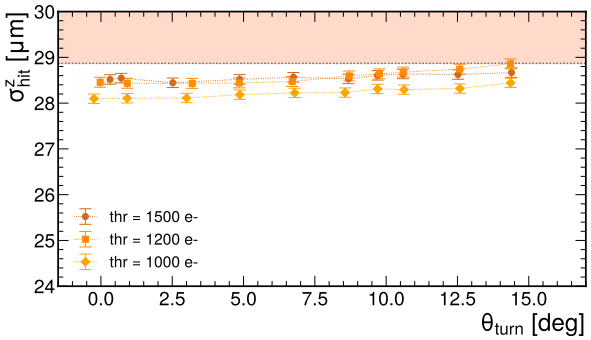

(h) Spatial resolution in the 100 µm direction.

Figure A.3.: Results of an angle scan for a section irradiated to $8 \times 10^{15}\,\mathrm{cm}^{-2}$, cooled to -20°C, tuned to 1000 e^- (red), 1200 e^- (green), and 1500 e^- (blue).

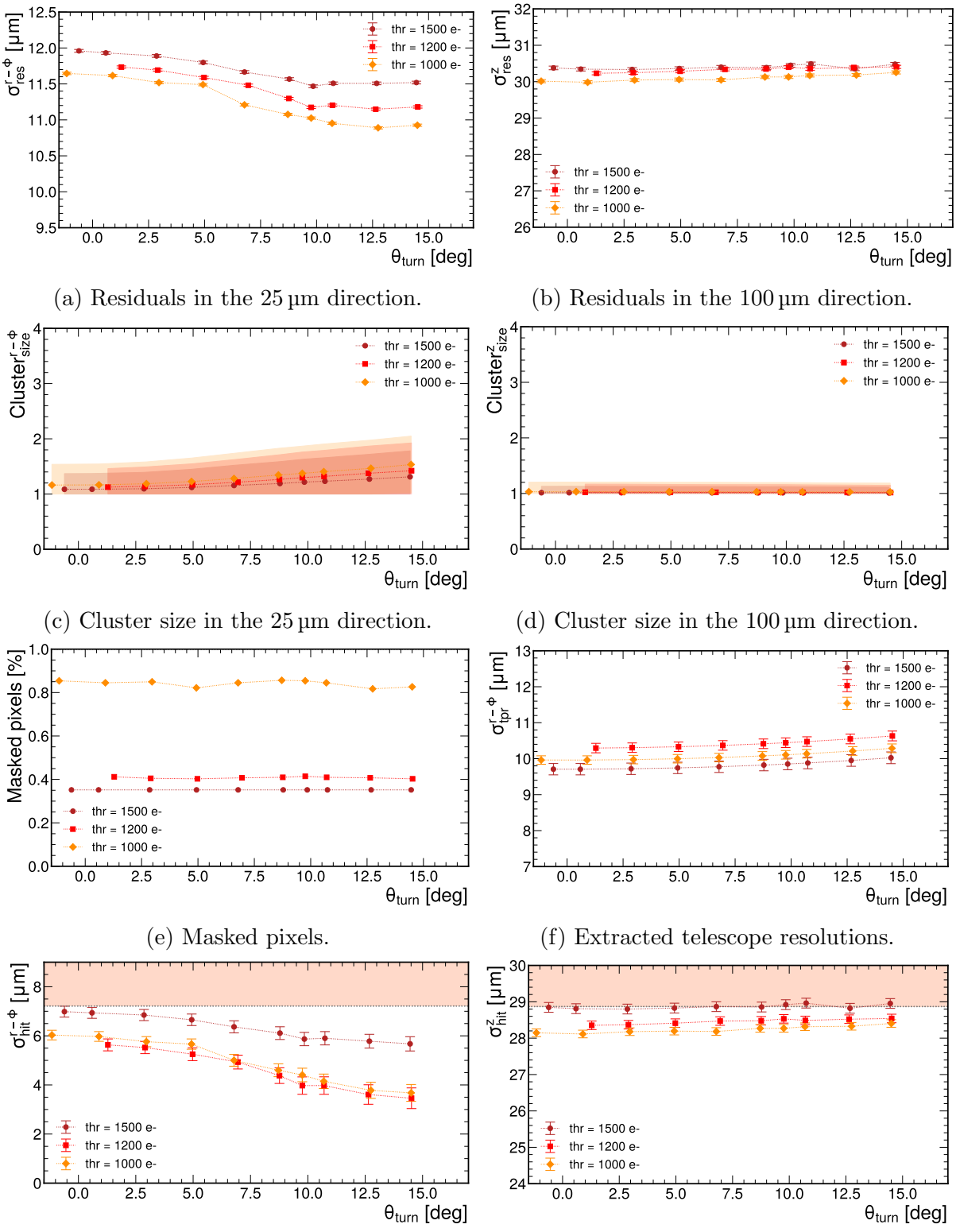

(a) Residuals in the 25 µm direction.

(b) Residuals in the 100 µm direction.

(c) Cluster size in the 25 µm direction.

(d) Cluster size in the 100 µm direction.

(e) Masked pixels.

(f) Extracted telescope resolutions.

(g) Spatial resolution in the 25 µm direction.

(h) Spatial resolution in the 100 µm direction.

Figure A.4.: Results of an angle scan for a section irradiated to $1 \times 10^{16}\,\text{cm}^{-2}$, cooled to -20°C, tuned to 1000 e^- (red), 1200 e^- (green), and 1500 e^- (blue).

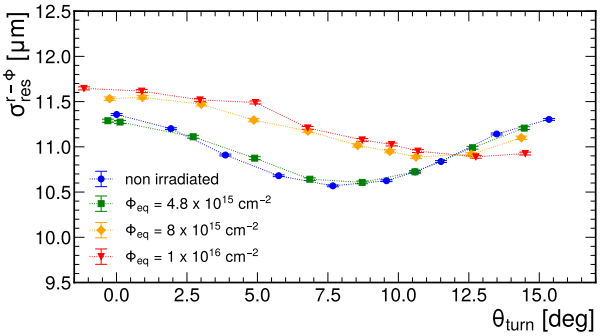

(a) Residuals in the 25 µm direction.

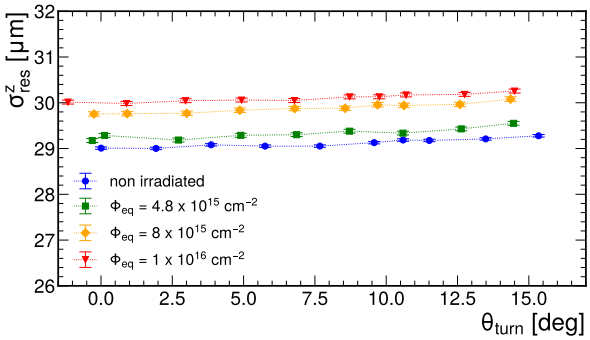

(b) Residuals in the 100 µm direction.

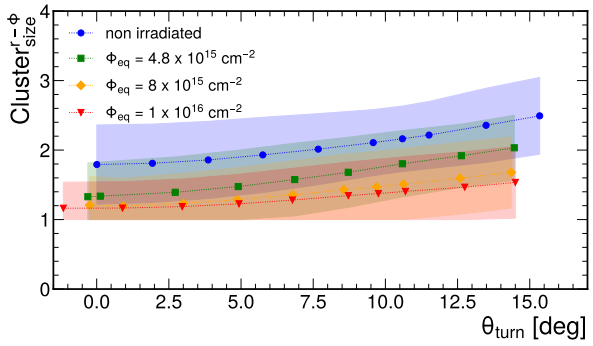

(c) Cluster size in the 25 µm direction.

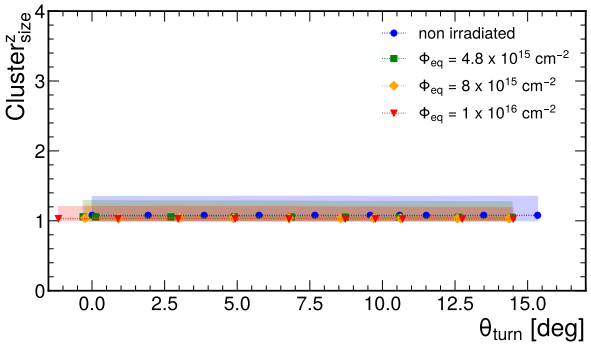

(d) Cluster size in the 100 µm direction.

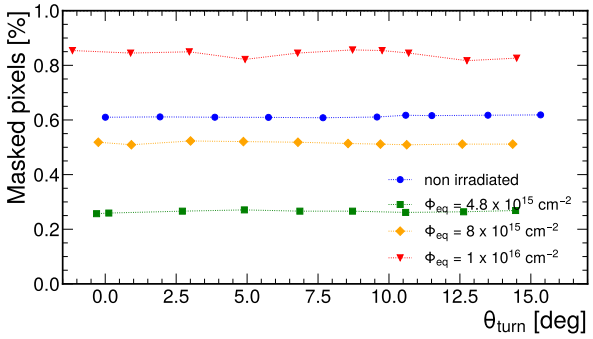

(e) Masked pixels.

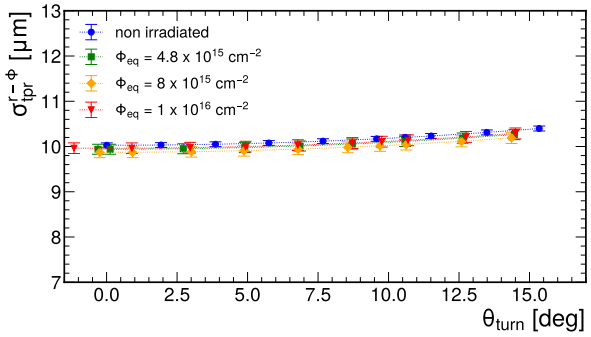

(f) Extracted telescope resolutions.

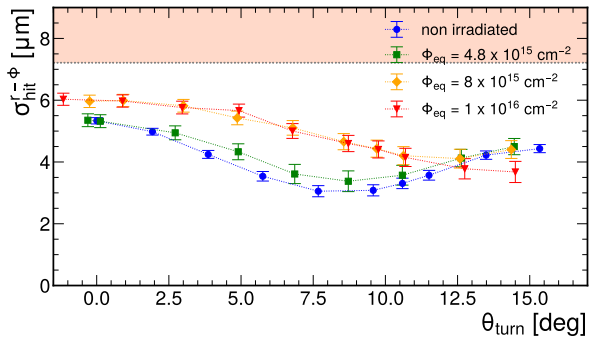

(g) Spatial resolution in the 25 µm direction.

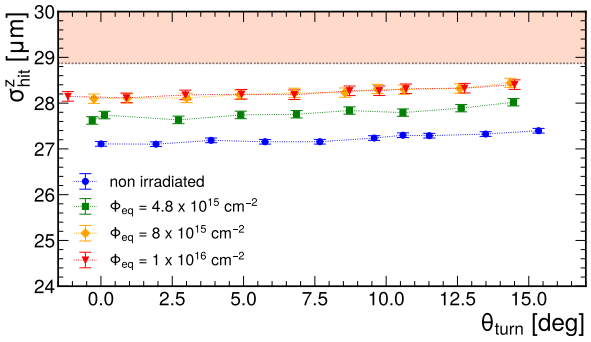

(h) Spatial resolution in the 100 µm direction.

Figure A.5.: Results of an angle scan for assemblies cooled to -20°C, tuned to 1000 e$^-$, with corresponding accumulated fluences of 1×10^{16} cm^{-2} (red), 8×10^{15} cm^{-2} (orange), 4.8×10^{15} cm^{-2} (green), and for a non-irradiated assembly (blue).

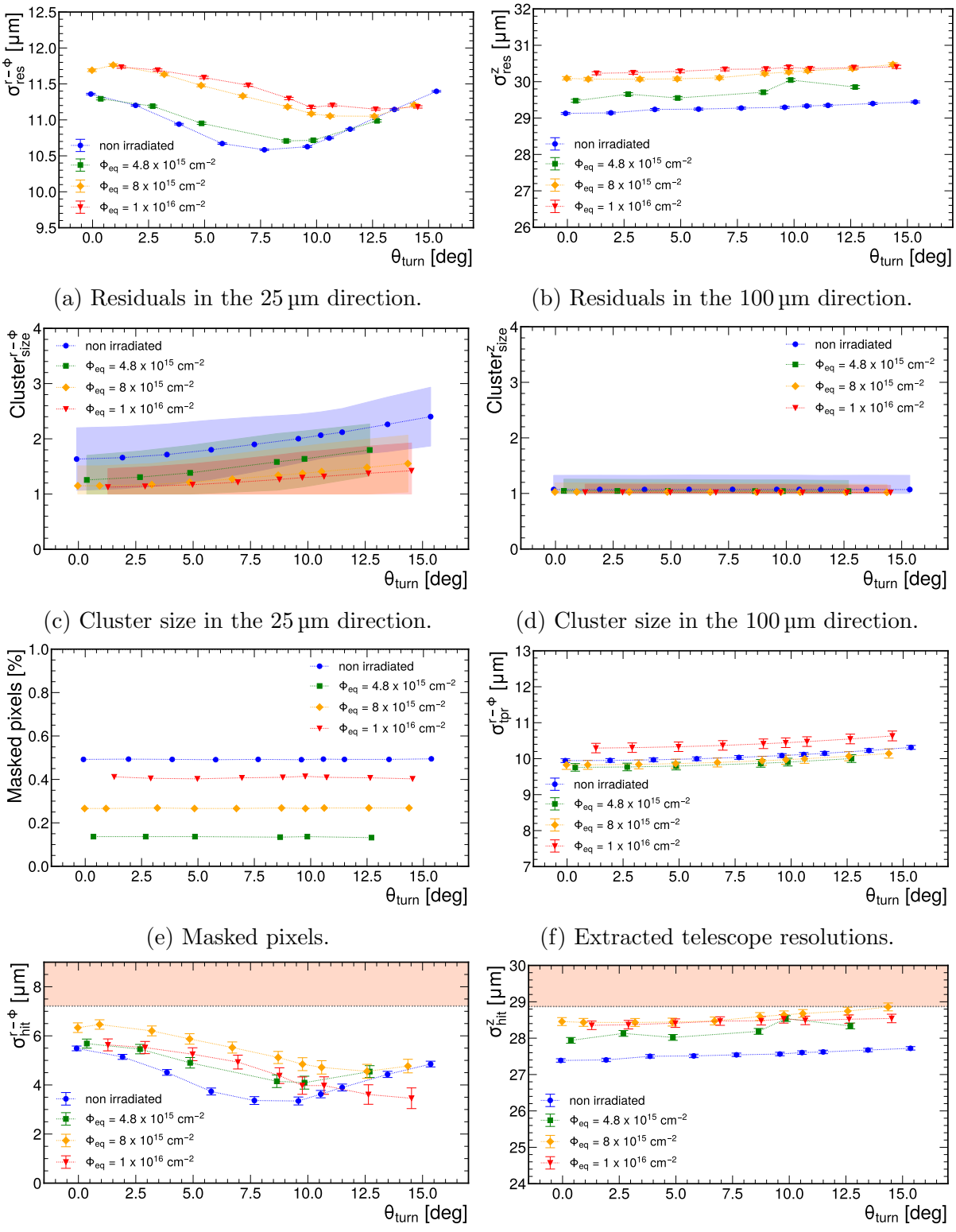

(a) Residuals in the 25 µm direction.

(b) Residuals in the 100 µm direction.

(c) Cluster size in the 25 µm direction.

(d) Cluster size in the 100 µm direction.

(e) Masked pixels.

(f) Extracted telescope resolutions.

(g) Spatial resolution in the 25 µm direction.

(h) Spatial resolution in the 100 µm direction.

Figure A.6.: Results of an angle scan for assemblies cooled to -20°C, tuned to 1200 e$^-$, with corresponding accumulated fluences of 1×10^{16} cm^{-2} (red), 8×10^{15} cm^{-2} (orange), 4.8×10^{15} cm^{-2} (green), and for a non-irradiated assembly (blue).

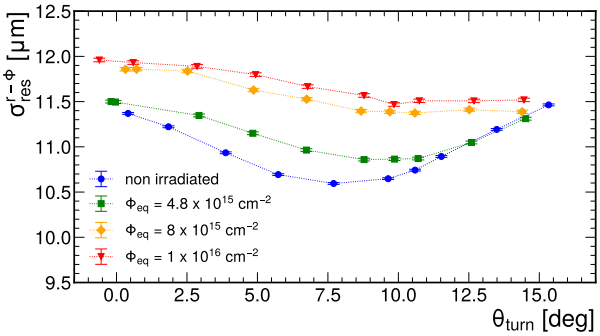

(a) Residuals in the 25 µm direction.

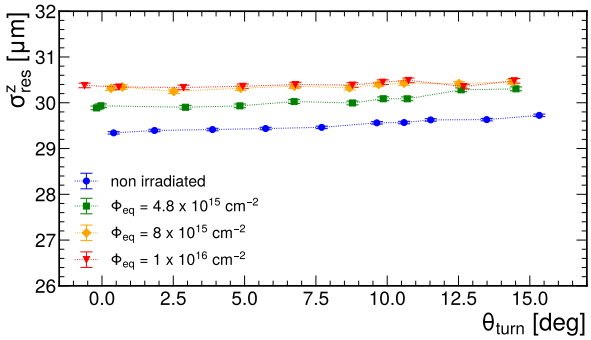

(b) Residuals in the 100 µm direction.

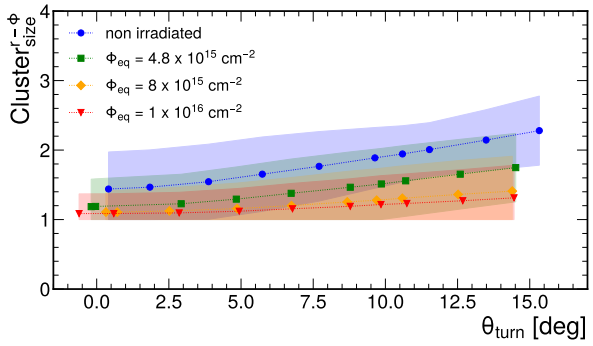

(c) Cluster size in the 25 µm direction.

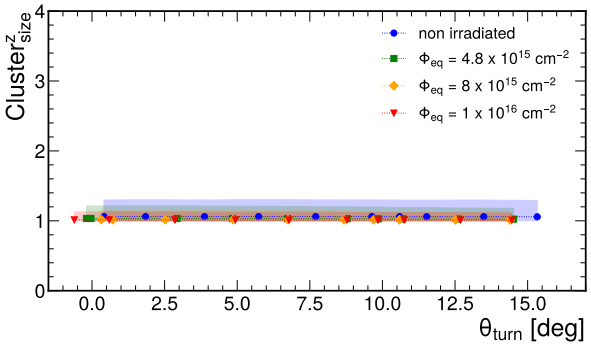

(d) Cluster size in the 100 µm direction.

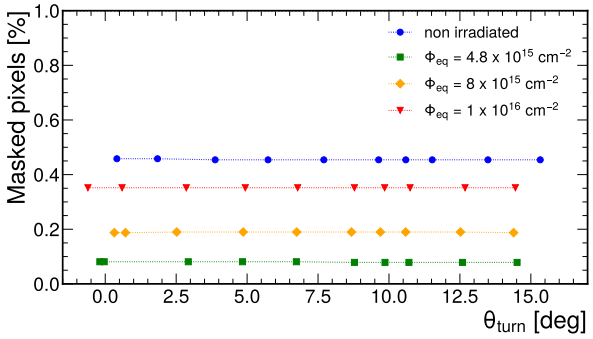

(e) Masked pixels.

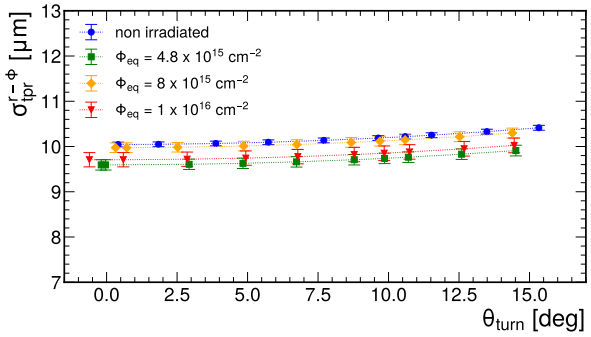

(f) Extracted telescope resolutions.

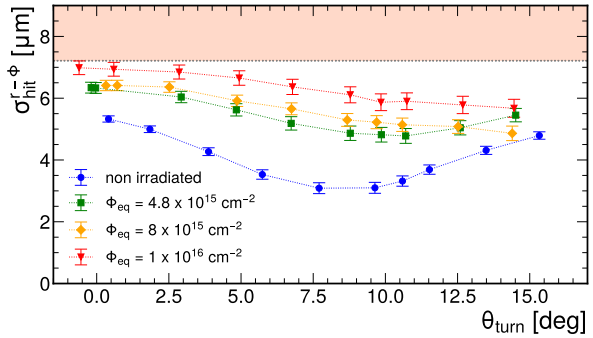

(g) Spatial resolution in the 25 µm direction.

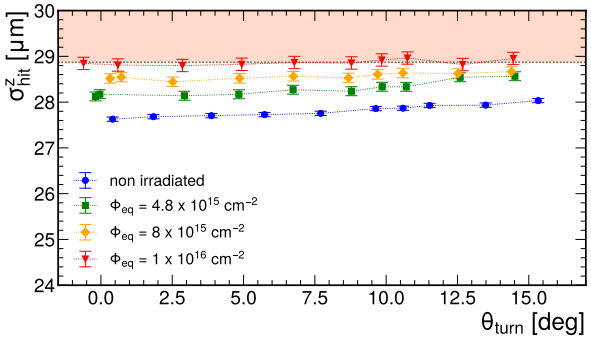

(h) Spatial resolution in the 100 µm direction.

Figure A.7.: Results of an angle scan for assemblies cooled to -20°C, tuned to 1500 e$^-$, with corresponding accumulated fluences of 1×10^{16} cm^{-2} (red), 8×10^{15} cm^{-2} (orange), 4.8×10^{15} cm^{-2} (green), and for a non-irradiated assembly (blue).

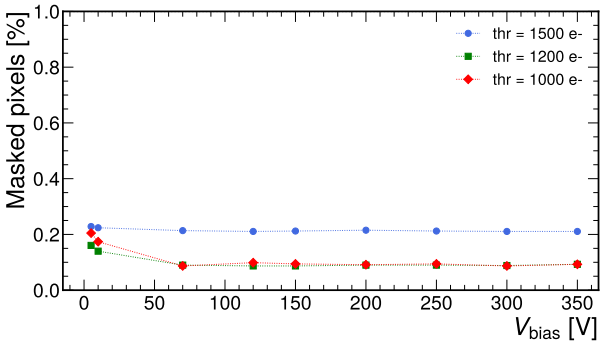

(a) Masked pixels.

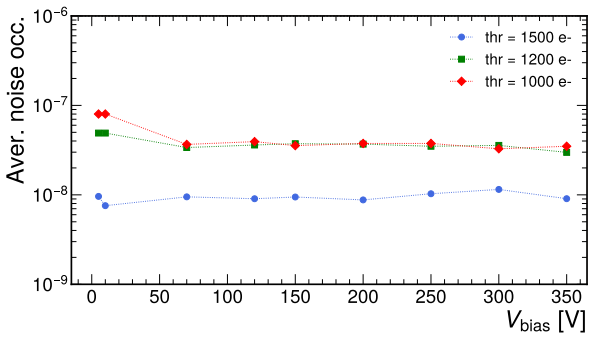

(b) Average noise occupancy after masking.

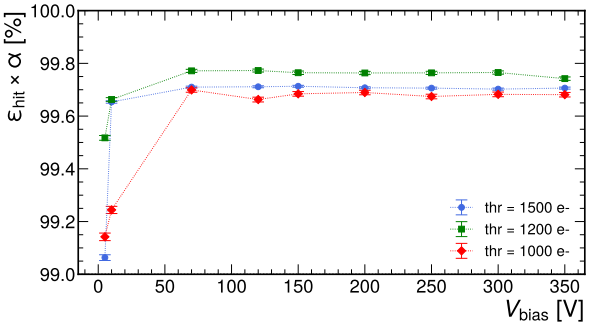

(c) Efficiency times acceptance.

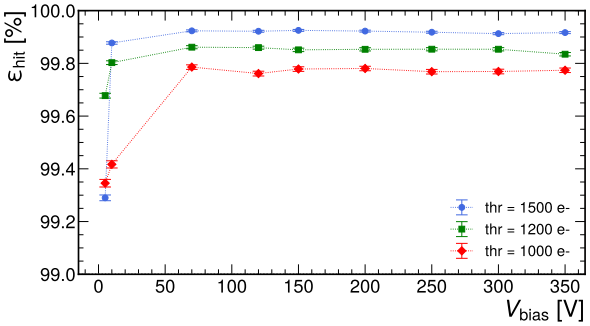

(d) Efficiency times acceptance.

Figure A.8.: Results of a bias scan for a non-irradiated assembly cooled to -20°C, tuned to 1000 e$^-$ (red), 1200 e$^-$ (green), and 1500 e$^-$ (blue).

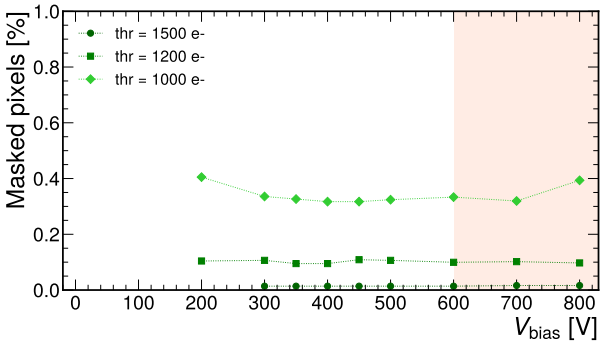

(a) Masked pixels.

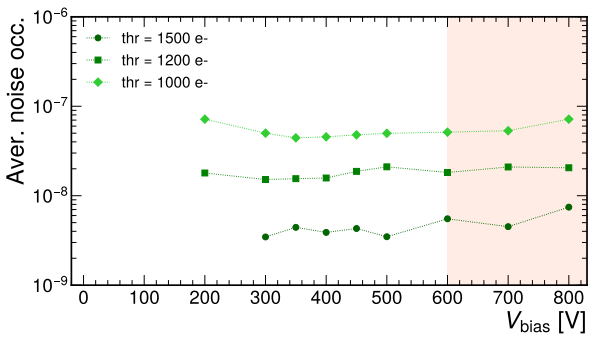

(b) Average noise occupancy after masking.

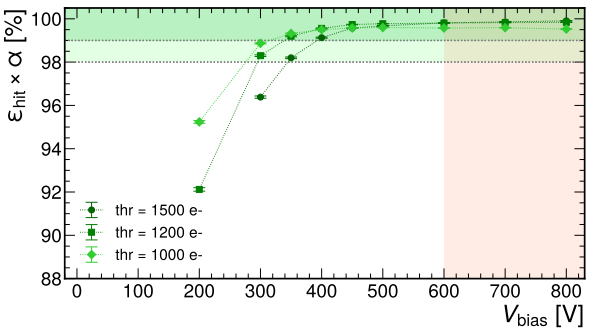

(c) Efficiency times acceptance.

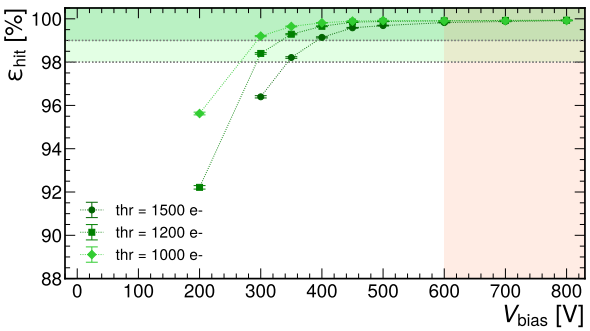

(d) Efficiency times acceptance.

Figure A.9.: Results of a bias scan for a section irradiated to $4.8 \times 10^{15}\,\mathrm{cm}^{-2}$, cooled to -20°C, tuned to 1000 e$^-$ (red), 1200 e$^-$ (green), and 1500 e$^-$ (blue).

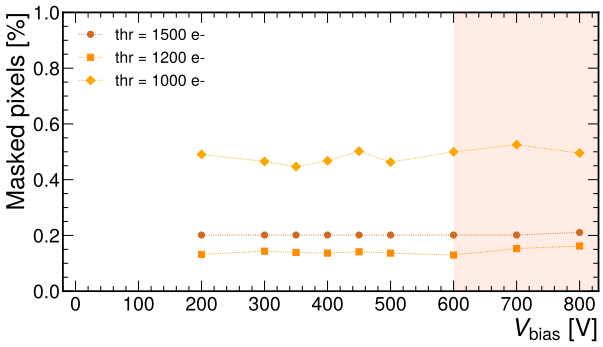

(a) Masked pixels.

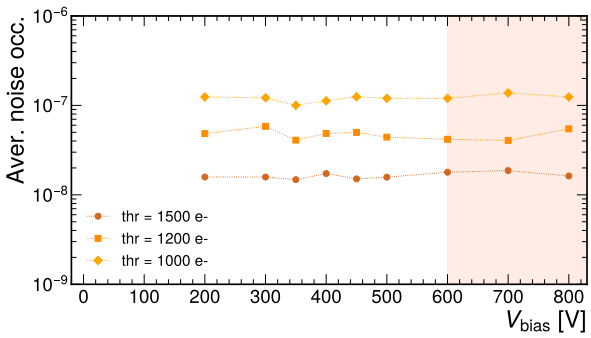

(b) Average noise occupancy after masking.

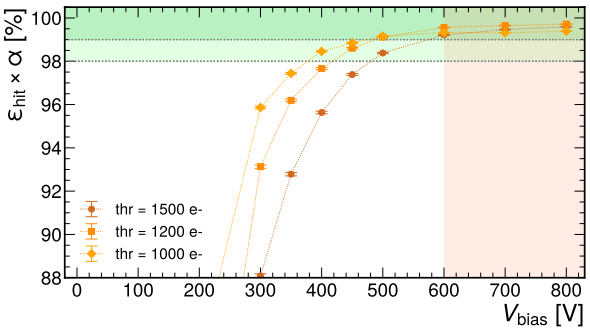

(c) Efficiency times acceptance.

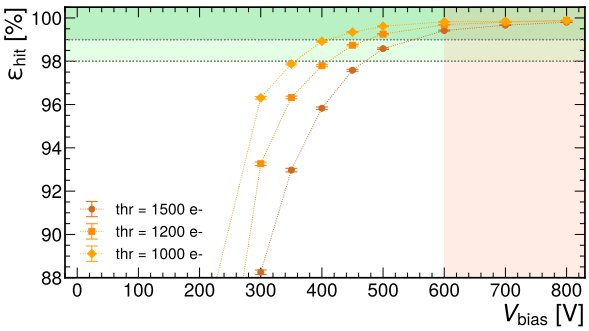

(d) Efficiency times acceptance.

Figure A.10.: Results of a bias scan for a section irradiated to $8 \times 10^{15}\,\mathrm{cm}^{-2}$, cooled to -20°C, tuned to 1000 e^- (red), 1200 e^- (green), and 1500 e^- (blue).

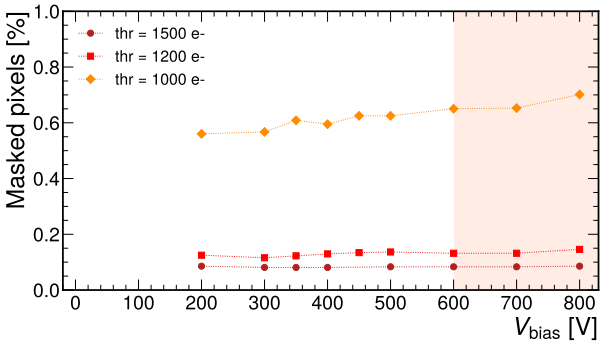

(a) Masked pixels.

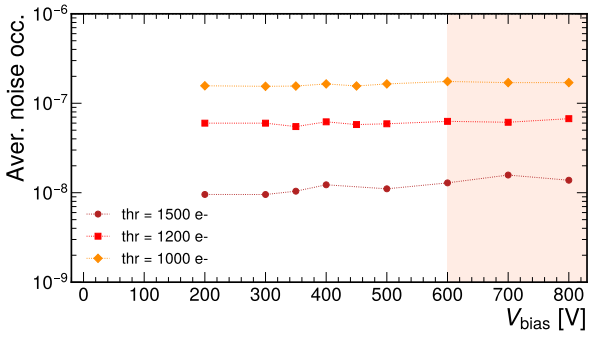

(b) Average noise occupancy after masking.

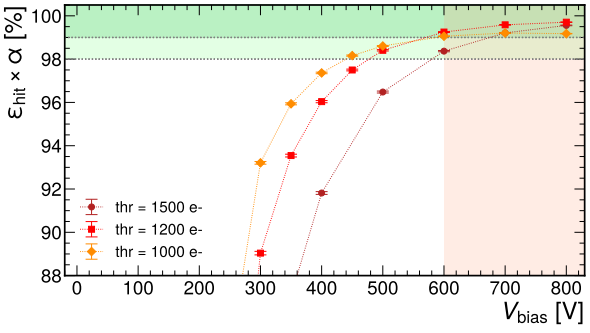

(c) Efficiency times acceptance.

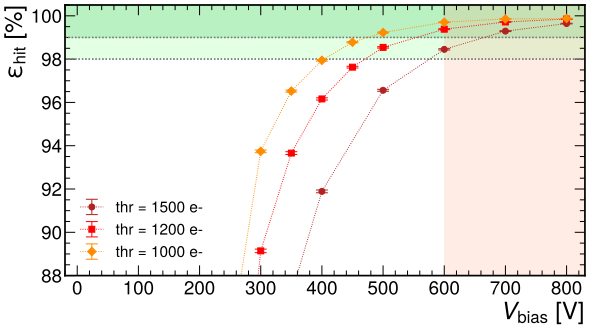

(d) Efficiency times acceptance.

Figure A.11.: Results of a bias scan for a section irradiated to $1 \times 10^{16}\,\mathrm{cm}^{-2}$, cooled to -20°C, tuned to 1000 e^- (red), 1200 e^- (green), and 1500 e^- (blue).

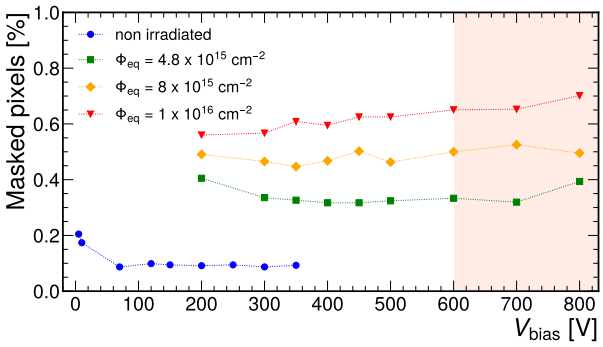

(a) Masked pixels.

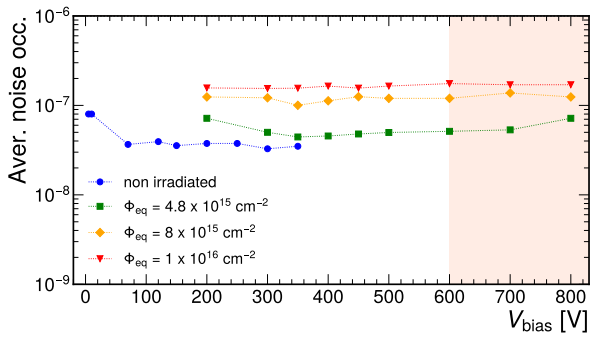

(b) Average noise occupancy after masking.

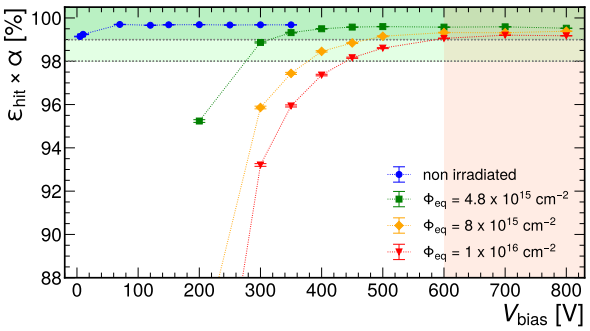

(c) Efficiency times acceptance.

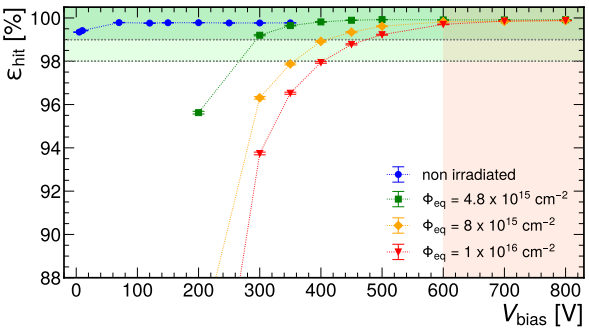

(d) Efficiency times acceptance.

Figure A.12.: Results of a bias scan for assemblies cooled to -20°C, tuned to 1000 e$^-$, with corresponding accumulated fluences of $1 \times 10^{16}\,\mathrm{cm}^{-2}$ (red), $8 \times 10^{15}\,\mathrm{cm}^{-2}$ (orange), $4.8 \times 10^{15}\,\mathrm{cm}^{-2}$ (green), and for a non-irradiated assembly (blue).

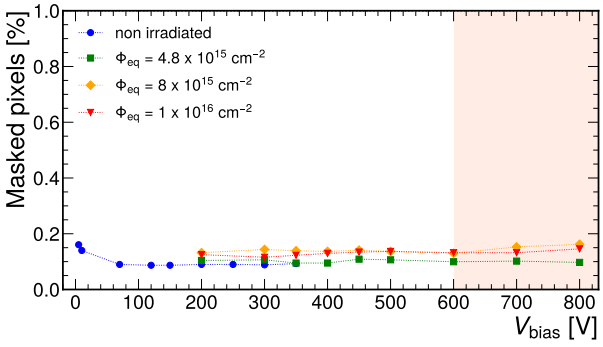

(a) Masked pixels.

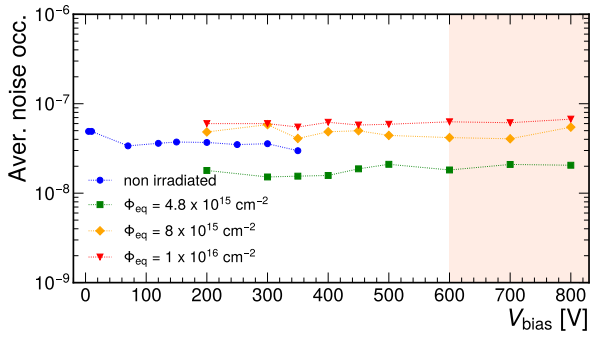

(b) Average noise occupancy after masking.

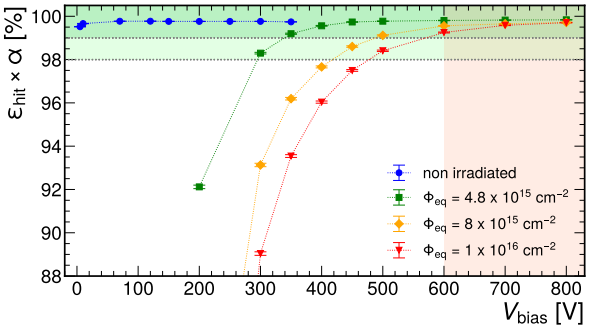

(c) Efficiency times acceptance.

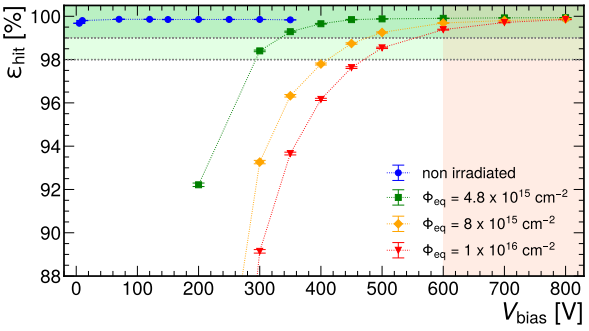

(d) Efficiency times acceptance.

Figure A.13.: Results of a bias scan for assemblies cooled to -20°C, tuned to 1200 e$^-$, with corresponding accumulated fluences of $1 \times 10^{16}\,\mathrm{cm}^{-2}$ (red), $8 \times 10^{15}\,\mathrm{cm}^{-2}$ (orange), $4.8 \times 10^{15}\,\mathrm{cm}^{-2}$ (green), and for a non-irradiated assembly (blue).

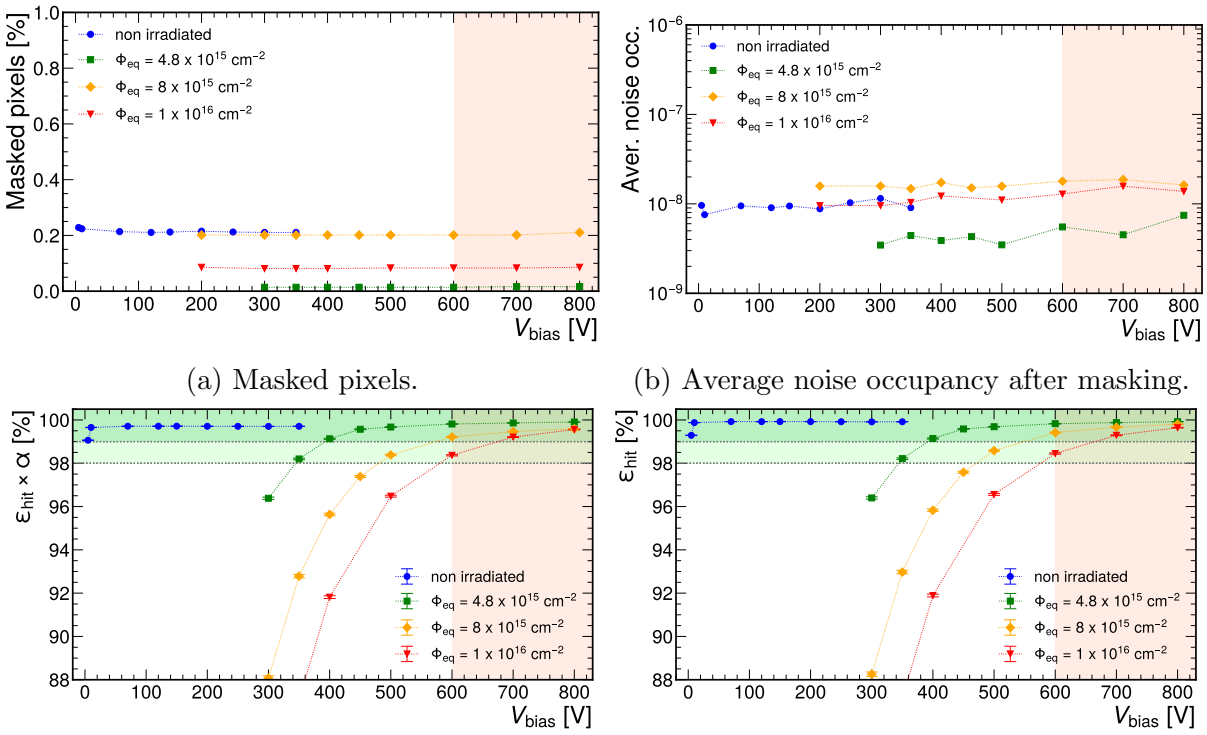

(a) Masked pixels.

(b) Average noise occupancy after masking.

(c) Efficiency times acceptance.

(d) Efficiency times acceptance.

Figure A.14.: Results of a bias scan for assemblies cooled to -20°C, tuned to 1500 e^-, with corresponding accumulated fluences of $1 \times 10^{16}\,\mathrm{cm}^{-2}$ (red), $8 \times 10^{15}\,\mathrm{cm}^{-2}$ (orange), $4.8 \times 10^{15}\,\mathrm{cm}^{-2}$ (green), and for a non-irradiated assembly (blue).

B. Appendix: Systematic studies of simulation parameters

Non-irradiated assemblies

A systematic investigation of the influence of the starting parameters on the relevant observables has been carried out.

For the threshold parameter, three values were studied: 1000 e^-, 1200 e^-, and 1500 e^-. Increasing the threshold led to a reduction in cluster size, as well as a decrease in both the most probable value (MPV) and the mean of the cluster and seed charge distributions. These trends are illustrated in Figure B.1 (a), Figure B.2 (a), and Figure B.3 (a).

The spread of the threshold was also investigated, by varying its value between 0 e^- (no threshold spread) and 350 e^- (circa five times the value measured at the test beam), keeping the mean value fixed to 1200 e^-. While increasing the spread did not affect the cluster size, it resulted in larger MPVs for the cluster and seed charge distributions. This behavior can be attributed to the enhanced contribution of events with large cluster (or seed) charges, which have a stronger influence on the mean compared to those with smaller charges. The corresponding results are presented in Figure B.1 (b), Figure B.2 (b), and Figure B.3 (b).

From the perspective of the analog front-end, increasing the electronic noise was found to produce effects equivalent to those observed when modifying the threshold spread. As shown in Figure B.1 (c), Figure B.2 (c), and Figure B.3 (c), simulations with noise values of 0 e^- (no noise) and 200 e^- (approximately twice the value measured at the test beam) were performed, confirming this correspondence.

For the crosstalk parameter, four configurations were explored: null crosstalk, as well as the minimum, average, and maximum values reported in Chapter 5. Increasing crosstalk resulted in broader cluster widths, together with higher MPVs and mean values of the cluster and seed charge distributions. These effects are displayed in Figure B.1 (d), Figure B.2 (d), and Figure B.3 (d).

Overall, these studies demonstrate the sensitivity of the observables to variations of the starting parameters. The results justify the use of the nominal values for the simulation of non-irradiated modules, measured prior to data taking, in the simulation of the test beam environment.

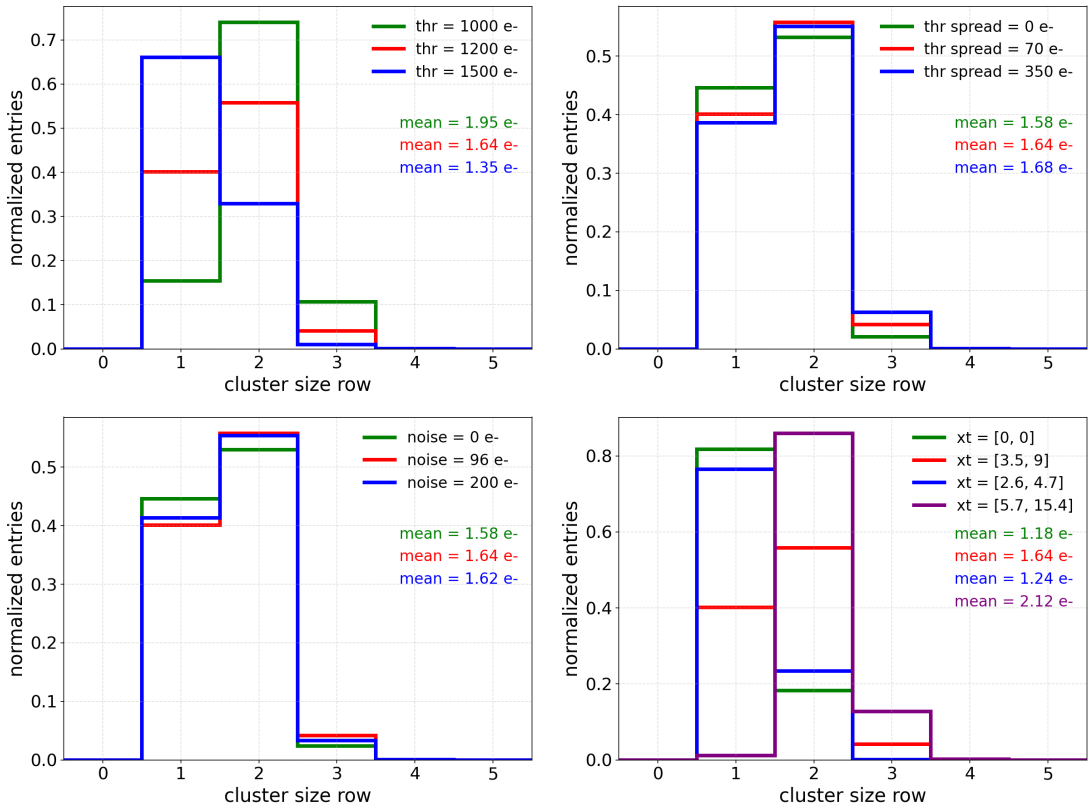

Figure B.1.: Cluster width for different threshold mean and spread, noise and crosstalk levels, respectively, for a simulated non-irradiated module biased to 120 V.

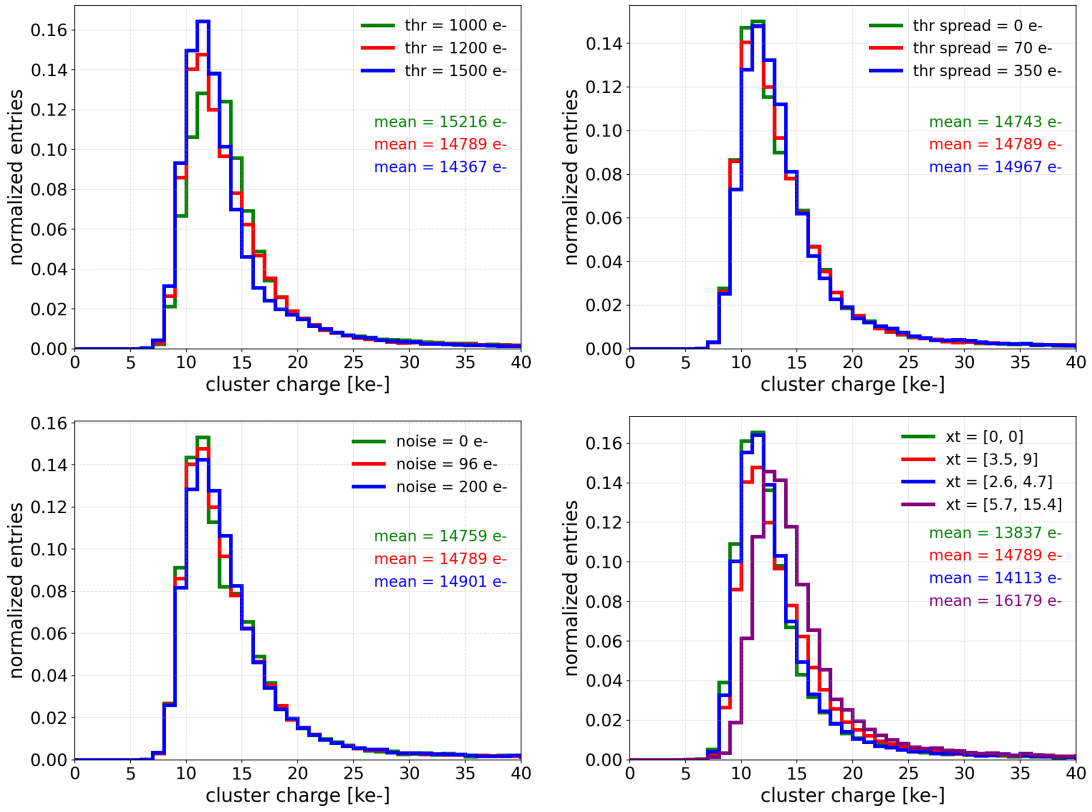

Figure B.2.: Cluster charge for different threshold mean and spread, noise and crosstalk levels, respectively, for a simulated non-irradiated module biased to 120 V.

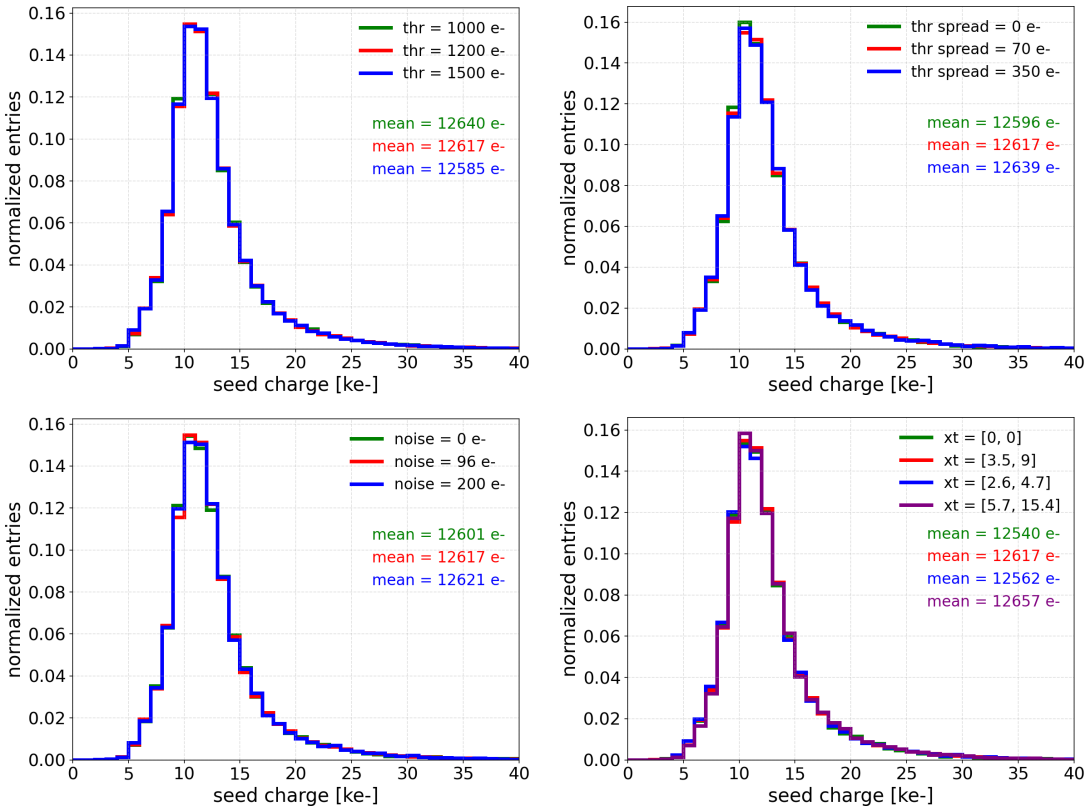

Figure B.3.: Seed charge for different threshold mean and spread, noise and crosstalk levels, respectively, for a simulated non-irradiated module biased to 120 V.

Irradiated assemblies

Systematic studies were also performed for the simulation of irradiated assemblies. Three configurations were explored for the trapping time, in addition to the one obtained with the nominal values: one with trapping times reduced by 15%, one with trapping times increased by 15%, and one with no trapping. From the distributions shown in Figure B.4, it can be observed that increasing the trapping time, or equivalently reducing the probability that a carrier is captured by a defect, leads to larger values of the cluster size, cluster charge, and seed charge. Conversely, shortening the trapping time results in a systematic reduction of the mean values of these distributions. This behaviour originates from the microscopic mechanism of charge transport in irradiated silicon: when carriers are trapped, they no longer contribute to the induced current at the readout electrode, thereby reducing the total collected signal. In contrast, longer trapping times allow a larger fraction of carriers to drift to the electrodes, increasing the collected charge per pixel.

Different combinations of Allpix Squared submodules were explored to simulate the irradiated assemblies. One of the main differences among them is the possibility to implement crosstalk. To assess its relevance, the main observables were evaluated for the two combinations of submodules that offer the possibility to implement this phenomenon, first by setting the parameters for crosstalk to their nominal values, and the by setting

them to zero. The results, shown in Figure B.5, indicate that crosstalk plays only a minor role, leading to differences in the order of 1% in the observables under study.

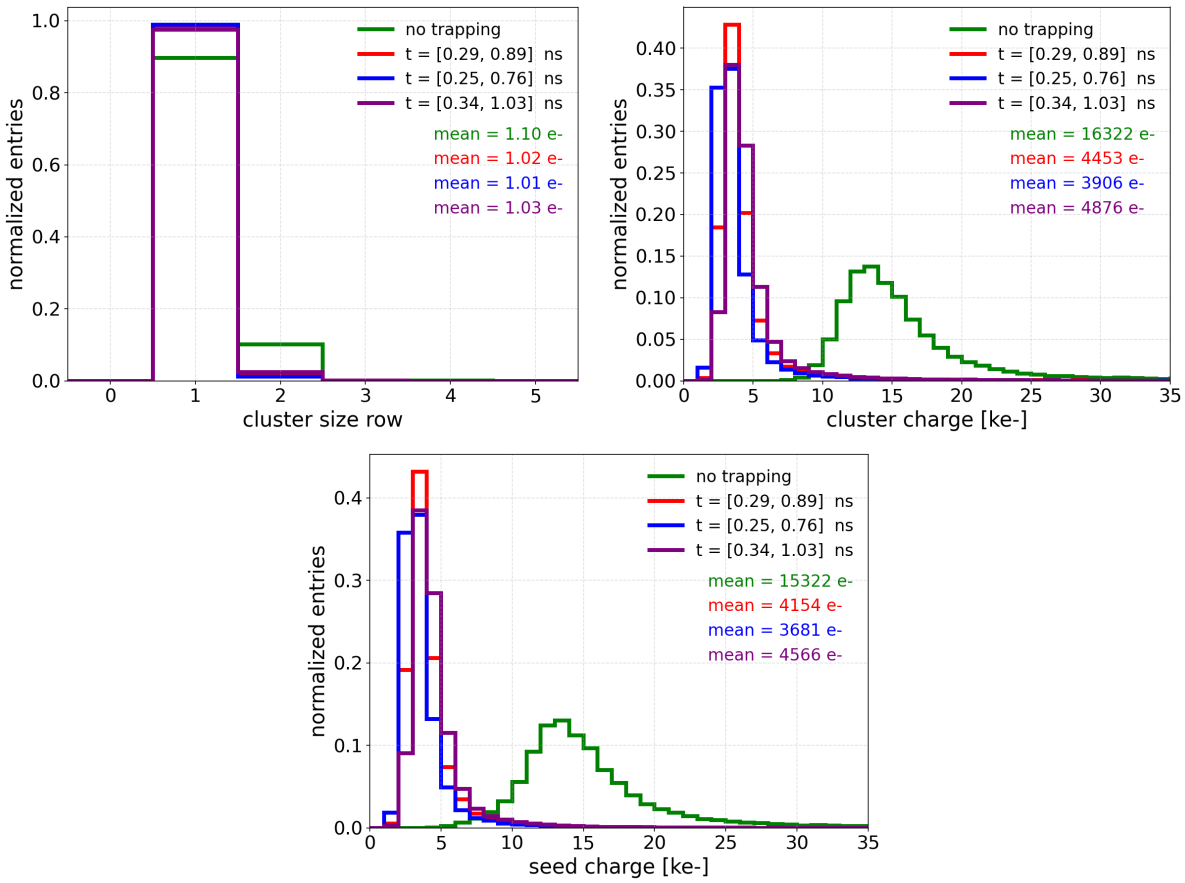

Figure B.4.: Cluster size, cluster charge and seed charge obtained for different trapping times, for a simulated irradiated module with an accumulated equivalent fluence of 8×10^{15} cm^{-2}, a set threshold of 1200 e- and a bias of 600 V.

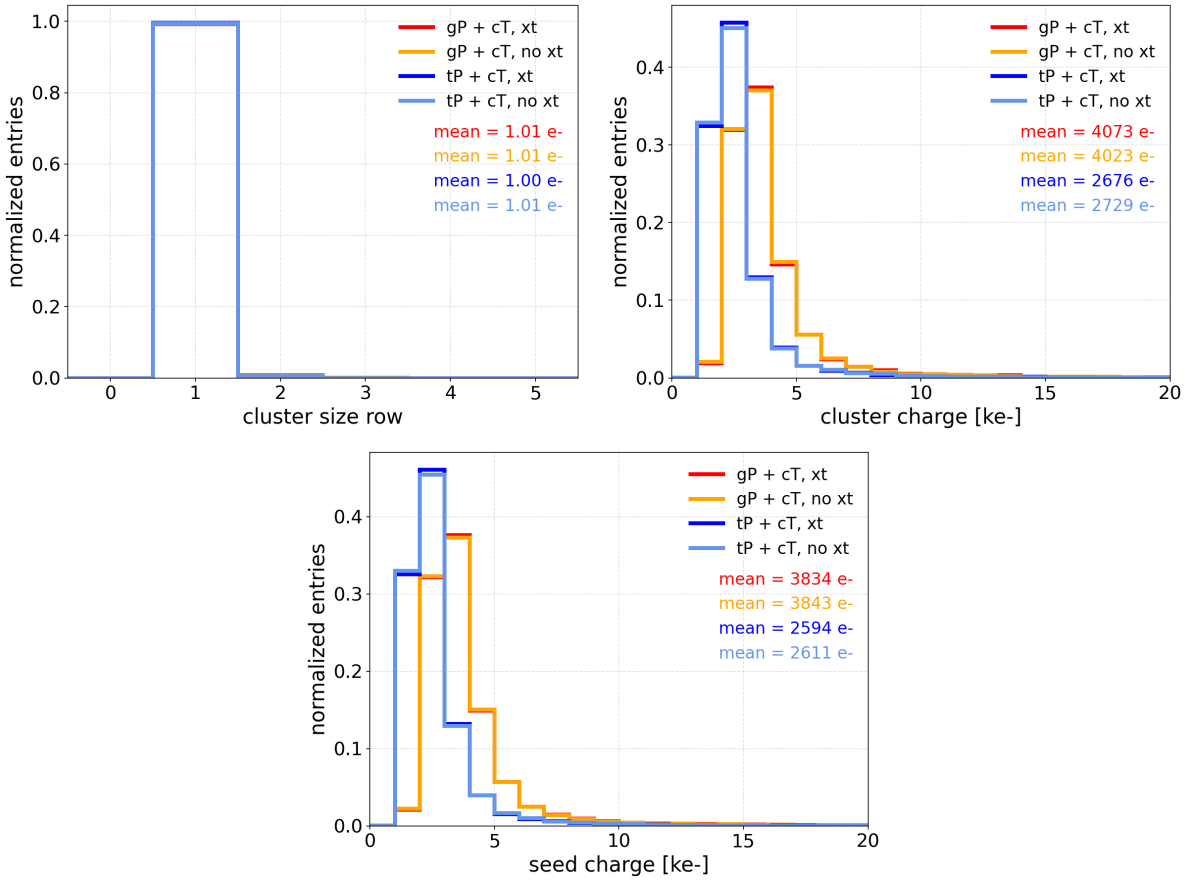

Figure B.5.: Cluster size, cluster charge and seed charge simulated with and without crosstalk for two submodules combinations: `GenericPropagation` and `CapacitiveTransfer` ("gP + cT" in the labels), and `TransientPropagation` and `CapacitiveTransfer` ("tP + cT"). These studies refer to a simulated irradiated module with an accumulated equivalent fluence of 8×10^{15} cm^{-2}, a set threshold of 1200 e- and a bias of 600 V.

C. Appendix: Simulation parameters

Sensor parameters

Table C.1.: Configuration parameters for the MIMOSA26 and RD53B_CMS pixel sensors.

Parameter	**MIMOSA26**	**RD53B_CMS**
type	monolithic	hybrid
geometry	pixel	pixel
number_of_pixels	1152 × 576	216 × 672
pixel_size	18.4 × 18.4 µm	100 × 25 µm
sensor_material	–	silicon
sensor_thickness	45 µm	150 µm
sensor_excess_top	200 µm	450 µm
sensor_excess_bottom	3000 µm	450 µm
sensor_excess_left	350 µm	450 µm
sensor_excess_right	0 µm	450 µm
bump_sphere_radius	–	15.0 µm
bump_cylinder_radius	–	10.0 µm
bump_height	–	30.0 µm
bump_offset	–	(0.0, 0) µm
chip_thickness	5 µm	150 µm
chip_excess_top	–	38.5 µm
chip_excess_bottom	–	1780 µm
chip_excess_left	–	26.5 µm
chip_excess_right	–	25 µm

Configuration file: non-irradiated assemblies

```
[Allpix]
number_of_events = 50000
detectors_file = "/path/geometry.geo"
output_directory = "/path/results"
root_file = "results.root"

[GeometryBuilderGeant4]
world_material = "air"

[DepositionGeant4]
physics_list = FTFP_BERT_EMZ
particle_type = "e-"
number_of_particles = 1
source_energy = 5.2GeV
source_position = 0um 0um -200mm
source_type = "beam"
beam_size = 5mm
beam_direction = 0 0 1
beam_divergence = 0.6mrad 0.6mrad
max_step_length = 1um

[ElectricFieldReader]
type = "mimosa26"
model = "linear"
bias_voltage = -4V
depletion_depth = 15um

[ElectricFieldReader]
name = "rd53b_214"
model = "linear"
bias_voltage = -100V
depletion_voltage = -65V

[ElectricFieldReader]
name = "rd53b_115"
model = "mesh"
file_name = "/path/E_TCAD.apf"
field_mapping = PIXEL_FULL

[GenericPropagation]
type = "mimosa26"
temperature = 290K
charge_per_step = 10
integration_time = 20ns

[GenericPropagation]
name = "rd53b_214"
temperature = 293K
charge_per_step = 10

[GenericPropagation]
name = "rd53b_115"
temperature = 253K # -20C
charge_per_step = 10
integration_time = 200ns
propagate_electrons = true
propagate_holes = true
mobility_model = "canali"

[SimpleTransfer]
```

```
name = "MIMOSA26_0","MIMOSA26_1","MIMOSA26_2","rd53b_214"
max_depth_distance = 5um

[CapacitiveTransfer]
name = "rd53b_115"
cross_coupling = true
nominal_gap = 0um
coupling_matrix = [[0 0.043 0],[0 0.868 0],[0 0.089 0]]
flip_odd_rows = true
max_depth_distance = 5um

[DefaultDigitizer]
type = "mimosa26"
electronics_noise = 13e
threshold = 60e
threshold_smearing = 4e
qdc_resolution = 1
qdc_smearing = 0e

[DefaultDigitizer]
name = "rd53b_214"
threshold = 2000e
threshold_smearing = 60e
electronics_noise = 100e

[DefaultDigitizer]
name = "rd53b_115"
threshold = 920e #1133e #1461e
threshold_smearing = 71e #70e #75e
electronics_noise = 96e #96e #97e

[DetectorHistogrammer]
name = "rd53b_115"
max_cluster_charge = 30ke

[CorryvreckanWriter]
file_name = "results"
geometry_file = "results-geo"
output_mctruth = true
reference = "MIMOSA26_2"
dut = "rd53b_115"
```

Configuration file: irradiated assemblies

```
[Allpix]
number_of_events = 50000
detectors_file = "/path/geometry.geo"
output_directory = "/path/results"
root_file = "results.root"

[GeometryBuilderGeant4]
world_material = "air"

[DepositionGeant4]
physics_list = FTFP_BERT_EMZ
particle_type = "e-"
number_of_particles = 1
source_energy = 5.2GeV
source_position = 0um 0um -200mm
source_type = "beam"
beam_size = 5mm
beam_direction = 0 0 1
beam_divergence = 0.6mrad 0.6mrad
max_step_length = 1um

[WeightingPotentialReader]
name = "rd53b_115"
model = "pad"
output_plots = true

[ElectricFieldReader]
type = "mimosa26"
model = "linear"
bias_voltage = -4V
depletion_depth = 15um

[ElectricFieldReader]
name = "rd53b_214"
model = "linear"
bias_voltage = -100V
depletion_voltage = -65V

[ElectricFieldReader]
name = "rd53b_115"
model = "mesh"
file_name = "/path/E_TCAD.apf"
field_mapping = PIXEL_FULL

[GenericPropagation]
type = "mimosa26"
temperature = 290K
charge_per_step = 10
integration_time = 20ns

[GenericPropagation]
name = "rd53b_214"
temperature = 293K
charge_per_step = 10

[GenericPropagation]
name = "rd53b_115"
temperature = 253K # -20C
charge_per_step = 10
integration_time = 200ns
```

```
propagate_electrons = true
propagate_holes = true
mobility_model = "canali"
trapping_model = "constant"
trapping_time_electron = 0.6222ns #0.2928ns #0.2292ns
trapping_time_hole = 1.909ns #0.893ns #0.7021ns
multiplication_model = "overstraeten"
output_plots = true

[SimpleTransfer]
name = "MIMOSA26_0","MIMOSA26_1","MIMOSA26_2","rd53b_214"
max_depth_distance = 5um

[InducedTransfer]
name = "rd53b_115"
max_depth_distance = 5um

[DefaultDigitizer]
type = "mimosa26"
electronics_noise = 13e
threshold = 60e
threshold_smearing = 4e
qdc_resolution = 1
qdc_smearing = 0e

[DefaultDigitizer]
name = "rd53b_214"
threshold = 2000e
threshold_smearing = 60e
electronics_noise = 100e

[DefaultDigitizer]
name = "rd53b_115"
threshold = 1180e #1185e #1202e
threshold_smearing = 84e #114e #133e
electronics_noise = 119e #131e #142e

[DetectorHistogrammer]
name = "rd53b_115"
max_cluster_charge = 30ke

[CorryvreckanWriter]
file_name = "results"
geometry_file = "results-geo"
output_mctruth = true
reference = "MIMOSA26_2"
dut = "rd53b_115"
```

Geometry file

```
[rd53b_214]
material_budget = 0.003
number_of_pixels = 432, 336
orientation = -0.11992deg,0.0882355deg,-0.112987deg
orientation_mode = "xyz"
pixel_pitch = 50um,50um
position = 898.953um,1.99278mm,-63mm
spatial_resolution = 14.4um,14.4um
time_resolution = 250ns
type = "cmsrd53b50x50"

[MIMOSA26_0]
material_budget = 0.00075
number_of_pixels = 1152, 576
orientation = -0.0585563deg,0.0494463deg,-0.10955deg
orientation_mode = "xyz"
pixel_pitch = 18.4um,18.4um
position = 728.735um,109.143um,0um
spatial_resolution = 5.3um,5.3um
time_resolution = 230us
type = "mimosa26"

[MIMOSA26_1]
material_budget = 0.00075
number_of_pixels = 1152, 576
orientation = 0.0429145deg,-0.0303668deg,0.0167304deg
orientation_mode = "xyz"
pixel_pitch = 18.4um,18.4um
position = 335.647um,279.766um,120mm
spatial_resolution = 5.3um,5.3um
time_resolution = 230us
type = "mimosa26"

[MIMOSA26_2]
material_budget = 0.00075
number_of_pixels = 1152, 576
orientation = 0.135619deg,-0.107372deg,0.205864deg
orientation_mode = "xyz"
pixel_pitch = 18.4um,18.4um
position = -3.335um,-21.688um,241mm
spatial_resolution = 5.3um,5.3um
time_resolution = 230us
type = "mimosa26"

[rd53b_115]
material_budget = 0.003
number_of_pixels = 216, 672
orientation = -0.0775785deg,-0.428229deg,-91.0688deg
orientation_mode = "xyz"
pixel_pitch = 100um,25um
position = 2.10947mm,556.372um,315mm
spatial_resolution = 28.9um,7.2um
time_resolution = 250ns
type = "cmsrd53b25x100"

[trg1]
type="box"
size = 10mm 30mm 3mm
position = 0mm 10mm -20mm
orientation = 0 0 0deg
```

```
material = "plexiglass"
role = "passive"
color = 0 0 1

[trg2]
type="box"
size = 30mm 10mm 3mm
position = -10mm 0mm -16.5mm
orientation = 0 0 0deg
material = "plexiglass"
role = "passive"
color = 0 0 1
```

Bibliography

[1] M. Thomson, Modern Particle Physics, Cambridge University Press, 2013.

[2] ATLAS Collaboration, Observation of a new particle in the search for the Standard Model Higgs boson with the ATLAS detector at the LHC, Phys. Lett. B 716 (1) (2012) 1–29. doi:https://doi.org/10.1016/j.physletb.2012.08.020.

[3] CMS Collaboration, Observation of a new boson at a mass of 125 GeV with the CMS experiment at the LHC, Phys. Lett. B 716 (1) (2012) 30–61. doi:https://doi.org/10.1016/j.physletb.2012.08.021.

[4] S. P. Martin, A Supersummetry primer, Perspectives on Supersymmetry, World Scientific, 1998, pp. 1–98. doi:10.1142/9789812839657_0001.

[5] H. Georgi, S. L. Glashow, Unity of All Elementary-Particle Forces, Phys. Rev. Lett. 32 (1974) 438–441. doi:10.1103/PhysRevLett.32.438.

[6] CMS Collaboration, The CMS experiment at the CERN LHC, J. Instrum. 3 (08) (2008) S08004–S08004. doi:10.1088/1748-0221/3/08/s08004.

[7] D. Contardo, Technical Proposal for the Phase-II Upgrade of the CMS Detector, CERN-LHCC-2015-010, LHCC-P-008, CMS-TDR-15-02 (6 2015).
URL https://cds.cern.ch/record/2020886

[8] M. E. Dinardo, The CMS Inner Tracker DAQ system for the High Luminosity upgrade of LHC: From single-chip testing, to large-scale assembly qualification, Vol. 295, EPJ Web of Conferences, EDP Sciences, 2024.

[9] S. Spannagel, Allpix2: A modular simulation framework for silicon detectors, Nucl. Instrum. Methods Phys. Res. A 901 (2018) 164–172.

[10] S. Sze, Semiconductor devices: physics and technology, John Wiley & Sons, 2008.

[11] S. Sze, Physics of Semiconductor Devices, John Wiley & Sons, 2006.

[12] A. Grove, Physics and Technology of Semiconductor Devices, John Wiley & Sons, 1967.

[13] G. Kramberger, Investigation of irradiated silicon detectors by edge-tct, IEEE Trans. Nucl. Sci. 57 (4) (2010) 2294–2302.

[14] C. Leroy and P. G. Rancoita, Principles of Radiation Interaction in Matter and Detection, World Scientific, 2016.

[15] P. A. Zyla, Review of Particle Physics, PTEP (2020). doi:10.1093/ptep/ptaa104.

[16] J. Deasy, ICRU report 49, Stopping powers and ranges for protons and alpha particles (1994).

[17] H. Bichsel, Straggling in thin silicon detectors, Rev. Mod. Phys. 60 (1988) 663–699. doi:10.1103/RevModPhys.60.663.

[18] F. Scholze, Determination of the electron–hole pair creation energy for semiconductors from the spectral responsivity of photodiodes, Nucl. Instrum. Methods Phys. Res. A 439 (2-3) (2000) 208–215.

[19] G. Lynch, O. Dahl, Approximations to multiple Coulomb scattering, Nucl. Instr. and Meth. A 58 (1991). doi:https://doi.org/10.1016/0168-583X(91)95671-Y.

[20] E. Moli, Theorie der streuung schneller geladener teilchen. i. einzelstreuung amabgeschirmten coulomb-field, Z. Naturforsch (1947).

[21] Y. S. Tsai, Pair production and bremsstrahlung of charged leptons, Rev. Mod. Phys. 46 (4) (1974) 815.

[22] H. J. Barnaby, Total ionizing dose effects in modern CMOS technologies, IEEE Trans. Nucl. Sci. 53 (6) (2006) 3103–3121.

[23] T. R. Oldham, F. McLean, Total ionizing dose effects in MOS oxides and devices, IEEE Trans. Nucl. Sci. 50 (3) (2003) 483–499.

[24] J. Schwandt, Optimization of the radiation hardness of silicon pixel sensors for high X-ray doses using TCAD simulations, J. Instrum. 7 (01) (2012) C01006.

[25] T. Poehlsen, Charge losses in segmented silicon sensors at the Si–SiO2 interface, Nucl. Instrum. Meth. A 700 (2013) 22–39. doi:https://doi.org/10.1016/j.nima.2012.10.063.

[26] J. Schwandt, Design of a radiation hard silicon pixel sensor for X-ray science, Tech. rep., Hamburg University (Germany). Deptartment of Physics (2014).

[27] J. Zhang, X-ray radiation damage studies and design of a silicon pixel sensor for science at the XFEL (2013).

[28] J. Crawford, Radiation effects in diamond lattice semiconductors, IEEE Trans. Nucl. Sci. 10 (5) (1963).

[29] M. Huhtinen, Simulation of non-ionising energy loss and defect formation in silicon, Nucl. Instrum. Meth. A 491 (1) (2002) 194–215. doi:https://doi.org/10.1016/S0168-9002(02)01227-5.

[30] M. Moll, Radiation damage in silicon particle detectors: Microscopic defects and macroscopic properties, Ph.D. thesis, Hamburg U. (1999).

[31] M. Moll, Displacement Damage in Silicon Detectors for High Energy Physics, IEEE Trans. Nucl. Sci. 65 (8) (2018) 1561–1582. doi:10.1109/TNS.2018.2819506.

[32] L. R. Weisberg and H. Schade, A Technique for Trap Determinations in Low-Resistivity Semiconductors, J. Appl. Phys. 39 (1968). doi:https://doi.org/10.1063/1.1655936.

[33] D. V. Lang, Deep-level transient spectroscopy: A new method to characterize traps in semiconductors, J. Appl. Phys. 45 (1974). doi:https://doi.org/10.1063/1.1663719.

[34] G. Pellegrini, et al., Technology developments and first measurements of low gain avalanche detectors (LGAD) for high energy physics applications, Nucl. Instrum. Methods Phys. Res. A 765 (2014) 12–16.

[35] M. Ferrero, Radiation resistant LGAD design, Nucl. Instrum. Methods Phys. Res. A 919 (2019) 16–26.

[36] V. Eremin, The origin of double peak electric field distribution in heavily irradiated silicon detectors, Nucl. Instrum. Meth. A 476 (3) (2002) 556–564. doi:https://doi.org/10.1016/S0168-9002(01)01642-4.

[37] G. Kramberger, Effective trapping time of electrons and holes in different silicon materials irradiated with neutrons, protons and pions, Nucl. Instrum. Meth. A (2002). doi:https://doi.org/10.1016/S0168-9002(01)01263-3.

[38] Synopsys TCAD, https://www.synopsys.com/, accessed: 2022-02-03 (2022).

[39] J. Schwandt, A new model for the TCAD simulation of the silicon damage by high fluence proton irradiation, IEEE Nuclear Science Symposium and Medical Imaging Conference Proceedings (NSS/MIC), 2018, pp. 1–3. doi:10.1109/NSSMIC.2018.8824412.

[40] I. Pintilie, Radiation-induced point-and cluster-related defects with strong impact on damage properties of silicon detectors, Nucl. Instrum. Methods Phys. Res. A 611 (1) (2009) 52–68.

[41] L. Rossi, Pixel detectors: From fundamentals to applications, Springer Science & Business Media, 2006.

[42] S. Cihangir, S. Kwan, Characterization of indium and solder bump bonding for pixel detectors, Nucl. Instrum. Methods Phys. Res. A 476 (3) (2002) 670–675.

[43] M. Swartz, Type inversion in irradiated silicon: a half truth, arXiv preprint physics/0409049 (2004).

[44] C. Jacoboni, A review of some charge transport properties of silicon, Solid-State Electronics 20 (2) (1977) 77–89.

[45] F. Feindt, Silicon Pixel Sensors in the Inner Tracking System of the CMS Experiment, Ph.D. thesis, Universität Hamburg (2021).

[46] P. Schütze, Silicon pixel detectors. Performance after irradiation and application in three-dimensional imaging, Tech. rep., Deutsches Elektronen-Synchrotron, Hamburg (Germany) (2019).

[47] W. Shockley, Currents to conductors induced by a moving point charge, J. Appl. Phys. 9 (10) (1938) 635–636. doi:10.1063/1.1710367.

[48] S. Ramo, Currents Induced by Electron Motion, Proceedings of the IRE 27 (9) (1939) 584–585. doi:10.1109/JRPROC.1939.228757.

[49] H. Spieler, Semiconductor Detector Systems, Oxford University Press, 2005.

[50] H. Kolanoski, N. Wermes, Particle Detectors: Fundamentals and Applications, Oxford University Press, USA, 2020.

[51] F. Feindt, Silicon pixel sensors in the inner tracking system of the cms experiment, Ph.D. thesis, Staats-und Universitätsbibliothek Hamburg Carl von Ossietzky (2021).

[52] R. Turchetta, Spatial resolution of silicon microstrip detectors, Nucl. Instrum. Meth. A 335 (1) (1993) 44–58. doi:https://doi.org/10.1016/0168-9002(93)90255-G.

[53] E. Belau, Charge collection in silicon strip detectors, Nuclear Instruments and Methods in Physics Research 214 (2-3) (1983) 253–260.

[54] M. Boronat, Physical limitations to the spatial resolution of solid-state detectors, IEEE Trans. Nucl. Sci. 62 (1) (2015) 381–386. doi:10.1109/TNS.2014.2376941.

[55] A. M. Sirunyan, Particle-flow reconstruction and global event description with the CMS detector, J. Instrum. 12 (10) (2017) P10003–P10003. doi:10.1088/1748-0221/12/10/p10003.

[56] The Phase-2 Upgrade of the CMS Tracker, Tech. rep., CERN, Geneva (Jun 2017). doi:10.17181/CERN.QZ28.FLHW.

[57] M. Benedikt, LHC Design Report, CERN Yellow Reports: Monographs, CERN, Geneva, 2004. doi:10.5170/CERN-2004-003-V-3.
URL http://cds.cern.ch/record/823808

[58] L. Evans, LHC machine, J. Instrum. 3 (08) (2008) S08001.

[59] The ATLAS Collaboration, The ATLAS experiment at the CERN large hadron collider (2008).

[60] The CMS Collaboration, The CMS experiment at the CERN LHC (2008).

[61] K. Aamodt, Quintana, The ALICE experiment at the CERN LHC, J. Instrum. 3 (08) (2008) S08002.

[62] A. Augusto, The LHCb detector at the LHC, J. Instrum. 3 (08) (2008) S08005.

[63] G. Apollinari, High-Luminosity Large Hadron Collider (HL-LHC): Technical Design Report V. 0.1, CERN Yellow Reports 4/2017 (2017). doi:10.23731/CYRM-2017-004.

[64] Full summary: proton-proton collisions since 2010 (Run 1 + Run 2 + Run 3), https://twiki.cern.ch/twiki/bin/view/CMSPublic/LumiPublicResults#Full_summary_proton_proton_colli, Accessed: 2025 (2025).

[65] S. R. Davis, CMS slice image view (transverse/longitudinal/3-D) (2016).
URL http://cds.cern.ch/record/2204863

[66] The CMS electromagnetic calorimeter project: Technical Design Report, Technical design report. CMS, CERN, Geneva, 1997.
URL https://cds.cern.ch/record/349375

[67] The CMS hadron calorimeter project: Technical Design Report, Technical design report. CMS, CERN, Geneva, 1997.
URL https://cds.cern.ch/record/357153

[68] The CMS magnet project: Technical Design Report, Technical design report. CMS, CERN, Geneva, 1997. doi:10.17181/CERN.6ZU0.V4T9.
URL https://cds.cern.ch/record/331056

[69] J. G. Layter, The CMS muon project: Technical Design Report, Technical design report. CMS, CERN, Geneva, 1997.
URL https://cds.cern.ch/record/343814

[70] G. Bayatyan, CMS TriDAS project: Technical Design Report, Volume 1: The Trigger Systems, Technical design report. CMS.
URL http://cds.cern.ch/record/706847

[71] S. Cittolin, A. Rácz, P. Sphicas, CMS The TriDAS Project: Technical Design Report, Volume 2: Data Acquisition and High-Level Trigger. CMS trigger and data-acquisition project, Technical design report. CMS, CERN, Geneva, 2002.
URL https://cds.cern.ch/record/578006

[72] G. Bayatian, J. D'Hondt, S. De Weirdt, J. Heyninck, R. Goorens, S. Lowette, S. Tavernier, L. Van Lancker, Cms physics: Technical design report. v. 1: Detector performance and software, CERN-LHCC-2006-001, CMS-TDR-008-1 1 (2006).

[73] V. Karimäki, The CMS tracker system project: Technical Design Report, Technical design report. CMS, CERN, Geneva, 1997.
URL https://cds.cern.ch/record/368412

[74] The CMS tracker: addendum to the Technical Design Report, Technical design report. CMS, CERN, Geneva, 2000.
URL https://cds.cern.ch/record/490194

[75] Tracker Group of the CMS Collaboration and others, The CMS Phase-1 pixel detector upgrade, arXiv preprint arXiv:2012.14304 (2020).

[76] CMS collaboration and others, Description and performance of track and primary-vertex reconstruction with the CMS tracker, J. Instrum. 9 (10) (2014) P10009.

[77] W. Adam, The CMS phase-1 pixel detector upgrade, J. Instrum. 16 (2021). doi:10.1088/1748-0221/16/02/p02027.

[78] J. Sonneveld, Commissioning and first results from the cms phase 1 upgrade pixel detector, arXiv preprint arXiv:1807.08987 (2018).

[79] J. C. Chistiansen, M. L. Garcia-Sciveres, RD Collaboration Proposal: Development of pixel readout integrated circuits for extreme rate and radiation, Tech. rep., CERN, Geneva (2013).
URL http://cds.cern.ch/record/1553467

[80] J. Schwandt, CMS Pixel detector development for the HL-LHC, Nucl. Instrum. Meth. A 924 (2019) 59–63. doi:https://doi.org/10.1016/j.nima.2018.08.121.

[81] M. Garcia-Sciveres, The RD53A Integrated Circuit, Tech. Rep. CERN-RD53-PUB-17-001, CERN, Geneva (Oct 2017).
URL https://cds.cern.ch/record/2287593

[82] F. Loddo, RD53 pixel chips for the ATLAS and CMS Phase-2 upgrades at HL-LHC, Nucl. Instrum. Methods Phys. Res. A 1067 (2024) 169682.

[83] "Fraunhofer IZM", https://www.izm.fraunhofer.de, Accessed: 2025 (2022).

[84] Ansys Fluent Software, Ansys.
URL https://www.ansys.com/products/fluids/ansys-fluent

[85] FBK, Fondazione bruno kessler.
URL https://sd.fbk.eu/en

[86] Tracker Group of the CMS Collaboration, Evaluation of 3D pixel silicon sensors for the CMS Phase-2 Inner Tracker, To be submitted to: Nucl. Instrum. Methods Phys. Res. A.

[87] G.-F. Dalla Betta, Development of a new generation of 3D pixel sensors for HL-LHC, Nucl. Instrum. Methods Phys. Res. A 824 (2016) 386–387, frontier Detectors for Frontier Physics: Proceedings of the 13th Pisa Meeting on Advanced Detectors. doi:https://doi.org/10.1016/j.nima.2015.08.032.
URL https://www.sciencedirect.com/science/article/pii/S0168900215009663

[88] ICEMOS, Icemos technology.
URL https://icemostech.com

[89] L. Gaioni, and RD53 Collaboration, Test results and prospects for RD53A, a large scale 65 nm CMOS chip for pixel readout at the HL-LHC, Nucl. Instrum. Methods Phys. Res. A 936 (2019) 282–285.

[90] F. Krummenacher, Pixel detectors with local intelligence: an ic designer point of view, Nucl. Instrum. Methods Phys. Res. A 305 (3) (1991) 527–532.

[91] L. Gaioni, Optimization of the 65-nm CMOS Linear Front-End Circuit for the CMS Pixel Readout at the HL-LHC, IEEE Trans. Nucl. Sci. 68 (11) (2021) 2682–2692.

[92] H. Träff, Novel approach to high speed cmos current comparators, Electronics Letters 28 (3) (1992) 310–311.

[93] L. Gaioni, RD53 analog front-end processors for the ATLAS and CMS experiments at the High-Luminosity LHC, in: 28th International Workshop on Vertex Detectors (Vertex 2019), Sissa Medialab, 2019, p. 021.

[94] G. Steinbrück, Development of planar pixel sensors for the CMS Inner Tracker at the High-Luminosity LHC, Nucl. Instrum. Meth. A 978 (2020) 164438. doi:https://doi.org/10.1016/j.nima.2020.164438.

[95] L. D. of the CMS Collaboration, Analysis of threshold oscillations observed in CMS Phase 2 Inner Tracker modules, Tech. Rep. 3, CERN, Geneva (2025). doi:10.1393/ncc/i2025-25128-8.
URL https://cds.cern.ch/record/2908786

[96] K. Kundert, The Designer's Guide to SPICE and SPECTRE®, Springer Science & Business Media, 2006.

[97] S. S. Platform, X. Spectre, Cadence design systems, inc.

[98] R. Diener, The DESY II test beam facility, Nucl. Instr. and Meth. A 922 (2019). doi:https://doi.org/10.1016/j.nima.2018.11.133.

[99] H. Jansen, Performance of the EUDET-type beam telescopes, EPJ Techniques and Instrumentation 3 (2016). doi:10.1140/epjti/s40485-016-0033-2.

[100] C. Hu-Guo, First reticule size MAPS with digital output and integrated zero suppression for the EUDET-JRA1 beam telescope, Nucl. Instr. and Meth. A 623 (2010). doi:https://doi.org/10.1016/j.nima.2010.03.043.

[101] C. Kleinwort, General broken lines as advanced track fitting method, Nucl. Instrum. Methods Phys. Res. A 673 (2012) 107–110.

[102] D. Cussans, Description of the JRA1 Trigger Logic Unit (TLU), v0.2c, Tech. rep., Univerity of Bristol (2009).

[103] P.Ahlburg, EUDAQ-a data acquisition software framework for common beam telescopes, JINST 15 (01) (2020) P01038. arXiv:1909.13725, doi:10.1088/1748-0221/15/01/P01038.

[104] M. E. Dinardo, The Data Acquisition System to Test and Characterize the Pixel Detector Modules of the CMS Inner Tracker for the High Luminosity Upgrade of LHC, in: 2021 IEEE Nuclear Science Symposium and Medical Imaging Conference (NSS/MIC), IEEE, 2021, pp. 1–7.

[105] M. Pesaresi, The FC7 AMC for generic DAQ & control applications in CMS, J. Instrum. 10 (03) (2015) C03036.

[106] J. Schwandt, E. Fretwurst, R. Klanner, I. Pintilie, J. Zhang, Optimization of the radiation hardness of silicon pixel sensors for high x-ray doses using tcad simulations, J. Instrum. 7 (01) (2012) C01006.

[107] D. Dannheim, Corryvreckan: a modular 4D track reconstruction and analysis software for test beam data, J. Instrum. 16 (03) (2021) P03008.

[108] G. Flucke, CMS silicon tracker alignment strategy with the Millepede II algorithm, J. Instrum. 3 (09) (2008) P09002.

[109] A. Lazzaro, L. Moneta, Minuit package parallelization and applications using the roofit package, in: Journal of Physics: Conference Series, Vol. 219, IOP Publishing, 2010, p. 042044.

[110] ROOT: TEfficiency() Class Reference), https://root.cern.ch/doc/master/classTEfficiency.html#ae80c3189bac22b7ad15f57a1476ef75b, Accessed: 2025 (2025).

[111] R. L. Workman, Review of Particle Physics, Prog. Theor. Exp. Phys. 2024 (8) (2024) 083C01. doi:10.1093/ptep/ptae072.

[112] M. Antonello, Precision determination of the track-position resolution of beam telescopes, Nucl. Instrum. Methods Phys. Res. A 1072 (2025) 170185.

[113] G. Steinbrueck, Radiation Hard Pixel Sensors for the Phase 2 Upgrade of the CMS Inner Tracker, Tech. rep. (2024).

[114] C. Lasaosa, Test beam results on 3d pixel sensors for the cms tracker upgrade at the high-luminosity lhc, JINST 19 (CMS-CR-2024-182) (2024) C03039.

[115] M. Hajheidari, Charge collection of irradiated silicon pad diodes and characterization of pixel sensor for the CMS experiment, Ph.D. thesis, Staats-und Universitätsbibliothek Hamburg Carl von Ossietzky (2022).

[116] C. Krause, Test beam performance of pixel detectors for the inner tracker upgrade of the atlas experiment, Tech. rep., ATL-COM-ITK-2024-002 (2024).

[117] A. Ebrahimi, Position reconstruction for segmented detectors, Nucl. Instrum. Methods Phys. Res. A 1014 (2021) 165744.

[118] W. Adam, Evaluation of planar silicon pixel sensors with the rd53a readout chip for the phase-2 upgrade of the cms inner tracker, JINST 18 (11) (2023) P11015.

[119] V. Chiochia, Simulation of heavily irradiated silicon pixel sensors and comparison with test beam measurements, IEEE transactions on nuclear science 52 (4) (2005) 1067–1075.

[120] V. Chiochia, A double junction model of irradiated silicon pixel sensors for LHC, Nucl. Instrum. Methods Phys. Res. A 568 (1) (2006) 51–55.

[121] E. Daubie, P-type silicon strip sensors for the new CMS tracker at HL-LHC, J. Instrum. 12 (P06018) (2017).

[122] G. Steinbruck, Experimental study of different silicon sensor options for the upgrade of the CMS Outer Tracker, JINST 15 (arXiv: 2001.02023) (2020).

[123] S. Agostinelli, Geant4—a simulation toolkit, Nucl. Instrum. Meth. A 506 (3) (2003) 250–303. doi:https://doi.org/10.1016/S0168-9002(03)01368-8.

[124] U. Fano, Ionization yield of radiations. ii. the fluctuations of the number of ions, Physical Review 72 (1) (1947) 26.

[125] R. Van Overstraeten, H. De Man, Measurement of the ionization rates in diffused silicon pn junctions, Solid-State Electronics 13 (5) (1970) 583–608.

[126] Allpix Squared GitLab, `https://gitlab.cern.ch/allpix-squared/allpix-squared/-/tree/master/models?ref_type=heads`, accessed: 2025-08-07 (2025).

[127] V. Bhopatkar, Argonne Pixel Tracking Telescope at the Fermilab Test Beam Facility, JINST 17 (11) (2022) P11030.

[128] D. Dannheim, Combining TCAD and Monte Carlo methods to simulate CMOS pixel sensors with a small collection electrode using the Allpix2 framework, Nucl. Instrum. Methods Phys. Res. A 964 (2020) 163784.

[129] M. Bomben, Simulation of irradiated hybrid planar pixels modules at fluences expected at hl-lhc, arXiv preprint arXiv:2506.10823 (2025).

Acknowledgments

First, I would like to express my gratitude to Erika Garutti, for the opportunity to work in this field and for providing helpful comments and advice throughout this journey.

I am deeply grateful to Jörn Schwandt, Georg Steinbrück and Massimiliano Antonello for providing valuable advice on the practical aspects of pixel sensors, sharing their expertise, and patiently answering my questions.

I would like to thank Chin-Chia Kuo for his insightful feedback and constructive criticism, which have significantly contributed to the quality of my research.

I am sincerely grateful to Luigi Gaioni, Mauro Dinardo, Elisabetta Gallo, Marco Meschini, Antonio Cassese, Anna Macchiolo and Stella Orfanelli for their guidance, insightful discussions, and steady support. Their clear suggestions and generous sharing of experience greatly shaped my approach and strengthened this work.

A massive, heartfelt thank you to Annika Vauth, Christoph Krieger, Hakan Wennlöf and Branislav Ristic, for being some of the kindest, most knowledgeable people I ever had the chance to meet, who helped me in countless ways through the last four years. I will never be able to put my gratitude into words.

When I met Lukas Eikelmann, Carmen Villalba and Lisa Herbers, I didn't know they would become my new family. I can't believe how lucky I was, stumbling into them.

I would like to thank my family for their unwavering support, patience, and encouragement throughout the course of my doctoral studies.

Last, I thank Maria Chiara, for being everything that matters, the love that brightens every day, and the most extraordinary person I ever met. This work is dedicated to you.

Eidesstattliche Versicherung
Declaration on Oath

I hereby declare and affirm that this doctoral dissertation is my own work and that I have not used any aids and sources other than those indicated. If electronic resources based on generative artificial intelligence (gAI) were used in the course of writing this dissertation, I confirm that my own work was the main and value-adding contribution and that complete documentation of all resources used is available in accordance with good scientific practice. I am responsible for any erroneous or distorted content, incorrect references, violations of data protection and copyright law or plagiarism that may have been generated by the gAI.

Hamburg, den 29.09.2025

Unterschrift der Doktorandin / des Doktoranden